Université de Caen/Basse-Normandie
U.F.R. de Sciences

Ecole Doctorale S.I.M.E.M.

THÈSE

présentée par

Mr. YAZIDJIAN Chabouh

et soutenue

le 20 Décembre 2006

en vue de l'obtention du

DOCTORAT de l'UNIVERSITE de CAEN
Spécialité : Constituants élémentaires
(*Arrêté du 07 août 2006*)

A new detector setup for ISOLTRAP and test of the Isobaric Multiplet Mass Equation

MEMBRES DU JURY :

Prof. Dr.	HEINZ-JÜRGEN KLUGE, University of Heidelberg	(Rapporteur)
Dr. habil.	KLAUS BLAUM, University of Mainz	(Rapporteur)
Mr.	NICOLAS ALAMANOS, Docteur d'état, CEA, DAPNIA	
Mr.	OSCAR NAVILIAT, Professeur, Université de Caen	
Mr.	GILLES BAN, Maître de conférence, LPC Caen	(Directeur de thèse)

A mes parents.

“Es ist leichter einen Atomkern zu spalten als ein Vorurteil.”

“It is easier to break an atomic nucleus than a prejudice.”

“Il est plus facile de briser un noyau atomique qu’un préjugé.”

Albert Einstein (1879-1955)

Table of Contents

List of Figures

List of Tables

Chapter 1

Introduction

In biology the DNA is the genetic fingerprint, which uniquely defines any living being. It comprises a large amount of information and particularities like hair and eye color. Thus, to unravel its mysteries will lead to a deeper understanding in the functioning of biologic systems. The counterpart of the DNA in nuclear physics is the mass of the atomic nucleus. It can be seen as a characteristic and unique fingerprint for thousands of different – mostly unstable – nuclides naturally occurring or artificially produced. All the information on the nuclear structure and the properties of the nuclides are hidden within this single mass value, and thus within the corresponding binding energy.

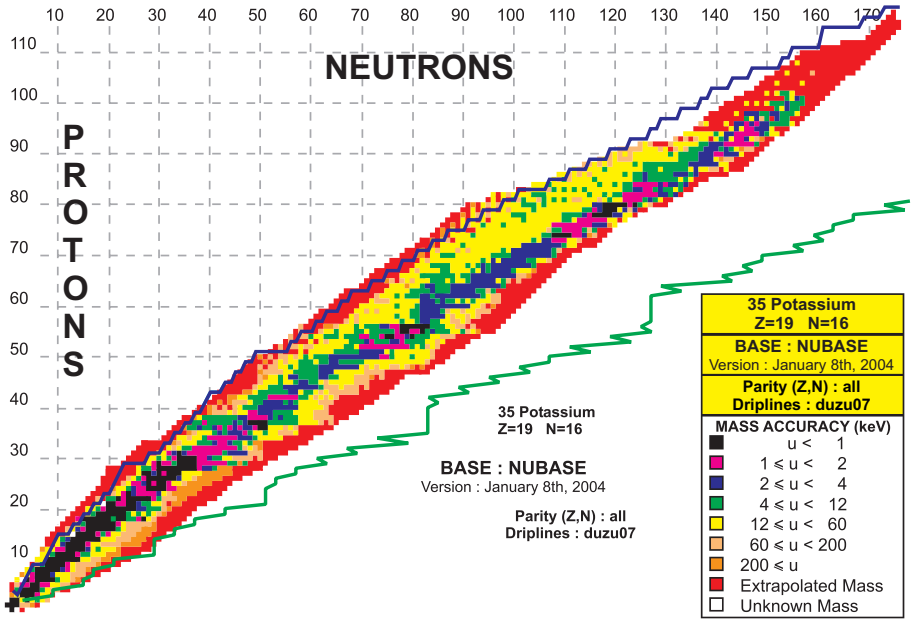

FIGURE 1.1: *Uncertainties of the experimental or extrapolated mass excess values [Audi04*]*[1].

[1]Notation: not quotable information, or references not available in journals are indexed with an asterisk.

In Fig. 1.1 the uncertainty on the mass excess for the about 3200 currently known nuclides is plotted where the absolute uncertainty is given with a color code (see legend)[2]. Except for the stables masses that are known with a relative mass precision of up to $\sigma(m)/m = 10^{-11}$ [Rain04], most of the short-lived nuclides are determined with a precision that ranges from 10^{-5} to 10^{-8} [AME03, Lunn03].

In the last decade, dramatic improvements in mass spectrometry have been achieved with the development of Penning trap-based experiments [Klug93, Blau03b, Audi06, Blau06]. The tandem Penning trap experiment ISOLTRAP is the pioneering experiment installed at the on-line separator ISOLDE [Kugl00] at CERN (Geneva). It is dedicated to high-precision mass measurements of short-lived nuclides. The measurement principle is based on the determination of the cyclotron frequency of the stored ions:

$$\nu_c = \frac{1}{2\pi} \cdot \frac{q}{m} \cdot B, \tag{1.1}$$

where q/m is the charge-to-mass ratio of the ion of interest and B the magnetic field strength in the trap region. The ISOLTRAP mass spectrometer achieves a resolving power of up to $R = 10^7$ for the separation of contaminating ions or isomers, and a relative mass uncertainty of typically $\sigma(m)/m = 10^{-8}$ [Kell03a] for most measured nuclides, some of them with less than 100 ms half-lives [Kell04a]. The Penning trap measurements do not only provide high-precision measurements but also high-accuracy mass determination. Those two notions, as illustrated in Fig. 1.2, are fundamentally complementary.

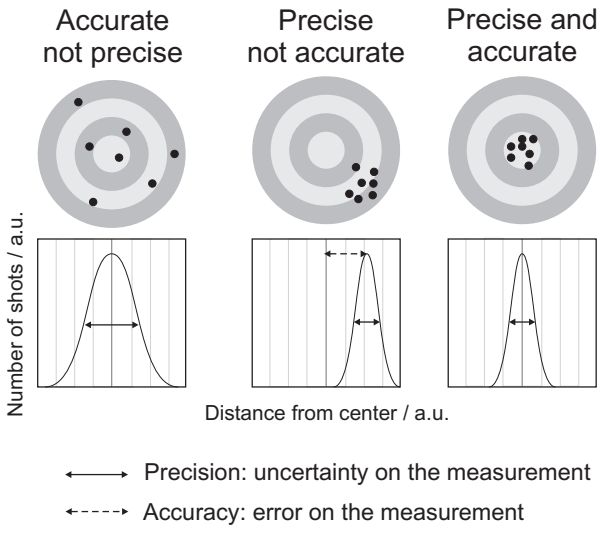

FIGURE 1.2: *Precision and accuracy, two complementary notions.*

[2]From Einstein's relation: $E = mc^2$, where E is the energy of the nuclide, m its mass and c the speed of light in vacuum, the mass should be expressed in 'keV $\cdot$ c^{-2}'. To simplify the notation the usual normalization $c = 1$ is used and the masses are expressed in 'keV'.

As an example, the mass determination of ^{22}Mg ([Mukh04b] and references therein) provides high-precision and accuracy for an astrophysics case. In the literature [AME03] two precise mass values were given for ^{22}Mg, but they were deviating by 3 standard deviations. Therefore one of them was assumed not to be accurate. The direct precise and accurate mass measurement performed at ISOLTRAP solved the discrepancy.

The impact of precise and accurate knowledge of nuclear masses in physics is manifold:

- They provide tests for astrophysics and nucleosynthesis of short-lived radioactive nuclides created during cataclysmic stellar processes like stellar explosions. During these explosive events, nucleosynthesis processes, such as rapid neutron or rapid proton capture (respectively r- and rp-process), strongly compete with radioactive decay. Precise and accurate mass determination of the respective exotic nuclides provides reliable calculations and a better understanding of the processes involved.

- Nuclear masses also provide stringent tests of the Standard Model: accurate and high-precision mass determination on both mother and daughter nuclides of a superallowed β-decay [Kell04a, Kell04b] are used to investigate the the conserved-vector-current (CVC) hypothesis of the the weak interaction and the unitarity of the Cabibbo-Kobayashi-Maskawa (CKM) quark-mixing matrix [Hard05].

- Scanning the mass surface across the nuclear chart reveals changes in the nuclear structure as, *e.g.*, shell closures or isomeric structures. The high-resolving power of the ISOLTRAP experiment, combined with a specific and selective laser ionization scheme, demonstrated for the first time the unambiguous spin assignment of the low-level isomers in ^{70}Cu [Roos04].

- Finally, the nuclear masses are used as a stringent test in nuclear physics for mass-prediction theoretical models. Accurate mass values help to distinguish between the diverging theoretical predictions of different nuclear mass models (see Fig. 1.3) by pointing out the weakness and the advantage of any global or local mass-prediction theory.

Together with the various global prediction theories, more simple but local mass formulae as the isobaric multiplet mass equation (IMME) are of great importance for mass extrapolation far from stability. The IMME describes the relation between the z-projection T_z of the isospin T and the mass of very similar nuclides, called isobaric analog states (IAS), *i.e.* having the same atomic mass number and same spin. The commonly adopted quadratic form [Brit98] has been investigated [Herf01a, Pyle02, Blau03a]. However, for some special cases, and in particular the $A = 35$, $T = 3/2$ quartet, some indication of a deviation is observed. To test the quadratic form of the IMME all the members of the multiplet have to be measured with the same level of precision and accuracy. The precision obtained with the Penning trap technique is inversely proportional to the observation (or excitation) duration of the nuclide of interest. Unfortunately, to test the limits of

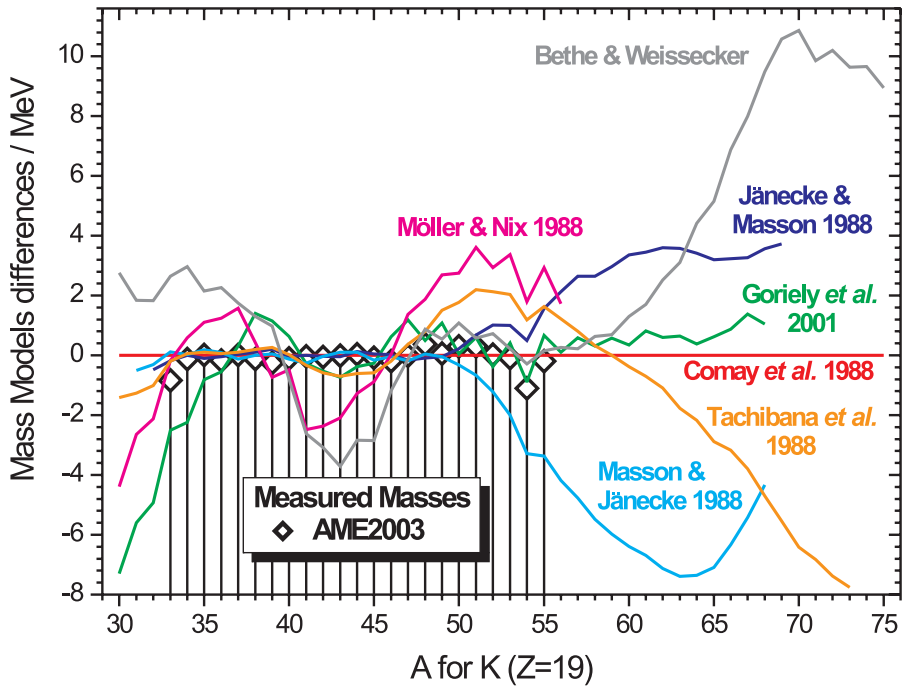

FIGURE 1.3: *Differences between some mass models [AME03, Lunn03]. It can be observed that close to stability, the different mass models agree with each other and with the experimental values [AME03]. Further away from stability, more and stronger discrepancies are observed. For detailed explanations concerning the mass models see [Coma88, Jäne88, Mass88, Möll88, Tach88, Gori01].*

the IMME means to get access to very short-lived nuclides, thus the achievable precision is limited by the half-life of the investigated radionuclide and the detection efficiency of the spectrometer.

The main idea is to optimize the detection efficiency of the ISOLTRAP spectrometer by replacing the existing micro-channel plate (MCP) detector by a newly designed Channeltron-based detection system that offers a detection efficiency of close to 100%. This improved detection efficiency will provide for the first time true single-ion experiments and exotic nuclides further away from the valley of stability, and hence very short life-times, will be easier accessible *e.g.* to test the predictive power of mass models.

This work is composed of a theoretical and an experimental part. The theoretical part is divided into two chapters. Chapter 2 gives a complete theoretical derivation and description of the quadratic form of the IMME as well as discusses the possible sources of deviations. Chapter 3 thoroughly describes the Penning trap device and the different

excitation schemes used to manipulate the ion motion in order to perform high-precision mass measurements. The technical and experimental part of this thesis is subdivided into four chapters. In Chapter 4 the experimental setup of ISOLTRAP is depicted and the mass determination procedure is shown in detail with respect to the experimental uncertainties. Recent technical developments in order to optimize the stability of the system and to reduce the experimental fluctuations are described in Chapter 5. The characterization of the new Channeltron detector and the associated ion beam simulations for the feasibility study of replacement of the MCP-based system are given in Chapter 6. The technical approach to the design and the constraints for the implementation of the new detection setup as well as the results concerning the efficiency gain are also developed in this chapter. Chapter 7 presents a detailed analysis procedure from the raw data to the final mass value for the investigated potassium isotopes. The potassium region has been examined because of the importance of ^{35}K in the $A = 35$, $T = 3/2$ ground state quartet system of the IMME. The former literature values [Brit98] for this quartet have shown a deviation from the IMME with a strong cubic term of $d = -4.8\ (3.5)$. However, the uncertainties have been too large to conclude a 'breakdown' of the IMME. The mass measurement performed at ISOLTRAP and presented in this work reduce the mass uncertainty for ^{35}K and neighboring nuclei by a factor of up to 40. The results of the high-precision mass measurements of the respective potassium isotopes and their discussion in the light of the IMME for the $A = 35$, $T = 3/2$ quartet (including the new mass value of ^{35}K) and the $A = 36$, $T = 2$ quintet (including ^{36}K) are also given in Chapter 7.

Theoretical Part

Chapter 2

Theory on the isobaric multiplet mass equation

2.1 Derivation of the Wigner–Eckart theorem

2.1.1 Symmetry and operators

The concept of symmetry in classical mechanics as well as in quantum mechanics is important for the understanding and the analysis of physical systems. In quantum mechanics one quantity that exhibits a special symmetry is the angular momentum j, where the quantum-mechanical states are represented by the momentum multiplets $\{|j,m\rangle\}$ and the projection along the z-axis, denoted by m, has discrete values in the interval:

$$m \in [-j, -j+1, \cdots, j-1, j] \stackrel{def}{=} [\![-j; j]\!]. \tag{2.1}$$

In the context of angular momentum, one of the most interesting relations is the so-called Wigner–Eckart theorem which will be derived in the following for a system composed of two coupled spins:

$$\begin{aligned} j &= j_1 \otimes j_2 \\ |j_1, m_1; j_2, m_2\rangle &= |j_1, m_1\rangle \otimes |j_2, m_2\rangle \,. \end{aligned} \tag{2.2}$$

The states $\{|j_k, m_k\rangle\}_{k=1,2}$ form an orthonormal basis of the j_k-space and $|j_1, m_1; j_2, m_2\rangle$ of the j-space for the angular momentum operator.

From the operator[1] $\mathbf{J}$ and its components J_x, J_y and J_z, the following relations can be defined:

$$\begin{aligned} J_+ &= J_\mathrm{x} + \imath J_\mathrm{y} \\ J_- &= J_\mathrm{x} - \imath J_\mathrm{y} \\ J^2 &= J_\mathrm{x}^2 + J_\mathrm{y}^2 + J_\mathrm{z}^2. \end{aligned} \tag{2.3}$$

[1] Notation: bold letters represents vectorial operators.

The action of those operators in both spaces are given by:

$$\begin{array}{rcl} J_{\rm z}\,|j,m\rangle & = & \hbar m\,|j,m\rangle \\ J_{\pm}\,|j,m\rangle & = & \hbar\sqrt{j(j+1)-m(m\pm1)}\,|j,m\pm1\rangle \\ J^2\,|j,m\rangle & = & \hbar^2 j(j+1)\,|j,m\rangle \end{array} \tag{2.4}$$

and

$$\begin{array}{rcl} J_{\rm z}\,|j_1,m_1;j_2,m_2\rangle & = & \hbar(m_1+m_2)\,|j_1,m_1;j_2,m_2\rangle \\ J_{\pm}\,|j_1,m_1;j_2,m_2\rangle & = & \hbar\sqrt{j_1(j_1+1)-m_1(m_1\pm1)}\,|j_1,m_1\pm1;j_2,m_2\rangle \\ & & +\hbar\sqrt{j_2(j_2+1)-m_2(m_2\pm1)}\,|j_1,m_1;j_2,m_2\pm1\rangle\,. \end{array} \tag{2.5}$$

In general, the transformation between two orthonormal bases can be described by the so-called Clebsch–Gordon coefficients:

$$\mathrm{CG}(j,m|j_1,m_1;j_2,m_2) = \langle j,m\ |j_1,m_1;j_2,m_2\rangle = \langle j_1,m_1;j_2,m_2\ |j,m\rangle^*.$$

Thus, any system in the two-coupled-spins j-space can be expressed as a linear combination of the eigenvectors of the total spin j and those of each individual spin j_1 and j_2:

$$|j,m\rangle = \sum_{m_1,m_2} |j_1,m_1;j_2,m_2\rangle\,\langle j_1,m_1;j_2,m_2\ |j,m\rangle. \tag{2.6}$$

To be self-consistent with an orthonormal basis, the Clebsch–Gordon coefficients should be normalized and will be considered as such for the demonstration.

Applying the $J_{\rm z}$ operator and using the results of Eq. (2.4) and Eq. (2.5) gives:

$$\begin{array}{rcrl} \langle j_1,m_1;j_2,m_2|\,J_{\rm z}\,|j,m\rangle & = & \hbar m & \langle j_1,m_1;j_2,m_2\ |j,m\rangle \\ & = & \hbar(m_1+m_2) & \langle j_1,m_1;j_2,m_2\ |j,m\rangle\,. \end{array} \tag{2.7}$$

This leads to the well-known relation $m = m_1 + m_2$. Thus, the spin multiplet has a total spin of $m \in [\![\ |j_1-j_2|;j_1+j_2\ ]\!]$. Note that in order to find all the multiplets with a total spin of m one can take the state $|j,m\rangle = |j_1+j_2,m_1+m_2\rangle$ and recursively apply the J_- operator. The normalization condition of the Clebsch–Gordon coefficients is therefore:

$$\sum_{m_1,m_2} |\ \mathrm{CG}(j,m|j_1,m_1;j_2,m_2)\ |^2 = 1, \tag{2.8}$$

where the m_i should obey the selection rules:

$$\left\{\begin{array}{rcl} m_i & \in & [\![-j_i;j_i]\!] \\ m & = & m_1+m_2. \end{array}\right. \tag{2.9}$$

Let us now focus on a tensor $\mathbf{T}^{(L)}$ of rank L with components $T_M^{(L)}$. If the states $\{|\alpha, j, m\rangle\}$ (where α represents a set of other quantum numbers) mix under rotation as well as the $T_M^{(L)}$, it follows that the states $\left\{T_M^{(L)}\,|\alpha, j, m\rangle\right\}$ also mix under rotation. As such this ensemble of states should divide into multiplets.

As previously done, the infinitesimal relations can be applied:

$$\begin{aligned}\left[J_z, T_M^{(L)}\right] &= M\hbar T_M^{(L)} \\ \left[J_\pm, T_M^{(L)}\right] &= \sqrt{L(L+1) - M(M\pm 1)}\hbar T_{M\pm 1}^{(L)}\end{aligned} \tag{2.10}$$

and it follows:

$$\begin{aligned}J_z\left(T_M^{(L)}\,|\alpha, j, m\rangle\right) &= \hbar(M+m)\left(T_M^{(L)}\,|\alpha, j, m\rangle\right) \\ J_\pm\left(T_M^{(L)}\,|\alpha, j, m\rangle\right) &= \hbar\sqrt{L(L+1) - M(M\pm 1)}\left(T_{M\pm 1}^{(L)}\,|\alpha, j, m\rangle\right) \\ &\quad +\hbar\sqrt{j(j+1) - m(m\pm 1)}\left(T_M^{(L)}\,|\alpha, j, m\pm 1\rangle\right).\end{aligned} \tag{2.11}$$

Since Eq. (2.5) and Eq. (2.11) are similar, Eq. (2.6) can also be written as:

$$|\alpha, j, m\rangle = \sum_{M,m'} T_M^{(L)}\,|\alpha', j', m'\rangle\,\langle L, M; j', m'\,|j, m\rangle, \tag{2.12}$$

where α is a function of α', j' and $T_M^{(L)}$. The Clebsch–Gordon coefficients represent the transformation between two orthonormal bases, and Eq. (2.12) can be easily inverted:

$$T_M^{(L)}\,|\alpha', j', m'\rangle = \sum_{j,m} |\alpha, j, m\rangle\,\langle j, m\,|j', m'; L, M\rangle. \tag{2.13}$$

The state $\langle\alpha'', j'', m''|$ can now be applied to Eq. (2.13). The result of this is zero except if $j = j''$ and $m = m''$:

$$\langle\alpha'', j'', m''|\,T_M^{(L)}\,|\alpha', j', m'\rangle = \langle\alpha'', j'', m''\,|\alpha, j'', m''\rangle\,\langle j'', m''\,|j', m'; L, M\rangle\,. \tag{2.14}$$

This result is proportional to the Clebsch–Gordon coefficients and the scalar product can be replaced using the reduced matrix element defined as:

$$\langle\alpha'', j'', m''\,|\alpha, j'', m''\rangle \overset{def}{=} \left\langle\alpha'', j''\left\|\widetilde{T^{(L)}}\right\|\alpha, j''\right\rangle.$$

Since α is a function of α' and j', this can be rewritten as:

$$\langle\alpha'', j'', m''\,|\alpha, j'', m''\rangle = \frac{\left\langle\alpha'', j''\left\|\widetilde{T^{(L)}}\right\|\alpha', j'\right\rangle}{\sqrt{2j''+1}} \quad \overset{def}{=} \quad \left\langle\alpha'', j''\middle\|T^{(L)}\middle\|\alpha', j'\right\rangle.$$

Note that the usually adopted notation for the reduced matrix element is without a tilde as explained in [Meun87] and used in [Wilk66]. Since the $(2j''+1)^{-1/2}$ factor does not enter explicitly in the calculations for the derivation of the isobaric multiplet mass equation (IMME), the scaling factor is often hidden within the reduced matrix element [Bene79] in order to simplify the notation.

2.1.2 The Wigner–Eckart theorem

As a result of the previous equations, the Wigner–Eckart theorem appears as:

$$\langle \alpha, j, m | \, T_M^{(L)} \, | \alpha', j', m' \rangle = \langle j, m | j', m'; L, M \rangle \left\langle \alpha, j \middle\| T^{(L)} \middle\| \alpha', j' \right\rangle . \tag{2.15}$$

This equation demonstrates that the matrix elements of $T_M^{(L)}$ only depend on two terms: the reduced matrix element, which is independent of m, m', and M, and the normalized Clebsch–Gordon coefficients.

Note that in the literature another form of the Wigner–Eckart theorem can be found:

$$\langle \alpha, j, m | \, T_M^{(L)} \, | \alpha', j', m' \rangle = (-1)^{m+j'-L} \begin{pmatrix} j' & L & j \\ m' & M & -m \end{pmatrix} \left\langle \alpha, j \middle\| \widetilde{T^{(L)}} \middle\| \alpha', j' \right\rangle , \tag{2.16}$$

where the rotational coupling coefficient in front of the true reduced matrix element is known as the Wigner 3j-symbol (see [Mess62] p. 1056). The Wigner 3j-symbol is a more symmetrical form of Clebsch–Gordon coefficients:

$$\langle j, m | j', m'; L, M \rangle = (-1)^{m+j'-L} \sqrt{2j+1} \begin{pmatrix} j' & L & j \\ m' & M & -m \end{pmatrix} . \tag{2.17}$$

2.2 From the Wigner–Eckart theorem to the isobaric multiplet mass equation

2.2.1 Description of the system and isospin formalism

An atom is made of a nucleus and electrons. The nucleus itself is a composition of protons p and neutrons n. Except for their charge state, these two particles are very similar. Especially the mass values of both p and n are very close to each other [AME03]. Moreover the strong nuclear force between two protons pp or neutrons nn and a proton–neutron pair pn is also similar. Therefore it can be assumed that protons and neutrons have the same mass (under a fair approximation) and are simply two different states of the same virtual particle, the 'nucleon'. Furthermore the strong force is invariant under the transformation $p \leftrightarrow n$. This symmetry is called the *isospin* and is represented by the operator T. Purely mathematically speaking, the formalism used to treat isospin is comparable to the coupled spin formalism presented in Section 2.1, except that the scaling factor $\hbar$ is not taken into account.

2.2.2 The Hamiltonian of the nucleus system

The isobaric multiplet mass equation (IMME) evolves directly from the application of the Wigner–Eckart theorem. The Hamiltonian of the nuclear system can be separated into two parts. The first part is charge-independent, whereas the second part can be treated as a charge-dependent perturbation force on the nuclear potential:

$$H = H_{\mathrm{CI}} + H_{\mathrm{CD}}, \tag{2.18}$$

where 'CI' stands for charge-independent and 'CD' for charge-dependent.

In this case, the charge dependence is a consequence of the electrostatic force which can be handled in first order approximation as a perturbation described by the sum of two-body interactions only. The Coulomb force between the nucleons can be written as :

$$H_{\mathrm{CD}} = \mathrm{e}^2 \sum_{i<j} \frac{\left(\frac{1}{2} - t_{\mathrm{z},i}\right)\left(\frac{1}{2} - t_{\mathrm{z},j}\right)}{r_{ij}}, \tag{2.19}$$

where r_{ij} is the relative distance between the nucleons (i,j) and t_{z} is the third component of the isospin. Like the J_{z} operator, t_{z} gives the isospin projection value T_{z} on the z axis: $t_{\mathrm{z}}|n\rangle = T_{\mathrm{z}}(n) = +1/2$ for neutrons and $t_{\mathrm{z}}|p\rangle = T_{\mathrm{z}}(p) = -1/2$ for protons[2] [Heis32, Wign37, Herf01a]. The relation (2.19) can be expanded to:

$$H_{\mathrm{CD}} = \sum_{i<j} \frac{\mathrm{e}^2}{r_{ij}} \left(\frac{1}{4} - \frac{1}{2}(t_{\mathrm{z},i} + t_{\mathrm{z},j}) + t_{\mathrm{z},i} t_{\mathrm{z},j} \right). \tag{2.20}$$

Since the perturbation force is the sum of two-body interactions only, the expansion of H_{CD} does not go beyond a tensor of rank 2. By adding and subtracting the term $\frac{1}{3}(\mathbf{t}_i \cdot \mathbf{t}_j)$, expression (2.20) can be rewritten as:

$$\begin{aligned} H_{\mathrm{CD}} \;=\; & \sum_{i<j} \frac{\mathrm{e}^2}{r_{ij}} \left(\frac{1}{4} + \frac{1}{3}\mathbf{t}_i \cdot \mathbf{t}_j \right) \\ & - \sum_{i<j} \frac{\mathrm{e}^2}{2r_{ij}} \left(t_{\mathrm{z},i} + t_{\mathrm{z},j} \right) \\ & + \sum_{i<j} \frac{\mathrm{e}^2}{r_{ij}} \left(t_{\mathrm{z},i} t_{\mathrm{z},j} - \frac{1}{3}\mathbf{t}_i \cdot \mathbf{t}_j \right). \end{aligned} \tag{2.21}$$

The Coulomb potential is thus given as a sum of tensors of rank 0 (iso-scalar), 1 (iso-vector) and 2 (iso-tensor):

$$H_{\mathrm{CD}} = H_{\mathrm{CD}}^{(0)} + H_{\mathrm{CD}}^{(1)} + H_{\mathrm{CD}}^{(2)}, \tag{2.22}$$

[2]The choice of $T_{\mathrm{z}}(n) = +1/2$ and $T_{\mathrm{z}}(p) = -1/2$ is arbitrary. Especially in elementary particle physics the opposite convention is taken $T_{\mathrm{z}}(p) = +1/2$, since the isospin of the u-quark is $+1/2$ [Jone90].

where $H_{\rm CD}^{(n)}$ is the $n^{\rm th}$ order isotensor with zero projection on the z-axis.

Since the Hamiltonian conserves the isospin T, its eigenvalues are $T_{\rm z}$-independent. They obviously depend on a set of other quantum numbers denoted by α:

$$H_{\rm CI}\,|\alpha,T,T_{\rm z}\rangle = E(\alpha,T)\,|\alpha,T,T_{\rm z}\rangle\,. \tag{2.23}$$

If the eigenvectors are not affected by the Coulomb perturbation, then:

$$\begin{aligned}\langle\alpha,T,T_{\rm z}|\,H\,|\alpha,T,T_{\rm z}\rangle &= \langle\alpha,T,T_{\rm z}|\,H_{\rm CI}+H_{\rm CD}\,|\alpha,T,T_{\rm z}\rangle\\ &= \quad\langle\alpha,T,T_{\rm z}|\,H_{\rm CI}\,|\alpha,T,T_{\rm z}\rangle\\ &\quad+\langle\alpha,T,T_{\rm z}|\,H_{\rm CD}^{(0)}\,|\alpha,T,T_{\rm z}\rangle\\ &\quad+\langle\alpha,T,T_{\rm z}|\,H_{\rm CD}^{(1)}\,|\alpha,T,T_{\rm z}\rangle\\ &\quad+\langle\alpha,T,T_{\rm z}|\,H_{\rm CD}^{(2)}\,|\alpha,T,T_{\rm z}\rangle\,,\end{aligned} \tag{2.24}$$

and the application of the Wigner–Eckart theorem (2.15) for the perturbation force gives:

$$\begin{aligned}\langle\alpha,T,T_{\rm z}|\,H_{\rm CD}^{(0)}\,|\alpha,T,T_{\rm z}\rangle &= \langle T,T_{\rm z}|T,T_{\rm z};0,0\rangle\ \left\langle\alpha,T\left\|H_{\rm CD}^{(0)}\right\|\alpha,T\right\rangle\\ \langle\alpha,T,T_{\rm z}|\,H_{\rm CD}^{(1)}\,|\alpha,T,T_{\rm z}\rangle &= \langle T,T_{\rm z}|T,T_{\rm z};1,0\rangle\ \left\langle\alpha,T\left\|H_{\rm CD}^{(1)}\right\|\alpha,T\right\rangle\\ \langle\alpha,T,T_{\rm z}|\,H_{\rm CD}^{(2)}\,|\alpha,T,T_{\rm z}\rangle &= \langle T,T_{\rm z}|T,T_{\rm z};2,0\rangle\ \left\langle\alpha,T\left\|H_{\rm CD}^{(2)}\right\|\alpha,T\right\rangle.\end{aligned} \tag{2.25}$$

2.2.3 Determining the values of the Clebsch–Gordon coefficients

To obtain the IMME, the values of the Clebsch–Gordon coefficients need to be derived. To this end, the Wigner–Eckart theorem as shown in Eq. (2.15) is used. For special cases ($T_{\rm z}=T$), it is possible to easily find all the Clebsch–Gordon coefficients that obey Eq. (2.8) and the selection rules Eq. (2.9). The value of the reduced matrix element can then be determined using this special set of coefficients. Afterwards, the general solution for the Clebsch–Gordon coefficients can be found.

The iso-scalar part – rank 0

For $\langle T,T_{\rm z}|T,T_{\rm z};0,0\rangle$ there is only one combination that obeys the selection rules Eq. (2.9). Therefore the Clebsch–Gordon coefficient is equal to 1.

The iso-vector part – rank 1

For $\langle T,T_{\rm z}|T,T_{\rm z};1,0\rangle$, the Clebsch–Gordon coefficients need to be found for the normalization in Eq. (2.8). For the special case $T_{\rm z}=T$, there are only two possibilities that fulfill the selection rules: $\langle T,T|T,T;1,0\rangle$ and $\langle T,T|T,T-1;1,1\rangle$.

In order to obtain those values the J_- operator can be introduced between $\langle T,T|T,T;1,1\rangle$ and applied to both sides:

$$\begin{aligned}\langle T,T|J_-|T,T;1,1\rangle &\overset{left}{=} 0 \\ &\overset{right}{=} \sqrt{2T}\,\langle T,T|T,T-1;1,1\rangle + \sqrt{2}\,\langle T,T|T,T;1,0\rangle\,.\end{aligned} \tag{2.26}$$

With $a = \langle T,T|T,T;1,0\rangle$ and $b = \langle T,T|T,T-1;1,1\rangle$ the normalization condition is $|a|^2 \cdot |1+1/T| = 1$. Giving arbitrarily a positive phase to a, this leads to:

$$\begin{aligned}\langle T,T|T,T;1,0\rangle &= \sqrt{\frac{T}{T+1}} \\ \langle T,T|T,T-1;1,1\rangle &= \frac{-1}{\sqrt{T+1}}.\end{aligned} \tag{2.27}$$

The Wigner–Eckart theorem can be applied using J_z since it is a component of a tensor of rank 1:

$$\langle \alpha,T,T_\mathrm{z}|J_\mathrm{z}|\alpha,T,T_\mathrm{z}\rangle = T_\mathrm{z} \tag{2.28}$$

$$= \langle T,T_\mathrm{z}|T,T_\mathrm{z};1,0\rangle\,\langle \alpha,T\,\|J_\mathrm{z}\|\,\alpha,T\rangle\,. \tag{2.29}$$

The Clebsch–Gordon coefficient has been previously calculated for $T_\mathrm{z} = T$, and using this value, the reduced matrix value can be written as:

$$\langle \alpha,T\,\|J_\mathrm{z}\|\,\alpha,T\rangle = \sqrt{T(T+1)}. \tag{2.30}$$

Note that, as explained before, this value does not depend on the isospin projection T_z. The value of the reduced matrix element can therefore be re-inserted into Eq. (2.29) which leads to:

$$\langle T,T_\mathrm{z}|T,T_\mathrm{z};1,0\rangle = \frac{T_\mathrm{z}}{\sqrt{T(T+1)}}. \tag{2.31}$$

The iso-tensor part – rank 2

The same procedure as previously shown will be applied in order to find the expression for $\langle T,T_\mathrm{z}|T,T_\mathrm{z};2,0\rangle$. Again, for the special case $T_\mathrm{z} = T$, there are only three possibilities according to the selection rules Eq. (2.9): $\langle T,T|T,T;2,0\rangle$, $\langle T,T|T,T-1;2,1\rangle$ and $\langle T,T|T,T-2;2,2\rangle$.

To get those values, the J_- operator is introduced between the two Clebsch–Gordon coefficients $\langle T,T|T,T;2,1\rangle$ and $\langle T,T|T,T-1;2,2\rangle$:

$$\begin{aligned}\langle T,T|J_-|T,T;2,1\rangle &\overset{left}{=} 0 \\ &\overset{right}{=} \sqrt{2T}\,\langle T,T|T,T-1;2,1\rangle + \sqrt{6}\,\langle T,T|T,T;2,0\rangle\end{aligned} \tag{2.32}$$

and

$$\begin{aligned}\langle T,T|J_-|T,T-1;2,2\rangle &\overset{left}{=} 0 \\ &\overset{right}{=} \sqrt{2T-1}\,\langle T,T|T,T-2;2,2\rangle + \sqrt{2}\,\langle T,T|T,T-1;2,1\rangle\,.\end{aligned} \tag{2.33}$$

With $a = \langle T,T|T,T;2,0\rangle$, $b = \langle T,T|T,T-1;2,1\rangle$ and $c = \langle T,T|T,T-2;2,2\rangle$ the normalization condition becomes:

$$|a|^2 \cdot \left|\big((T+1)(2T+3)\big)/\big(T(2T-1)\big)\right| = 1. \tag{2.34}$$

Giving arbitrarily a positive phase to a, this leads to:

$$\begin{aligned}
\langle T,T|T,T;2,0\rangle &= \sqrt{\frac{T(2T-1)}{(T+1)(2T+3)}} \\
\langle T,T|T,T-1;2,1\rangle &= -\sqrt{\frac{3(2T-1)}{(T+1)(2T+3)}} \\
\langle T,T|T,T-2;2,2\rangle &= \sqrt{\frac{6}{(T+1)(2T+3)}}.
\end{aligned} \tag{2.35}$$

Now the Wigner–Eckart theorem can be applied with $J_{\rm z}^{(2)}$ which can be adjusted to be a tensor of rank 2 from $J_{\rm z}$ and $\mathbf{J}$:

$$J_{\rm z}^{(2)} = J_{\rm z}J_{\rm z} - \frac{1}{3}\mathbf{J}\cdot\mathbf{J} = J_{\rm z}^2 - \frac{1}{3}J^2. \tag{2.36}$$

This leads to:

$$\begin{aligned}
\left\langle \alpha,T,T_{\rm z}|J_{\rm z}^{(2)}|\alpha,T,T_{\rm z}\right\rangle &= T_{\rm z}^2 - \tfrac{1}{3}T(T+1) \\
&= \langle T,T_{\rm z}|T,T_{\rm z};2,0\rangle \left\langle \alpha,T\left\|J_{\rm z}^{(2)}\right\|\alpha,T\right\rangle.
\end{aligned} \tag{2.37}$$

As previously demonstrated, $\left\langle \alpha,T\left\|J_{\rm z}^{(2)}\right\|\alpha,T\right\rangle$ can be evaluated for $T_{\rm z} = T$:

$$\langle \alpha,T\,\|J_{\rm z}\|\,\alpha,T\rangle = \frac{1}{3}\sqrt{T(2T-1)(T+1)(2T+3)}. \tag{2.38}$$

The value of the reduced matrix element is then re-entered into Eq. (2.37):

$$\langle T,T_{\rm z}|T,T_{\rm z};2,0\rangle = \frac{3T_{\rm z}^2 - T(T+1)}{\sqrt{T(2T-1)(T+1)(2T+3)}}. \tag{2.39}$$

Clebsch–Gordon coefficients

To summarize, the Clebsch–Gordon coefficients are given by:

$$\begin{aligned}
\langle T,T_{\rm z}|T,T_{\rm z};0,0\rangle &= 1 \\
\langle T,T_{\rm z}|T,T_{\rm z};1,0\rangle &= \tfrac{T_{\rm z}}{\sqrt{T(T+1)}} \\
\langle T,T_{\rm z}|T,T_{\rm z};2,0\rangle &= \tfrac{3T_{\rm z}^2-T(T+1)}{\sqrt{T(2T-1)(T+1)(2T+3)}}.
\end{aligned}$$

Note that the Clebsch–Gordon coefficients from the scalar part of the Hamiltonian give a constant, the one from the vector part (rank 1) gives a term proportional to $T_{\rm z}$, and the tensor of rank 2 produces a term that depends on $T_{\rm z}^2$.

2.2.4 The quadratic form of the Isobaric Multiplet Mass Equation

In Eq. (2.24), the term coming from the charge-independent Hamiltonian is a constant. The expanded terms resulting from the Coulomb perturbation force can be sorted according to the power of the isospin projection T_z. Since the isospin T is constant for a given multiplet, the energy of the system (*i.e.* its mass) becomes:

$$M = \langle \alpha, T, T_\mathrm{z} | \, H \, | \alpha, T, T_\mathrm{z} \rangle = c_0(\alpha, T) + c_1(\alpha, T) T_\mathrm{z} + c_2(\alpha, T) T_\mathrm{z}^2. \tag{2.40}$$

All the calculations are performed under the isospin-hypothesis that protons and neutrons have the same mass. Since the mass difference is negligible compared to the absolute mass of a proton (or neutron), it can be handled as a perturbation as well. A term taking into account this mass difference can be implemented into the previous equation Eq. (2.40). With the isospin projection T_z, which is equal to half of the neutron–proton difference, the neutron–proton mass difference perturbation can be described by:

$$V(\Delta m) = A \frac{M_\mathrm{n} + M_\mathrm{p}}{2} + (M_\mathrm{n} - M_\mathrm{p}) T_\mathrm{z}. \tag{2.41}$$

This perturbation also linearly depends on T_z, therefore it can be included in the c_0 and c_1 terms of Eq. (2.40). For a multiplet of a given isospin T, the $c_i(\alpha, T)$ coefficients are constant. This leads to the quadratic form of the isobaric multiplet mass equation (IMME):

$$M = a + bT_\mathrm{z} + cT_\mathrm{z}^2. \tag{2.42}$$

This equation links the isotopes that belong to the same multiplet for a given atomic mass number $A = Z + N$. In other words, the ions of the multiplet are mirror nuclei and their small mass difference is described by the IMME. The quadratic form of the IMME assumes that only the charge state of the nucleus induces this mass difference between the members of the multiplet. Therefore the Coulomb shift term can be used as an indicator for the study of the validity of the IMME.

2.3 Testing the quadratic form of the Isobaric Multiplet Mass Equation

2.3.1 Is the quadratic form correct?

The quadratic form of the IMME has been previously derived under the assumption that the Coulomb force is the only perturbation. With a second rank operator of the Hamiltonian of the system, a quadratic form of the isobaric multiplet mass equation is implied. In order to validate this assumption, other perturbation forces and/or higher order effects have to be investigated.

Even though the representation of the Coulomb force is described by a second order Hamiltonian, it is not correct. It has been noted in [Henl69] that the Coulomb charge density is not a real two-body force since it needs higher order terms to be completely described. With isospin symmetry and for a pure proton-neutron interaction the quadratic form might be valid, but for higher order interactions with other protons or neutrons the IMME can be just considered to be a reasonably good approximation. In addition, other effects like pairing [Seng60] can also play an important role in the IMME.

Moreover, by measuring the mass of all the mirror nuclei of a multiplet experimental results provide a stringent test of the IMME and validate or disprove the quadratic form of the IMME. Even though the masses experimentally provided are quite reliable, and even if the quadratic form of the IMME seems to be verified, other effects cannot be decoupled from the experimental data. Indeed, if any other perturbation force that is also based on a two body interaction force is involved, its effects will be hidden in the experimental quadratic form of the formula, as for example the case of the neutron–proton mass difference correction, Eqs. (2.41) and (2.42). In that case, these additional forces and effects can only be investigated theoretically with simulations and by comparison to experimental data. In order to find any higher terms in the IMME, the experimental data has to concentrate on n-plets with $n \geq 4$.

2.3.2 Experimental investigations

The isobaric multiplet mass equation has been thoroughly studied in the late 70s by Beneson and Kashy [Bene79] and was found to work very well for most cases (*i.e.* 21 out of 22). Since then, many measurements and tests of the IMME have been performed and reported. From the latest data compilation [Brit98] and the recent works performed [Herf01a, Pyle02, Blau03a] for testing the commonly accepted quadratic form of the IMME, only few examples show a deviation and need additional higher terms to be fully described [Bert70]. As previously stated the search for higher order terms in the IMME implies studying systems with at least four nuclides in the multiplet, *i.e.* with an isospin $T \geq 3/2$. Up to now, only one case for the $A = 9$, $T = 3/2$ quartet as well as one for the $A = 8$, $T = 2$ quintet system are known to deviate significantly by more than three standard deviations from the quadratic form of the IMME. For those multiplets higher order terms have to be added either dT_z^3, eT_z^4, or both.

As a consequence, the present work focusses on the quartet multiplets and gives as an example the latest compilation of the data for the ground state and excited state quartets as well as quintets. Fig. 2.1 represents an update of the data in [Brit98] plus the latest corrections for the ground states isotopes from [AME03] as well from [Herf01a, Pyle02,

Blau03a][3]. Shown is the coefficient d of the cubic term under the assumption that the IMME has a cubic rather than a quadratic polynomial form. As shown in the upper graph (a), most of the measured quartets agree with the quadratic form of the IMME, since within the errors bars, most of the data are consistent with a cubic term equal to zero $d = 0.3\ (2.6)$. Fig. 2.1 (b) shows the relative uncertainty of the coefficient d.

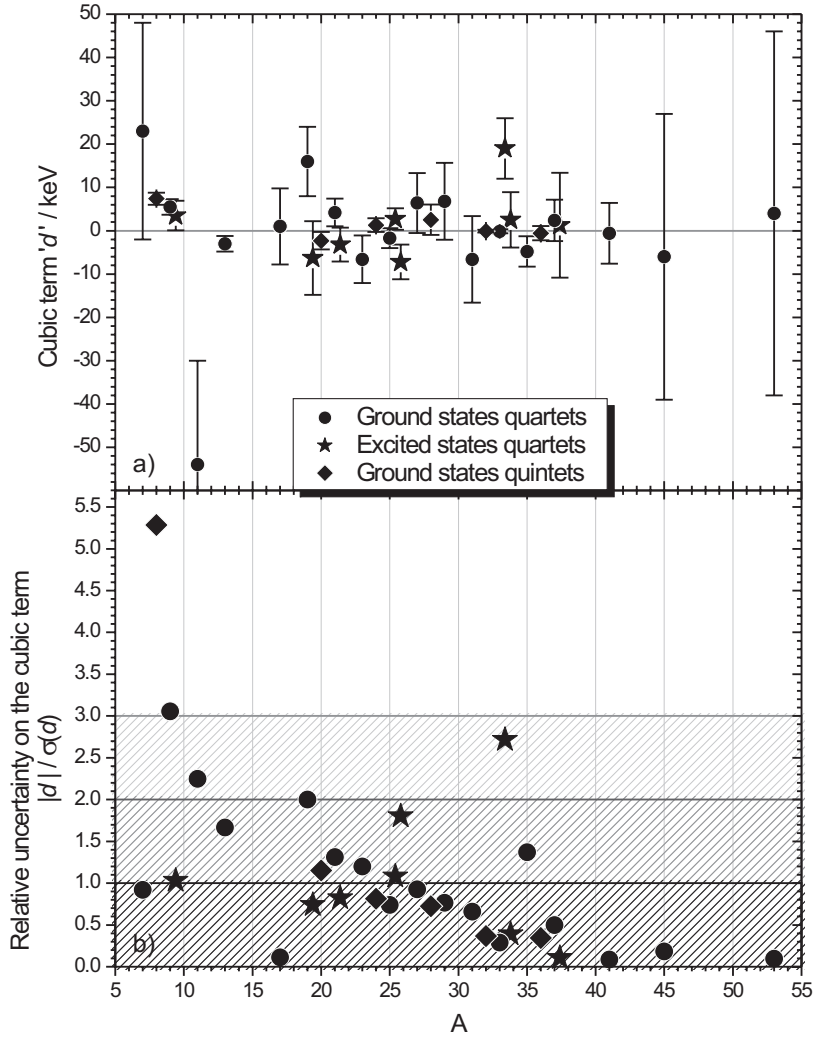

FIGURE 2.1: *Compilation of the deduced coefficient d of the cubic term for quartets. The first plot (a) shows the compilation for the ground and excited states for quartets and the second one (b) shows the relative uncertainty of the coefficient d [Brit98, AME03]. For more detailed explanations see text.*

[3][Blau03a] has a typo. The value presented for the cubic coefficient (noted as 'c_3') in the case of the $A = 33, T = 3/2$ quartet (Tab. II) is given with a wrong sign. It should read: -0.13 (45) for the quartet.

The present work focusses on the mass determination for the nuclides of the $A = 35$, $T = 3/2$ quartet which before this investigation showed a deviation from the quadratic form with a cubic term $d = -4.5\ (3.5)$ keV. The uncertainty of the quartet was mainly due to the lack of knowledge of the mass of ^{35}K. The outline of the experimental part will be the mass determination of this nuclide and a thorough study of the $A = 35$, $T = 3/2$ quartet and its consequences for a 'breakdown' of the IMME [Herf01a] or a (re)validation as in [Pyle02].

As can be seen from Fig. 2.1(b), the ground state quartet of $A = 35$ has a large relative uncertainty on the cubic term d compared to other quartets in that mass region. This uncertainty is mainly due to the lack of knowledge on the ^{35}K mass. A precise measurement of this mass could therefore significantly improve the current understanding of the IMME and nuclear structure in this region of the nuclear chart. To this aim, very precise and accurate mass measurements have been performed with the Penning trap-based mass spectrometer ISOLTRAP. Chapter 3 describes in detail the Penning trap system used in mass measurements experiments like the ISOLTRAP spectrometer (see Chapter 4).

Chapter 3

The Penning trap

The pioneering experiment ISOLTRAP is based on a unique combination of Penning traps. In this chapter, the basics of a Penning trap and methods of ion manipulation will be thoroughly described in order to better understand the mass measurement technique used at the ISOLTRAP spectrometer (Chapter 4) and the ion motion simulations performed for the new detector (Chapter 6).

3.1 Application of traps in physics

In physics, the best conditions to study any object very precisely require two main constraints. First of all, the system should be at rest, and secondly, the environment should be clean and not affect the system. To this end, physicists use dedicated tools aimed at storage or confinement of atoms and/or ions. These tools can be classified in the following main groups: magneto-optical, electrostatic, electrodynamic (rf-fields), and static electromagnetic traps.

(a) Magneto-Optical Trap (MOT)

MOTs are used to confine and cool atoms by means of laser beams and magnetic fields. One of the applications of MOTs is the investigation of the general behavior of an atomic cloud cooled down to the coldest temperature in the universe, leading for certain systems to the so-called Bose-Einstein Condensation [Ande95, Brad95, Davi95].

(b) Paul trap

The Paul trap invented by W. Paul (Nobel Prize in Physics in 1989) is an electrodynamic trap used to confine ions with a pure electrodynamic RF (Radio-Frequency) field (for more details see [Schw98]). The main use of a Paul trap is to cool, clean, and perform an isobaric selection of ions among an ion cloud. Such a device can be used for spectroscopy [Hoff99, Zhao96] and atomic or particle physics, *e.g.*, the investigation of β-neutrino angular correlation for superallowed β-decays (LPC Caen - GANIL) [Ban05, Seve06].

(c) Penning trap

The Penning trap was invented by H.G. Dehmelt (Nobel Prize in Physics in 1989). It is based on a superposition of a strong homogeneous magnetic field and a weak quadrupolar electrostatic field to store ions. This instrument is commonly used in physical chemistry, biochemistry, chemistry [Hoff99, Majo05], and nuclear physics for weak interaction studies [Beck03, Kozl05]. Penning traps are mainly used for mass spectrometry since they provide precise and accurate mass determination capabilities [Blau06].

At the ISOLTRAP mass spectrometer, the latter two types of traps are used. A more detailed description of the apparatus is given in Section 4.2, based on the general explanation of the Penning trap below.

3.2 Characterization of the Penning trap

Depending on the application of the Penning trap, different configurations for the electrodes are possible in order to achieve the wanted quadrupolar field. This instrument can be designed either as a simple cubic cell for basic ion storage, or with cylindrical or hyperbolical electrodes for more sophisticated ion manipulation and precise mass measurements. The symmetry axis of the electrodes is parallel with the magnetic field lines.

Since one of the main objectives of this work is the study and simulation of the hyperbolic precision trap of ISOLTRAP, most of the figures will be based on that specific geometry (see Fig. 3.1). The Penning trap theory is analytically solvable only for the ideal case of infinite electrodes creating a pure quadrupolar field. However, it can be applied to different electrode shapes, provided that close to the center of the trap a quadrupolar field is nicely reproduced. In practice, the results are valid to a very good approximation, and deviations from the ideal case are known and can be corrected if needed.

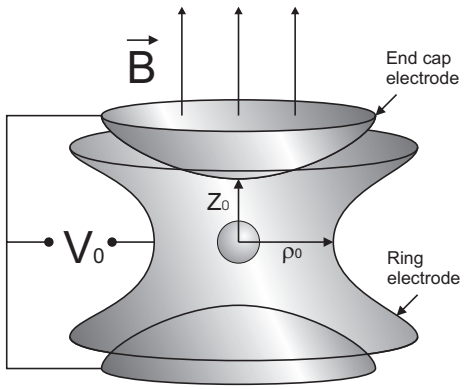

FIGURE 3.1: *Electric and magnetic field configuration of a hyperbolical Penning trap.*

The strong magnetic field and the weak electric field

In a Penning trap device, the magnetic field confines the ion in the radial plane, while the electric field constrains the particle motion along the trap axis.

In general, when a charged particle enters a magnetic field perpendicular to the field lines, its motion is distorted and the particle spins around the magnetic field lines. In the ideal case, it will be trapped. However in practice, even at low temperatures[1], ions have a velocity component parallel to the magnetic field lines that leads to the loss of ions. Therefore, another field is needed to trap the particles.

The quadrupolar electric field that results from the special polarities of the electrodes shown in Fig. 3.1 confines the ions along the symmetry axis of the trap. The equipotential lines describe an hyperbolic curve (z vs. x/y-projection), so that the ions are stored along the field's revolution axis.

Symmetry and properties of Penning trap

The Penning trap has a cylindrical symmetry with coordinates $\{\rho = \sqrt{x^2+y^2}; z\}$, and the electrical field potential $\phi(\rho, z)$ is described by:

$$\phi(\rho, z) = \frac{V_0}{4D^2}\left(2z^2 - \rho^2\right) \tag{3.1}$$

- where V_0 is the voltage difference between the ring electrode and the endcap during storage time. For ISOLTRAP V_0 is equal to 8.5V.
- D is a geometrical parameter characterizing the Penning trap. The following value describes the ISOLTRAP's hyperbolical trap:

$$D = \sqrt{\frac{1}{2}\left(z_0^2 + \frac{\rho_0^2}{2}\right)} \approx 10.2 \text{ mm}, \tag{3.2}$$

- $z_0 = 11.2$ mm and $\rho_0 = 13$ mm are the distances from the center of the trap to the endcaps and to the ring electrode, respectively (see Fig. 3.1).

With the general equation of motion given by Newton's second law $\sum_i \vec{F_i} = m\vec{a}$, as well as the electric $\vec{F} = -q\vec{E}$ and magnetic force $\vec{F} = q\vec{v} \times \vec{B}$, analytical solutions of the motion of a charged particle stored in a Penning trap can be found in [Brow86].

[1] At room temperature T = 300 K, the thermal kinetic energy of an ion is roughly $E = k_B T = 25$ meV, where $k_B = 8.62510^{-5}$ eV/K is the Boltzman constant. That corresponds to a velocity of a non-relativistic ion of mass 100 u, $v = \sqrt{2E/m} \approx 220$ m/s (1 u = 931.494009 MeV/c^2).

3.3 Ion storage and manipulation

In the following, the different operating modes of a Penning trap will be described. The first one deals with trapping only, the second one is meant for the excitation of the ion motion inside the trap.

3.3.1 Ion motion in an ideal Penning trap

The electric field $\vec{E}$ created by the potential $\phi(x, y, z)$ can be written as:

$$\vec{E} = -\vec{\nabla}\phi = \frac{V_0}{2D^2} \begin{bmatrix} x \\ y \\ -2z \end{bmatrix}. \tag{3.3}$$

The magnetic field $\vec{B}$ is given by $\left(\|\vec{B}\| = B\right)$:

$$\vec{B} = B \cdot \vec{e}_{\mathrm{z}}.$$

According to Newton's second law of motion, a particle of mass *m* and charge *q* in an electromagnetical field ($\vec{E}, \vec{B}$) experiences the so-called Lorentz force:

$$m\,\vec{a} = q(\vec{E} + \vec{v} \times \vec{B}), \tag{3.4}$$

which for the Penning trap is:

$$\begin{bmatrix} \ddot{x} \\ \ddot{y} \\ \ddot{z} \end{bmatrix} = \frac{qV_0}{2mD^2} \begin{bmatrix} x \\ y \\ -2z \end{bmatrix} + \frac{qB}{m} \begin{bmatrix} \dot{y} \\ -\dot{x} \\ 0 \end{bmatrix}. \tag{3.5}$$

To simplify the expressions, the angular frequencies ω_{z} and ω_{c} are introduced. The given values (see Appendix A) correspond to $^{39}\mathrm{K}^{+}$ in the hyperbolical trap of ISOLTRAP with $B = 5.9$ T and $V_0 = 8.5$ V:

$$\begin{aligned} \omega_{\mathrm{z}} &= \sqrt{\tfrac{qV_0}{mD^2}} \approx 448 \cdot 10^3\ \mathrm{s}^{-1}, \\ \omega_{\mathrm{c}} &= \tfrac{qB}{m} \approx 14.649 \cdot 10^6\ \mathrm{s}^{-1}, \end{aligned} \tag{3.6}$$

where:

- ω_{z} is the axial angular frequency of the ion motion.
- ω_{c} is the cyclotron angular frequency.

In the case of an ideal Penning trap, the axial and radial motions are decoupled. Thus, the axial and radial part of the equation of motion can be solved separately as shown in the following:

Solving the equations of motion

The motion along the symmetry z-axis is given by the simple form:

$$\ddot{z} + \omega_z^2 \, z = 0. \tag{3.7}$$

The solution of this differential equation is a harmonic oscillator:

$$z(t) = A_z(0) \cos\big(\omega_z \cdot t + \theta_z(0)\big), \tag{3.8}$$

where $A_z(0)$ and $\theta_z(0)$ are determined by the initial conditions.
As qualitatively explained before in 3.2, this motion only depends on the electric field.

The equations of motion in the radial plane are:

$$\ddot{x} - \omega_c \dot{y} - \frac{\omega_z^2}{2} x = 0, \tag{3.9}$$

$$\ddot{y} + \omega_c \dot{x} - \frac{\omega_z^2}{2} y = 0. \tag{3.10}$$

The effect of the magnetic field $\vec{B}$ can be directly observed with the ω_c term, whereas the weak electric field $\vec{E}$ effect appears in the ω_z term.
In order to solve these equations of motion, a complex number representation can be used (another representation to solve the equations can be found in [Brow86, Kret92a, Kret92b]).
The motion of a particle in a plane is described by the coordinate doublet point $\{x(t), y(t)\}$, where in the complex space the substitution: $u(t) = x(t) + \imath y(t)$ will be used. The system described by equations (3.9) and (3.10) can be rewritten in the following form:

$$\ddot{u} + \imath\omega_c \dot{u} - \frac{\omega_z^2}{2} u = 0. \tag{3.11}$$

Since the variable u is by definition a complex number, $u(t)$ can be written as $u_0(t) \cdot e^{-\imath\omega t}$. In the following, the modulus is either constant $|u(t)| = u_0$, or has negligible variations $|u(t)| = u_0 \pm (\delta u)(t)$ during a given time δt specified being small compared to a period of the motion (*i.e.* $\delta t \ll 1/\nu_\pm$). Even if this assumption is not needed here, it stays applicable in case of excitations schemes. Substituting $u(t)$ in (3.11) implies:

$$\omega^2 - \omega_c \omega + \frac{\omega_z^2}{2} \; = \; 0. \tag{3.12}$$

The solutions of Eq. (3.11) are given by the general form:

$$u(t) = \rho_+ e^{\imath\omega_+ t} + \rho_- e^{\imath\omega_- t}, \tag{3.13}$$

where the angular eigenfrequencies $\omega_\pm$ are the roots of the quadratic equation (3.12):

$$\omega_\pm = \tfrac{1}{2}(\omega_\mathrm{c} \pm \sqrt{\triangle}) \quad \text{with} \quad \triangle = \omega_\mathrm{c}^2 - 2\omega_\mathrm{z}^2 > 0.\ ^{(2)} \tag{3.14}$$

The basic relations between the roots of a second order polynomial equation lead to:

$$\begin{aligned} \omega_+ + \omega_- &= \omega_\mathrm{c}, \\ 2 \cdot \omega_+ \cdot \omega_- &= \omega_\mathrm{z}^2, \\ \omega_+^2 + \omega_-^2 + \omega_\mathrm{z}^2 &= \omega_\mathrm{c}^2. \end{aligned} \tag{3.15}$$

Back to the cartesian coordinate system, the solutions of the motion in the radial plane are (using counter clockwise rotation):

$$\begin{bmatrix} x(t) \\ y(t) \end{bmatrix} = \rho_+ \begin{bmatrix} \cos(\omega_+ t + \theta_+) \\ \sin(\omega_+ t + \theta_+) \end{bmatrix} + \rho_- \begin{bmatrix} \cos(\omega_- t + \theta_-) \\ \sin(\omega_- t + \theta_-) \end{bmatrix}. \tag{3.16}$$

As qualitatively explained in Section 3.2, the radial motion mainly depends on the magnetic field. The effect of the crossed magnetic and electric fields leads to a splitting of the radial motion into two modes driven by the angular frequencies $\omega_\pm$.

Since $\omega_\mathrm{z} \ll \omega_\mathrm{c}$, a second order Taylor expansion of relation (3.14) in ω_z gives the following expressions for $^{39}\mathrm{K}^+$, stored in the precision trap of ISOLTRAP:

$$\begin{aligned} \omega_+ &= \omega_\mathrm{c} - \tfrac{\omega_\mathrm{z}^2}{2\omega_\mathrm{c}} + \mathrm{O}(\omega_\mathrm{z}^4) \approx q\tfrac{B}{m} - \tfrac{V_0}{2D^2B} = 14.642 \cdot 10^6\ \mathrm{s}^{-1} \\ \omega_- &= \tfrac{\omega_\mathrm{z}^2}{2\omega_\mathrm{c}} + \mathrm{O}(\omega_\mathrm{z}^4) \approx \tfrac{V_0}{2D^2B} = 6.855 \cdot 10^3\ \mathrm{s}^{-1}. \end{aligned} \tag{3.17}$$

With the Taylor expansion, it has to be emphasized that the magnetron angular frequency ω_- is mass independent on the first order (higher order can be found in [Schw89]). Moreover, the first order Taylor expansion with respect to ω_+ is used as a starting point of the trap field optimization (see Section 4.4).

Ion trajectories

As a result from the solutions of the equations (3.8) and (3.16), the ion trajectory in a Penning trap is composed of three eigenmotions characterized by their angular frequency:

- ω_z, the axial angular frequency, depends only on the electric field and characterizes the motion along the z-axis.
- ω_+, is the reduced cyclotron angular frequency of the cyclotron motion in the plane orthogonal to the z-axis. The term *reduced* is due to the effect of the crossed electric and magnetic fields that reduces the cyclotron angular frequency ω_c.

[2] $\triangle$ is assumed to be always positive for trapping and this implies the relation $\omega_\mathrm{c} > \sqrt{2}\omega_\mathrm{z}$. The latter defines the stability condition of the ion trajectory in a Penning trap.

- ω_-, the magnetron angular frequency, corresponds to a secondary motion in the radial plane due to the effect of the electric and magnetic field (drift motion).

In Fig. 3.2 the general motion of an ion in the trap without additional forces is shown. It emphasizes the three eigenmotions as previously demonstrated.

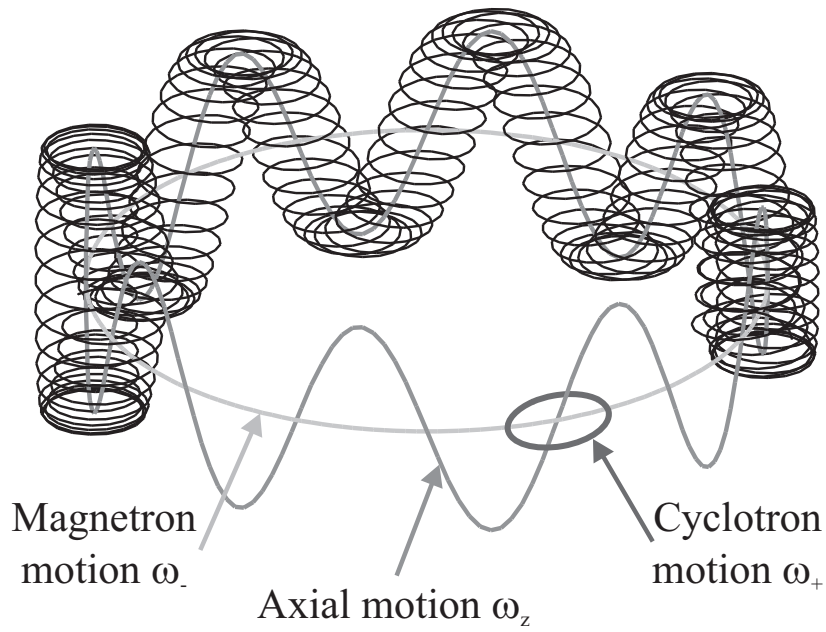

FIGURE 3.2: *Superposition of the different motions of an ion in a Penning trap. For a better readability, the ratio between the magnetron (respectively the reduced cyclotron) and the axial angular frequency $\omega_\pm/\omega_z$ has been arbitrarily reduced by a factor 2.5, so that Eq.* (3.15) *is not obeyed ($\nu_- = 1$ Hz, $\nu_+ = 200$ Hz, and $\nu_z = 8$ Hz).*

3.3.2 Manipulation of the ion motion: excitation schemes

In order to manipulate the ion motion, different excitations are applied. The two main excitation schemes commonly used with a Penning trap device are the dipolar and quadrupolar radiofrequency (rf) excitations. Higher order excitations (*e.g.* octupolar) are possible and presently under investigation [Schw03]. Those excitation modes are obtained by applying a rf-electric field in the radial plane of the trap. To this end, the ring electrode of the Penning trap is segmented into four equally sized parts. As shown in Fig. 3.3, a dipolar excitation is obtained by applying a rf-field on two opposite segments whereas a quadrupolar field results from applying rf-fields on all electrodes with the same phase on opposing segments. In the ideal Penning trap, the axial motion is not disturbed by those excitations.

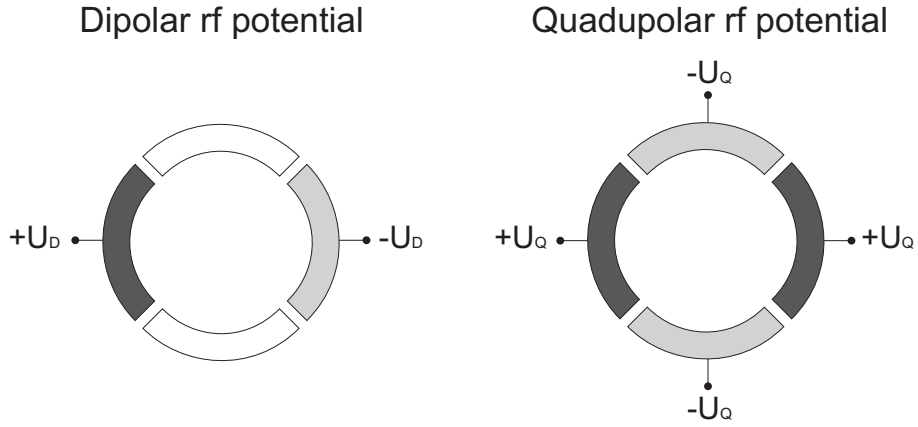

FIGURE 3.3: *Application of rf voltages for the different excitation schemes.*

Dipolar excitation

In the case of a dipolar excitation, a sinusoidal rf voltage with an angular frequency ω_{D} and an amplitude V_{D} is applied to two segments of the ring electrode as shown in Fig. 3.3. The electrical dipolar field created can be described by the following potential ϕ_{D} using $A_{\mathrm{D}} \propto \frac{V_{\mathrm{D}}}{\rho_0}$:

$$\phi_{\mathrm{D}}(x,t) = A_{\mathrm{D}} \cos(\omega_{\mathrm{D}} t + \theta_{\mathrm{D}}) \cdot x. \tag{3.18}$$

The electric field $\vec{E}_{\mathrm{D}}$ due to this dipolar rf field can be written as:

$$\vec{E}_{\mathrm{D}} = -\vec{\nabla}\phi_{\mathrm{D}} = -A_{\mathrm{D}} \cos(\omega_{\mathrm{D}} t + \theta_{\mathrm{D}}) \cdot \vec{e}_{\mathrm{x}}. \tag{3.19}$$

Adding this new force to Eq. (3.5) leads to:

$$\begin{bmatrix} \ddot{x} \\ \ddot{y} \\ \ddot{z} \end{bmatrix} - \omega_{\mathrm{c}} \begin{bmatrix} \dot{y} \\ -\dot{x} \\ 0 \end{bmatrix} - \frac{\omega_{\mathrm{z}}^2}{2} \begin{bmatrix} x \\ y \\ -2z \end{bmatrix} = \begin{bmatrix} -k_{\mathrm{D}} \cos(\omega_{\mathrm{D}} t + \theta_{\mathrm{D}}) \\ 0 \\ 0 \end{bmatrix}, \tag{3.20}$$

where $k_{\mathrm{D}} = \frac{q}{m} A_{\mathrm{D}}$.
The radial part of the differential equation becomes in the complex plane:

$$\ddot{u} + \imath\omega_{\mathrm{c}}\dot{u} - \frac{\omega_{\mathrm{z}}^2}{2} u = -k_{\mathrm{D}} \cos(\omega_{\mathrm{D}} t + \theta_{\mathrm{D}}). \tag{3.21}$$

The solutions of the motion have the same form as before. The main difference is that the radii $\rho_{\pm}$ are now time dependent:

$$\begin{bmatrix} x(t) \\ y(t) \end{bmatrix} = \rho_+(t) \begin{bmatrix} \cos(\omega_+ t + \theta_+) \\ \sin(\omega_+ t + \theta_+) \end{bmatrix} + \rho_-(t) \begin{bmatrix} \cos(\omega_- t + \theta_-) \\ \sin(\omega_- t + \theta_-) \end{bmatrix}. \tag{3.22}$$

Using the substitution $V_{\pm}(0) = (\omega_+ - \omega_-) \cdot \rho_{\pm}(0)$, $\Delta\omega_{\pm} = \omega_{\mathrm{D}} - \omega_{\pm}$, and $\Delta\theta_{\pm} = \theta_{\mathrm{D}} - \theta_{\pm}$ the time-dependent radii can be written as [Blau03a]:

$$\rho_{\pm}(t) = \sqrt{\frac{V_{\pm}^2(0) + \frac{k_{\mathrm{D}}^2}{\Delta\omega_{\pm}^2}\sin^2\left(\frac{\Delta\omega_{\pm}}{2}t\right) \mp V_{\pm}(0)\frac{k_{\mathrm{D}}}{\Delta\omega_{\pm}}\Big(\cos(\Delta\omega_{\pm}t + \Delta\theta_{\pm}) - \cos\Delta\theta_{\pm}\Big)^2}{(\omega_+ - \omega_-)^2}}. \tag{3.23}$$

The dipolar excitation is resonant when the excitation angular frequency is either equal to the reduced cyclotron or to the magnetron angular frequency. Taking the limit of $\rho_{\pm}(t)$ when $\omega_{\mathrm{D}} = \omega_{\pm}$ leads to:

$$\lim_{\Delta\omega_{\pm}\mapsto 0}\rho_{\pm}(t) = \sqrt{\rho_{\pm}^2(0) + \frac{k_{\mathrm{D}}^2}{4(\omega_+ - \omega_-)^2}t^2 \mp \frac{\rho_{\pm}(0)k_{\mathrm{D}}\,\sin(\theta_{\mathrm{D}} - \theta_{\pm})}{\omega_+ - \omega_-}t}, \tag{3.24}$$

which illustrates that at the resonant angular frequencies, the dipolar excitation increases the corresponding radius. All different excitations schemes and related effects are summarized in Section 3.4.

Quadrupolar excitation

In the case of quadrupolar excitation, a sinusoidal rf-voltage with an angular frequency ω_{Q} and an amplitude V_{Q} is applied to the segments of the ring electrode. The created electrical quadrupolar field can be described by the following potential ϕ_{Q} using $A_{\mathrm{Q}} \propto \frac{V_{\mathrm{Q}}}{\rho_0}$:

$$\phi_{\mathrm{Q}}(x, y, t) = A_{\mathrm{Q}}\cos(\omega_{\mathrm{Q}}t + \theta_{\mathrm{Q}}) \cdot (x^2 - y^2). \tag{3.25}$$

The electric field $\vec{E}_{\mathrm{Q}}$ due to this rf-field can be written as:

$$\vec{E}_{\mathrm{Q}} = -\vec{\nabla}\phi_{\mathrm{Q}} = -2A_{\mathrm{Q}}\cos(\omega_{\mathrm{Q}}t + \theta_{\mathrm{Q}}) \cdot \begin{bmatrix} x \\ -y \\ 0 \end{bmatrix}. \tag{3.26}$$

Adding this new force into Eq. (3.5) gives:

$$\begin{bmatrix} \ddot{x} \\ \ddot{y} \\ \ddot{z} \end{bmatrix} - \omega_{\mathrm{c}}\begin{bmatrix} \dot{y} \\ -\dot{x} \\ 0 \end{bmatrix} - \frac{\omega_{\mathrm{z}}^2}{2}\begin{bmatrix} x \\ y \\ -2z \end{bmatrix} = \begin{bmatrix} -2k_{\mathrm{Q}} \cdot x \cdot \cos(\omega_{\mathrm{Q}}t + \theta_{\mathrm{Q}}) \\ 2k_{\mathrm{Q}} \cdot y \cdot \cos(\omega_{\mathrm{Q}}t + \theta_{\mathrm{Q}}) \\ 0 \end{bmatrix}, \tag{3.27}$$

where $k_{\mathrm{Q}} = \frac{q}{m}A_{\mathrm{Q}}$.

As for the dipolar excitation, the axial motion stays unaffected. Concerning the trajectory in the radial plane, the equation of motion becomes in the complex description:

$$\ddot{u} + \imath\omega_{\mathrm{c}}\dot{u} - \left(\frac{\omega_{\mathrm{z}}^2}{2} - 2\imath k_{\mathrm{Q}}\cos(\omega_{\mathrm{Q}}t + \theta_{\mathrm{Q}})\right)u = 0. \tag{3.28}$$

The solutions of the trajectory $\{x(t); y(t)\}$ have the same structure as before. The solutions of the motion $\rho_{\pm}(t)$ are given in [Köni95a] under the rotating wave assumption, *i.e.*, negligible variations of $u(t) = u_0 \pm (\delta u)(t)$ during a given time δt:

$$\rho_{\pm}(t) = \left(\rho_{\pm}(0)\cos(\omega_{\mathrm{B}}t) \mp \frac{1}{2}\frac{\rho_{\pm}(0)\Big(\imath(\omega_{\mathrm{Q}} - \omega_{\mathrm{c}})\Big) + \rho_{\mp}(0)k_{\mathrm{Q}}^{\pm}}{\omega_{\mathrm{B}}}\sin(\omega_{\mathrm{B}}t) \right) e^{\imath\frac{1}{2}(\omega_{\mathrm{Q}}-\omega_{\mathrm{c}})t}, \tag{3.29}$$

with $\omega_{\mathrm{B}} = \frac{1}{2}\sqrt{(\omega_{\mathrm{c}} - \omega_{\mathrm{Q}})^2 + k_{\mathrm{Q}}^2}$ and $k_{\mathrm{Q}}^{\pm} = k_{\mathrm{Q}}e^{\pm\imath\Delta\vartheta}$.

The effect of the quadrupolar excitation is a conversion of the magnetron motion into the cyclotron motion (and vice versa) under the condition that the angular frequency ω_{Q} is equal to $\omega_{\mathrm{c}} = \omega_{+} + \omega_{-}$. For more details see [Köni95a] and Section 3.4.

3.3.3 Damping of the ion motion in the Penning trap

The equation of motion previously studied was solved under the assumption of no frictional damping. Thus for the handling of charged particles, ultra high vacuum conditions are required (10^{-8} mbar or better). However, the effects of damping can still be observed for the ion trajectory, especially when applying rf-excitations. In the following, a frictional damping force is introduced. It can be written as $\overrightarrow{F_{\delta}} = -\delta\vec{v}$, where δ is the damping coefficient.

Damped motion without external forces

The equations can be once again solved independently for the motions along the z-axis and in the radial plane. Concerning the sinusoidal motion along the z-axis, the main difference is that the amplitude of the motion is damped:

$$\ddot{z} + \frac{\delta}{m}\dot{z} + \omega_{\mathrm{z}}^2 z = 0. \tag{3.30}$$

The solution for this kind of equation is given by:

$$z(t) = A_{\mathrm{z}}e^{-(\delta/2m)t}\cos(\widetilde{\omega}_{\mathrm{z}}t + \theta_{\mathrm{z}}), \tag{3.31}$$

where

$$\widetilde{\omega}_{\mathrm{z}} = \sqrt{\omega_{\mathrm{z}}^2 - \left(\frac{\delta}{2m}\right)^2}. \tag{3.32}$$

It is worth to note that not only the amplitude is affected by the frictional damping but also the angular frequency, which is shifted to a lower frequency.

In the same way, the equation of motion in the plane can be written as:

$$\ddot{u} + \left(\imath\omega_{\mathrm{c}} + \frac{\delta}{m}\right)\dot{u} - \frac{\omega_{\mathrm{z}}^2}{2}u = 0. \tag{3.33}$$

Because of the phase that appears in the first order term and since a damping term for the motions is expected in the plane as well, the following substitution can be used: $\widetilde{u}(t) = u_0(t)e^{-\imath\widetilde{\Omega}t}$, where $\widetilde{\Omega}$ is expected to be a complex number. The real part $\Re\left\{\widetilde{\Omega}\right\}$ characterizes the angular frequency of the corresponding motion, whereas the imaginary part $\Im\left\{\widetilde{\Omega}\right\}$ represents the associated damping coefficient. The general form for the solution of the equation is a linear combination of the eigenterms:

$$\widetilde{\Omega}_{\pm} = \frac{1}{2}\left(\omega_{\mathrm{c}} - \imath\frac{\delta}{m} \pm \sqrt{\left(\omega_{\mathrm{c}} - \imath\frac{\delta}{m}\right)^2 - 2\omega_{\mathrm{z}}^2}\right) \tag{3.34}$$

$$\widetilde{u}(t) = u_+ e^{-\imath\alpha_+}e^{-\imath\widetilde{\omega}_+ t} + u_- e^{-\imath\alpha_+}e^{-\imath\widetilde{\omega}_- t}, \tag{3.35}$$

where $\alpha_{\pm} = \Im\left\{\widetilde{\Omega}_{\pm}\right\}$ and $\widetilde{\omega}_{\pm} = \Re\left\{\widetilde{\Omega}_{\pm}\right\}$.
Coming back to the cartesian coordinates, the equations are:

$$\begin{bmatrix} x(t) \\ y(t) \end{bmatrix} = \rho_+ e^{\alpha_+ t}\begin{bmatrix} \cos(\widetilde{\omega}_+ t + \theta_+) \\ \sin(\widetilde{\omega}_+ t + \theta_+) \end{bmatrix} + \rho_- e^{\alpha_- t}\begin{bmatrix} \cos(\widetilde{\omega}_- t + \theta_-) \\ \sin(\widetilde{\omega}_- t + \theta_-) \end{bmatrix}. \tag{3.36}$$

After the separation into the real and imaginary part, the Taylor expansion of Eq. (3.34) in δ to the 4[th] order[3] gives the following angular frequencies:

$$\widetilde{\omega}_{\pm} = \omega_{\pm} \pm \Delta\omega \tag{3.37}$$

$$\Delta\omega = \frac{1}{2}\left(\frac{\delta}{m}\right)^2 \frac{\omega_{\mathrm{z}}^2}{\left(\omega_{\mathrm{c}}^2 - 2\omega_{\mathrm{z}}^2\right)^{3/2}} - \frac{1}{4}\left(\frac{\delta}{m}\right)^4 \frac{\omega_{\mathrm{z}}^2\left(2\omega_{\mathrm{c}}^2 + \omega_{\mathrm{z}}^2\right)}{\left(\omega_{\mathrm{c}}^2 - 2\omega_{\mathrm{z}}^2\right)^{7/2}} + \mathrm{O}(\delta^6). \tag{3.38}$$

Compared to the ideal undamped case, the angular frequencies are slightly shifted. The magnetron angular frequency (respectively the reduced cyclotron angular frequency) is shifted towards lower angular frequency (respectively higher angular frequency). Moreover the shifts for both angular frequencies have the same value so that the relation given in Eq. (3.15) is still valid.

The radii of the motions are modulated by an exponential function with the respective time constant $\alpha_{\pm}$ given in the first order of δ by [4]:

$$\alpha_{\pm} = -\frac{\delta}{2m}\left(1 \pm \frac{\omega_{\mathrm{c}}}{\sqrt{\omega_{\mathrm{c}}^2 - 2\omega_{\mathrm{z}}^2}}\right) + \mathrm{O}(\delta^3). \tag{3.39}$$

[3]Even though the δ^4 term does not have a large contribution on the frequency shift, Talyor expansion to the 4[th] order can be found in the literature. However, in [Fors01] and [Mukh04b], the result in the 4 [th] order disagrees on the last term. In [Fors01], the Taylor expansion Eq. (B.7) is wrong due to the ansatz, whereas in [Mukh04b] the higher terms in $\left(\omega_{\mathrm{c}}^2 - 2\omega_{\mathrm{z}}^2\right)^k$ for $k > 3/2$ might have been implicitly neglected. Here the corrected Taylor expansion is presented.

[4]Eq. (3.48) in [Mukh04b] is only valid up to the first power of δ for the same reasons as before.

As a consequence of Eq. (3.15), $(\omega_c^2 - 2\omega_z^2)^{-1/2}$ can be redefined as $\omega_p = \omega_+ - \omega_-$, which can lead to parametric resonances [Schw90], so that:

$$\alpha_\pm = \mp\frac{\delta}{m} \cdot \frac{\omega_\pm}{\omega_+ - \omega_-} + O(\delta^3), \tag{3.40}$$

where $\omega_\pm$ are the angular frequencies without damping [Dill01a, Schm01].

With a damping force, the magnetron radius increases during time with a time constant $\alpha_- \approx \frac{\delta}{m}\frac{\omega_-}{\omega_+}$ whereas the cyclotron radius decreases with a larger time constant $\alpha_+ \approx -\frac{\delta}{m}$. Due to the positive time constant for the magnetron motion, ions can be lost in the trap if the vacuum is not good enough or if the ions are stored for a too long period.
As an example, the following frequency shifts and constants are obtained for $^{39}K^+$: (see Appendix A)

$$\begin{aligned} \Delta\omega &= 1.6 \cdot 10^{-11}\ s^{-1}, \\ \alpha_- &= 3.3 \cdot 10^{-4}\ s^{-1}, \\ |\alpha_+| &= 0.7\ s^{-1}, \\ \Delta\omega_z &= 1.8 \cdot 10^{-7}\ s^{-1}. \end{aligned}$$

Damped motion with dipolar and quadrupolar excitations

Solutions for the ion motion in a Penning trap for dipolar and quadrupolar excitations with a damping force can be found in the literature [Köni95a, Schm01].

During a dipolar excitation at $\omega_\pm$ with no damping, it has been stated that the radii $\rho_\pm$ are increasing during time. A damping force speeds up the increase of the magnetron radius, whereas it counteracts the increase of the cyclotron motion. In order to center and cool an ion cloud, the buffer-gas cooling technique [Sava91] can be used.

The general form of the motion during a dipolar excitation in the presence of frictional damping can be found in [Schm01]:

$$\rho_\pm(t) = \frac{1}{\omega_+ - \omega_-}\sqrt{\left[(\omega_+ - \omega_-)\rho_\pm(0)e^{\alpha_\pm t} + \frac{k_D}{2} \cdot \frac{\zeta_\pm}{\kappa_\pm}\right]^2 + \left[\frac{k_D}{2} \cdot \frac{\xi_\pm}{\kappa_\pm}\right]^2}. \tag{3.41}$$

with $\alpha_\pm$ as defined in Eq. (3.40), $\Delta\omega_\pm = \omega_D - \omega_\pm$ and $\Delta\phi_\pm = \phi_D - \phi_\pm$:

$$\begin{aligned} \kappa_\pm &= \Delta\omega_\pm^2 + \alpha_\pm^2 \\ \zeta_\pm &= \Delta\omega_\pm \left\{\pm(\cos\Delta\phi_\pm)(e^{\alpha_\pm t} - \cos(\Delta\omega_\pm t)) + (\sin\Delta\phi_\pm)(\sin(\Delta\omega_\pm t))\right\} + \\ &\quad \alpha_\pm \left\{\ \ (\sin\Delta\phi_\pm)(e^{\alpha_\pm t} - \cos(\Delta\omega_\pm t)) \mp (\cos\Delta\phi_\pm)(\sin(\Delta\omega_\pm t))\right\} \\ \xi_\pm &= \Delta\omega_\pm \left\{\mp(\sin\Delta\phi_\pm)(e^{\alpha_\pm t} - \cos(\Delta\omega_\pm t)) + (\cos\Delta\phi_\pm)(\sin(\Delta\omega_\pm t))\right\} + \\ &\quad \alpha_\pm \left\{\mp(\cos\Delta\phi_\pm)(e^{\alpha_\pm t} - \cos(\Delta\omega_\pm t)) - (\sin\Delta\phi_\pm)(\sin(\Delta\omega_\pm t))\right\}. \end{aligned}$$

It has been noted earlier that a quadrupolar excitation transforms the magnetron motion into the cyclotron motion, if the applied angular frequency matches the cyclotron frequency of the ion. Since with a damping force the radius of the cyclotron motion decreases faster than the magnetron radius increases, and since the axial motion is damped too, a quadrupolar excitation can be used to center the ion bunch in the trap.

The solution of a quadrupolar excitation with a frictional damping force is given in [Köni95a][5] under the rotating wave approximation:

$$\begin{aligned}\rho_{\pm}(t) &= e^{-\frac{\delta}{2m}t}\cdot e^{\imath\frac{1}{2}(\omega_{\mathrm{Q}}-\omega_{\mathrm{c}})t}\cdot \\ &\left(\rho_{\pm}^{0}\cosh(\omega_{\mathrm{B}}e^{i\theta t})\mp\frac{\rho_{\pm}^{0}\left(\gamma\omega_{\mathrm{c}}+\imath(\omega_{\mathrm{Q}}-\omega_{\mathrm{c}})\right)+\rho_{\mp}^{0}k_{\mathrm{Q}}^{\pm}}{2\omega_{\mathrm{B}}e^{\imath\theta}}\sinh(\omega_{\mathrm{B}}e^{\imath\theta t})\right),\end{aligned} \tag{3.42}$$

with $\rho_{\pm}^{0}\stackrel{def}{=}\rho_{\pm}(t=0)$ and:

$$\begin{aligned}k_{\mathrm{Q}}^{\pm} &= k_{\mathrm{Q}}e^{\pm\imath\Delta\vartheta}\\ \gamma &= \frac{\delta}{m(\omega_{+}-\omega_{-})}\\ \omega_{\mathrm{B}} &= \sqrt{\omega_{B_{+}}\omega_{B_{-}}}\\ \omega_{B_{\pm}} &= \frac{1}{2}\sqrt{(\omega_{\mathrm{c}}-\omega_{\mathrm{Q}})^{2}+(\gamma\omega_{\mathrm{c}}\mp k_{\mathrm{Q}})^{2}}\\ \theta &= \frac{1}{2}(\theta_{+}+\theta_{-})\\ \theta_{\pm} &= \arctan\left(\frac{\omega_{\mathrm{Q}}-\omega_{\mathrm{c}}}{\gamma\omega_{\mathrm{c}}\mp k_{\mathrm{Q}}}\right).\end{aligned}$$

The general solutions Eq. (3.41) and (3.42) presented in this Section reduce to the previously discussed results Eq. (3.23) and Eq. (3.29) in case of no damping. For more detailed explanations see [Köni95a, Schm01].

3.4 Illustration of the ion motion excitation schemes

The presented excitation schemes, if performed at the respective resonance frequencies, can be used to manipulate the stored ion. The illustrations of the ion motion are given in Fig. 3.4 to 3.6. They represent the azimuthal projection of the trajectories during application of the excitation schemes at the resonant excitation frequency ($\nu_{\pm}$ for the dipolar excitation and the cyclotron frequency ν_{c} for the quadrupolar excitation) and compare the action of the damping force due to residual gas. The following set of figures can be considered as the basic 'How To' of ion trapping and ion manipulation in a Penning trap.

[5] Note that in [Köni95a] an alternative definition of the damping coefficient is used: $\delta_{\mathrm{Lit}}=\delta/m$.

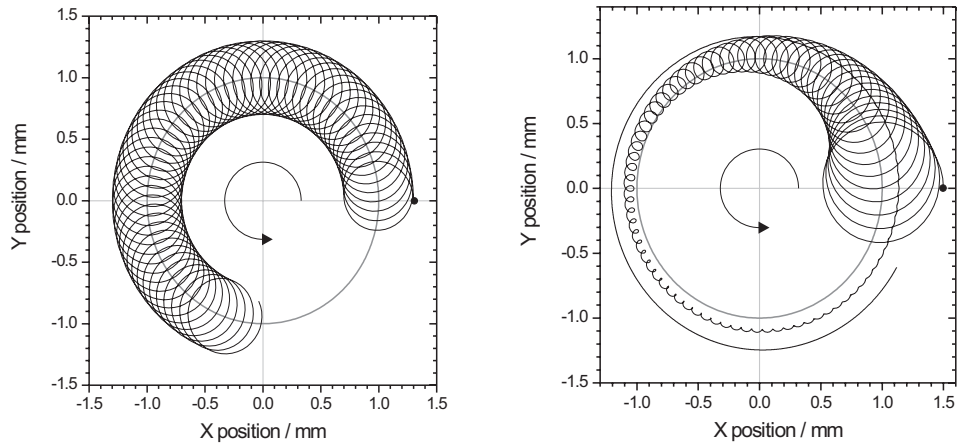

FIGURE 3.4: *Ion motion in a Penning trap without excitation.*
The start of the ion motion is specified by the dot and the direction of the motion is given by the arrow. The trajectory on the left represents the ion motion in the ideal case without damping according to Eq. (3.16)*. The radial harmonic oscillations of the motion can be nicely observed. On the right according to Eq.* (3.36)*, the effect of residual gas is shown, which leads to a damping of the cyclotron motion (ρ_+ decreases) and to an increase of the unstable magnetron motion (ρ_- increases).*

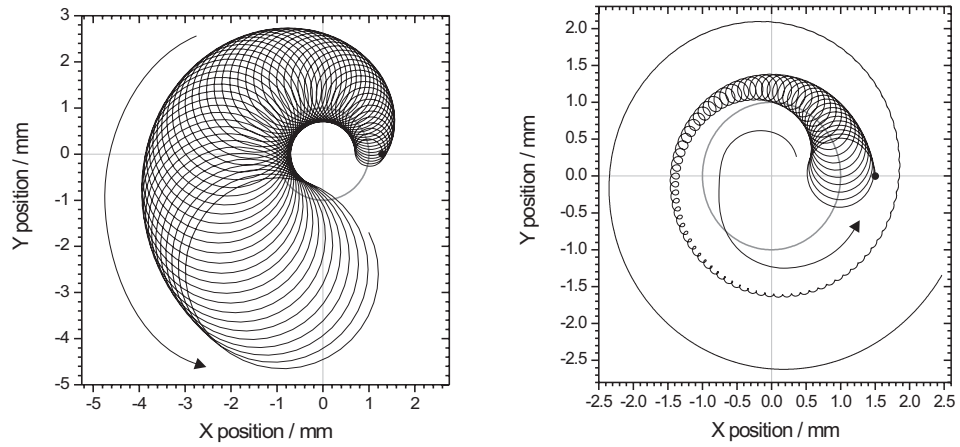

FIGURE 3.5: *Ion motion in a Penning trap with dipolar excitation.*
The start of the ion motion is specified by the dot and the direction of the motion is given by the arrow. The trajectory on the left represents the ion motion in case of no damping plotted according to Eq. (3.23)*. An increase of the two radii $\rho_\pm$ can be observed. On the right, according to Eq.* (3.41)*, the effect of residual gas is shown in addition to the dipolar excitation. The magnetron radius increases faster due to the damping force. The cyclotron radius increases as well but the damping overcomes this effect and as a result ρ_+ decreases.*

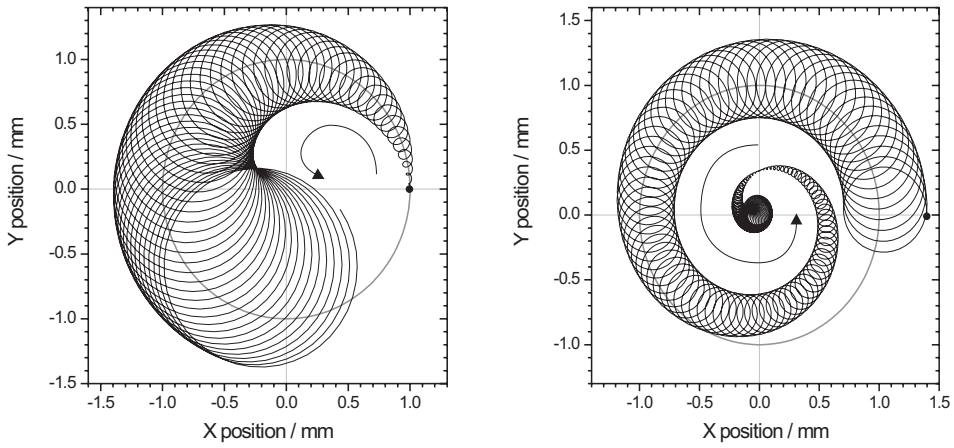

FIGURE 3.6: *Ion motion in a Penning trap with quadrupolar excitation at* ω_c*. The start of the ion motion is specified by the dot and the direction of the motion is given by the arrow. The trajectory on the left represents the ion motion in case of no damping, which is plotted according to Eq.* (3.29)*. The conversion between the two eigenmotions can be observed. Here only the magnetron to cyclotron conversion is shown, but for longer excitation time, the conversion will go from pure cyclotron to magnetron motion as well. On the right, see Eq.* (3.42)*, the effect of residual gas is shown in addition to the quadrupolar excitation. The conversion takes places, as in the no-damping case, so that the magnetron radius is converted to cyclotron motion which is damped. Since the conversion from magnetron to cyclotron motion and the damping of the cyclotron motion are faster than the increase of the magnetron radius, the ions are centered.*

It has been stated and demonstrated that the Penning trap device is the tool of choice concerning the ion storage and manipulation with an extreme precision and efficiency [Boll03, Blau06]. Therefore, high-precision mass spectrometers such as ISOLTRAP [Herf03], SHIPTRAP [Dill01b], SMILETRAP [Frit02], JYFLTRAP [Kolh03], and LEBIT [Schw03] use Penning trap systems to perform their radioactive isotope mass measurements.

Experiment and Technique

Chapter 4

The ISOLTRAP mass spectrometer at ISOLDE/CERN

4.1 The ISOLDE Facility at CERN

4.1.1 Overview of the facility

Since 1992, the ISOLDE (Isotope On-Line Mass Separator) facility [Kugl92, Kugl00] is located at the Proton-Synchrotron Booster of CERN. It is aimed to the production of radioactive beams by means of impinging high-energetic protons (1–1.4 GeV) on a thick target. The protons produced and accelerated by the LINAC/Booster facility are delivered as bunches every 1.2 seconds (a cycle of 900 ms is under commissioning) with an energy varying from 1 to 1.4 GeV and an intensity of up to $3{\cdot}10^{13}$ protons per pulse.

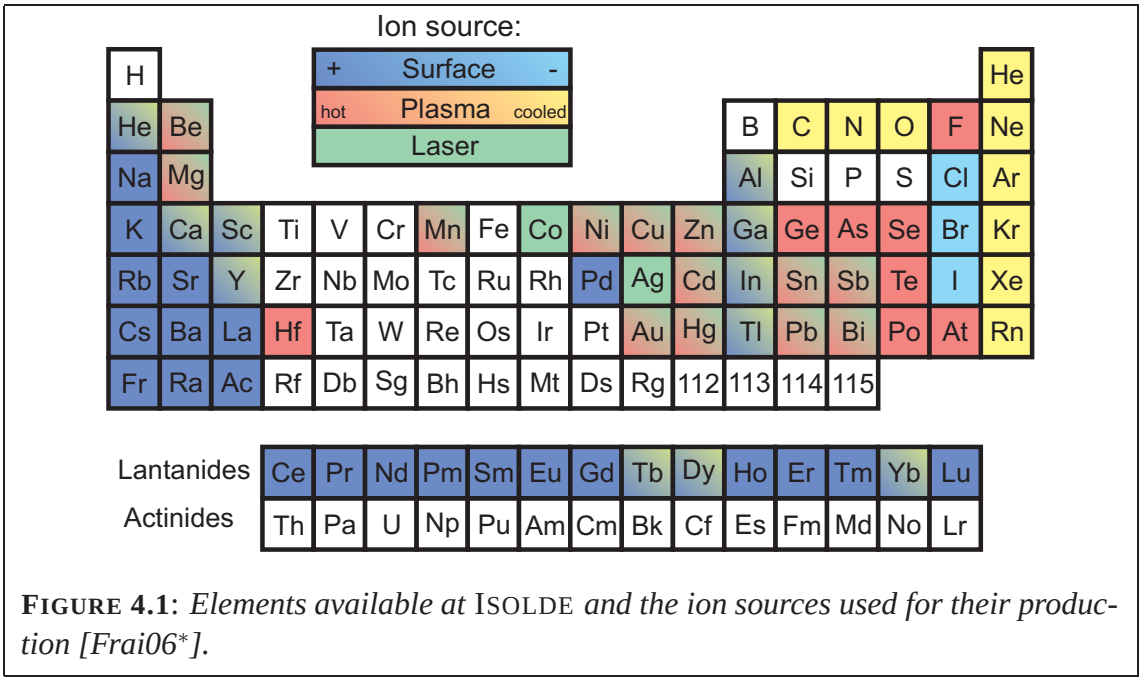

FIGURE 4.1: *Elements available at* ISOLDE *and the ion sources used for their production [Frai06*].*

Upon impact of the high energetic proton pulse on the ISOLDE thick target, radioactive short-lived nuclides are produced via spallation, fission or fragmentation of the target material. With the ISOL technique [Ravn92, Dill01a] not all radioactive isotopes of the nuclear chart can be produced, *e.g.* no refractory elements are not provided due to their long release time. More than 70 elements and about 1100 isotopes from He ($Z = 2$) to Actinium ($Z = 89$), and with half-lives down to a few milliseconds, are available with an intensity from a few ions per second up to a few ten nA. The radioactive atoms created in the target are extracted by thermal diffusion [Rodr02] and then ionized by means of electron impact, surface or resonant laser ionization (RILIS) [Köst02] (see Fig. 4.1). The usually singly charged ions are then extracted and accelerated up to 60 keV.

4.1.2 The beam distribution system

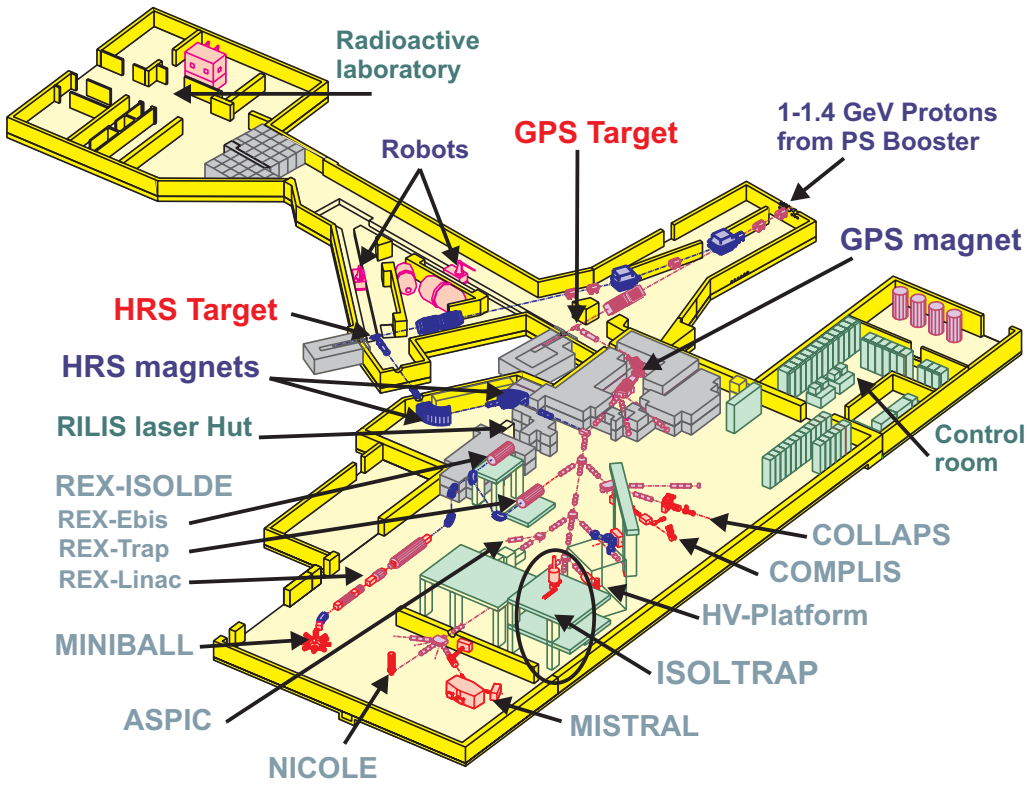

FIGURE 4.2: *Sketch of the experimental hall of the* ISOLDE *facility at* CERN.

Before being delivered to the different experiments in the ISOLDE hall, the fast 60-keV beam is isobarically separated via either one of the two mass separators GPS (General Purpose Separator) or HRS (High Resolution Separator):

- The GPS has been designed to provide three parallel beams, one main central beam line for experiments located downstream in the ISOLDE hall, and two side lines for collections and/or check of the beam properties. The resolving power of the 69° magnet is $m/\Delta m \approx 800$.
- The HRS is composed of two sequentially aligned magnets with 90° and 60° bending angle, respectively. With a mass resolution of up to $m/\Delta m = 4000$, almost pure isobaric beams can be delivered to the experiments.

The large variety of radioactive ion-beam species produced at ISOLDE can be delivered with a beam emittance of about 35π·mm·mrad at 60 keV [Fors01] to different experiments (see Fig. 4.2) that are dedicated to various branches of physics such as nuclear and atomic physics (*e.g.* MISTRAL, ISOLTRAP or COLLAPS), solid-state physics (*e.g.* ASPIC), and life and material sciences.

4.2 The ISOLTRAP experiment

4.2.1 General description

ISOLTRAP is an experimental setup installed at the CERN/ISOLDE facility. Relying on a unique Penning-trap combination, the ISOLTRAP mass spectrometer is devoted to on-line high-precision mass measurements on short-lived radionuclides produced at ISOLDE.

In order to perform precise and accurate mass measurements, ISOLTRAP takes the ion beam delivered by ISOLDE, prepares and cleans it from isobaric and even isomeric contaminants, and then performs the mass measurement on a clean ion cloud of a few ions at once.
The mass measurement is based on the determination of the cyclotron frequency ν_c in a Penning trap, see Eq. (3.6). With this method, the versatile experiment ISOLTRAP has shown its ability to perform very precise mass determinations on rare short-lived nuclides [Boll03, Blau05a, Herf05]. It allows mass determinations with an uncertainty of better than 10 parts per billion even for unstable nuclides that decay within a few tens of milliseconds [Kell04a].

The ISOLTRAP mass spectrometer is a combination of Paul and Penning traps. It is composed of three main parts (see Fig. 4.3) that will be further described:

- the radio frequency quadrupole (RFQ) – buncher (also known as RICB for RFQ Ion Cooler and Buncher),
- the cylindrical purification Penning trap,
- and the hyperbolical precision Penning trap.

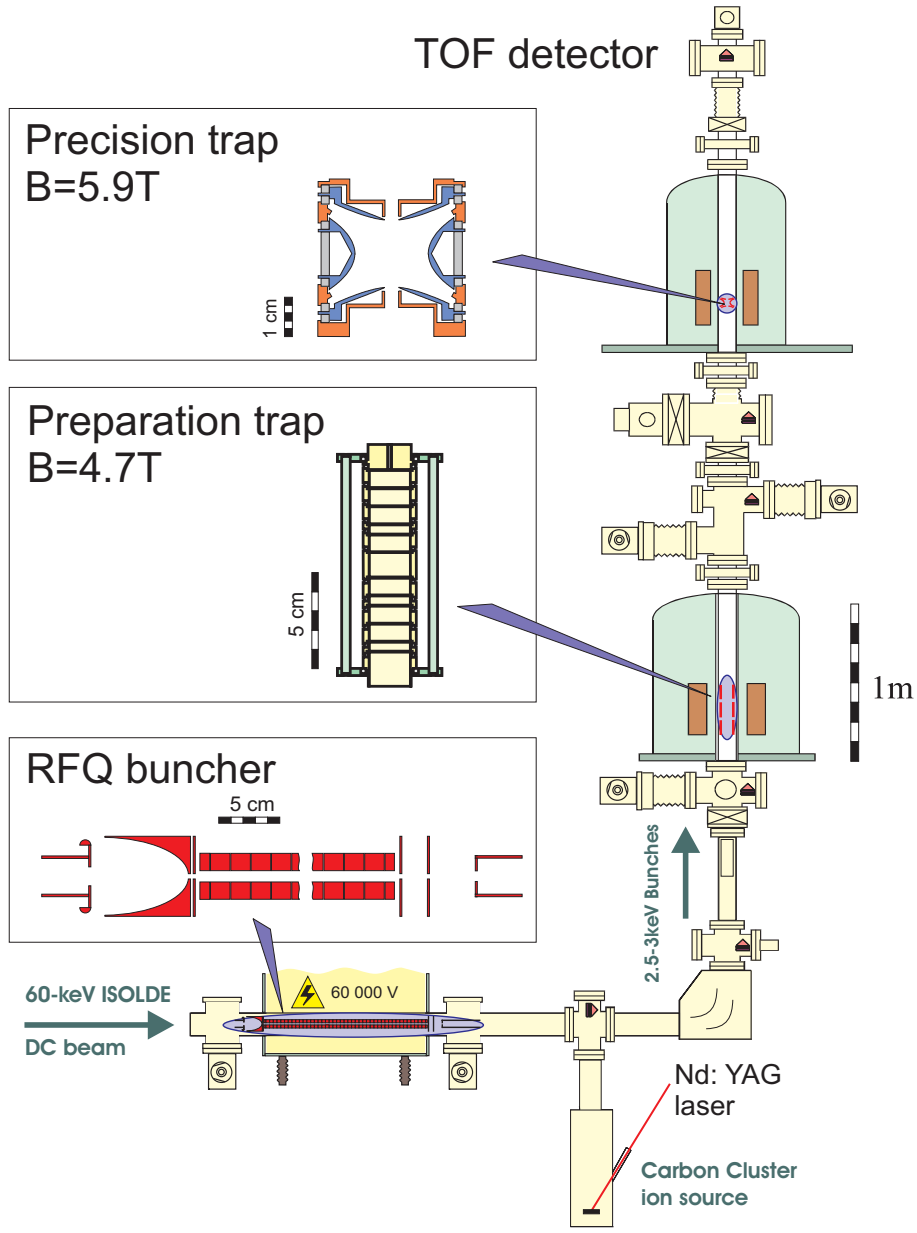

FIGURE 4.3: *Sketch of the* ISOLTRAP *experiment, located at* ISOLDE/CERN.

4.2.2 The Radio Frequency Quadrupole ion beam cooler and buncher

The RFQ (see Fig. 4.4) is a linear Paul trap filled with helium buffer gas, and is used for accumulation, cooling, and bunching of the 60-keV ISOLDE ion beam in order to reach the requirements for the injection into the first Penning trap [Herf01b]. The RFQ buncher is composed of four longitudinally segmented rods in order to axially and radially store the ions.

FIGURE 4.4: *Photo of the radio frequency quadrupole (RFQ) of* ISOLTRAP *[Herf01b].*

The ion beam from ISOLDE is decelerated and focused by the first egg-shaped electrode [Kell01]. The energy of the beam decreases from 60 keV to a few hundreds of eV. The beam enters the RFQ itself. The voltages applied to the longitudinally segmented rods produce a potential well to trap the ion beam (see Fig. 4.5). The trap is filled with helium as buffer gas under a partial pressure of $3{\cdot}10^{-6}$ mbar. This value is not measured in the trap itself but just outside, therefore it can only be assumed that the pressure value inside the RFQ is in the order of 10^{-2} to 10^{-3} mbar. Due to the collisions with the buffer gas the ions lose their remaining kinetic energy: the ion beam is cooled and its emittance is reduced. Finally, after a few milliseconds the last electrodes of the segmented rods are switched down in order to release the ion bunch so that it can be transported via ion-optical elements to the second stage of the spectrometer.

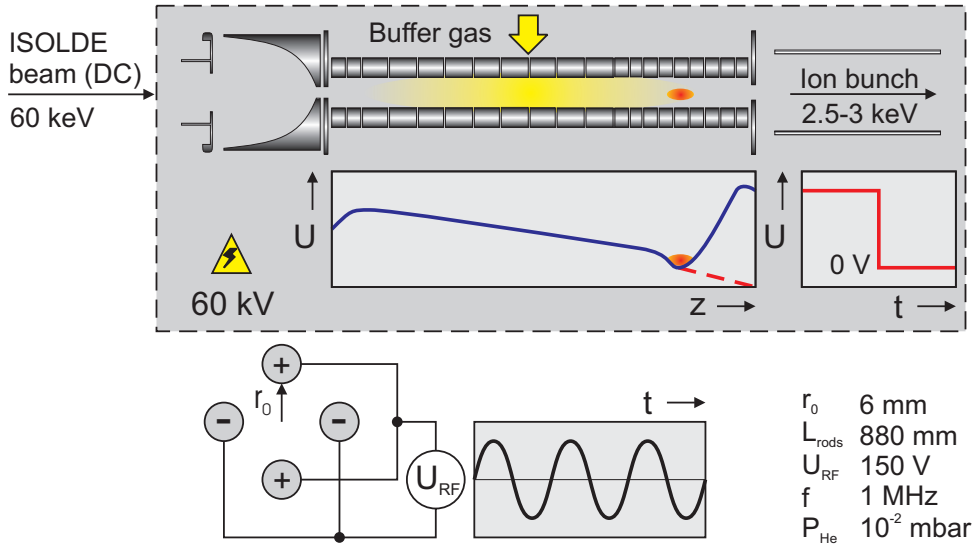

FIGURE 4.5: *Principle of the RFQ-buncher.*

With the RFQ, the cooled ions are extracted with an efficiency of at present around 15% towards the preparation trap. After the ejection from the RFQ, the energy of the beam is reduced to 2.5-3 keV by use of a pulsed cavity (see Appendix B). A typical ion bunch has an emittance of less than $10\pi{\cdot}$mm·mrad at 3 keV [Dill01a, Herf01b, Rodr02, Ban04].

4.2.3 The preparation Penning trap

Located in a strong magnetic field of 4.7 T, the cylindrical Penning trap (Fig. 4.6) is used for both, cooling and isobaric cleaning of the ion bunch delivered by the RFQ. Employing a mass selective buffer-gas cooling technique [Sava91] (see also Section 3.4), the trap can release an isobaric-contamination free ion bunch to the precision trap.

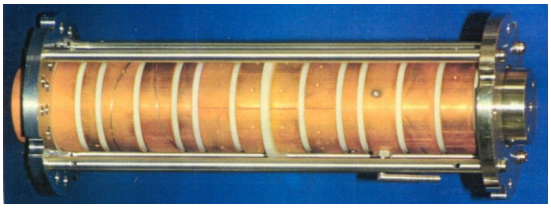

FIGURE 4.6: *Photo of the cylindrical preparation Penning trap of* ISOLTRAP.

The ions coming from the buncher are captured and trapped axially by a potential well as shown in Fig. 4.7. The ion bunch can be cooled and the removal of contaminants be performed. To this end, a series of excitations of the ion motion is used. First, a dipolar magnetron excitation is applied, which increases the ion magnetron radius as demonstrated in Section 3.3.2. Since to first order ν_- does not depend on the mass, a fixed frequency can be applied for all ions (see Section 3.4). The amplitude of this excitation is chosen such that after the dipolar excitation none of the ions initially stored in the trap can be ejected, *i.e.*, the radius reached after the excitation is larger than the aperture hole at the end of the trap.

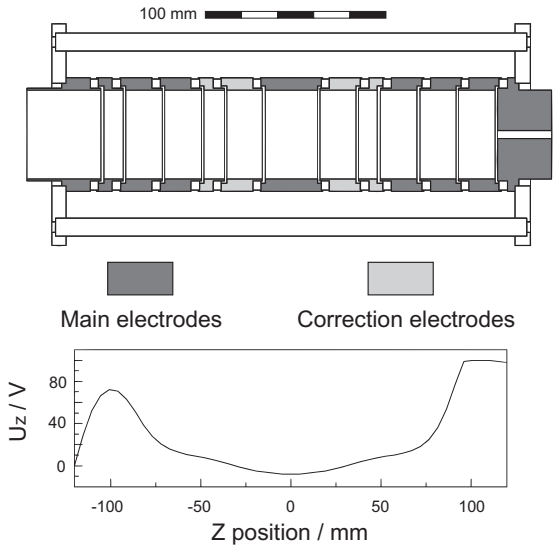

FIGURE 4.7: *Sketch of the stack of electrodes (top) and trapping electric field of the preparation trap (bottom) [Raim97].*

In order to eject the ions of interest towards the precision trap, they have to be re-centered along the axis. This is achieved by use of a quadrupolar excitation at ν_c (see Section 3.4). The rf-excitation converts the magnetron motion into cyclotron motion and with the action of the helium buffer gas, the cyclotron motion is damped and the ions are centered. Since the resonant frequency ν_c is mass dependent, the rf-excitation only centers the ions of interest. Thus, the excitations leads to an isobaric selection and therefore a removal of contaminants with a resolving power of up to R=10^5, depending on the excitation time of ν_c. Further removal of contaminants is possible with additional dipolar cleaning by resonant excitation at the respective cyclotron frequency ν_+ of the contaminants.

After isobaric cleaning the prepared ion bunch is ejected towards the precision trap. The pulse length of the ion bunch is of the order of one microsecond so that its properties are well defined for the injection into the precision trap.

4.2.4 The precision Penning trap

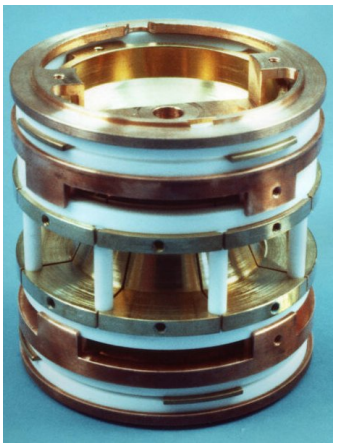

FIGURE 4.8: *Photo of the hyperbolical Penning trap of* ISOLTRAP [1].

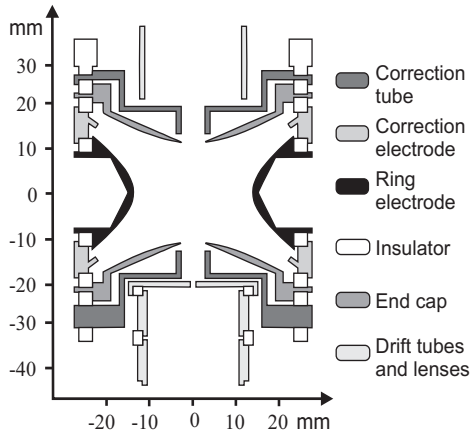

FIGURE 4.9: *Design of the precision Penning trap.*

The hyperbolic precision Penning trap (Fig. 4.8 and 4.9) is located in a 5.9 T magnetic field. For the mass measurement it uses a specific combination of dipolar and quadrupolar excitation schemes and a resonant time-of-flight (TOF) detection technique [Gräf80]. An optional dipolar cleaning by resonant excitation at the respective cyclotron frequency ν_+ can also be applied in order to remove remaining contaminants like isobars or isomers [Blau04, Roos04].

[1] Note: The picture actually shows SMILETRAP's precision trap [Berg02]. The only difference is that ISOLTRAP's trap is 4-fold segmented whereas SMILETRAP's one has 8 equally sized segments.

The ions ejected from the preparation trap to the precision trap have a very low energy spread. Once captured and stored in the precision trap they are very close to the magnetic field axis if the optimization procedure has been done properly (see Section 4.4). The stored ions have initially almost no cyclotron radius ($\rho_+ \approx 0$ mm) and a very small magnetron radius ($\rho_- \approx 0.2$ mm).

For the cyclotron frequency determination, the ions are manipulated as follows:

- First the magnetron radius is increased by applying a phase sensitive dipolar excitation at ν_- [Blau03b] as in the case of the preparation trap. In contrast to the dipolar excitation in the preparation trap, the aim is not remove the ions, but to excite the motion to a specific magnetron radius.

- The second step can be skipped if no contamination is observed in the trap. Otherwise, a selective cleaning can be used by applying a dipolar excitation at the cyclotron frequency ν_+ of the contaminants. This leads to an increase of the cyclotron motion of the unwanted ions. The strength of the excitation is chosen such that the ions are radially ejected from the trap. This cleaning reaches a resolving power of $m/\Delta m \approx 10^7$ for about 1 s excitation time.

- Finally, in order to find the cyclotron frequency of the remaining pure ion ensemble in the trap, a quadrupolar rf-excitation is used, which is resonant for $\nu_\mathrm{Q} = \nu_\mathrm{c}$. In resonance and for an optimal rf-amplitude a full conversion from pure magnetron to cyclotron motion is achieved and since $\nu_+ \gg \nu_-$ the radial energy gain has a maximum.

Once this series of excitations is completed, the ions are ejected towards a detector, where the time of flight and thus the initial radial energy of the ions is measured. The indices '$_\mathrm{D}$' and '$_\mathrm{Q}$' for the frequencies ν_D for dipolar and ν_Q for quadrupolar excitation, respectively, were introduced to distinguish between these two cases. Since the mass determination only relies on the measurement of the cyclotron frequency using a quadrupolar rf-excitation, in the following and as far as cyclotron frequency determination is concerned ν_Q will be noted as ν_RF (as well as any other related variable).

4.3 Mass determination procedure

4.3.1 Resonant energy conversion

Magnetron to cyclotron conversion

Since the magnetron angular frequency is negligible in comparison to the reduced cyclotron frequency $\omega_- \ll \omega_+$, the conversion due to the rf-excitation leads to the following radial energy [Brow86, Schw93], which is composed of two parts:

$$\begin{aligned} E_{\mathrm{rad}} &= E_{\mathrm{rad}}^{\mathrm{kin}} + E_{\mathrm{rad}}^{\mathrm{pot}} \\ E_{\mathrm{rad}} &= \frac{1}{2}m\left(\rho_+^2\omega_+^2 + \rho_-^2\omega_-^2\right) - \frac{1}{2}m\omega_+\omega_-\left(\rho_+^2 + \rho_-^2\right) \\ &\approx \frac{1}{2}m(\rho_+\omega_+)^2. \end{aligned} \tag{4.1}$$

A more detailed study of the solutions given for the motion of an ion after a quadrupolar rf-excitation at ω_{RF} applied during a time T_{RF} (see Eq. (3.42)) shows that the radial kinetic energy E_{rad} of a single ion stored in the Penning trap is [Köni95a]:

$$E_{\mathrm{rad}}(\omega_{\mathrm{RF}}) \propto \frac{\sin^2(\omega_{\mathrm{B}}T_{\mathrm{RF}})}{\omega_{\mathrm{B}}^2}, \tag{4.2}$$

with (cf. Eq. (3.42))

$$\omega_{\mathrm{B}} = \omega_{\mathrm{B}}(\omega_{\mathrm{RF}}) = \sqrt{\omega_{\mathrm{B}_+}\omega_{\mathrm{B}_-}}$$

$$\omega_{\mathrm{B}_\pm} = \omega_{\mathrm{B}_\pm}(\omega_{\mathrm{RF}}) = \frac{1}{2}\sqrt{(\omega_{\mathrm{c}} - \omega_{\mathrm{RF}})^2 + (\gamma\omega_{\mathrm{c}} \mp k_{\mathrm{RF}})^2}.$$

At $\omega_{\mathrm{RF}} = \omega_{\mathrm{c}}$ the energy of the system is maximal. In order to see the effect of energy gain on the TOF, the radial energy needs to be converted into axial energy.

Radial to axial energy conversion

After the rf-excitation, the ions are extracted from the Penning trap (where a strong magnetic field is present) to the detector area (where almost no magnetic field remains). Thus the ions experience a strong magnetic field gradient. This creates a force on the orbital magnetic moment of the ion given by:

$$\vec{F} = -\frac{E_{\mathrm{rad}}(\omega_{\mathrm{RF}})}{B}\frac{\partial B}{\partial z}\vec{e_{\mathrm{z}}}. \tag{4.3}$$

For an adiabatic motion, *i.e.* $\Delta B/B \ll 1$ for one cyclotron period, the magnetic moment of the system is conserved. The effect of this force is a conversion of the radial motion into an axial motion.

Thus, due to the quadrupolar rf-excitation, which resonantly increases the radial energy of the system, and the magnetic field gradient, which converts radial into axial energy, the cyclotron frequency of the ion of interest can be determined by monitoring the time of flight as a function of the frequency of the applied rf-excitation. When it reaches ν_{c}, the conversion from magnetron to cyclotron motion is maximal, and therefore the radial energy, leads to the shortest TOF.
The TOF is given by [Köni95a]:

$$TOF(\omega_{RF}) = \int_0^{z_{\mathrm{detector}}} \sqrt{\frac{m}{2\left(E_0 - qV(z) - E_{\mathrm{rad}}(\omega_{RF})B(z)/B_0\right)}}dz \tag{4.4}$$

where E_0 is the initial axial energy of the ion, $V(z)$ the electric potential created by the drift electrodes, $B(z)$ the strength of the magnetic field on the z-axis, and B_0 the magnetic field value in the trap region.

For an ion with a charge q and a resonant TOF spectrum, the relation:

$$\nu_{\mathrm{RF}} = \nu_{\mathrm{c}} = q \cdot \frac{1}{2\pi} \cdot \frac{B}{m}, \tag{4.5}$$

provides the derivation of the unknown mass m of radionuclide under the condition that the ion the strength of the magnetic field B is known with sufficient precision.

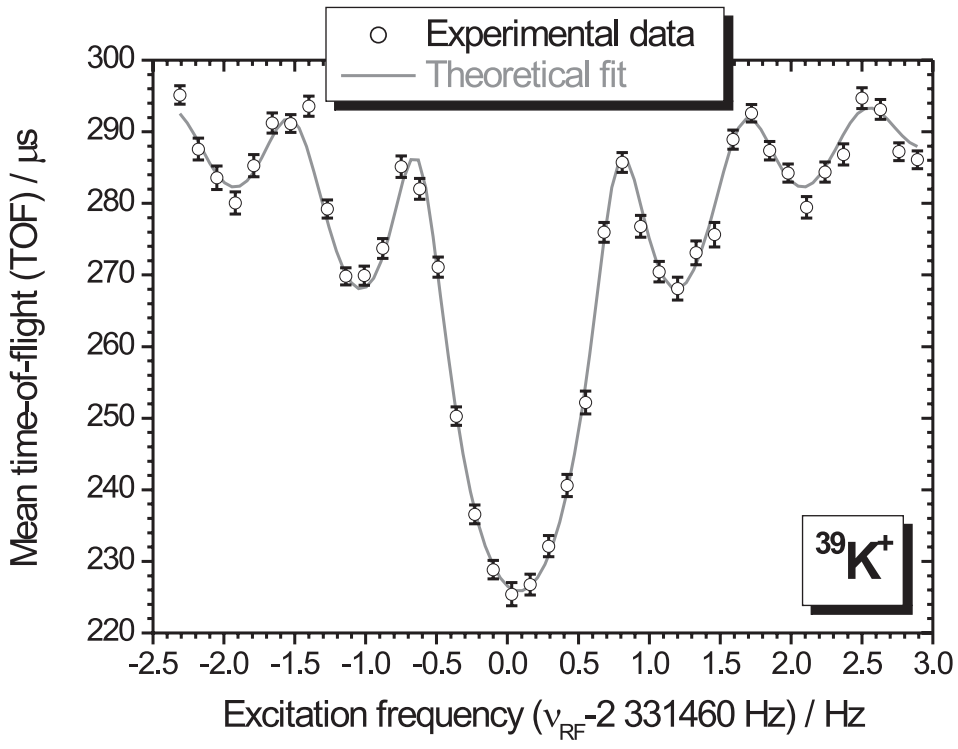

FIGURE 4.10: *Typical TOF resonance for the reference ion $^{39}K^{+}$.*

Fig. 4.10 shows a typical TOF resonance curve. The experimental points (with their associated error bars) are fitted with the theoretically expected line shape [Köni95a]. For more details on the fitting parameters and the fitting routine the reader is referred to Appendix A.

4.3.2 Cyclotron frequency determination

With the ISOLTRAP experiment, a relative mass precision of the order of 10^{-8} is commonly achieved [Blau05a]. Based on the ν_c determination, the mass of the ion of interest is derived from a 'sandwich' measurement of well-known stable masses which serves as a calibration of the spectrometer (for more details see the example given in Section 7.1.1).

The value and thus the uncertainty of the cyclotron frequency depends on the value (respectively on the fluctuations) of the magnetic field B. Both, the preparation and measurement Penning trap are located in strong magnetic fields with a homogeneity of better than 10^{-7} T per cm^3 and a constant decrease of the field in the order of 10^{-8} T/h. Relative to the volume of the homogeneous region, trapping and manipulating the ions on a small radius ($\rho_\pm \leq$1 mm) makes the inhomogeneity of the field of no concern. On the other hand, the magnetic drift plays a dominant role in the uncertainty of the measurements, since in addition to the other experimental uncertainties it introduces systematic uncertainties as well. The mass uncertainty that can be reached by ISOLTRAP is directly limited by the magnetic field drift [Kell03a]. Therefore, if a mass uncertainty of $\sigma(m)/m \approx 1 \cdot 10^{-8}$ is aimed for, the magnetic field strength has to be known to the same precision.

To this end, mass measurements on reference ions are performed in order to determine the magnetic field and calibrate the ISOLTRAP spectrometer. Either alkali ions, *e.g.* $^{39}K^+$, $^{85}Rb^+$, or $^{133}Cs^+$ can be used as a reference, or monoisotopic carbon clusters as absolute mass references [Blau02, Kell02, Mukh04b] since the unified atomic mass unit u is defined as 1 u = $\frac{1}{12}M(^{12}\mathrm{C})$. The mass M of the nuclide of interest (with a cyclotron frequency ν_c and charge $q = n_q\, e$) can be derived from the ratio of the cyclotron frequencies between the ion of interest and the reference mass (for detailed explanations see Section 7.1.1 and [Kell02]). With M_{ref} being the mass of the reference atom, $n_{q_{\mathrm{ref}}}$ the charge state of the ion stored in the Penning trap, and taking into account the mass of the electron M_{e^-} and their binding energy BE, the mass M of the atomic radionuclide is given by:

$$M = \frac{q}{q_{\mathrm{ref}}} \cdot \frac{\nu_c^{\mathrm{ref}}}{\nu_c}\left(M_{\mathrm{ref}} - n_{q_{\mathrm{ref}}} M_{e^-} - \sum_{|n_q|} BE(e_i^-) \right) + n_q M_{e^-} + \sum_{|n_{q_{\mathrm{ref}}}|} BE(e_i^-). \quad (4.6)$$

It has to be emphasized that with the current precision of ISOLTRAP, typically a few hundred eV, the binding energy of the electrons can be neglected since only singly or doubly charged ions are investigated (for more details see Section 7.1.1). Particular care is taken to ensure the small fluctuations of the magnetic field during the measurements, since the cyclotron-frequency-based mass determination implies that the magnetic field is constant and homogeneous during the measurement process (see Section 4.4.2). A new temperature stabilization regulation has been installed in order to reduce the influence of the room temperature on the magnetic field amplitude. It is currently under commissioning and will be further discussed in Section 5.3.1.

4.3.3 Sources of mass uncertainty

Effect of ion contamination

The mass determination described above implies the storage of only one or a few ions of interest in the Penning trap. Experimentally, those ideal conditions cannot always be achieved. Two main sources expected to produce systematic errors on the measurements are first, a rather large ion cloud of identical ions and second, ion-ion interaction of different contamination ions in the trap (*e.g.* isomeric states). A combination of both sources is also possible and very difficult to quantify.

The first source of a frequency shift is a field deformation due to the space charge created by an ion cloud in the trap. This case has been extensively studied in [Boll90] and can be to some extend controlled by playing with the settings of the ISOLTRAP experiment as, *e.g.*, a minimized collection time in the RFQ buncher. The ion cloud in the trap can then be reduced to a few ions stored simultaneously in the Penning trap.
The second case, where frequency shifts are due to ion-ion interaction between two (or more) different ions, is more difficult to handle. The problem of different ion species in a Penning trap at the same time and its influence on the cyclotron frequency has been thoroughly studied in [Boll92, Rusi95]. The ion-ion interaction causes a splitting of the resonance into two peaks for two different ions [Schw05]. In the first order this splitting can be understood as each peak being the resonance for one kind of ion. Unfortunately, this is not the only effect, the weighted center frequency of the peaks is at the same time shifted to a lower frequency.

To counteract those space charge effects and/or ion-ion interaction, different procedures are available at different levels of the beam time. First, a preventive analysis of the possible contaminations for the ions of interest can be performed. To minimize the influence of the ion-ion interaction, a C++ interface has been developed (see next paragraph) in order to find the possible ion contaminations from the ISOLDE target and prevent unwanted species appearing during the run, using specific cleaning procedures for predicted possible contaminants from the ISOLDE beam, as explained and illustrated in Section 3.4. Secondly, a new Channeltron based detection system has been developed and implemented at the ISOLTRAP experiment. The details of the simulation, characterization, commissioning and results of the new system is given in Chapter 6. The detection efficiency of about 90% of this new detector reduces consequently the probability of having different ions species at the same time in the trap, and true single ion experiments can be performed. Finally, an off-line analysis allows for the correction of contamination and frequency shifts, by means of count rate class (or Z-class) analysis. The cyclotron frequencies are determined for different ion numbers in the Penning trap and a linear fit is performed. The slope of the fit gives an indication of the possible contamination of the data and the cyclotron frequency extrapolation to a single ion (see [Kell03a]) corrects for

the frequency shift due to the contamination, if any. To illustrate the reliability of the ISOLTRAP spectrometer such an analysis is performed with the off-line ion source before the beam time and systematically used for radioactive ions frequency determination (see Section 7.1.2).

'Search4Contaminant' program

As previously mentioned, possible contaminations can be predicted by simply calculating the frequencies of isobaric molecular and atomic ions whose mass is close to the mass of the investigated short-lived nuclide. The program takes as input data the atomic-mass table [AME03] and compares the cyclotron frequency of all possible combinations with the cyclotron frequency of the investigated nuclide.

Fig. 4.11 is a screen shot of the program. Due to the large number of possible combinations with the specified settings, only part of the contaminants is shown. Input parameters used for the calibration of the search program are stored in an '*.ini' file. The information on the reference ion, its charge state as well as its cyclotron and magnetron frequencies for the magnetic field in the preparation trap (or Lower Trap, LT) or in the precision trap (Upper Trap, UT), as shown in the 'Reference' box of the interface, can be saved and loaded at any time by using 'Load/Save Ini File' buttons. In the 'Investigated' box, either the contamination for a given nuclide, or a specified center frequency can be chosen for a given charge state, and a frequency range for the search. The 'Search and Filters' box, as indicated by the name, contains different tools and options to minimize the number of combination and optimize the search for contaminants. Information on the reference or investigated nuclide is given in the 'Info Ion' box.

As an example, part of the 'possible' contaminants of $^{35}K^{+}$ are listed. The settings and the results are shown in Fig. 4.11. Only molecules with stable isotopes are given in the figure, not shown are 43 molecules with at least one stable isotope and 11 with only unstable isotopes fulfill the research criteria. Isotopes preceded by an asterisk (as $*^{35}$Al and $*^{35}$Ca) fulfill all search criteria except for the half-life. Since the program is simply checking the mass excess and the cyclotron frequency most of the molecules found are not relevant and therefore are not presented here. From the results no contamination has to be expected, and indeed no contamination has been observed during the $^{35}K^{+}$ measurement.

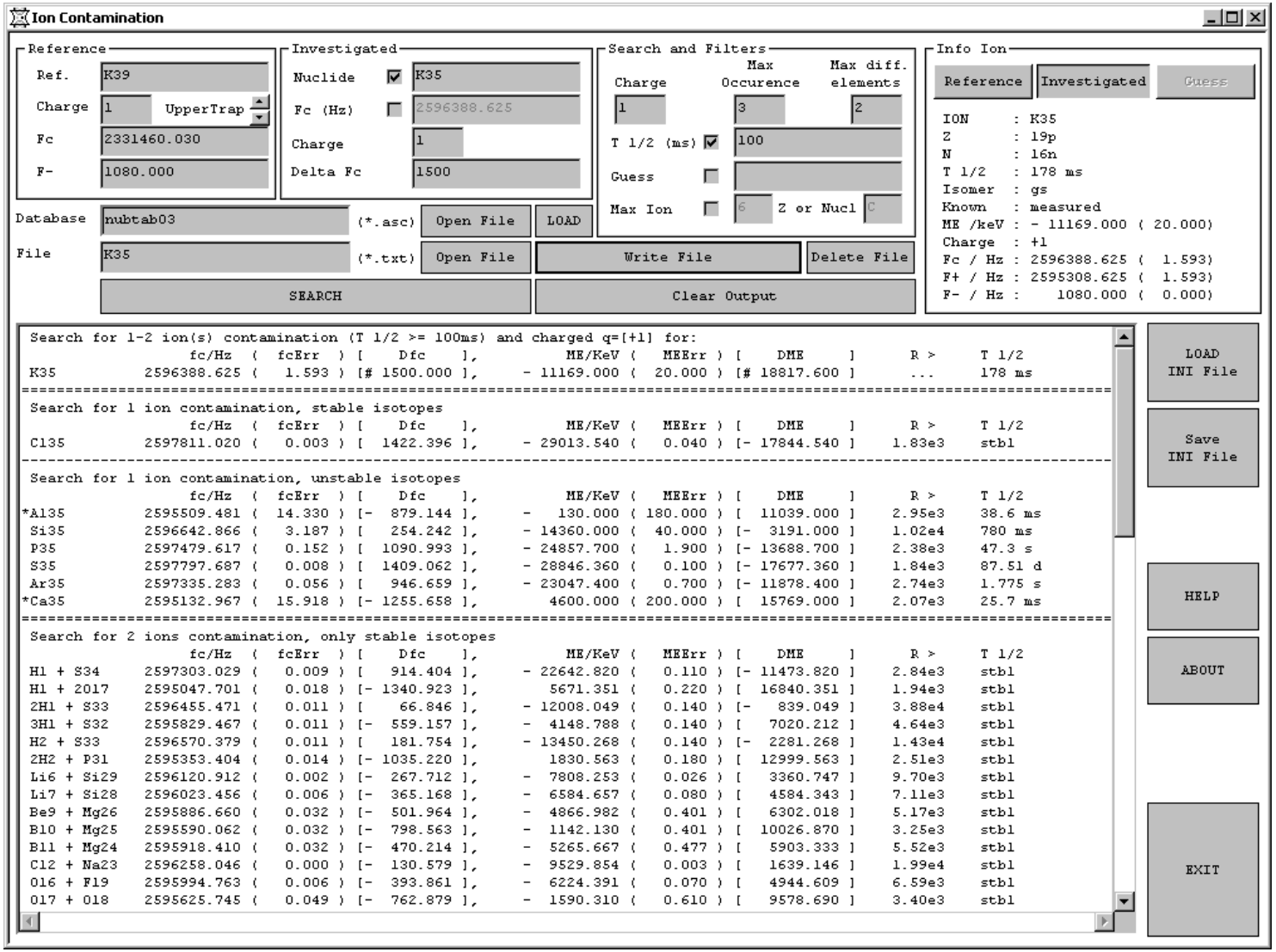

FIGURE 4.11: *Screen shot of the 'Search4Contaminant' program and results for the $^{35}K^{+}$ contaminants.*

4.4 Optimization and calibration

4.4.1 Stable beam tuning and transfer optimization

From the off-line ion source of ISOLTRAP, or the last section of the ISOLDE beam line, more than 150 parameters can be varied to guide and store the ions, like voltages for steerers, quadrupoles, deflectors, and trapping voltages. Since the beam tuning is mass dependent, a standard optimization procedure has to be followed as described in Appendix B from either the ISOLDE target area or the off-line ion source of ISOLTRAP, to the preparation trap and the precision trap. Moreover, special care is required on crucial devices needed for the high-precision mass measurements, especially trapping parameters, in order to obtain identical trapping conditions and identical ejection pulses during the whole run. Once the first round of this beam tuning optimization procedure is done, the fine tuning and checking for the stability, precision and accuracy of the measurements has to be performed by optimizing the magnetic and electric fields in the precision trap in order to correct for field distortions and field inhomogeneity, as described in the following.

Capturing time in the precision trap: Delay #1

For the mass measurements the magnetic field has to be stable since the mass determination is performed via the cyclotron frequency ratio which assumes the same magnetic field for both species. Even if the magnetic field is stable over time (except for a small linear temporal drift), it is not homogeneous within the entire Penning trap volume. Due to the finite homogeneity of the magnet itself in addition to the magnetic susceptibility of the trap material, the magnetic field is distorted in the trapping volume, *i.e.* $B = B(r,t)$ where r is the distance of the ion to the center of the trap. In order to counteract these effects, shim coils are used. To scan the inhomogeneity of the magnetic field inside the Penning trap, the capturing time of the ion can be varied, so that the ions are initially given more or less axial energy, making them to probe the local field. Varying the capture timing does not affect the position of the stored ions in the trap but their axial energy, when the trap is switched to the capture mode, since the ions are initially not captured exactly at the center along the axis. Therefore, the ions experience an axial electric force that gives an initial axial energy, so that the ions oscillate around the center of the trap. The capture time $\mathrm{T_{capture}}$ determines the initial capture position $r = \{x, y, z\}$ with respect to the center of the trap and therefore the initial axial energy (see Fig. 4.12). Since in the precision trap damping effects are negligible for the given timescale of about 1 s, the axial motion is not damped and the ions probe the magnetic field in a large volume around the trap center during the quadrupolar excitation, and therefore the inhomogeneity of the magnetic field will influence the cyclotron frequency, which can be monitored as a function of the capture time.

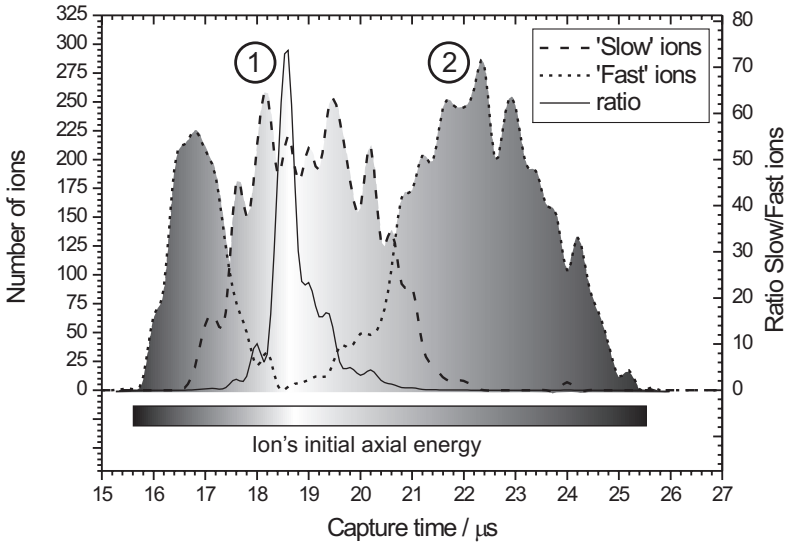

FIGURE 4.12: *Accurate determination of the correct capture timing. For more details see text.*

It should be emphasized that in case the magnetic field is not corrected and the capture time is set to a non-optimal value, systematic frequency shifts may result. To find the correct capturing time corresponding to an initial capture exactly in the center of the trap, and thus with almost no axial energy, the following procedure is used.

The method is based on recording the ion number as a function of the capture time. Indeed, the ejection condition from the preparation trap produces an ion bunch for which the spatial resolution (respectively a time resolution $<1\mu$s) is a few times smaller than the size of the trap (respectively a time resolution of a few μs for potassium isotopes). If the ion bunch is captured at the correct time, a maximal ion number will be trapped and then detected, whereas if the capture time is detuned, part of the ion bunch is lost. The ion count rate follows a gaussian distribution. However, a better resolution can be reached using a special ejection scheme. Instead of switching the ring and endcap electrodes at once, a ramping scheme is used. During the ramping higher-energetic (or 'faster') ions are ejected, *i.e.* those with larger axial energy that encountered the field inhomogeneity, whereas only lower-energetic (or 'slow') ions, *i.e.* with low axial energy, are kept in the trap, until the ejection pulse occurs. Corresponding TOF spectra are schematically represented in lower part of Fig. 4.13. The ions ejected before the pulse due to their larger axial energy correspond to a wrong capture time. Taking the ratio of the 'cooled'/'hot' ions improves the signal to noise ratio, and narrows the full width at half maximum (FWHM) of the capture time curve. With this method the correct capture timing is determined, which corresponds to the center of the trap.

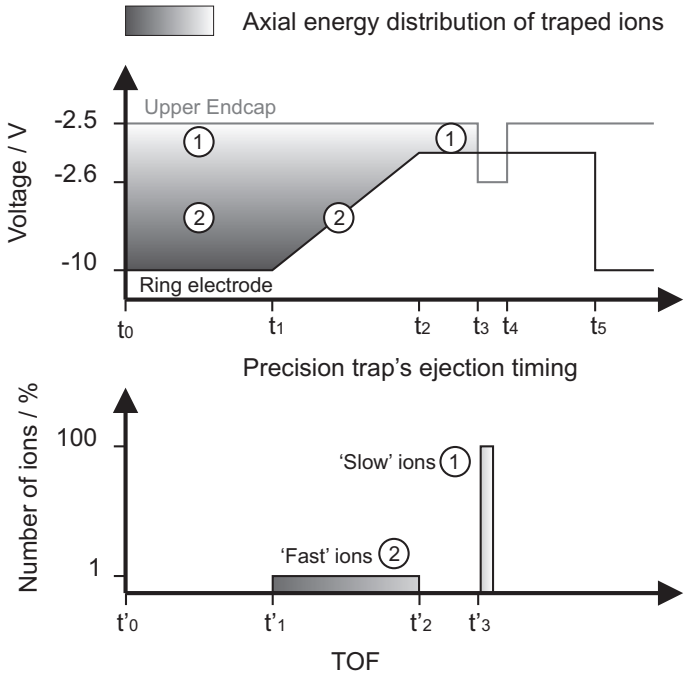

FIGURE 4.13: *Consequence of the capture timing on the ion energy.*
Upper part: voltages of the ring electrode and the upper endcap as a function of time.
Lower part: Number of detected ions as a function of time.

As previously underlined, the capture timing can be seen as initially trapping the ions at a certain position in the trap. Therefore, a simple relation can be found that links the capture time $\mathrm{T_{capture}}$ and the initial position of the ion in the trap r. In the following and in order to simplify the notation, the frequency $\omega(T_{\mathrm{capture}})$ – respectively the magnetic field $B(T_{\mathrm{capture}})$ – for an ion when using a certain value $\mathrm{T_{capture}}$ will be noted as $\omega(T_{\mathrm{capture}}) = \omega(r)$.

4.4.2 Optimization of the (B,E) fields in the precision Penning trap

One of the main obstacles for accurate mass determination is the random fluctuation of the magnetic field. It does not only depend on the time but the magnetic field homogeneity depends on the position along the field axis. There are different aspects entering the problem and that can be written as $B = B(\{f_i(t), g_i(r)\})$. The $\{f_i(t)\}$ represents a set of perturbations depending only on the time and can be, *e.g.*, the temperature of the experimental hall, the liquid helium pressure in the recovery line, or the flux creep effect [Kell03a], and the $\{g_i(r)\}$ represents a set of perturbations depending only on the position in the field.

To first order:

$$B(r,t) \approx B(r_0,t_0) + \sum_k \frac{\partial B(\{f_i(t_0)\})}{\partial f_k(t)} df_k + \sum_k \frac{\partial B(\{g_i(r_0)\})}{\partial g_k(r)} dg_k \qquad (4.7)$$

Experimentally it has been observed that the main perturbation arises from the flux creep, which can be considered as being linear for short timescales, and the position in the field. The dependence of the magnetic field on the room temperature and the helium pressure in the recovery line, whose effects can be neglected on a short time range (typically a few hours), have been recently diminished by installing new PID-based regulation systems, which are under commissioning. A detailed discussion of the helium pressure and temperature stabilization is given in Section 5.3.1, as a technical improvement towards more precise and accurate mass determination.

For a short-time procedure as described in the following discussion, the magnetic field fluctuations due to the helium pressure or temperature can be neglected. Therefore, all influences other than the flux creep and the field homogeneity will be neglected for the demonstration of the magnetic and electric field optimization procedure.

Optimization of the magnetic field

The cyclotron frequency determination for a reference nuclide is used to improve the homogeneity of the magnetic field in the respective trap volume. By varying the capturing time, the ions get different axial energies, so that they experience the inhomogeneity [Boll90] of the magnetic field far from the center of the trap. As a consequence the cyclotron frequency is shifted. The field inhomogeneity, and thus the frequency shift, is corrected by means of room-temperature shim coils.

Around r_0=$\{x_0; y_0; z_0\}$, the center of the trap, and at time t_0, the magnetic field can be written to first order as:

$$B(r,t) = B(r_0,t_0) + \frac{\partial B(r_0,t_0)}{\partial r}(r-r_0) + \frac{\partial B(r_0,t_0)}{\partial t}(t-t_0). \qquad (4.8)$$

The magnetic field is calculated from the cyclotron frequency ω_c for different conditions $\omega_c(r_i,t_j) = q/m\ B(r_i,t_j)$. The measurement of the magnetic field $B(r,t_0)$ at a position r at t_0 is surrounded by two measurements performed at the center of the trap shortly before (t_-) and after (t_+) such as $t_- < t_0 < t_+$. From the latter two the magnetic field strength $B(r_0,t_0)$ can be derived and then compared to $B(r,t_0)$ by a series of three measurements:

$$\begin{cases} B(r_0,t_-) &= B(r_0,t_0) + \dfrac{\partial B(r_0,t_0)}{\partial t}(t_- - t_0) \\ B(r,t_0) &= B(r_0,t_0) + \dfrac{\partial B(r_0,t_0)}{\partial r}(r-r_0) \quad . \\ B(r_0,t_+) &= B(r_0,t_0) + \dfrac{\partial B(r_0,t_0)}{\partial t}(t_+ - t_0) \end{cases} \qquad (4.9)$$

The estimated value $\widehat{B}(r_0,t_0)$ of the magnetic field strength $B(r_0,t_0)$ is interpolated by:

$$\widehat{B}(r_0,t_0) = \frac{(t_+ - t_0)\cdot B(r_0,t_-) - (t_- - t_0)\cdot B(r_0,t_+)}{t_+ - t_-}. \tag{4.10}$$

The effect of the inhomogeneity $\delta B(r)$ of the magnetic field can be evaluated by:

$$\delta B_r = \frac{\partial B(r_0,t_0)}{\partial r}(r - r_0) = B(r,t_0) - \widehat{B}(r_0,t_0). \tag{4.11}$$

The superconductive coils at liquid helium temperature are surrounded by room temperature shim coils which can be scanned for the fine optimization of the magnetic field homogeneity. To this purpose, the current in three coils (the closest to the trap location) are tuned. Scanning the shim-coil current I and plotting $\delta B_r = f(I)$ leads to the best value for the correction of the magnetic field so that δB_r reaches zero.

Optimization of the electric field

In addition to the magnetic field, the electric field has to be as close as possible to an ideal case [Boll90]. Eq. (3.1) is a first order approximation, higher terms can be found in [Geor05]. Indeed, the optimization procedure implies not only scanning ω_c but also ω_+ which depends on the electric field. Since ω_+ depends on the magnetic field (see Eq. (3.17)), this optimization has to be performed after the magnetic field optimization. To find the contributions that are only due to the electric field inhomogeneity, the following condition has to be verified: $\|\frac{\partial B(r,t)}{\partial r}\| \ll \|\frac{\partial B(r,t)}{\partial t}\|$, where the norm has to be understood as the integral of the absolute value of the derivatives, *i.e.* $\|f\| \equiv \int |f|$.

Using Eq. (3.17) and assuming that the potential V in the trap only depends on r, *i.e.* $V = V(r)$, around r_0, the center of the trap and at t_0, ω_+ can be written to first order as being:

$$\begin{aligned}\omega_+(r,t) \;=\;& \omega_+(r_0,t_0) \\ &+\frac{\partial B(r_0,t_0)}{\partial t}\left(\frac{q}{m} + \frac{V(r_0)}{2D^2B^2(r_0,t_0)}\right)(t - t_0) \\ &+\frac{q}{m}\frac{\partial B(r_0,t_0)}{\partial r}(r - r_0) \\ &-\frac{1}{2D^2B^2(r_0,t_0)}\left(B(r_0,t_0)\frac{dV(r_0)}{dr} - V(r_0)\frac{\partial B(r_0,t_0)}{\partial r}\right)(r - r_0).\end{aligned} \tag{4.12}$$

With the previous optimization of the magnetic field the term $\partial B(r_0,t_0)/\partial r$ can be neglected. This reduces Eq. (4.12) to:

$$\begin{aligned}\omega_+(r,t) &= \omega_+(r_0,t_0) \\ &+\frac{\partial B(r_0,t_0)}{\partial t}\left(\frac{q}{m}+\frac{V(r_0)}{2D^2B^2(r_0,t_0)}\right)(t-t_0) \\ &-\frac{1}{2D^2B^2(r_0,t_0)}B(r_0,t_0)\frac{dV(r_0)}{dr}(r-r_0).\end{aligned} \tag{4.13}$$

The procedure is the same as for the magnetic field optimization. Since ω_+ depends on the electric field, an additional series of three measurements is performed at $(r_0,t_\pm)$ for the calibration and (r,t_0):

$$\begin{cases}\omega_+(r_0,t_-) = \omega_+(r_0,t_0) \\ \qquad +\dfrac{\partial B(r_0,t_0)}{\partial t}\left(\dfrac{q}{m}+\dfrac{V(r_0)}{2D^2B^2(r_0,t_0)}\right)(t_- - t_0) \\ \omega_+(r,t_0) = \omega_+(r_0,t_0) - \dfrac{1}{2D^2B(r_0,t_0)}\dfrac{dV(r_0)}{dr}(r-r_0) \\ \omega_+(r_0,t_+) = \omega_+(r_0,t_0) \\ \qquad +\dfrac{\partial B(r_0,t_0)}{\partial t}\left(\dfrac{q}{m}+\dfrac{V(r_0)}{2D^2B^2(r_0,t_0)}\right)(t_+ - t_0).\end{cases} \tag{4.14}$$

The estimated value $\widehat{\omega}_+(r_0,t_0)$ of the reduced cyclotron angular frequency $\omega_+(r_0,t_0)$ can be interpolated by:

$$\widehat{\omega}_+(r_0,t_0) = \frac{(t_+-t_0)\cdot\omega_+(r_0,t_-) - (t_- - t_0)\cdot\omega_+(r_0,t_+)}{t_+ - t_-}, \tag{4.15}$$

and the effect of the inhomogeneity δV_r of the electric field evaluated:

$$\delta V_r = -\frac{1}{2d^2B(r_0,t_0)}\frac{dV(r_0)}{dr}(r-r_0) = \omega_+(r,t_0) - \widehat{\omega}_+(r_0,t_0). \tag{4.16}$$

Scanning the voltages v of correction electrodes (shown in Fig. 4.9) and plotting $\delta V_r = f(v)$ leads to the best value for the correction of the electric field so that δV_r vanishes.

Chapter 5

Towards better mass measurements on short-lived nuclides

5.1 What can be (and what has to be) improved?

In the last years the applicability of ISOLTRAP has been extended to cover almost all nuclides produced at ISOLDE. ISOLTRAP can reach a relative mass uncertainty of only $8{\cdot}10^{-9}$ and routinely measures nuclides that are produces with only 100 ions per second (as *e.g.* ^{32}Ar [Blau03a]), and with half-lives ranging from stable nuclides to short-lived nuclides with $\tau_{1/2}$ as low as 65 ms (as *e.g.* ^{74}Rb [Kell04a]). In order to further push the limits and the performances of ISOLTRAP, *i.e.* measuring shorter-lived nuclides and more rarely produced isotopes with a better precision, different options are investigated. First of all, the main concern is the stability of the mass measurement procedure. With more than a hundred parameters, the data acquisition system has to run stable during the complete run, *i.e.* typically a few days. To this aim, a new LabVIEW based control system has been implemented [Beck04, Yazi05]. The second point concerns the fluctuations of the magnetic field that influence the cyclotron-frequency values of both the investigated and the reference ions. In order to compensate for the fluctuations of the field due to the variation of the helium overpressure of the magnet helium dewar and of the temperature around the trap area, new regulation systems have been implemented. Finally, to reach both shorter-lived nuclides and rarer isotopes, the detection efficiency of the spectrometer has been improved.

5.2 A new control system for stability and reliability [1]

The manipulation of the stored ions requires a reliable and fast control system, especially in case of short-lived nuclides with half-lives in the millisecond range. A new versatile LabVIEW-based control system has been developed and implemented at ISOLTRAP. It allows easy experiment handling as well as improved flexibility and reliability, and it is flexible enough to be used for other experiments as well. From the new general control system framework, *CS*, developed at DVEE/GSI, a dedicated control system for ISOLTRAP has been constructed and implemented by adding experiment-specific add-ons to the framework [Beck04].

5.2.1 Design of the control system

The old control system was based on a VME-bus crate controlled via a Motorola processor E6 CPU using the OS9 operating system. For more than a decade, it was successfully used, but the hardware had become outdated and was not any longer reliable since no support was available. To operate ISOLTRAP more than 150 voltages and other experimental parameters must be remotely controlled, such as ion optics, regulation of the buffer-gas pressures, 8 delay-time devices, and up to 10 different frequency generators. The complex timing scheme, especially for short-lived ions, needs to synchronize the different steps with a precision of better than 1 μs. Thus a modular control system with the ability to follow the growth of the experimental setup in size and complexity was required.

The *CS* framework

The old VME based system was used to control the hardware devices and the measurement procedure. A Graphical User Interface (GUI) was operated from a PC connected to the VME-bus via TCP/IP to setup the measurement and display the on-line data. In spring

[1] This section is mainly taken from [Yazi05].

C. YAZIDJIAN, D. BECK, K. BLAUM, H. BRAND, F. HERFURTH, AND S. SCHWARZ
"Commissioning and first on-line test of the new ISOLTRAP *control system"*
Eur. Phys. J. A **25**, s01, 193–197 (2005). DOI: 10.1140/epjad/i2005-06-096-x

2003, a new control system has been implemented and commissioned. The GUI is reused as well as practically all existing hardware devices of ISOLTRAP, whereas the VME-bus is replaced by a PC. Instead of trying to port the old system from VME to the new PC platform, the all-new object-oriented *CS* framework [Beck04] has been implemented in about nine man months. It does not only replace the old system but provides more functionality, and enhances the experimental capabilities of ISOLTRAP.

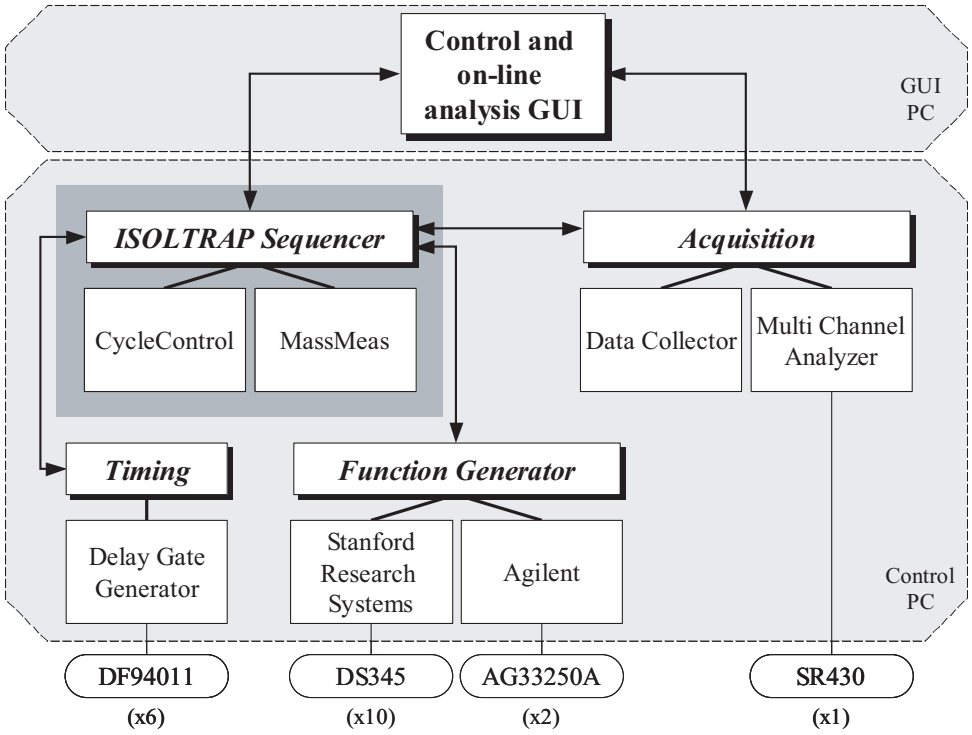

FIGURE 5.1: *Simplified sketch of the* ISOLTRAP *control system [Yazi05]. Shadowed boxes represent a package of software modules (depicted by boxes) attached to their hardware component (rounded boxes). Arrows indicate the communication path.*

Fig. 5.1 shows a simplified overview of the control system hierarchy. The hardware devices (rounded boxes) are represented by objects (boxes) which are organized in a corresponding package (shadowed boxes). The hardware devices (the number of modules used at ISOLTRAP in brackets) are addressed either by GPIB or OPC interfaces (not shown in Fig. 5.1). In the Function-Generator package, two different kinds of hardware are shown: *DS345* from Stanford Research Systems and *AG33250A* from Agilent. Following the same principle, *SR430* is a multichannel analyzer for data acquisition and *Data Collector* which collects and buffers data from acquisition devices. *DF94011* is a programable delay box. The highlighted part with a darker grey box is experiment specific. The Se-

quencer (with the *CycleControl* and *MassMeas*) is the conductor of the control system. Once the user starts a measurement from the GUI, the Sequencer takes over the control of the experiment. It communicates with the other objects via events. The arrows show the communication paths between the objects (for better understanding the arrows target the package, but not the objects themselves).

Thanks to this object-oriented structure, a broken hardware device can be easily replaced by another one belonging to the same package. The only change in the *CS* is the one of the object associated to the hardware part. As an example of its flexibility, a *DS345* function generator can be exchanged by a *AG33250A* in a few minutes without shutting down the *CS* or the experiment.

5.2.2 Commissioning of the control system

The new control system was put into operation by late summer 2003, and after extensive off-line tests all the on-line radioactive beam experiments in 2004 were performed with it. In full operation, about 80 objects are required simultaneously for controlling the hardware. The control system runs stable for at least one week of operation.

With such a versatile concept, the easy maintenance of the new control system is one more advantage to add to those that allow higher stability and flexibility. Also enhanced is the comfortable handling by having a quick parameter setup feature for the requirement of high-precision mass measurements, especially for short-lived nuclides. The new flexible *CS* framework fulfilled the requirement of this versatile apparatus and enhances the experimental capabilities of ISOLTRAP. The *CS* framework has also shown its numerous advantages and its new powerful features during on-line runs. Meanwhile, this control system is also in operation at the Penning trap mass spectrometers SHIPTRAP [Dill01b, Bloc05] and LEBIT [Schw03].

5.3 Reducing the systematic errors of ISOLTRAP

5.3.1 Stabilization of the magnetic field

As previously mentioned, one critical point for performing high-precision and accurate mass measurements is the stability of the magnetic field. To compensate for the magnetic field fluctuations – due to the external temperature and the helium pressure of the recovery line – new regulations systems are under commissioning.

PID regulation loop

Because of their low cost and their straight-forward implementation, PID-feedback-loops are commonly used in industry to regulate a physical parameter $y(t)$ of a given system Σ. In order to follow the set-point $y^*(t)$, three main actions $u_{\mathrm{P,I,D}}(t)$: proportional (P), integral (I), and derivative (D) are sent to the system.

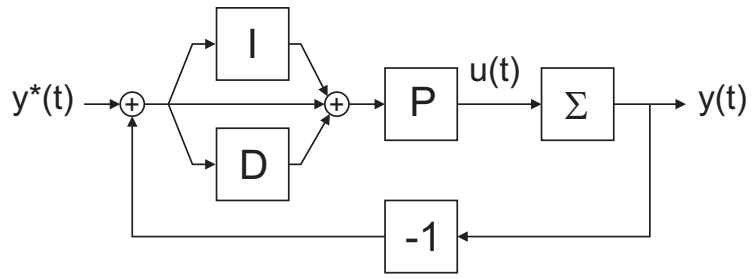

FIGURE 5.2: *Standard PID regulation loop.*

As illustrated in Fig. 5.2, the PID regulation loop is characterized by the command:

$$u(t) = u_{\mathrm{P}}(t) + u_{\mathrm{I}}(t) + u_{\mathrm{D}}(t), \tag{5.1}$$

In the case of a discrete PID controller, sampled in time step of T_{s}, the integration part (respectively the derivation) are given under the 'forward difference', (respectively 'backward difference') approximation as illustrated for an arbitrary function f:

$$\begin{aligned} \int_0^t f(\tau)d\tau = f_i(t) &= f_i(t - T_{\mathrm{s}}) + T_{\mathrm{s}} f(t - T_{\mathrm{s}}), & (5.2)\\ \frac{d}{dt} f(t) = f_d(t) &= \frac{1}{T_{\mathrm{s}}}\left[1 - q^{-1}\right] f(t) & (5.3)\\ &= \frac{1}{T_{\mathrm{s}}}\left[f(t) - f(t - T_{\mathrm{s}})\right]. \end{aligned}$$

The $u_{\mathrm{P,I,D}}(t)$ are given by:

$$\begin{aligned} u_{\mathrm{P}}(t) &= Ke(t), & (5.4)\\ u_{\mathrm{I}}(t) &= \frac{K}{T_i}\left[e_i(t - T_{\mathrm{s}}) + T_{\mathrm{s}} e(t - T_{\mathrm{s}})\right],\\ u_{\mathrm{D}}(t) &= \frac{KT_d}{T_{\mathrm{s}}}\left[e_f(t) - e_f(t - T_{\mathrm{s}})\right], \end{aligned}$$

with $e(t) = y^*(t) - y(t)$, which represents the error of the system, K is the proportionality factor, T_i (respectively T_d) corresponds to the integration (respectively the derivation) time. A pure derivation of a signal is a mathematical nonsense since the signal is only known in 'the past', the future values of the system cannot be predicted with a pure PID.

In addition, a Bode diagram of a 'pure' derivation function D, $\mathrm{Bode}\,[D(p)] = |p|$ in the Laplace-space, exhibits an amplification of high frequency signals, and since noise usually is composed of high frequency signals, a pure derivation will amplify the unwanted noise of the system, which should be avoided. Thus, to realize a derivation module, the following filter has to be applied to the error $e(t)$:

$$\begin{aligned} e_f(t) &= \left[\frac{1}{\left(1+\frac{T_d}{T_\mathrm{s}N}\right)-\frac{T_d}{T_\mathrm{s}N}q^{-1}}\right] e(t) \\ &= \left[\sum_{n=0}^{\infty}\frac{\left(\frac{T_d}{T_\mathrm{s}N}\right)^n}{\left(1+\frac{T_d}{T_\mathrm{s}N}\right)^{n+1}}\,q^{-n}\right]\, e(t) \\ &= \frac{1}{1+\frac{T_d}{T_\mathrm{s}N}}\,e(t)+\frac{\frac{T_d}{T_\mathrm{s}N}}{1+\frac{T_d}{T_\mathrm{s}N}}\,e_f(t-T_\mathrm{s}) \end{aligned} \tag{5.5}$$

where $N = \frac{T_d}{T_f} > 10$, and T_f corresponds to the time constant of the filter.

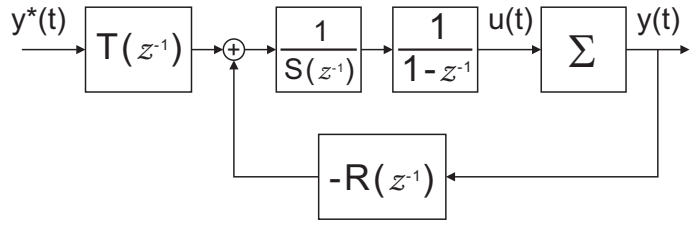

FIGURE 5.3: *Advanced RST regulation loop.*

It has to be emphasized that PID systems are a particular case of advanced regulations [MSaad00*], see Fig. 5.3, (for more details see Appendix C):

$$\begin{aligned} T_{\mathrm{PID}}(q^{-1}) &= t_0 + t_1 q^{-1} + t_2 q^{-2} \\ S_{\mathrm{PID}}(q^{-1}) &= s_0 + s_1 q^{-1} \\ R_{\mathrm{PID}}(q^{-1}) &= r_0 + r_1 q^{-1} + r_2 q^{-2} \end{aligned} \tag{5.6}$$

and

$$\begin{gathered} t_0 = K\tfrac{T_d+N(T_d+T_\mathrm{s})}{(T_d+NT_\mathrm{s})T_i},\ t_1 = -K\tfrac{2(N+1)T_dT_i+(NT_i-NT_\mathrm{s}-T_d)T_\mathrm{s}}{(T_d+NT_\mathrm{s})T_i},\ t_2 = K\tfrac{T_dT_i+NT_dT_i-T_iT_\mathrm{s})}{(T_d+NT_\mathrm{s})T_i} \\ s_0 = 1,\ s_1 = -\tfrac{T_d}{T_d+NT_\mathrm{s}} \\ r_0 = t_0,\ r_1 = t_1,\ r_2 = t_2. \end{gathered} \tag{5.7}$$

Since the polynomial forms $T_{\mathrm{PID}}(q^{-1})$ and $R_{\mathrm{PID}}(q^{-1})$ are equal, the dynamics for the regulation of the system and the noise rejection are not only coupled but identical. This correlation can be an important issue for performances and stability for slow systems (or with important delay) and/or non step-like perturbations.

Experimental setup and first results

Concerning the back-line helium pressure, the adopted solution is the same as developed in Stockholm for SMILETRAP [Frit01]. The sensor and the PID controller are provided by the MKS Instruments company [MKS*]. The helium pressure in the line, *i.e.* $y(t)$, is measured by a sensor *MKS Type 627B Baratron.* The pressure flow controller *MKS Type 250E* sends the command $u(t)$ to open/close the control valve *MKS Type 248A/B/C* used to regulate the helium flow as illustrated in Fig. 5.4. The regulation system allows a stability of the helium pressure in the back-line of the order of a few $\pm$0.05 mbar.

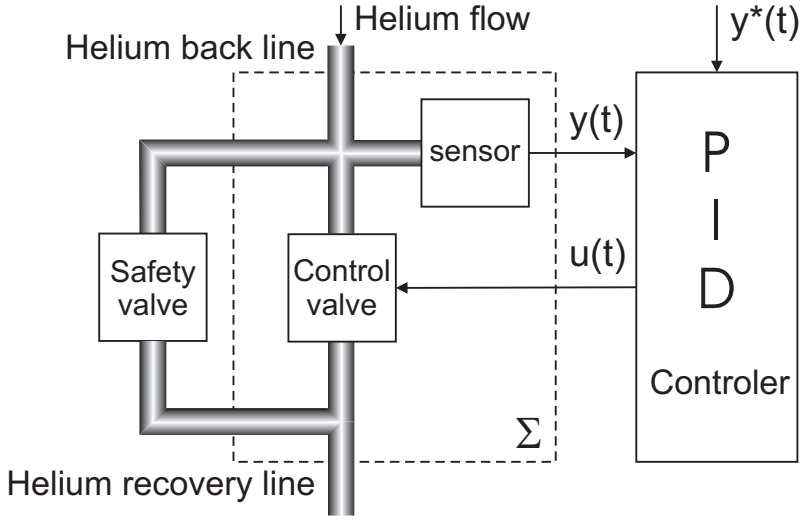

FIGURE 5.4: *Helium pressure stabilization setup.*

In contrast, the adopted solution for the temperature regulation of the magnet is not commercial but a home-made solution. It consists of temperature sensors placed close to the bore of the magnet which measure the temperature in the vicinity of the trap, $y(t)$ (see Fig. 5.5). In order to achieve the set point $y^*(t)$, a heater, $u(t)$, controlled by the PID loop, is installed in a tube and blows hot air into the magnet area. As illustrated in Fig. 5.6, the temperature stabilization seems to be working properly ($\pm$5 mK) when performed under ideal conditions. However, additional factors, *e.g.* the temperature in the experimental hall, have to be taken into account as a perturbation of the regulation. In summer for example, the already regulated temperature of the experimental area can vary by $\pm$3 K over 24 h (day-night fluctuations).

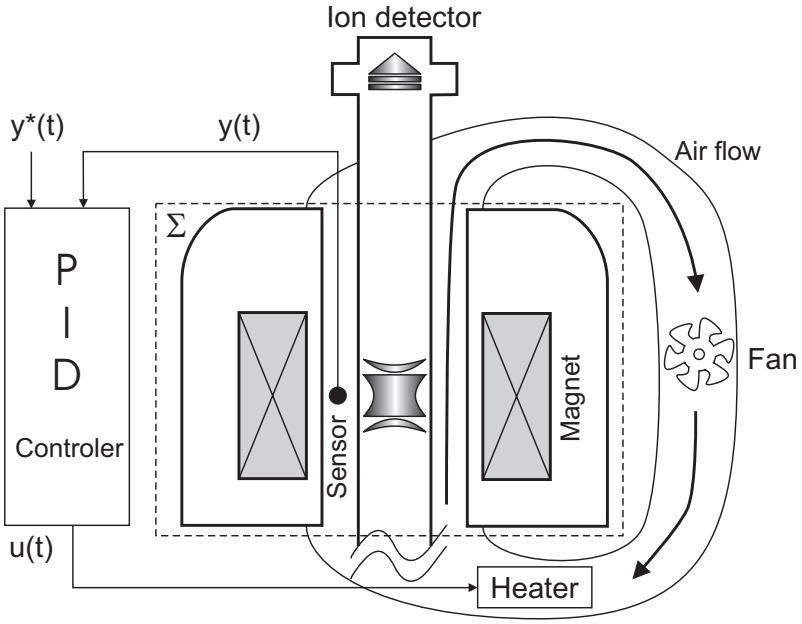

FIGURE 5.5: *Temperature stabilization setup.*

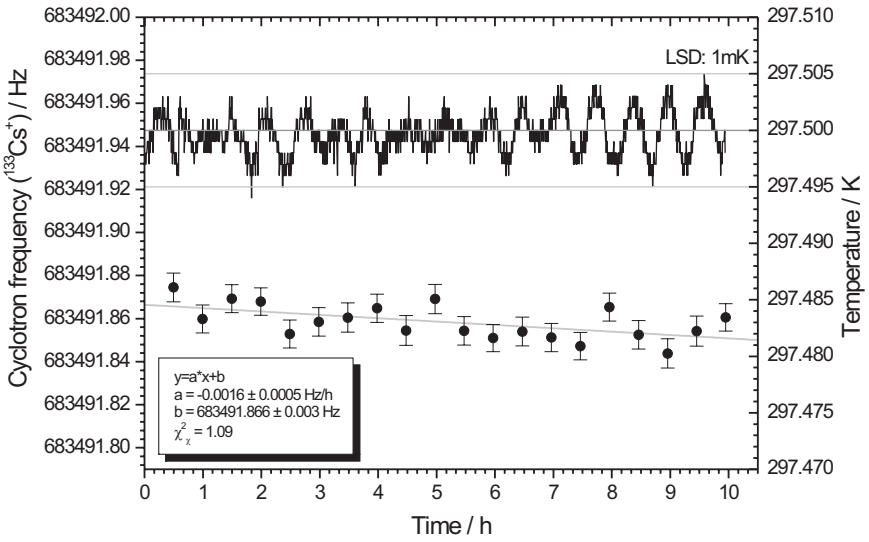

FIGURE 5.6: *First non-optimized results of the temperature stabilization. The temperature stabilization and the cyclotron frequency of ^{133}Cs recorded as a function of time. The relative decay of the magnetic field $\frac{\delta B}{\delta t}\frac{1}{B}$ is given by the relation: $\frac{\delta B}{\delta t}\frac{1}{B} = \frac{\delta \nu_c}{\delta t}\frac{1}{\nu_c} = -2.3(2)\cdot 10^{-9}$/h.*

As mentioned, PID systems are easy to tune since there are only three free parameters K, T_i and T_d. The drawback is that the dynamics of the system for regulation and noise rejection are coupled (see the RST structure, Eq. (5.7)). Without a careful optimization of the PID values as described in [Zieg42, Åström95], the perturbation will be only partially compensated. One of the consequences of the correlation is that a set $\{K,\ T_i,\ T_d\}$ will only be valid for a short range of temperatures (in the order of 1 K, not sufficient for rejection of the perturbation due to the room temperature). In the worst case the PID regulation loop will not be able to regulate and start to become unstable. Another important problem of the adopted solution is that the hot air flow is quite low because of space and experimental constrains. For that reason, the regulated system exhibits a large response delay. PID regulations loops are not meant for such an extreme application. However, more elaborate controllers as described in Appendix C are capable to handle the large delay and the perturbation rejection under certain conditions which are due to the system itself.

5.3.2 A new carbon cluster ion source

As illustrated in Eq. (4.6), the accuracy of mass determination does not only depend on the magnetic field homogeneity and stability, the mass of the reference ion enters the formula as well. Thus its uncertainty influences the final result of the mass of the investigated nuclide. A complete discussion of the mass determination and the analysis from the raw data to the final mass value is given in Section 7.1.1.

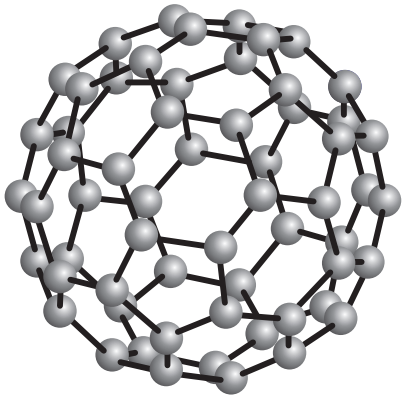

FIGURE 5.7: *A $(^{12}C)_{60}$ carbon cluster: The Fullerene molecule [Krot85].*

Carbon clusters (see Fig. 5.7) are the reference ions of choice. Since the atomic mass unit u is defined as being one twelfth of the ^{12}C mass, they provide mass references for an absolute calibration of the magnetic field during the mass determination procedure. Moreover, systematic studies performed with carbon clusters showed a slight systematic deviation with the mass difference between the investigated ion and the reference [Kell03c]. The use of carbon clusters has another advantage that reduces this systematic

ion-mass-difference uncertainty effect: Neglecting the isotopic ratio of ^{13}C/^{12}C=1.1%, carbon clusters $^{12}C_n$ provide ion references equally distributed all over the nuclear chart, separated by 12 u each (see Fig. 5.8). As a consequence, the mass difference between the investigated and reference ion will be equal to 6 u in the worst cases (see [Blau05a]).

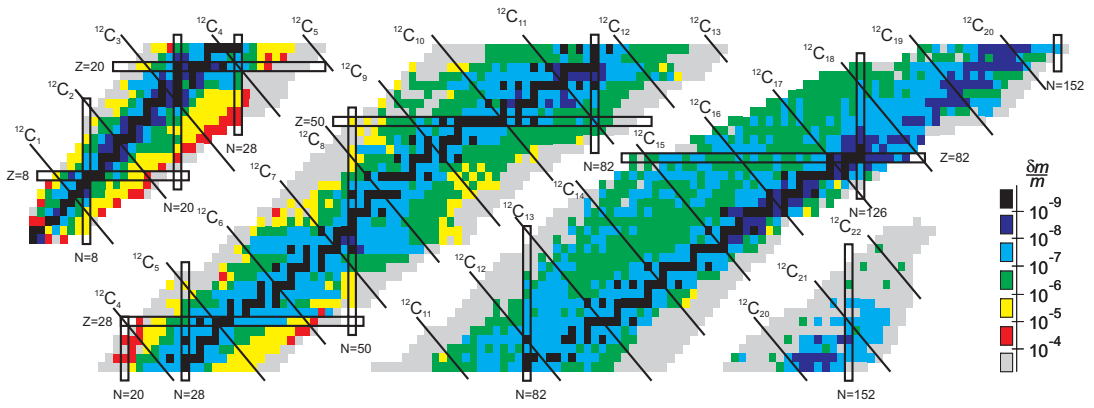

FIGURE 5.8: *Carbon cluster mass grid [Blau05a].*
The nuclear chart with the relative mass uncertainties $\delta m/m$ in color code is shown, stable nuclide are shown in black. The isobaric lines of carbon clusters C_1 to C_{22} demonstrate the advantage of using a 'carbon cluster mass grid' for calibration purposes.

Therefore, carbon clusters as reference ions do not only allow to perform absolute mass measurements, but also to reduce the systematics of the experiment. A complete study of the influence of carbon clusters on the mass uncertainty can be found in [Kell02]. Due to technical developments and space constrains, a new carbon cluster ion source has been designed [Mukh04b] and is under commissioning at ISOLTRAP.

5.4 Towards lower yields and shorter-lived nuclides

To further push the limits of ISOLTRAP and get access to shorter-lived and rarer radionuclides, the detection efficiency of the TOF-end detector of the spectrometer had to be considerably improved. Indeed, with a detection efficiency close to 100%, low ion yields can be handled without degrading the performances of the experiment due to the low statistics.

Assuming two different isotopes N_1 and N_2, with respective half-lives of τ_1, τ_2 such as $\tau_1 = 2\tau_2$ and assuming that they are initially produced with the same yield, the nuclides decay during the beam transport from the source to the experiment and the duration of the excitations in the different traps. Let us furthermore assume that the duration of the experimental cycle T (beam transfer, ion preparation, and cyclotron frequency measurement)

is taken to be $T = 1.5\tau_1$. From the initially $N_1(0)$ particles, $N_1(T) \approx 0.35N_1(0)$ particles survived the whole measurement procedure and only $0.1N_1(0)$ are detected assuming a detection efficiency of about 30%. If mass determination on isotope N_2 is performed, after the same duration $T = 1.5\tau_1 = 3\tau_2$ only $N_2(T) = 0.125N_2(0)$ particles are left from the initial $N_2(0)$, and $0.04N_2(0)$ are detected. To get the same precision on the mass determination, *i.e.* to collect the same amount of statistic, the run should be close to three times longer or the performances on the precise mass determination have to be sacrificed to $\sigma(m)/m \approx 10^{-7}$ instead of 10^{-8}. Increasing the detection efficiency by a factor 3, the yield of N_2 becomes now equal to the former yield of N_1 so that the measurement of N_2 is possible without any compromise between mass-precision or statistical significance.

To get more statistics for short-lived nuclides, and to reach exotic nuclei further away from the valley of stability, which have very short life-times, a new Channeltron-based detection setup has been designed and installed at ISOLTRAP. Chapter 6 describes in details the proposed solution and the new concept of the detection setup as well as the results and performances obtained with respect to the simulations.

Chapter 6

A new detector setup for ISOLTRAP [1]

6.1 Channeltron detector

6.1.1 Micro Channel Plate vs. Channeltron

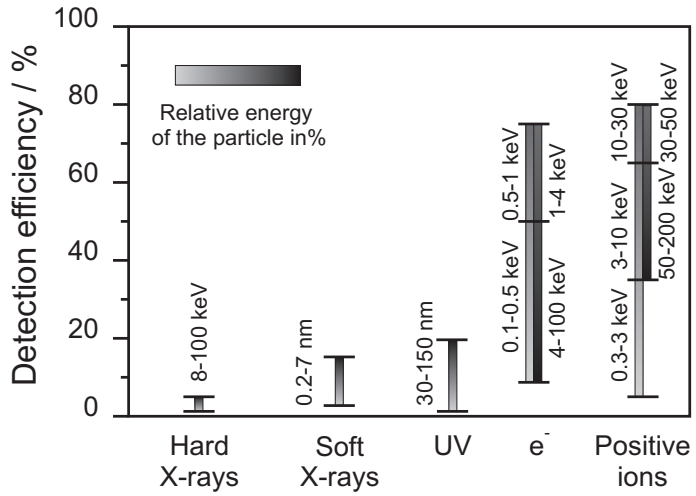

FIGURE 6.1: *Detection efficiency of a MCP for different particles at various energy ranges [Burl01*].*

The need for a new ion detector for the ISOLTRAP experiment was motivated by the fact that low energy ions (less than 3 keV)[2] are not efficiently detected with MCPs (up to 30% for a few keV ions, see Fig. 6.1). Therefore, other solutions were investigated including conversion plates or dynodes in order to convert the ions to electrons, which are easily detected (up to 90% detection efficiency).

[1] This chapter is mainly taken from [Yazi06].

[2] It has to be pointed out that the detection efficiency does not directly depend on the energy of the particles. For ions the detection efficiency depends on the velocity [Fras02]. Therefore mass-dependent detection efficiency is observed.

One simple and effective solution would have been to put the whole setup on high voltage as done at the JYFLTRAP experiment in Jyväskylä [Kolh03], but this was not feasible for the existing setup. Two other main ideas were competing: The first one consists of a high voltage conversion plate coupled with a MCP (a so called Daly-type detector [Daly60]), whereas the second solution is based on a Channeltron type detector.

For both solutions a spare detector had to be implemented in order to switch from one to the other in case of failure during operation without breaking the vacuum. In contrast to one stacked MCP system, the two possible new solutions are off-axis detectors: The Channeltron cone is already an off-axis type, whereas the MCPs have to be placed perpendicular to the beam line in order to detect the secondary electrons emitted after impact of the ions on the conversion electrode. The TOF-end detector and the spare have to fit in a standard CF-100 double cross, where only three sides are available for connections (one is connected to drift tube, a turbo molecular pump is mounted on the second one and the last flange is reserved for the electrical connections of the drift tubes and gauges). In order to collect all the ions extracted from the precision trap the MCPs should have a diameter of 5 cm due to the large emittance.

For the setup of a MCP detector coupled to a high voltage plate, one solution would have been to put the two MCPs at opposite positions in the cross and rotate the plate to select either one or the other. For the Channeltron-based system, one solution for a backup would have been to use two detectors on opposite sides of the cross, for which a mini-quadrupole bender system has to be implemented. In addition to the extra cost of the bender, the beam's spot size has to be considered since the diameter of the opening window of the Channeltron detector is only 11.2 mm. Because of those reasons it has been decided to go for a spare MCP detector which can be put in/out with a linear feedthrough.

Fig. 6.2 shows the relative detection efficiency for different types of charged particles and detectors. In order to detect most of the ions with a MCP, the ions need a sufficiently high energy (E > 3 keV). With a Channeltron detector, the same beam energy as before can be taken and the detection efficiency is increased. Moreover, the use of the Channeltron detector allows to shoot through it and thus to deliver *e.g.* an isomerically pure beam to another experiment or to a tape station for measuring the half-life of a single excited state [Hage07*]. Therefore it has been decided to install a Channeltron type detector plus a MCP mounted on a feedthrough.

6.1.2 The Channeltron

The detection procedure of the chosen Channeltron (see Fig. 6.3) is slightly different from that of a MCP. Instead of having only an avalanche plate and an anode, this Channeltron detector has an additional conversion dynode, whose role is to collect the impinging

ions and convert them into electrons thanks to an electron-emissive layer. This conversion increases the detection efficiency slightly since the electrons have a higher detection probability.

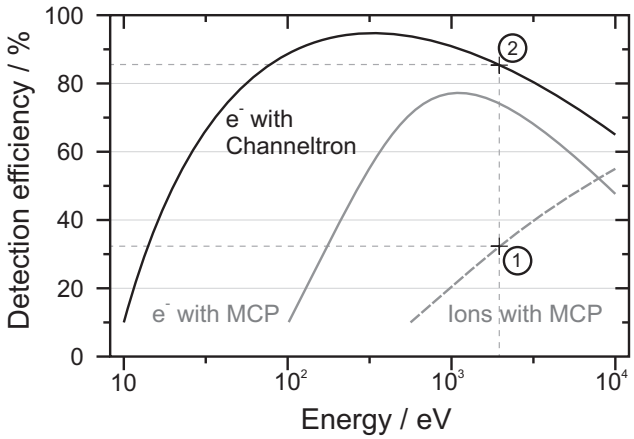

FIGURE 6.2: *Detection efficiency as a function of the particle energy. The approximate detection efficiencies of a MCP for ions and electrons are shown in solid and dashed grey-lines respectively. Position (1) shows the actual estimated detection efficiency and position (2) the efficiency planned to be reached.*

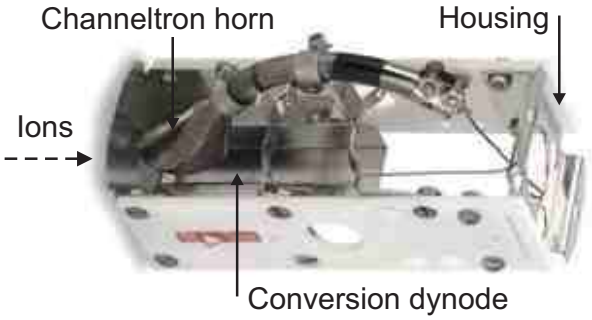

FIGURE 6.3: *Photo of the 402A-H model Channeltron detector from DeTech (Palmer, MA, USA) installed at* ISOLTRAP. *Real size about 8 cm in length.*

Detection principle

The Channeltron detector is composed of a horn-shaped electrode and a conversion dynode (see Fig. 6.3), which has electron emissive layer properties. When an ion hits the conversion dynode, secondary electrons are emitted. Those electrons are directed to the horn-shaped electrode and multiplied with an avalanche effect in order to produce a pulsed signal.

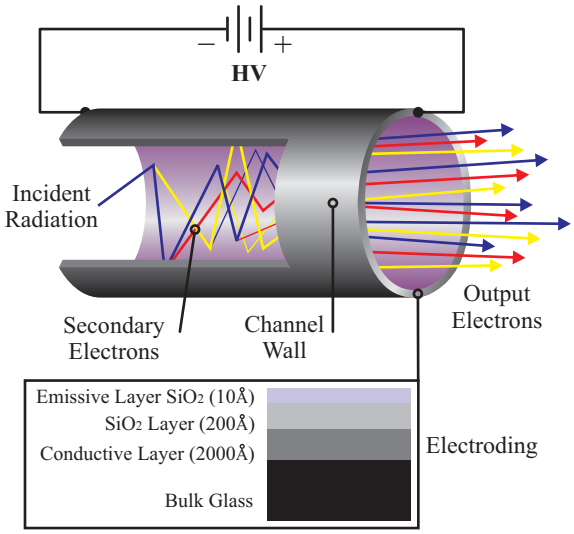

FIGURE 6.4: *Avalanche effect: the secondary electrons are multiplied by the detector [Burl01*].*

Fig. 6.4 illustrates the induced avalanche effect when a charged particle hits the electrode of the detector. An impinging ion hits the emissive layer of the dynode and it creates m secondary electrons. Each of those m electrons will then hit the layer of the horn-shaped electrode and produces n other electrons and so on. The number N of secondary emitted electrons follows a geometric law with a ratio n, *i.e.* after k collisions $N(k) = m \cdot n^k$ electrons are created and directed towards the detection electrode. Due to the dead time of the Channeltron horn ($\sim$25 ns, see Tab. 6.1) and the time spread of the first m secondary electrons on the horn (typically 1 ns), the ion-to-electron conversion ratio from the point of view of the detected signal can be considered to be 1:1.

Characteristics of the Channeltron

Tab. 6.1 gives the characteristics of the Channeltron detector as compared with a MCP. The recovery time of the detector is an important issue and has to be compared with the dead time of a MCP. Since a MCP has many channels to amplify the incident radiation, the probability of having the same channel being hit during the dead time ($\sim$2 ns) of this channel is very low, except for a high count rate (10^8 ions per second) or point-like spatial ion distribution on the MCP. For a Channelton there is only one single channel that amplifies the charge particle signal, therefore the recovery time of a Channeltron is its dead time $\sim$25 ns. To avoid dead-time loses due to this phenomenon, the count rate has to be kept below $\leq 10^5$ Hz. At ISOLTRAP, the idea is to go for a single ion detection for every cycle of the mass determination procedure (typically a few hundred ms). For precision mass measurements, ideally only one single ion at a time will be in the trap, thus, the dead time of such a device is not a drawback for the use at ISOLTRAP.

TABLE 6.1: *Characteristics of the Channeltron 402A-H model from DeTech and of a standard MCP.*

	Channeltron	MCP
Typical gain at 2500 Volts	$5{\cdot}10^7$	$5{\cdot}10^7$
Impedance	40-120 MΩ	66-400 MΩ
Work pressure	10^{-6} mbar	10^{-6} mbar
Dark count rate	< 0.05 cps	2 cps
Maximal count rate	10^5 Hz	10^8 Hz
Pulse width (or dead time)	∼25 ns	∼2 ns *
Rise time	∼5 ns	∼0.5 ns
Aperture plate size	Ø11.2 mm	Ø10 to 50 mm
Cost	€ 600	€ 600

* Depends on the dimension of the MCP pores.

6.1.3 Detection efficiency of particles

As for any other detector, Channeltrons do not behave identically depending on the properties of the particles that are detected. Fig. 6.5 shows the evolution of the detection efficiency of the Channeltron as a function of the energy of the particle. The higher the mass, the lower the detection efficiency (see footnote on page 69).

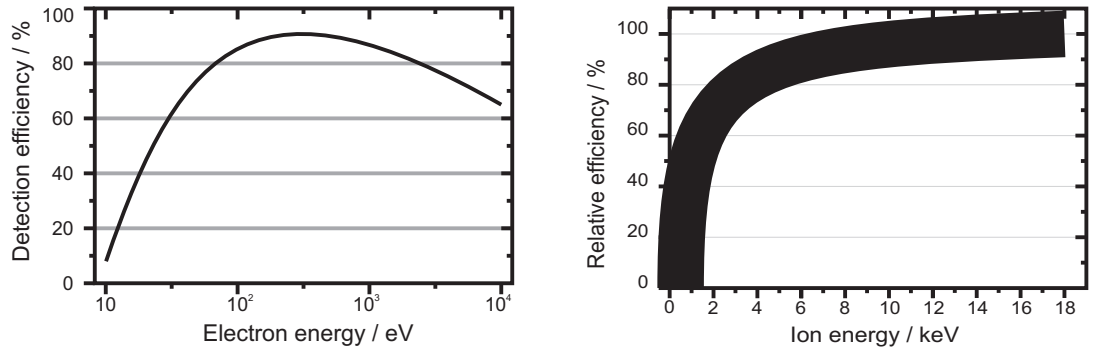

FIGURE 6.5: *Detection efficiency of a Channeltron as a function of energy of electrons (left) and ions (right) [Burl01**].

The detection efficiency for electrons observed in Fig. 6.5 (left) is maximal for a few hundred eV energy electrons, whereas for direct-ion detection on the Channeltron (Fig. 6.5 (right)), the detection efficiency increases with their energy (*i.e.* the velocity) and is pretty much the same as for a MCP.

Enhancing the detection efficiency of low energy and singly charged heavy ions: converting ions to electrons

Since ISOLTRAP is designed for a broad range of masses, the detection efficiency of the new detector should not depend on the mass of the investigated ions. As shown in Fig. 6.5 (right), the direct detection efficiency of a Channeltron (30-50%) is not much better than that of a MCP (30%). However, in order to improve the detection efficiency, one solution is to convert the positive ions into electrons on a conversion dynode to reach close to 90% detection efficiency.

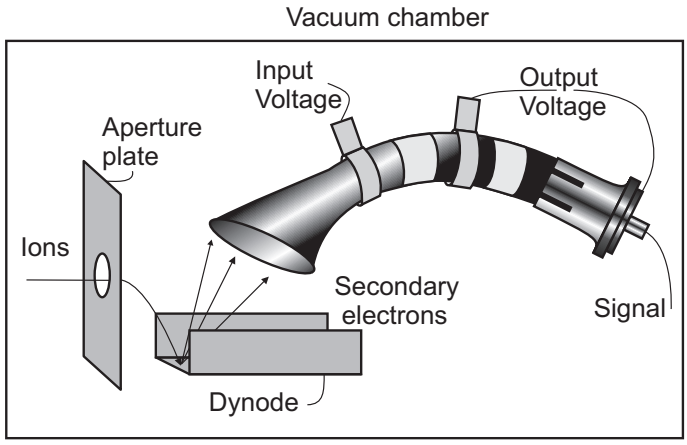

FIGURE 6.6: *Principle of the conversion dynode and connection scheme of the Channeltron detector [Burl01*].*

The principle of the ion-to-electron conversion is illustrated in Fig. 6.6: A high negative voltage is applied to the dynode (typically -3 to -5kV) in order to attract the positive ions. They hit the conversion electrode which emits electrons as well as ions. Due to their positive charge state, those secondary light ions will not reach the Channeltron. The high voltage value of the dynode creates a strong gradient towards the Channeltron horn, thus the secondary electrons are attracted by the Channeltron amplifier electrode and hit it with an energy equal to the potential difference between the dynode and the horn itself. This potential difference can be easily tuned in order to reach the maximum detection efficiency according to Fig. 6.5 (left). With this method light ions as well as heavier ones can be detected with almost the same detection efficiency (neglecting the conversion probability).

Implementation of the detector

In contrast to the MCP, the chosen Channeltron-type detector is an intrinsic off-axis device. The major difficulty is the focussing of the primary beam from the precision trap to the conversion dynode, and the secondary electrons to the main electrode. In this work the

voltages are chosen to be -4kV for the conversion dynode and -2kV for the horn-shaped electrode of the Channeltron. The fine tuning of the voltages is given by the output of ion trajectory simulations described in Section 6.2.4. The field created by this potential difference is used to steer the beam to the detection area of the Channeltron. Fig. 6.6 and Tab. 6.2 show a typical setup and voltages for positive ion conversion and secondary electrons detection:

TABLE 6.2: *Typical voltages for a Channeltron detector*

	Applied voltage
Input voltage	≈ -2kV
Output voltage	Ground
Signal	Ground
Conversion dynode	≈ -4kV
Aperture plate	-1 keV to ground

Higher detection efficiency but smaller detection surface

As previously explained, the main advantage of the Channeltron detector is its detection efficiency of up to 90% even in the case of a low energy heavy ion beam, if the conversion dynode is used. A standard MCP has an intrinsic detection efficiency of 30% [Breh95, Ober97]. However, the detection surface for the MCPs used at ISOLTRAP is a 5 cm diameter area, and thus much larger than the opening window of the Channeltron (only 1 cm diameter).

Therefore, the exchange of the existing MCP by a Channeltron will increase the ion detection efficiency by a factor 3, but the drawback is that a factor of up to 25 can be lost because of the smaller detection surface. To solve this problem, the beam profile after the extraction of the precision Penning trap has been thoroughly studied using a dedicated ion trajectory simulation software. The first step was to understand the behavior of the beam and its reaction to the complete set of parameters and to focus the ion beam in order to reach the Channeltron opening window with almost 100% efficiency.

6.2 Simulation studies

The SimIon software [Sim7.0] is dedicated to the computation and simulation of ion trajectories in an electric field $\vec{E}$ and/or a magnetic field $\vec{B}$, similar to other software packages, such as COSY infinity [Cosy8.1*, Maki99] (used at CERN), or Poisson super Fish [PSF7.16*]. Based on solving the Poisson equation for the electrode configuration, SimIon is used for the simulation of the beam profile as well as for beam tuning.

6.2.1 Simulation of the ion trajectory

Geometry of the system

First of all, the geometry of the setup had to be implemented into the SimIon software. The electric and magnetic fields can be programmed in different ways. Either the geometry of the field has a simple shape with *e.g.* a cylindrical symmetry, for which the electrodes can be directly drawn, or the geometry is more complex and creating the electrodes geometry as well as the magnetic field requires building special geometry files within SimIon ('*.gem').

Those files contain a source code that describes the electrodes of the system. Basic geometric figures are already predefined (Box, Cylinder, Hyperbola) and can be added or subtracted in order to fully describe the electrodes. This method is more complicated than directly drawing the electrode with SimIon, but it is much more versatile and leads to a precise description of the system.

After giving either directly the field geometry of the system or the description of the electrodes, the software creates the 3D-space geometry corresponding to the problem with the associated electric and/or magnetic fields. In this work, the hyperbolically-shaped precision trap of ISOLTRAP as well as the the extraction electrodes and the drift tubes have a cylindrical symmetry. However, since the Channeltron is an off-axis planar-symmetry detector, the use of the special geometry files is mandatory.

Superposition theorem

One of the basic theorems in electromagnetism used by the SimIon software in order to compute the electric and magnetic fields is the superposition theorem. It is of great use in order to simplify the creation of the fields and to minimize the computation time.

The theorem states that the fields created by two different electrodes (or magnets) can be added if – and only if – there is no discontinuity at the limits. That means for two electrodes (1) and (2), the electric field has to obey the relation:

$$\text{For } i = x, y, z, \quad \lim_{i \to \pm\infty} V_{(1)}(x, y, z, t) = \lim_{i \to \pm\infty} V_{(2)}(x, y, z, t). \tag{6.1}$$

Moreover, the electric $\vec{E}$ and magnetic $\vec{B}$ fields have to be continuous in all directions.

Using this theorem, a complex problem can be subdivided into much simpler subsystems, which can be handled easily. Analytically the continuity at the limits is often canceled out by the fact that the field is zero at infinity. The superposition theorem with a numerical approach implies that the space where the field is computed is not infinite. The conditions at the limits have to be explicitly given in order to make the field values match

at the border of the mesh. This superposition principle has been used in this work to add sets of electrodes with a different geometry in SimIon.

Computing the fields to get the ion trajectories

Once the geometry of the system, *i.e.*, of the electrodes and magnets, is given to the software, the field map is computed solving the Poisson equation:

$$\Delta V = -\frac{\rho}{\varepsilon_0 \varepsilon_r}, \tag{6.2}$$

where ρ is the charge density, ε_0 is the electric permittivity in the vacuum and ε_r the relative permittivity in the material. The Laplace operator Δ is defined as:

$$\Delta \ : \ f(\{x_i\}_{i\in I}) \mapsto \sum_{i\in I} \frac{\partial^2 f\left(\{x_i\}_{i\in I}\right)}{\partial x_i^2}, \tag{6.3}$$

where I is an interval included in $\mathbb{N}$.

As most softwares packages, SimIon faces the problem of numerical infinitesimal elements. The system is not continuous, but is an assembly and superposition of small volume elements $\delta\tau$. In order to compute the field for each point of the system, SimIon has to take an average of the value of the field around the volume $\delta\tau$ with respect to its 6 neighbors in 3D as shown in Fig. 6.7, or, 4 neighbors in 2D or cylindrical symmetry.

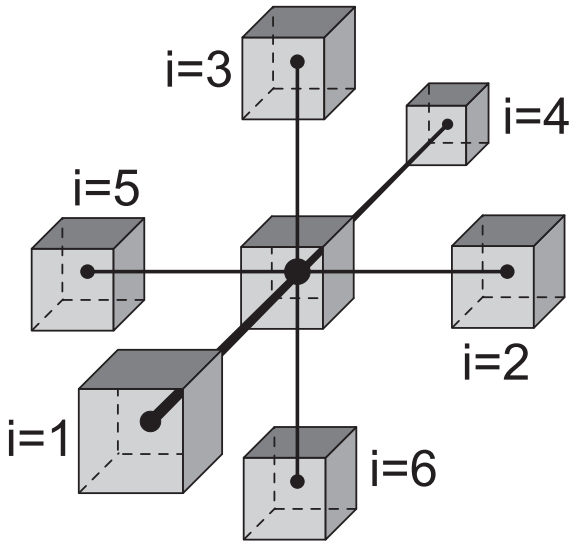

FIGURE 6.7: *Extrapolation and computation of the fields in SimIon.*

Fig. 6.7 illustrates the way SimIon computes the fields for the Poisson equation. The potential created at the center is given by:

$$V_0 = \frac{1}{6}\sum_{i=1}^{6} V_i, \tag{6.4}$$

where the V_i are the potentials of the neighboring infinitesimal elements.

The Runge–Kutta 4$^{\text{th}}$ order method

Once the fields are fully determined for each point, the ion trajectories are calculated by use of a Runge–Kutta 4$^{\text{th}}$ order numerical technique [NumRec*] to solve the differential equation of motion. This problem is also known as the *Cauchy Problem*. It consists of a closed interval $[a;b]$ of $\mathbb{R}^m$ and a fixed point $x_0 \in [a,b]$. Assuming that $y_0 \in \mathbb{R}^m$ and f is a defined and continuous application from $[a;b] \times \mathbb{R}^m$ to $\mathbb{R}^m$, an application y differentiable from $[a,b]$ to $\mathbb{R}^m$, and verifying the following properties is expected to satisfy the solution of the problem:

$$\forall x \in [a;b],\ \left\{ \begin{array}{rcl} y'(x) & = & f(x,y(x)) \\ y(x_0) & = & y_0 \end{array} \right. . \tag{6.5}$$

Runge–Kutta-solution methods are based on the Taylor expansion to a given order of the solutions, without having to compute each time the higher order derivatives. Assuming that I is an interval and $\forall x \in I,\ y : x \mapsto y(x)$ an application $N+1$-differentiable, for $x_0 \in I$ the second Taylor formula demonstrates the existence of $\xi \in \mathbb{R}$, between x_0 and x such as:

$$y(x) = \sum_{k=0}^{N} \frac{(x-x_0)^k}{k!} y^{(k)}(x_0) + \frac{(x-x_0)^{N+1}}{(N+1)!} y^{(N+1)}(\xi). \tag{6.6}$$

In general, the value of the solution which is given after one integration step can be written as:

$$y_{i+1} = y_i + \varepsilon(x_i, y_i, h) \tag{6.7}$$

where the function $\varepsilon(x_i, y_i, h)$ can be interpreted as being a mean slope for a time interval h. It is given by:

$$\varepsilon(x_i, y_i, h) = \sum_{k=1}^{n} \alpha_k \lambda_k, \tag{6.8}$$

with $n \leq N$ the order of the Taylor expansion and λ_k the corresponding small variation.

The Runge–Kutta 4 algorithm (4$^{\text{th}}$ order for the Taylor expansion) is described by:

Repeat:
1) Evaluation of the function (4 times per integration step)

$$\begin{aligned}\lambda_1 &= h \cdot f\left(x_i, y_i\right)\\ \lambda_2 &= h \cdot f\left(x_i + \tfrac{1}{2}h, y_n + \tfrac{1}{2}\lambda_1\right)\\ \lambda_3 &= h \cdot f\left(x_i + \tfrac{1}{2}h, y_n + \tfrac{1}{2}\lambda_2\right)\\ \lambda_4 &= h \cdot f\left(x_i + h, y_i + \lambda_3\right)\end{aligned}$$

2) Incrementing of the function

$$y_{i+1} = y_i + \frac{1}{6}(\lambda_1 + 2\lambda_2 + 2\lambda_3 + \lambda_4)$$

3) Incrementing of the independent variable

$$x_{i+1} = x_i + h$$

Until convergence.

With this method, the error on y is $\mathrm{O}(h^5)$. Advantages and drawbacks of Runge–Kutta methods are summarized in Tab. 6.3:

TABLE 6.3: *Advantages and drawbacks of Runge–Kutta methods.*

Advantages	Drawbacks
Easy to program	Long computation time
Numerically stable	Local error difficult to estimate
Adaptable integration step	

6.2.2 Simulation of the precision trap and extraction of ISOLTRAP

The last stage of the ISOLTRAP spectrometer is composed of the precision hyperbolical trap (see Chapter 4) and a beam transfer section to the TOF detector. The above mentioned geometry files have been created according to the latest technical drawings of the setup [Otto90*] in order to get a simulation as close as possible to the experimental reality. After validation of the model and the simulation as well as comparing the results of the simulation and the experiment, the geometry of the setup has been reprogrammed with respect to the modifications due to the new detector system.

Validation and tests of the system's geometry

In order to validate and verify the simulation, each part of the simulated setup has to be thoroughly tested and compared with known experimental results. Of interest was the

precision Penning trap and the extraction scheme of the ions. In particular, the correction electrodes have been taken into account in the geometry file, even if their task is merely the correction of the electric field inhomogeneity and to compensate for the quadrupolar field imperfections due to the fact that the trap has finite electrodes. Indeed, they also play an important role in the ion trapping potential just before the extraction to the drift tubes section.

FIGURE 6.8: *Precision Penning trap of* ISOLTRAP *simulated with SimIon. The electrodes are shown in black and the electric quadrupolar equipotential lines in grey.*

Fig. 6.8 illustrates the hyperbolical field created by the trap, when used in capturing mode. This figure shows a good agreement with the expected quadrupolar field described in Chapter 3. In order to check the magnetic field gradient from the trap to the detector, the simulation results have been compared with experimental measurements of the magnetic field performed by *Oxford Instruments* along the axis of the beam line [Beck97]. To this end, a simulated ion has been extracted from the Penning trap to the detector flying through the drift tube section. With a special choice of initial conditions, *i.e.* the ion starting on the axis without any initial radial velocity, the ion will follow the symmetry axis of the system. The values of the electric and magnetic field can be monitored and recorded according to the position of the ion along the axis.

Fig. 6.9 shows no discontinuity for the electric $\vec{E}$ and magnetic $\vec{B}$ fields, especially between the drift tubes # 6&7, where the superposition of two different sets of electrode geometry files has been used, and hence a discontinuity might have occurred because of

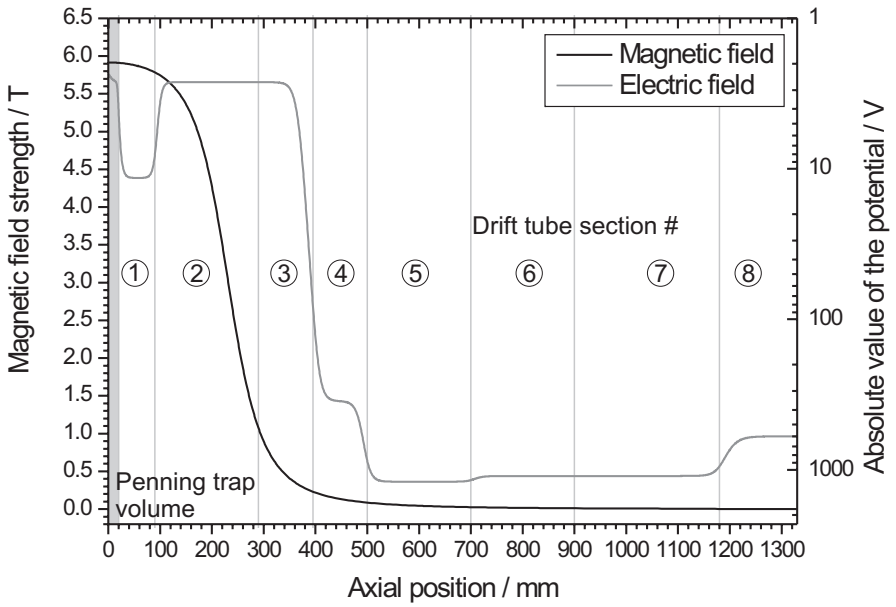

FIGURE 6.9: *Electric and magnetic field strength as a function of the distance to the trap center for the last stage of* ISOLTRAP.

the finite dimension of the SimIon workbench. From this it can be stated that the superposition of the field has followed the selection rules of the superposition theorem. Note that in the area where the gradient of the magnetic field is stronger, the electric field is higher in order to allow for an complete conversion of the ion magnetic moment into an axial acceleration while passing through the gradient of the magnetic field. The small electric potential well will slow down the ions to allow an adiabatic transition.

The obtained results of the simulation agree with the expected and experimental data. In the following, the geometry of the Channeltron detector is fully described as well as entered to the simulation software. The most complicated part of the Channeltron detector, the horn-shaped electrode has simply been simulated by a plate, since the aim of the cone shape is to induce the electron avalanche in order to magnify the detection signal. This choice does not only simplify the geometry of the system, but also saves time of the compilation in order to get the electric field map and saves as well computer memory.

Thus, the complete final stage of the ISOLTRAP spectrometer has been simulated and tested according to the experimental setup and cross checked with known and/or measured data. Fig. 6.10 shows an overview of the whole simulated section of the 3rd stage of ISOLTRAP.

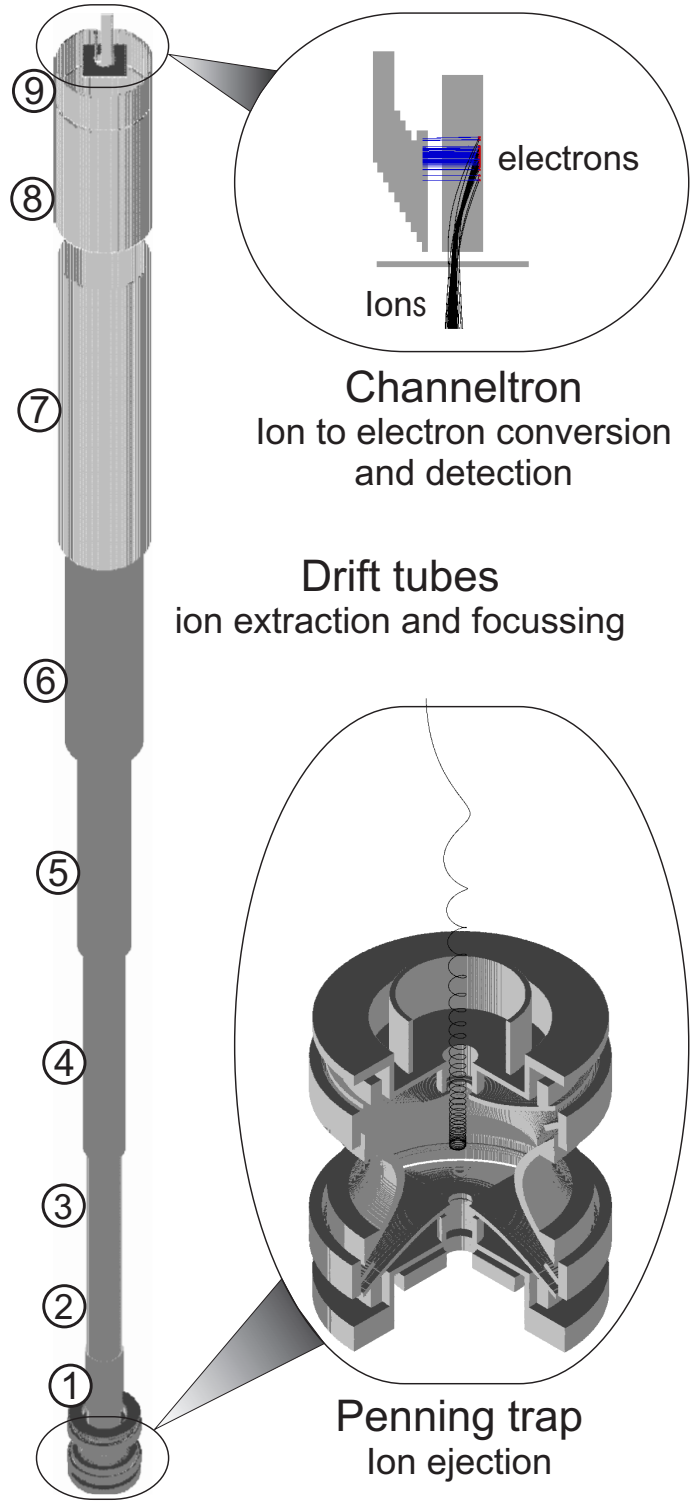

FIGURE 6.10: *Last section of the* ISOLTRAP *spectrometer simulated with SimIon. Shown in the figure are the Penning trap, the drift tube section and the Channeltron detector.*

6.2.3 Simulation of the ion ejection

Since the aperture window of the Channeltron is much smaller than the opening area of a MCP, and in order to optimize the ion transfer from the trap to the detector, the particular scheme of the ion ejection has to be taken into account and simulated as well. Indeed, the extraction scheme preceded by the magnetron dipolar and cyclotron quadrupolar excitation implies special and well defined initial conditions for the ions. In order to focus the ions onto the aperture of the Channeltron, realistic initial conditions have to be used.

For the calculation of the ion trajectory, the SimIon software requires the following set of initial conditions: the initial position $\vec{r}_0 = \{x_0; y_0; z_0\}$, the initial velocity $\vec{v}_0 = \{v_0^x; v_0^y; v_0^z\}$, and the initial energy (in our case purely radial) E_0^{rad}. Even though SimIon can generate randomly distributed sets of initial conditions, these will not correspond to the initial conditions of the ions after the measurement scheme in the Penning trap.

Since the solution for a dipolar and a quadrupolar excitation are analytically known (see Chapter 3), it is possible to reduce the set of the initial conditions. For a better ergonomic and flexible handling of the initial data set, a small interface within the SimIon software has been written in order to create realistic initial distributions of ions. Moreover thanks to this modification, the computation time with SimIon has been drastically reduced.

Getting the proper set of initial conditions

In order to create an initial set of parameters for the simulation, the initial conditions before the dipolar and quadrupolar excitations have to be experimentally determined. Unfortunately, those initial conditions are not directly accessible. However, the most important parameter such as the magnetron and cyclotron radii $\rho_{\pm}(0)$ after the dipolar excitation, as well as the damping coefficient δ, are accessible by fitting a resonance curve with the theoretical line shape, Eq. (3.42). The fitting routine is based on a least mean square method comparing the theoretical TOF to the measured curve. It can be written as Eq. (4.4):

$$TOF_{\mathrm{th}}(\omega_Q) = TOF_{\mathrm{th}}(\omega_Q, a_0, \cdots, a_i, \cdots, a_N), \tag{6.9}$$

where the N parameters a_i are $(R_{\pm}(0), \delta, T_Q, \cdots)$. For more details see Appendix A.

The fitting routine determines the best set of parameters that minimize the following expression:

$$\chi^2 = \sum_{k=1}^{K} \left(TOF_k^{\mathrm{exp}} - TOF_k^{\mathrm{th}}\right)^2, \tag{6.10}$$

where k is the index of the measured points. The values given by the fitting routine are the ones used as starting conditions for the simulation.

Up to this point it could be assumed that those initial conditions are directly used in SimIon to reproduce and simulate the quadrupolar excitation. But to this end, the simulated trap has to be equally segmented into four parts on which rf fields are applied. This would lead to a break of the symmetry of the electrodes in SimIon with a dramatic increase of the file size. For each electrode with a cylindrical symmetry, the typical file size is 39.2 Mb for a 1500×40×40 mm^3 volume, whereas for the Channeltron detector it is 36.6 Mb for a 60×40×40 mm^3 planar symmetry, *i.e.* 24 times more for the same volume. Therefore it would have been expected to handle close to Gigabyte sized files if breaking the symmetry of the electrodes and the trap.

In order to simulate the quadrupolar excitation, a C++ based program has been developed. Its role is to create a set of initial conditions for SimIon. With this program, the coordinates and the energy of the ions after the quadrupolar excitation can be computed according to the equations given in Chapter 3, especially Eq. (3.42).

The program takes as input values the initial conditions given by the fitting routine and then creates a set of initial conditions distributed around the initial values for SimIon. The energy of the ions, mainly due to the radial cyclotron energy, is computed according to an applied excitation frequency, so that it simulates a frequency scan around the cyclotron frequency, and creates artificially a resonant TOF spectrum once injected into the ion trajectory simulation software.

Programming the ejection and the ion drift with SimIon

Once the initial parameters are found and the initial conditions are correctly reproduced, the remaining task is to follow the ion extraction scheme out of the Penning trap. To simulate the extraction and perform at the same time an on-line analysis, SimIon dedicated programming files ('*.prg') have been developed. The main drawback of the use of those programming files is an increase of the execution time.

Concerning the ejection scheme of the ion from the trap, the voltages of the extraction electrodes have to reproduce the changes applied at a given time t_i. The SimIon program takes the different steps for the extractions and updates the corresponding voltages for the simulation (see Fig. 6.11):

- at $t_0 = 0$ ms: The trap is still in trapping mode, just after the quadrupolar excitation scheme.

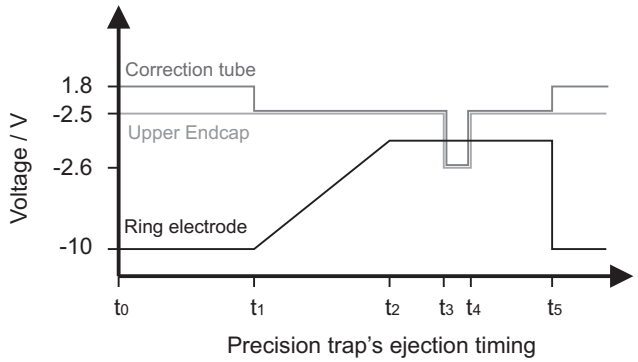

FIGURE 6.11: *Timing for the ion extraction from the precision trap. The figure is not to scale, in order to make the ejection pulse more visible.*

- at $t_1 = 1$ ms: Beginning of the ramping of the ring electrode to eject undesirable fast ions (see Section 4.4.1). During the same time the correction tube electrode voltage is set to the value of the end cap.
- at $t_2 = 17$ ms: The ring electrode reaches the optimal value so that only low energy and cooled ions are left in the trap.
- at $t_3 = 18$ ms: An ejection pulse is applied to both upper end cap and correction tube in order to extract the ion from the trap.
- at $t_4 = 18.1$ ms: End of the ejection pulse.
- at $t_5 = 33.1$ ms: Back to the initial state, after the quadrupolar excitation and before a new ejection of ions.

Concerning the on-line analysis with the SimIon program, several sections of interest have been defined: first, the drift tubes section, from the trap to the detector, and second, the detector itself, subdivided into the conversion dynode and the horn-shaped electrode. Thanks to those sections, the exact position of the ions can be monitored in order to simulate the ion to electron conversion:

- If the ions reach the dynode, the program converts them into electrons, using special SimIon internal flags.
- Eventually, the secondary electrons are detected on the Channeltron horn.
- In all cases, the initial conditions as well as the final ones, plus the TOF and the detection code (see Tab. 6.4) are stored by the program and send to a text form file for further analysis.

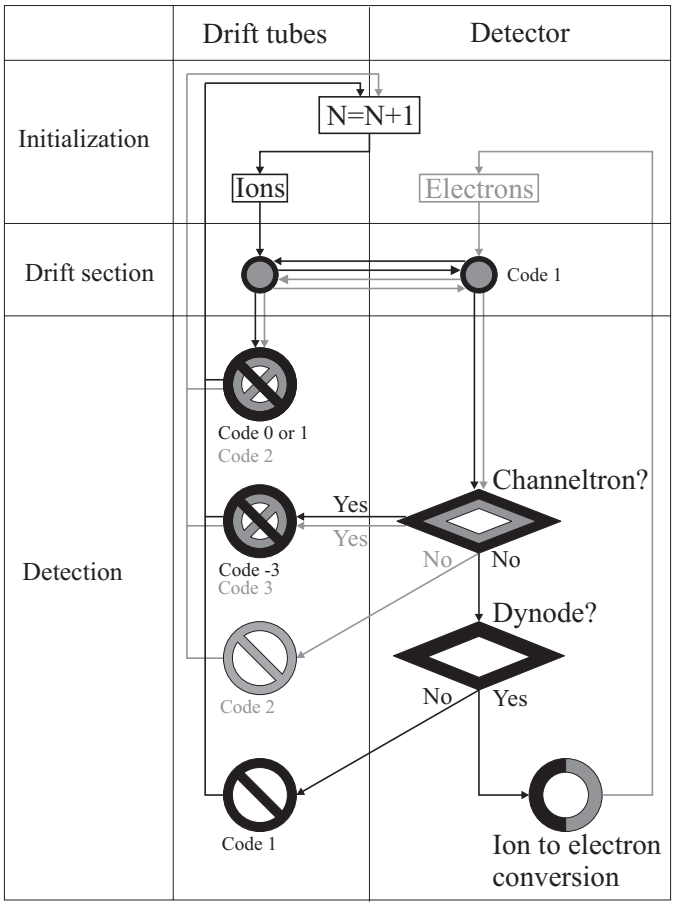

FIGURE 6.12: *Flow diagram of the program for the simulation of the ion and electron trajectories.*
The ions are created and move in the drift section until they are lost or they enter the detector volume and reach one of the different electrodes (conversion dynode, or Channeltron horn). For the explanation of the detection code the reader is referred to Tab. 6.4.

TABLE 6.4: *Detection code used by the program to identify the different events at the detector.*

code	Description
0	Ion lost in the drift tube section.
1	Ion extracted but does not reach the detector.
2	Ion reach the conversion dynode, but the secondary electron is not detected.
3	Secondary electron is detected on the Channeltron horn.
-3	Ion directly on the Channeltron, according to the polarity of the detector, or ion directly detected by the MCP, if used.

Fig. 6.12 shows the automation scheme of the program and Tab. 6.4 summarizes the detection codes given by the program. The same source code is used for both electrons and ions, since the only difference is their mass and charge state. To make the flow diagram more readable, the paths of both electrons and ions have been disentangled using respectively black color for the ions and gray for the electrons.

6.2.4 Optimization of the beam focussing

Before proceeding to the real beam tuning and the optimization for the focussing, the simulations should reproduce the TOF spectrum obtained with the experimental setup. Indeed, some systematic effects due to the simulation could interfere with the focussing and produce unwanted effects like focussing of the ion only in resonance or off-resonance.

Frequency scan for mass determination

In order to validate the whole simulation process, a good test is the comparison of an experimental resonance with a simulated one. In the previous sections the different parts of the simulations have been explained. Fig. 6.13 shows how the subprograms are interconnected in order to reduce the memory load as well as the computation time and to perform an on-line analysis.

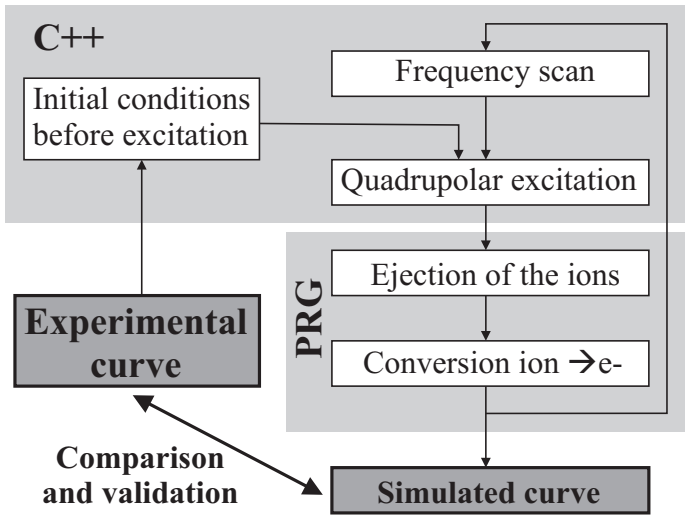

FIGURE 6.13: *Steps of the whole simulation.*

First, the initial conditions have to be extracted from an experimental data set, then they are used as an input for a C++ based program in order to simulate the quadrupolar excitation. The C++ program's output file is used as an input for the SimIon software which performs the ejection scheme for the ion extraction and the on-line analysis using the program files ('*.prg').

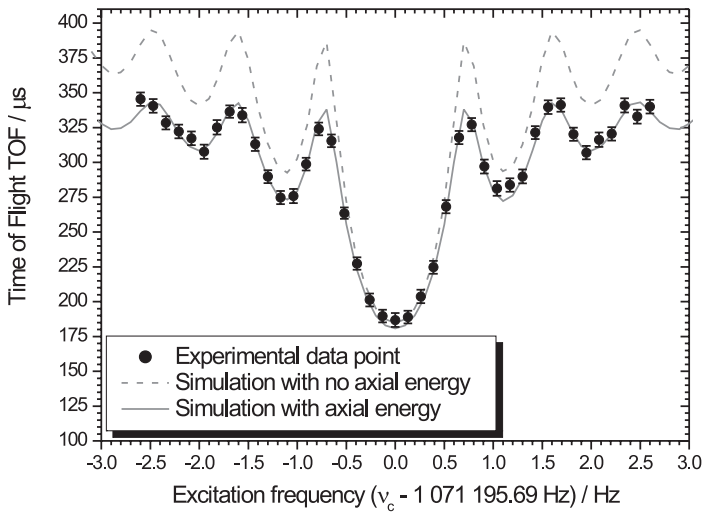

FIGURE 6.14: *Comparison between experimental and simulated frequency scans.*

In Fig. 6.14 (dashed line), it can be observed that the simulations reproduce the side bands around the center frequency as well as the absolute value of the TOF for resonantly excited ions. The slight difference for the base line (off-resonance ions) can be easily explained. In the simulation the initial conditions are chosen such that the ions are trapped exactly in the middle of the trap, *i.e.* with no initial axial energy. It is known (see Appendix A) that the energy E_{conv} affects only the non-resonantly excited ions. It corresponds to the voltage difference close to the drift tubes # 1 and 2. Since there is no read-back from those electrodes, only the nominal voltages are used for the simulation. However, they might not correspond to what is really applied. Moreover, the initial axial energy E_{z} is a weak parameter that affects the general TOF. A combination of slightly deviating values of E_{conv} and E_{z}, in addition to the fact that the waiting time after the capturing time is not taken into account, can easily explain the small differences observed for the off-resonance ions, Fig. 6.14 (solid line) ([Beck97] Sections 4.2.2 and A.2.4).
The whole scheme from the excitation, the ejection and the detection have been successfully reproduced simulating a MCP detector. Still to do was the optimization of the focussing on the Channeltron.

Focussing the ion beam on the Channeltron entrance window

The ratio of the active detection windows of a MCP as compared to a Channeltron is close to 25. This rough estimate is done under the assumption that the impinging beam is equally distributed on the surface of the MCP. With the simulations it has been shown that 90% of the beam is located on a 25 mm diameter area on the MCP. Therefore, without any changes in beam focussing the count rate gained by exchanging the old MCP with the Channeltron would be close to one, instead of a factor 2.5 to 3 as expected and envisaged.

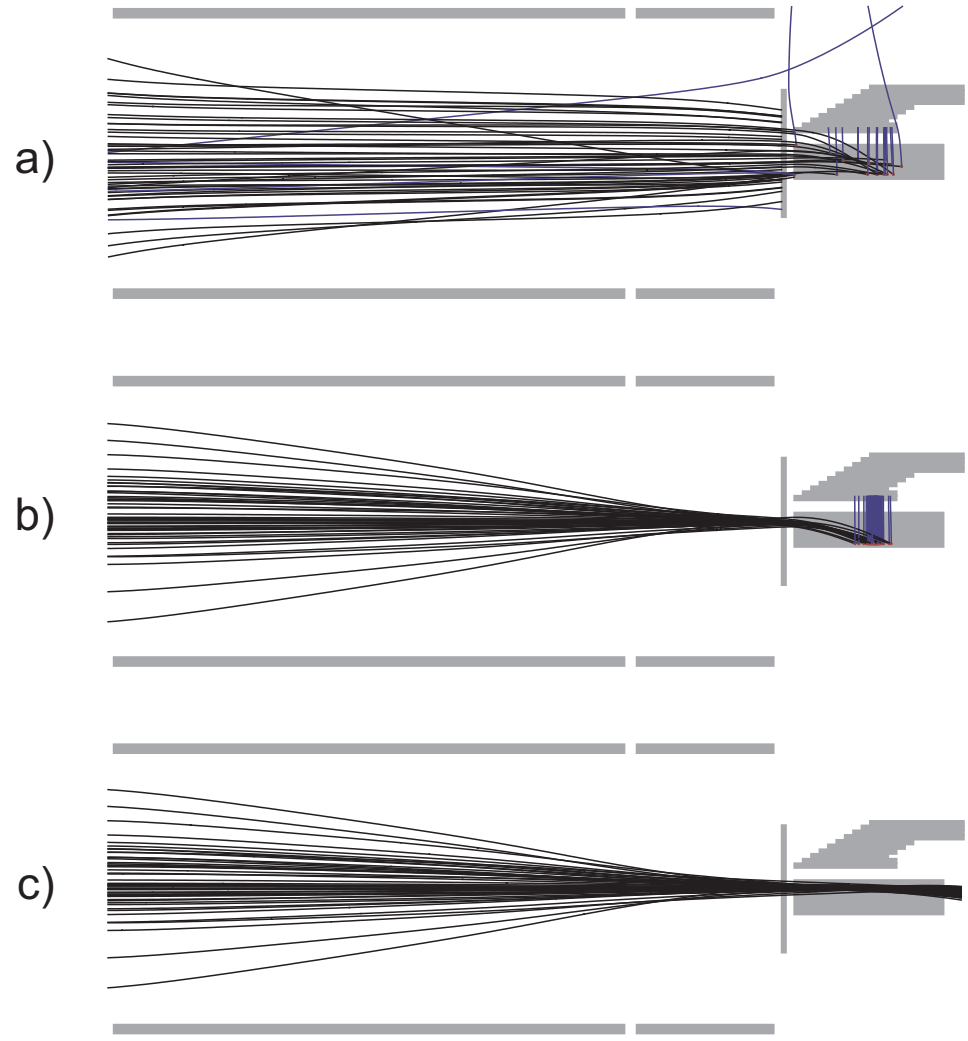

FIGURE 6.15: *Simulation of the new setup: (a) with the MCP settings, i.e. no focussing, (b) with focussing, (c) shooting through the Channeltron detector.*

TABLE 6.5: *Detection efficiency with and without focussing.*

	No focussing	Focussing	Shooting through
Ions out of the drift tubes	100%	100%	100%
Ions on the dynode	40%	100%	—
Secondary electrons detected	75%	100%	—
Total efficiency	30%	100%	≈100%

The adopted solution included the addition of another drift tube (tube #9 in Fig. 6.10) mounted on a linear feedthrough to replace the MCP when the Channeltron is used. This additional drift tube gives a further degree of freedom in order to realize an Einzel lens

system for focussing the beam on the Channeltron. Systematic studies and different beam tuning options have been investigated to reach the best set of parameters for the focussing, which were first simulated and then verified *in situ*.

Fig. 6.15 (a) and (b) show the optimization performed to focus the beam to the detector. Fig. 6.15 (a) illustrates the beam profile without any changes of the voltages, and Fig. 6.15 (b) shows the successful beam focussing on the Channeltron. One other advantage of the chosen off-axis Channeltron is that ions can be shot trough the the detector. In the case of a isomerically contaminated beam, it has been demonstrated that the ISOLTRAP spectrometer has sufficient resolving power (up to 10^7) to clean away unwanted isomers in the precision trap and then produce a pure isomeric beam [Roos04]. After checking the purity of the beam with a cyclotron resonance, the pure isomeric beam can be delivered by shooting through the Channeltron to other experiments, as *e.g.*, a tape station for isomeric-free half-life measurement of radionuclides [Hage07*]. Fig. 6.15 (c) demonstrates the feasibility of such a technique. However, in order to reshape the beam and focuss it to a tape station, additional drift sections and lenses are needed. A summary for each part of the Channeltron transfer efficiency is summarized in Tab. 6.5. Tab. 6.6 gives the appropriate values of the electrodes voltages for the different modes.

TABLE 6.6: *Voltages and beam tuning settings using the MCP or the Channeltron detector.*

	MCP mode	Channeltron mode	Shooting through
Drift tube #5	-1200 V	-1200 V	-1200 V
Drift tube #6-7	-1100 V	-1100 V	-1100 V
Drift tube #8	- 600 V	- 250 V	- 250 V
MCP	-2000 V	—	—
Channeltron tube (9)	—	-1100 V	-1100 V
Channeltron plate	—	-2000 V	-1100 V
Channeltron dynode	—	-4000 V	-1100 V
Channeltron cone	—	-2000 V	-1100 V

For a comparison of the simulation with experimental data, an identical set of $^{85}Rb^{+}$ isotopes distributed with an initial magnetron radius between 0 and 1.8 mm was chosen. With the MCP, almost all ions reach the detector. However, with a detection efficiency of 30%, only one third is actually detected. With the same set of initial conditions, close to 95% of the ions reach the conversion dynode and only a few secondary electrons are lost (possibly due to the simulated field approximation). Taking into account the detection efficiency of the Channeltron of 90%, close to 85% of the ions/secondary electrons are detected. The expected gain in count rate, when replacing the MCP with the Channeltron detector is therefore around 2.8.

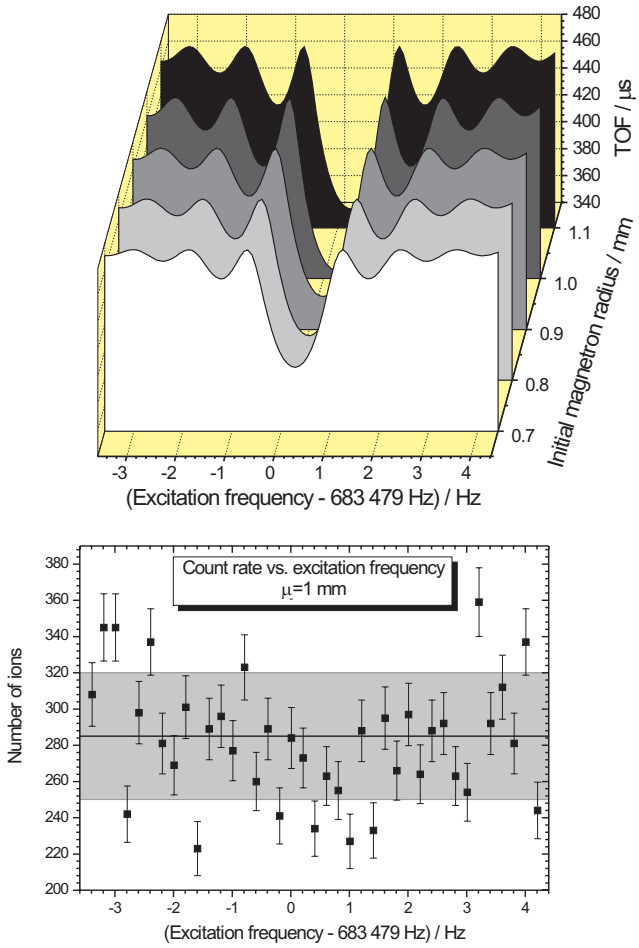

FIGURE 6.16: *Resonance curve (fitted to experimental data) and count rate as a function of the initial magnetron radius.*

In the bottom plot, no count rate resonance as a function of excitation is observed, i.e., the focussing does not create an artificial efficiency decrease.

It has to be emphasized that the larger the initial magnetron radius is, the higher the loss of beam on the Channeltron will be. The maximum magnetron radius that can still be monitored by the MCP is 1.8 mm. However, even with the MCP a count rate decrease can be observed for radii larger than 1.3 mm. In fact the ions are lost in the drift tube section, especially in the first part (drift tubes # 1 to 3). To be on the safe side, initial magnetron radii above 1.3 mm should be avoided for the detection with the Channeltron. Fortunately, the optimum experimental value for the initial magnetron radius is 0.7 mm, and very rarely larger than 1.2 mm, experimental resonance curves, shown in Fig. 6.16, have been studied for different initial magnetron radii. No count rate effect has been observed for initial magnetron radii between $\rho_- = 0.7$ and 1.1 mm.

6.3 Implementation and performance of the new detector

6.3.1 Technical design

Constraints

The simulations demonstrated the feasibility of the new detection system. The next step was the realization and implementation at ISOLTRAP. One main concern about ion detectors is the vacuum, *i.e.* not to lose the ions due to charge exchange with the residual gas molecules.

Space constraints are the most critical challenge. ISOLTRAP is the highest experiment in the ISOLDE experimental hall. In order to give access to heavy objects, like cryogenic dewars or shielding material, a bridge crane is used. Due to the space constraints of the crane only few elements can be added or changed at the present experimental setup. Therefore it was decided to save as much space as possible while proceeding to the exchange of the detector system. The former TOF-end MCP detector was located in a CF-100 double cross. In order to design a movable drift tube with an attached MCP system in addition to the Channeltron detection device, a larger cross (CF-150) would have been suitable. Unfortunately, due to space constraints, especially to allow the filling of the magnet dewar with liquid helium, it was decided to stay with a CF-100 cross. The system composed of the Channeltron detector, the movable additional drift tube, and a spare MCP had to be fitted in this CF-100 double cross. In order to do so, the shape of each part of the new detection scheme has been optimized, especially the MCP-tube holder (Fig. D.11 and Fig. D.12), and designed to fit the space requirement of the setup.

A direct consequence of the lack of space in the cross concerns the insulation of the different electrodes. The new drift tube has to hold a 1 kV high voltage and the detector up to 4 kV (2 kV for the MCP and 4 kV for the Channeltron, see Tab. 6.2). In order to avoid sparks in this double cross system, sharp edges have been avoided as much as possible. Moreover, insulation material such as Kapton layers and aluminium oxide ceramics Al_2O_3 have been used in order to isolate the different electrodes against each other.

The use of the insulating material leads to another concern, which is the vacuum in the double cross cavity. Again, due to space constraints and the residual magnetic field from the 5.9 T superconducting magnet of ISOLTRAP, only a single 210 l/h turbo molecular pump is used for pumping the detection part down to the trap itself. Although in this section of the ISOLTRAP setup no notable residual gas is present, this represents a large (and crowded) volume for such a small pump. One of the main drawbacks of using insulators is the outgasing. Macor ceramics are known to be better for vacuum than Al_2O_3, but unfortunately they are by far much more fragile and would not have supported the stress applied. Most of the setup has been also designed with respect to this vacuum constraint:

the drift tube and the detector holders are made of Oxygen-Free electronic grade Copper (OFE) and special vacuum aluminium, respectively.

Another point that has been taken into account for the design of the new setup is the remaining magnetic stray field from the superconducting magnet. Any magnetic parts have been avoided in order not to disturb the magnetic fringe field. All screws and washers used to assemble the detection system and especially the CF-flanges (Stainless steel 316LN EFR / 1.4429ESU [Caburn*]) are made of low-magnetic permeability material ($\mu_{\mathrm{M}} < 1.005$ [Caburn*]).

Technical drawings

All those constraints have been taken into account in the design of the new detection system. To avoid any unforeseen problems during the assembly of the system, each element has been designed and reproduced with an appropriate 3D-CAD engineering design software. As an example, the 3D-view of the Channeltron detector is shown in Fig. 6.17. Figures 6.18 and 6.19 show the new detection system using the Channeltron detector and the backup MCP, respectively. Note that not all the devices, such as blind flanges or the turbo pump are represented in order to make the pictures more readable.

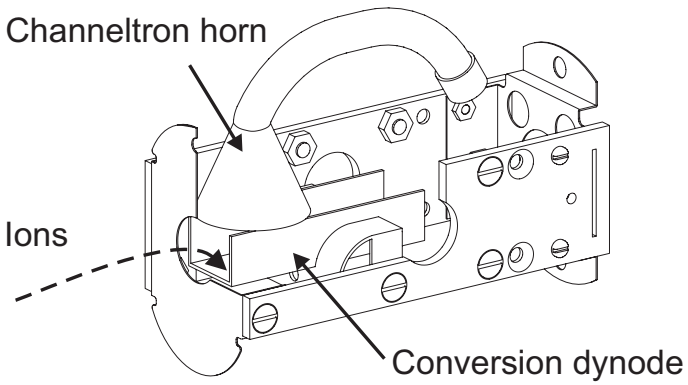

FIGURE 6.17: *3D-view of the Channeltron detector.*

The complete set of technical drawings and pictures of the detector setup is given in Appendix D. The system has been slightly modified to build a copy for the future FT-ICR (Fourier Transform Ion Cyclotron Resonance) experiment at Mainz, later to be moved to SHIPTRAP. The same drawings have been scaled to fit into a CF-150 double cross. Most of the parts are identical, only the zero-length adaptation flanges, the drift tube and the Channeltron holders have been adapted for a larger cross and the design of the MCP–tube holder has been considerably simplified thanks to the larger volume available.

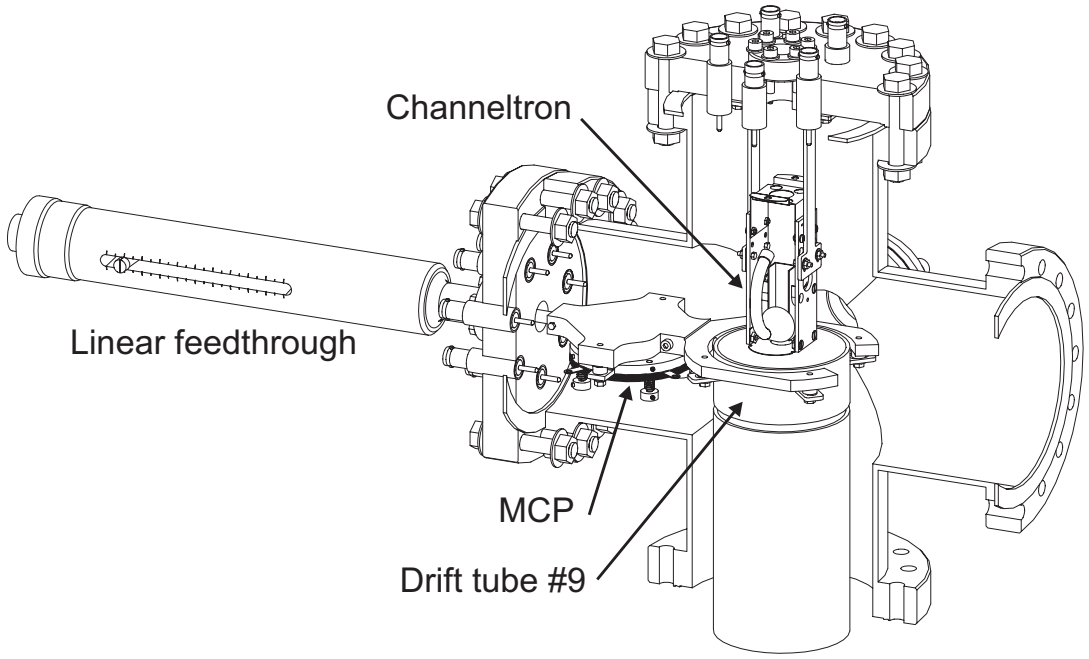

FIGURE 6.18: *New double detector system: Channeltron mode.*

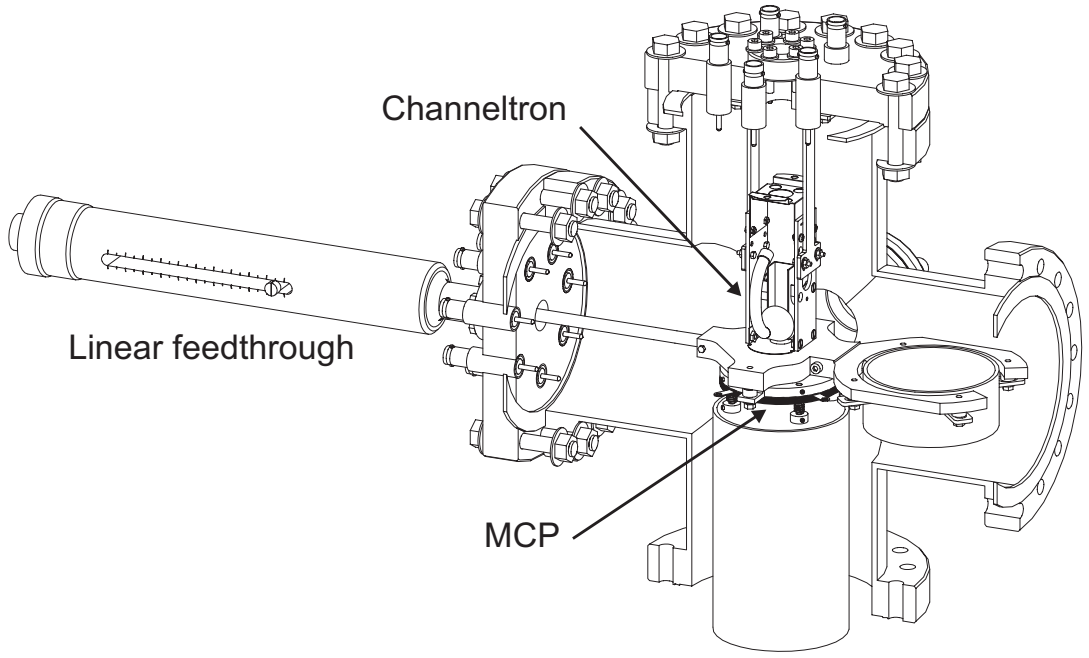

FIGURE 6.19: *New double detector system: MCP mode.*

Electrical connections

One of the last points before the implementation of the new detection system at ISOLTRAP was the connection for the high voltage supply of the detectors and the shaping of the signal from the detectors.

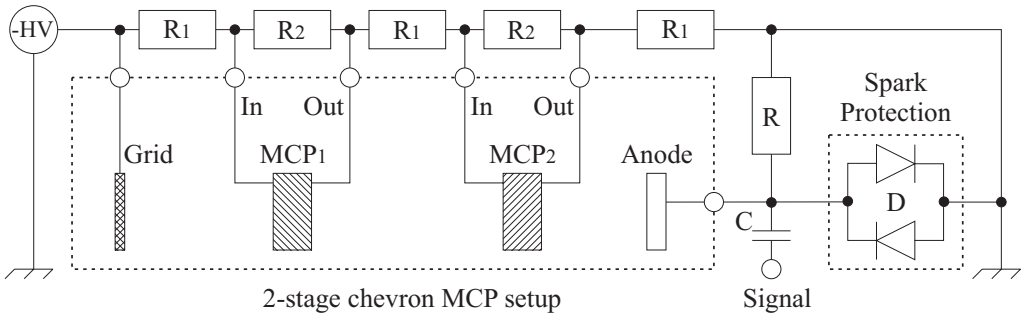

FIGURE 6.20: *Electrical scheme for a 2-stage Chevron MCP. The values of the voltage divider resistors are* $R_1 = 100\ k\Omega$ *and* $R_2 = 1\ M\Omega$*. For the spark protection, D are high-speed switching, low capacitance (2 pF) diodes of type 1N4151 [Phill99*]. The signal is collected after the blocking capacitor* $C = 470\ pF$ *protected by a resistor* $R = 1\ M\Omega$*. High voltage resistors are used.*

The different electrodes of the Channeltron (the aperture plate, the dynode, and the horn) have separate connections. Therefore, special security high voltage SHV connectors have been welded to the flange of the Channeltron part, in order to apply the voltages. The MCP detector is a Chevron (or V-Stack) MPCs system, which means the detector is a combination of two MCPs with the bias angles aligned to 180° in order to improve the secondary electron detection and production. To apply the voltages to such a system, a brute force solution is to connect the front part of the first MCP to the HV, the back side is then connected to the front side of the second MCP, whose back is connected to ground. This simple system allows to save power supplies, since only one power supply is needed to apply the voltage on the MCP setup. However, in case a spark occurs, or if the power supply trips, both MCPs can be damaged. The proposed solution is to connect the MCPs to a simple resistor chain in order to get the desired voltage.

One possibility could have been to directly solder the resistors to the electrodes in the vacuum. To avoid outgasing, an external box with SHV connectors has been designed (see Fig. 6.20). Another advantage of the proposed electric scheme is that between the first and second MCP as well as between the second MCP and the anode, the electrons are given a slight acceleration, which is experimentally known to increase the signal detection. The signal is then directed to a standard instrumentation scheme composed of an amplifier (*Lecroy 612A*) and a discriminator (*Lecroy 623B*, signal shaper) [Eide04].

6.3.2 Results and efficiency gain

The different parts (MCP and Channeltron, respectively) of the new detection system have been implemented at the ISOLTRAP experiment in two steps. Each of the 'plug and play' modules have been mounted at the experiment without any unexpected problems, and everything went as initially planned.

First, the old double MCP setup was removed and the new MCP–drift tube combination mounted instead. It was installed in the beginning of April 2005, and after a few hours of pumping, a vacuum of a few times 10^{-7} mbar was reached. The dark count rate of the MCP detector has been measured to be 0.03 counts/shot, and was significant even for different threshold values of the discriminator. The reason for these dark counts was a cold cathode Penning gauge, which produces electrons by ionization of residual gas to measure the quality of the vacuum in the double cross section. Since this gauge is located relatively close to the MCP detector, residual electron-ionized particles were detected on the MCP as dark counts. In addition to unplugging the gauge, window flanges have been covered to avoid unwanted signals coming from incident photon detection on the MCP. Within a few days of pumping a vacuum in the order of $2{\cdot}10^{-8}$ mbar was reached, and the dark count rate of the MCP decreased to less than 5‰. This result is in good agreement with the value given in Tab. 6.1 taking into account the two orders of magnitude better vacuum.

The Channeltron setup has been installed shortly after testing the MCP (beginning of June 2005). Within one day of pumping, the pressure in the cross reached $2{\cdot}10^{-7}$ mbar and after one week it reached the ISOLTRAP nominal vacuum pressure of close to $1{\cdot}10^{-8}$ mbar. To test the count rate of the Channeltron, the above-mentioned Penning gauge was unplugged. No dark counts were observed on the Channeltron (less than 10^{-4} count/shot).

The second part of the tests focussed on the ion beam tuning from the trap to the Channeltron. Since there is only a small difference between the old detection system and the newly designed setup while using the MCP-mode (see Fig. 6.19), the settings did not need to be changed and similar count rates as with the former setup have been measured. In fact, a slight increase in the count rate by a factor of 1.2–1.3 has been observed, and is the result of using a new Chevron (or V-stack) MCP (detection efficiency estimated from 30 to 35% [Breh95, Ober97]) instead of the older MCPs, for which the efficiency has dropped within the last years (detection efficiency estimated to be 25%).

To test and optimize the focussing of the beam onto the dynode and the detection with the Channeltron, the voltages from the simulations (see Tab. 6.6) have been applied to the corresponding electrodes and fine tuning was performed around those values. No important changes have been observed between the simulations and the experimental values.

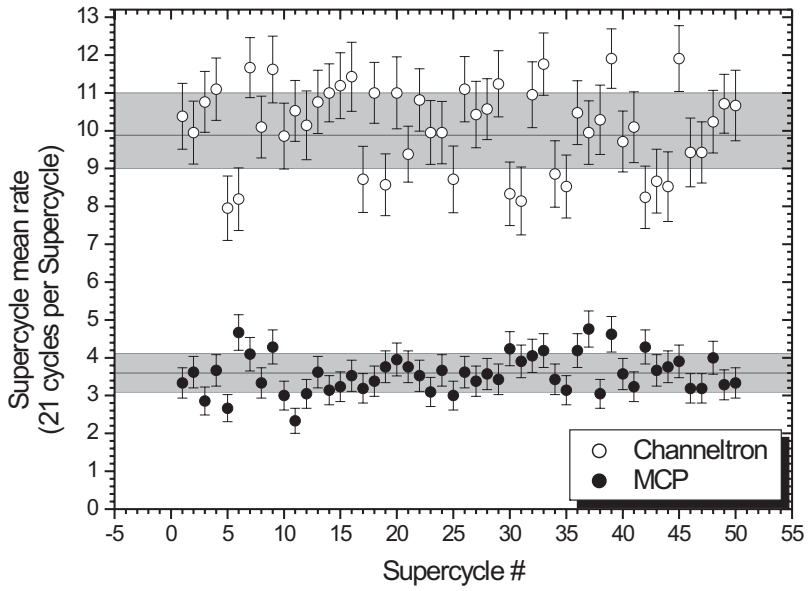

FIGURE 6.21: *Comparison of the detection efficiency of the MCP and Channeltron setup at* ISOLTRAP.

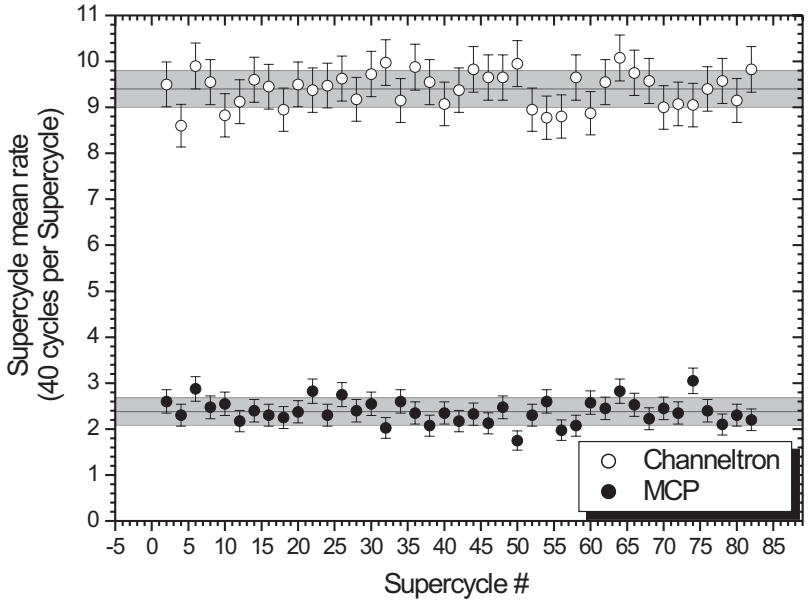

FIGURE 6.22: *Comparison of the detection efficiency of the MCP and Channeltron setup at Mainz.*

In order to compare the ion detection efficiency, the ISOLTRAP experiment has been optimized as described in Appendix B but using the Channeltron detector. Afterwards, the mean count rate for a given accumulation time in the buncher was measured. It has to be emphasized at this point that the ion production from the ISOLTRAP off-line alkali ion source is not stable. The ionization of the sample is done by heating an oven containing alkali metal powder (Zeolith) and W wires for surface ionization. Thus, the ion production depends on the temperature of the oven and unfortunately fluctuates. To average those fluctuations, the collection of the ions has been split into two parts.

A 'cycle' corresponds to a standard measurement procedure of ISOLTRAP, starting from ion accumulation in the RFQ-buncher to the TOF-end detector. A 'supercycle' is the accumulation of a given number of ion shots (*i.e.* an accumulation of 'cycles'). For each 'supercycle' the mean value of the ion count rate and the corresponding uncertainties have been recorded in order to smooth the fluctuations of the ion production. A series of measurements of the mean ion count rate has been performed under the same experimental conditions using the MCP detector and the Channeltron.

The plots presented in Fig. 6.21 for the ISOLTRAP experiment and in Fig. 6.22 at Mainz, respectively, show the mean ion count rate per 'supercycle'. The ratio between the count rate measured with the Channeltron and with the MCP gives the detection efficiency gain reached with the new setup. The experimental values for ISOLTRAP lead to a detection efficiency gain of 2.8 (5), and to a factor of 3.8 (7) for the Mainz experiment. Assuming a detection efficiency of 90% for the Channeltron detector (see Fig. 6.2), the absolute detection of the MCP detector can be estimated. For the ISOLTRAP MCP setup, the efficiency is estimated to be 30%, which perfectly agrees with the commonly agreed detection efficiency of a MCP [Breh95, Ober97]. Concerning the absolute detection efficiency at Mainz, it can be estimated to be 25%. Even if the MCPs used for the Mainz setup are new, a detection efficiency drop can occur if the MCPs bias angles is not 180° opposite for the Chevron configuration. For more details on the Mainz setup and experiment see [Ferr07*].

Chapter 7

Mass measurements on short-lived potassium isotopes[1]

For the production of the radioactive potassium isotopes a Ti-foil target type was used. It consists of a series of thin Ti-foils (30 μm each) for a total thickness of 19 g·cm^{-2} and a quantity of 50.1 g of Ti. Traces of Ca, Fe, C, F and Mo were also present in the target material. Impinging 1.4-GeV protons from the CERN Proton-Synchrotron Booster on the ISOLDE target produced the radioactive potassium isotopes, which were surface ionized using a hot W ionizer. The target was heated to 1500°C, and the transfer line to 2000°C. The potassium ions were then accelerated to 60 kV and delivered to the ISOLTRAP experiment via the HRS separator.

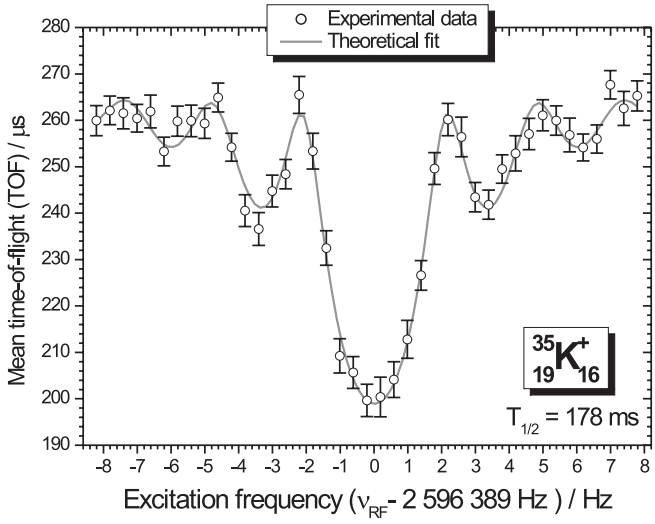

FIGURE 7.1: *Typical Time-of-flight cyclotron resonance for the radioactive $^{35}K^{+}$ ions. The quadrupolar excitation time was T_{RF}=300ms.*

[1]This section is mainly taken from [Yazi07].

During three days, the isotopic chain of potassium has been explored from ^{35}K for the neutron-deficient side, up to ^{46}K for the neutron-rich side. A total of 29 exploitable cyclotron resonances for radioactive potassium isotopes (as shown in Fig. 7.1 for $^{35}K^{+}$) have been recorded, together with 39 resonances of $^{39}K^{+}$, which was used as a reference. No ion contamination has been observed during the beam time (see resonance curves given in Appendix E). In the following, the procedure for the data analysis and the mass determination will be described in detail, and the results for the ^{35}K mass as well as the consequences for the quadratic form of the IMME are discussed.

7.1 Evaluation of the experimental data

7.1.1 Analysis procedure

From raw data to absolute mass and mass excess determination

Notation:

- For $y = f(\{x_i\})$, the law of propagation of the uncertainty is given by:

$$\sigma^2(y) = \sum_{i=1}^{N} \left(\frac{\partial f}{\partial x_i} \right)^2 \sigma^2(x_i) + 2 \sum_{i=1}^{N-1} \sum_{j<i}^{N} \frac{\partial f}{\partial x_i} \frac{\partial f}{\partial x_j} \mathrm{cov}(x_i, x_j). \qquad (7.1)$$

  In the following, the variables are supposed to be independent, thus the correlation part will be omitted. A detailed approach taking into account correlations can be found in Appendix A of [Hage04].

- Estimated values are noted with a hat: $\widehat{x}$
- Corrected values are noted with a tilde: $\widetilde{x}$
- For all following equations the masses M_{i} and mass excess values ME_{i} are expressed in 'atomic mass unit' (u)[2] if not mentioned otherwise.

Numerical applications are given for the ^{35}K run of the present work.

Mainly due to a flux creep (linear decrease) and a temperature dependence, the small fluctuations of the magnetic field, and therefore of the frequencies, have to be considered in the analysis. Getting the mass ratio between a nuclide of interest and the reference implies having the same magnetic field or measuring both investigated and reference ion at the same time in the Penning trap. For technical reasons at ISOLTRAP, the magnetic field

[2] As explained in [Audi06], 'u' should be used instead the erroneous notation a.m.u. For this part, in order not to confuse people, the author uses 'u' as the unit, and '$\mathcal{U} \pm \sigma(\mathcal{U})$' its value and associated uncertainty in keV.

TABLE 7.1: *Raw data from the ^{35}K experiment.*
The frequencies are determined according to the method described in Appendix A.

Type	#	Isotope	File #	Time 08/05/2004	T_{RF} / ms	ν_{c} / Hz
Ref.	1a	^{39}K	149	00:22	900	2331460.087 (0.012)
Meas.	1b	^{35}K	150	01:09	300	2596389.002 (0.070)
Ref.	1c	^{39}K	151	02:00	900	2331460.074 (0.013)
Ref.	2a	^{39}K	153	02:56	900	2331460.090 (0.013)
Meas.	2b	^{35}K	154	03:45	400	2596388.996 (0.065)
Ref.	2c	^{39}K	155	04:39	900	2331460.106 (0.018)
Ref.	3a	^{39}K	157	05:25	900	2331460.096 (0.014)
Meas.	3b	^{35}K	158	06:21	400	2596389.073 (0.086)
Ref.	3c	^{39}K	159	07:15	900	2331460.086 (0.010)
Ref.	4a	^{39}K	161	08:02	1200	2331460.087 (0.011)
Meas.	4b	^{35}K	162	08:52	510	2596388.924 (0.055)
Ref.	4c	^{39}K	163	09:43	1200	2331460.077 (0.011)

is linearly interpolated over a short period of time by means of two reference measurements, one before and one after the nuclide of interest (see Tab. 7.1 for ^{35}K). Assuming that the frequency depends on parameters $\nu_{\mathrm{c}}(\{f_i\})$, that depend on time $f_i(t)$, the first order approximation of the frequency $\widehat{\nu}_i$ between two points ν_{i-1} and ν_{i+1} can be expressed as:

$$\widehat{\nu}_i^{\mathrm{ref}} = \nu_{i-1}^{\mathrm{ref}} + \sum_k \frac{\partial \nu\left(\{f_j(t)\}\right)}{\partial f_k(t)} df_k(t)\Big|_{t_{i-1}}^{t_{i+1}} \times (t_i - t_{i-1}) \tag{7.2}$$

$$= \nu_{i+1}^{\mathrm{ref}} + \sum_k \frac{\partial \nu\left(\{f_j(t)\}\right)}{\partial f_k(t)} df_k(t)\Big|_{t_{i-1}}^{t_{i+1}} \times (t_i - t_{i+1}) \tag{7.3}$$

$$= \overline{\nu}^{\mathrm{ref}} + \sum_k \frac{\partial \nu\left(\{f_j(t)\}\right)}{\partial f_k(t)} df_k(t)\Big|_{t_{i-1}}^{t_{i+1}} \times (t_i - \overline{t}). \tag{7.4}$$

The first equation Eq. (7.2) takes the ν_{i-1} at t_{i-1} as the origin of the interpolation whereas the second one Eq. (7.3) takes ν_{i+1} at t_{i+1}. The last equation Eq. (7.4) considers the origin being the mid point $\overline{\nu}^{\mathrm{ref}} = (\nu_{i+1}^{\mathrm{ref}} + \nu_{i-1}^{\mathrm{ref}})/2$ taken as being the mean frequency at $\overline{t} = (t_{i+1} + t_{i-1})/2$.

Assuming small variations of the frequency $\delta\nu^{\mathrm{ref}}/\delta t = (\nu^{\mathrm{ref}}_{i+1} - \nu^{\mathrm{ref}}_{i-1})/(t_{i+1} - t_{i-1})$ between t_{i-1} and t_{i+1}, the last equation Eq. (7.4) can be rewritten as:

$$\widehat{\nu}^{\mathrm{ref}}_i \simeq \overline{\nu}^{\mathrm{ref}} + \left.\frac{\delta\nu^{\mathrm{ref}}}{\delta t}\right|_{t_{i-1}}^{t_{i+1}} \times (t_i - \overline{t}). \tag{7.5}$$

The former equation implies that the measurement is taken exactly at $\overline{t}$, which is not always the case. To correct for this, another form of the parametrization is used. The points ν_{i-1} at t_{i-1} and ν_{i+1} at t_{i+1} are used to interpolate linearly for $\widehat{\nu}_i$ at t_i (see Tab. 7.2 for ^{35}K):

$$\widehat{\nu}^{\mathrm{ref}}_i \simeq \frac{\left(t^{\mathrm{ref}}_{i+1} - t^{\mathrm{ref}}_i\right)\cdot\nu^{\mathrm{ref}}_{i-1} + \left(t^{\mathrm{ref}}_i - t^{\mathrm{ref}}_{i-1}\right)\cdot\nu^{\mathrm{ref}}_{i+1}}{t^{\mathrm{ref}}_{i+1} - t^{\mathrm{ref}}_{i-1}} \tag{7.6}$$

$$\sigma(\widehat{\nu}^{\mathrm{ref}}_i) = \frac{\sqrt{\left(t^{\mathrm{ref}}_{i+1} - t^{\mathrm{ref}}_i\right)^2\cdot\sigma^2(\nu^{\mathrm{ref}}_{i-1}) + \left(t^{\mathrm{ref}}_i - t^{\mathrm{ref}}_{i-1}\right)^2\cdot\sigma^2(\nu^{\mathrm{ref}}_{i+1})}}{t^{\mathrm{ref}}_{i+1} - t^{\mathrm{ref}}_{i-1}} \tag{7.7}$$

TABLE 7.2: *Interpolated reference frequencies for $^{39}K^+$.*

Type #	Isotope	Time 08/05/2004	$\widehat{\nu}_c$ / Hz
$\widehat{\text{Ref.}}$ 1b	^{39}K	01:09	2331460.080 (0.009)
$\widehat{\text{Ref.}}$ 2b	^{39}K	03:45	2331460.098 (0.011)
$\widehat{\text{Ref.}}$ 3b	^{39}K	06:21	2331460.091 (0.009)
$\widehat{\text{Ref.}}$ 4b	^{39}K	08:52	2331460.082 (0.008)

The cyclotron frequency-to-charge ratio r_i can be determined from Eq. (4.5) for each single measurement using the interpolated reference cyclotron frequency. In the general case and with its associated uncertainty, it is written as:

$$r_i = \frac{\widehat{\nu}^{\mathrm{ref}}_i}{\nu^{\mathrm{Nucl}}_i}\cdot\frac{q_{\mathrm{Nucl}}}{q_{\mathrm{ref}}} \tag{7.8}$$

$$\sigma(r_i) = |r_i|\cdot\sqrt{\left(\frac{\sigma(\widehat{\nu}^{\mathrm{ref}}_i)}{\widehat{\nu}^{\mathrm{ref}}_i}\right)^2 + \left(\frac{\sigma(\nu^{\mathrm{Nucl}}_i)}{\nu^{\mathrm{Nucl}}_i}\right)^2}, \tag{7.9}$$

where the q_i are the respective charges of the investigated and the reference ion. Note that here the ratio between the charge of the investigated and reference ion is taken. Therefore, the q_i can be also seen as a dimensionless charge state n_q. Except for special cases of higher charge states as in [Herl06], for a standard ISOLTRAP mass measurement only singly charged ions are used.

A systematic uncertainty corresponding to the magnetic drift with time $\sigma_{\delta \mathrm{B}/\delta \mathrm{t}}$ (as given in [Kell03a][3]) is added in the following way:

$$\widetilde{\sigma}(r_i) = \sqrt{\sigma^2(r_i) + \left(t^{\mathrm{ref}}_{i+1} - t^{\mathrm{ref}}_{i-1}\right)^2 \cdot \sigma^2_{\delta \mathrm{B}/\delta \mathrm{t}} \cdot r_i^2}. \tag{7.10}$$

TABLE 7.3: *Frequency ratios, uncertainties and corrected uncertainties for single measurements of $^{35}K^+$, relative to $^{39}K^+$.*

Type #	Isotope	r_i	$\sigma(r_i)$	$\widetilde{\sigma}(r_i)$
Meas. 1b	^{35}K	0.897962547	24	25
Meas. 2b	^{35}K	0.897962556	23	24
Meas. 3b	^{35}K	0.897962526	30	31
Meas. 4b	^{35}K	0.897962574	19	20

The weighted mean value of the frequency ratios listed (see Tab. 7.3 for ^{35}K) is then expressed as:

$$\begin{aligned} R = \overline{r} &= \frac{\sum\limits_i \frac{r_i}{\widetilde{\sigma}^2(r_i)}}{\sum\limits_i \frac{1}{\widetilde{\sigma}^2(r_i)}} \\ \sigma(R) &= \sqrt{\frac{1}{\sum\limits_i \frac{1}{\widetilde{\sigma}^2(r_i)}}} \\ R\left(^{35}\mathrm{K}^+/^{39}\mathrm{K}^+\right) &= 0.897962556\ (12). \end{aligned} \tag{7.11}$$

The mass M_{Nucl} and mass excess ME_{Nucl} of the ion of interest can be derived from the mean ratio R according to Eq. (4.6). As mentioned previously, for ISOLTRAP the binding energies of the electrons can be neglected (and thus the associated uncertainties). However, for completeness all the terms are given here:

$$M_{\mathrm{Nucl}} = R \cdot \left(M_{\mathrm{ref}} - n_{q_{\mathrm{ref}}} M_{\mathrm{e}^-} - BE^{\mathrm{e}^-}_{\mathrm{ref}}\right) + n_{q_{\mathrm{Nucl}} M_{\mathrm{e}^-}} + BE^{\mathrm{e}^-}_{\mathrm{Nucl}} \tag{7.12}$$

$$\begin{aligned} \sigma^2(M_{\mathrm{Nucl}}) = & \left(M_{\mathrm{ref}} - M_{e^-} - BE^{\mathrm{e}^-}_{\mathrm{ref}}\right)^2 \cdot \sigma^2(R) \\ & + \sigma^2(M_{\mathrm{ref}}) \cdot R^2 \\ & + \sigma^2(M_{e^-}) \cdot \left(n_{q_{\mathrm{Nucl}}} - R \cdot n_{q_{\mathrm{ref}}}\right)^2 \\ & + \sigma^2\left(BE^{\mathrm{e}^-}_{\mathrm{ref}}\right) \cdot R^2 \\ & + \sigma^2\left(BE^{\mathrm{e}^-}_{\mathrm{Nucl}}\right), \end{aligned}$$

[3]The value given in [Kell03a] contains a typo in equation (9) p. 59.
It should read $\frac{\delta B}{\delta t}\frac{1}{B} = -2.30(3)\ 10^{-9}$/h. The value found in this work is $\frac{\delta B}{\delta t}\frac{1}{B} = -1.95(3)\ 10^{-9}$/h, see Section 7.1.2.

where $BE_{\mathrm{x}}^{\mathrm{e}^-} = \sum_{|n_{q\mathrm{x}}|} BE(\mathrm{e}_i^-)$, and $\sigma^2\left(BE_{\mathrm{x}}^{\mathrm{e}^-}\right) = \sum_{|n_{q\mathrm{x}}|} \sigma^2\left(BE(\mathrm{e}_i^-)\right)$.
From this mass value, the mass excess can be calculated with:

$$\begin{aligned} ME_{\mathrm{Nucl}} &= M_{\mathrm{Nucl}} - A_{\mathrm{Nucl}} \\ \sigma(ME_{\mathrm{Nucl}}) &= \sigma(M_{\mathrm{Nucl}}). \end{aligned} \tag{7.13}$$

The values have to be corrected for a mass dependent effect observed in systematic studies with carbon clusters [Kell03a]. A good estimated value of $\widehat{M}_{\mathrm{Nucl}}$ can be taken from Eq. (7.12)[4], since the corrections are usually small. From that statement it is obvious that the estimated mass is correlated to the measurements. But usually an independent estimate from literature tables [AME03] can be used as well. Therefore, the correlations are not taken into account calculating $\widetilde{\sigma}(\widetilde{R})$. Moreover, the uncertainty is computed adding two systematics: the first systematic uncertainty is due to the correction of the mass dependent effect and overestimates any possible correlations, whereas the second one ($\sigma_{\mathrm{Syst}} = 8 \cdot 10^{-9}$ [Kell03a]) contains all remaining (and so far unknown) effects:

$$\widetilde{R} = R + \left(\widehat{M}_{\mathrm{Nucl}} - M_{\mathrm{ref}}\right) \cdot \sigma_{\Delta\mathrm{m}} \cdot R \tag{7.14}$$

$$\begin{aligned} \widetilde{\sigma}^2(\widetilde{R}) = {} & \sigma^2(R) \cdot \left(1 + (\widehat{M}_{\mathrm{Nucl}} - M_{\mathrm{ref}}) \cdot \sigma_{\Delta\mathrm{m}}\right)^2 \\ & + \left(\sigma^2(\widehat{M}_{\mathrm{Nucl}}) + \sigma^2(M_{\mathrm{ref}})\right) \cdot \sigma_{\Delta\mathrm{m}}^2 \cdot R^2 \\ & + \left(\widehat{M}_{\mathrm{Nucl}} - M_{\mathrm{ref}}\right)^2 \cdot \sigma^2(\sigma_{\Delta\mathrm{m}}) \cdot R^2 \\ & + \left(\widehat{M}_{\mathrm{Nucl}} - M_{\mathrm{ref}}\right)^2 \cdot \sigma_{\Delta\mathrm{m}}^2 \cdot R^2 \\ & + \sigma_{\mathrm{Syst}}^2 \cdot R^2 \end{aligned} \tag{7.15}$$

$$\widetilde{R}\left({}^{35}\mathrm{K}^+/{}^{39}\mathrm{K}^+\right) = 0.897962555\,(14).$$

The corrected mass $\widetilde{M}_{\mathrm{Nucl}}$ and mass excess $\widetilde{ME}_{\mathrm{Nucl}}$ of the ion of interest are finally derived from the corrected mean ratio $\widetilde{R}$ similarly to Eq. (7.12):

$$M_{\mathrm{Nucl}} = \widetilde{R} \cdot \left(M_{\mathrm{ref}} - q_{\mathrm{ref}} M_{\mathrm{e}^-} - BE_{\mathrm{ref}}^{\mathrm{e}^-}\right) + q_{\mathrm{Nucl}} M_{\mathrm{e}^-} + BE_{\mathrm{Nucl}}^{\mathrm{e}^-} \tag{7.16}$$

$$\begin{aligned} \sigma^2(M_{\mathrm{Nucl}}) = {} & \left(M_{\mathrm{ref}} - M_{e^-} - BE_{\mathrm{ref}}^{\mathrm{e}^-}\right)^2 \cdot \widetilde{\sigma}^2(\widetilde{R}) \\ & + \sigma^2(M_{\mathrm{ref}}) \cdot \widetilde{R}^2 \\ & + \sigma^2(M_{e^-}) \cdot \left(q_{\mathrm{Nucl}} - \widetilde{R} \cdot q_{\mathrm{ref}}\right)^2 \\ & + \sigma^2\left(BE_{\mathrm{ref}}^{\mathrm{e}^-}\right) \cdot \widetilde{R}^2 \\ & + \sigma^2\left(BE_{\mathrm{Nucl}}^{\mathrm{e}^-}\right). \end{aligned}$$

[4]Instead of the estimate $\widehat{M}_{\mathrm{Nucl}}$, the atomic number A (expressed in u) can be used, but depending on the sign of $A - M_{\mathrm{ref}}$, the correction and the uncertainty are slightly underestimated/overestimated.

The corrected mass excess is given by:

$$\begin{aligned} \widetilde{ME}_{\mathrm{Nucl}} &= \widetilde{M}_{\mathrm{Nucl}} - A_{\mathrm{Nucl}} \\ \sigma(\widetilde{ME}_{\mathrm{Nucl}}) &= \sigma(\widetilde{M}_{\mathrm{Nucl}}). \end{aligned} \tag{7.17}$$

The inner uncertainty results from individual uncertainties, whereas the outer uncertainty represents the fluctuations around the mean value. The ratio of both is defined as being the Birge ratio [Birg32], which is equal to the square root of χ^2_n, the reduced χ^2:

$$\sigma^2_{\mathrm{in}} = \frac{1}{\sum\limits_i \frac{1}{\widetilde{\sigma}^2(r_i)}} \qquad \text{and} \qquad \sigma^2_{\mathrm{out}} = \frac{\sum\limits_i \frac{1}{\widetilde{\sigma}^2(r_i)} (r_i - \overline{r})^2}{(n-1)\sum\limits_i \frac{1}{\widetilde{\sigma}^2(r_i)}} \tag{7.18}$$

$$\text{Birge ratio} \quad = \frac{\sigma_{\mathrm{out}}}{\sigma_{\mathrm{in}}} = \quad 0.8, \tag{7.19}$$

where n is the number of measurements, *i.e.* $n-1$ is the degree of freedom of the system. The value obtained for the ^{35}K experiment clearly shows an overestimation of the corrected individual uncertainties $\widetilde{\sigma}(r_i)$ since the Birge ratio is lower than 1.

The results $\{x;\sigma(x)\}$ are given in the atomic mass unit u and can be expressed in keV. Unfortunately, the conversion from u to keV is not without uncertainty, and therefore a standard error propagation has to be used. Assuming that $\mathcal{C}$ is the operation that converts the atomic mass unit (u) to keV, it is writen as $\mathcal{C}$: $1\ \mathrm{u} \mapsto\ \mathcal{U} + \sigma(\mathcal{U})\ \mathrm{keV}$. The value of $\{\mathcal{U};\sigma(\mathcal{U})\}$ according to the different definitions of the keV unit is available in [AME03]. It follows:

$$\begin{aligned} \{x;\sigma(x)\} \quad &\overset{\mathcal{C}}{\longmapsto} \quad \{X;\sigma(X)\} \\ \text{with } X = x\cdot\mathcal{U} \quad &\text{and} \quad \sigma(X) = \sqrt{\mathcal{U}^2\cdot\sigma^2(x) + x^2\cdot\sigma^2(\mathcal{U})}, \end{aligned} \tag{7.20}$$

and

$$\begin{aligned} \{X;\sigma(X)\} \quad &\overset{\mathcal{C}^{-1}}{\longmapsto} \quad \{x;\sigma(x)\} \\ \text{with } x = X/\mathcal{U} \quad &\text{and} \quad \sigma(x) = \sqrt{\left(\sigma^2(X) - x^2\cdot\sigma^2(\mathcal{U})\right)/\mathcal{U}^2}. \end{aligned} \tag{7.21}$$

However, the propagation of errors is usually not a bijective function, which means that in case of composition with other function(s) the results may differ.

Results in u or keV and associated uncertainties

Particular attention should be paid when giving the results in keV. Since the error propagation σ and the conversion $\mathcal{C}$ do not commute, *i.e.* $\sigma_\circ\mathcal{C} \neq \mathcal{C}_\circ\sigma$, results for the uncertainty might differ. In this Section, two methods (shown in Fig. 7.2) for the calculation of the mass and mass excess from the measured frequency ratio as well as the equations presented in the former section will be discussed.

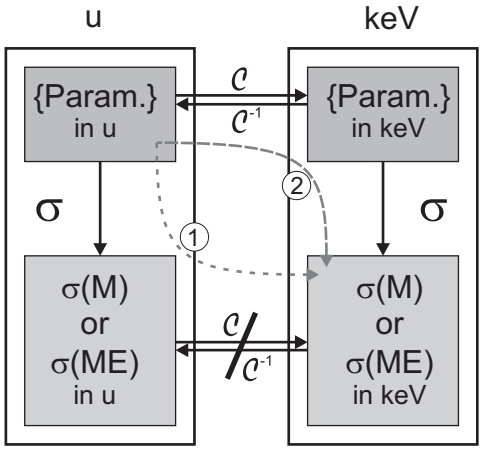

FIGURE 7.2: *Different computational paths from the raw data to the results. Shown are the two spaces in units 'u' and 'keV'. Even if the conversion application is bijective, the error propagation leads to different results according to the computational pathway of Method(1) or Method(2).*

Method (1) gives all results (values and uncertainties) in u first and then converts them to keV with the conversion function $\mathcal{C}$ as described in Eq. (7.20), whereas Method (2) directly takes all values as well as the corresponding uncertainties in keV.

As explained in Eq. (3) of [Audi03b], the values given in the literature include the uncertainty of the atomic-mass unit when expressed in keV. Therefore, for all data taken the uncertainties follow the standard propagation error described by $\mathcal{C}$:

$$\begin{aligned} M_{\mathrm{keV}} &= M_{\mathrm{u}} \cdot \mathcal{U} \\ \sigma^2(M_{\mathrm{keV}}) &= \sigma^2(M_{\mathrm{u}}) \cdot \mathcal{U}^2 + M_{\mathrm{u}}^2 \cdot \sigma^2(\mathcal{U}). \end{aligned} \tag{7.22}$$

From Eq. (7.12) – the demonstration is identical for Eq. (7.16) – and neglecting the binding energies and assuming $q_{\mathrm{ref}} = q_{\mathrm{Nucl}} = \mathrm{e} = 1.602\,176\,463\,(63) \cdot 10^{-19}$ C, the mass and mass excess can be calculated using the two methods:
Method (1):

$$\begin{aligned} M^{\mathrm{u}}_{(1)} &= R \cdot (M^{\mathrm{u}}_{\mathrm{ref}} - M^{\mathrm{u}}_{\mathrm{e^-}}) + M^{\mathrm{u}}_{\mathrm{e^-}} \\ \sigma^2_{(1)}(M^{\mathrm{u}}_{(1)}) &= \sigma^2(R) \cdot (M^{\mathrm{u}}_{\mathrm{ref}} - M^{\mathrm{u}}_{e^-})^2 \\ &\quad +\sigma^2(M^{\mathrm{u}}_{\mathrm{ref}}) \cdot R^2 \\ &\quad +\sigma^2(M^{\mathrm{u}}_{e^-}) \cdot (1-R)^2. \end{aligned} \tag{7.23}$$

The result $\{M^{\mathrm{u}}_{(1)}; \sigma(M^{\mathrm{u}}_{(1)})\}$ in u can be converted in keV using $\mathcal{C}$:

$$\begin{aligned} M^{\mathrm{keV}}_{(1)} &= M^{\mathrm{u}}_{(1)} \cdot \mathcal{U} \\ \sigma^2_{(1)}(M^{\mathrm{keV}}_{(1)}) &= \sigma^2(M^{\mathrm{u}}_{(1)}) \cdot \mathcal{U}^2 + (M^{\mathrm{u}}_{(1)})^2 \cdot \sigma^2(\mathcal{U}). \end{aligned} \tag{7.24}$$

Method (2):

$$\begin{aligned} M^{\mathrm{keV}}_{(2)} &= R\cdot\left(M^{\mathrm{keV}}_{\mathrm{ref}}-M^{\mathrm{keV}}_{\mathrm{e^-}}\right)+M^{\mathrm{keV}}_{\mathrm{e^-}} \\ \sigma^2_{(2)}(M^{\mathrm{keV}}_{(2)}) &= \sigma^2(R)\cdot\left(M^{\mathrm{keV}}_{\mathrm{ref}}-M^{\mathrm{keV}}_{e^-}\right)^2 \\ &\quad +\sigma^2(M^{\mathrm{keV}}_{\mathrm{ref}})\cdot R^2 \\ &\quad +\sigma^2(M^{\mathrm{keV}}_{e^-})\cdot(1-R)^2. \end{aligned} \tag{7.25}$$

The values for the masses are the same for both methods $M^{\mathrm{keV}}_{(1)} = M^{\mathrm{keV}}_{(2)} = M^{\mathrm{keV}}$ (and therefore the values in u: $M^{\mathrm{u}}_{(1)} = M^{\mathrm{u}}_{(2)} = M^{\mathrm{u}}$), but not the uncertainties. Replacing the mass and the uncertainty in keV by their value using Eq. (7.22) gives:

$$\begin{aligned} \sigma^2_{(2)}(M^{\mathrm{keV}}) &= \mathcal{U}^2\cdot\sigma^2_{(1)}(M^{\mathrm{u}}) \\ &\quad +\sigma^2(\mathcal{U})\left((M^{\mathrm{u}}_{\mathrm{ref}})^2\cdot R^2+(M^{\mathrm{u}}_{e^-})^2\cdot(1-R)^2\right). \end{aligned} \tag{7.26}$$

Since for all (a,b) such that $0\le a\le b$, it can be written $a^2+b^2\le(a+b)^2$, the equations (7.24) and (7.26) show that for giving a mass value in keV using Method (1), there is an overestimation of the factor in front of $\sigma^2(\mathcal{U})$. Therefore computing a mass value and its corresponding uncertainty in keV should follow Method 2. To illustrate this, the case of ^{35}K is presented with $\mathcal{U} = 931494.009\ (7)$ keV [AME03]:

$$\begin{aligned} \text{Method (1):}\quad M(^{35}\mathrm{K}) &= 32591117.59\ (59)\ \mathrm{keV} \\ \text{Method (2):}\quad M(^{35}\mathrm{K}) &= 32591117.59\ (58)\ \mathrm{keV}. \end{aligned}$$

However, to give mass excess values, all the computations have to be done first in u and then converted into keV according to Method (1). The reason for this is the uncertainty of the unit u when expressed in keV. The consequence of taking all the masses in keV is an artificial increase of the uncertainty. From the definition of the mass excess it can be written for whatever unit used (indexed by u, keV):

$$ME^{\mathrm{u,keV}} = M^{\mathrm{u,keV}} - \mathscr{A}^{\mathrm{u,keV}} \tag{7.27}$$

Method (1): in u $\quad \sigma^2(ME^{\mathrm{u}}) = \sigma^2(M^{\mathrm{u}})$

applying $\mathcal{C}$ $\quad \sigma^2(ME^{\mathrm{keV}}) = \sigma^2(ME^{\mathrm{u}})\cdot\mathcal{U}^2+(ME^{\mathrm{u}})^2\cdot\sigma^2(\mathcal{U})$ (7.28)

Method (2): $\quad \sigma^2(ME^{\mathrm{keV}}) = \sigma^2(M^{\mathrm{keV}})+A^2\sigma^2(\mathcal{U})$ (7.29)

where $\mathscr{A}$ corresponds to the atomic mass number (A) multiplied by the atomic mass unit expressed in the corresponding unit. It becomes obvious that the uncertainty on $\mathcal{U}$ in keV has no negligible effect on the mass excess when directly computed in keV, since it scales with the atomic mass of the investigated ion, whichever definition of $\sigma^2(M^{\mathrm{keV}})$, Method (1) or (2) is taken. As an example, the corrected mass excess in keV of ^{35}K for both methods are given:

$$\begin{aligned} \text{Method (1):}\quad ME(^{35}\mathrm{K}) &= -11172.73\ (54)\ \mathrm{keV} \\ \text{Method (2):}\quad ME(^{35}\mathrm{K}) &= -11172.73\ (63)\ \mathrm{keV}. \end{aligned}$$

The increase of the uncertainty in the second case is only due to the wrong choice of unit during the calculation. Using u implies no intrinsic uncertainty whereas using directly the values in keV implies hidden correlations: in fact, the corresponding uncertainties for the conversion from u to keV are already included in $\sigma(M^{\mathrm{keV}})$. Therefore, a mass excess value and its corresponding uncertainty has to be computed according to Method (1). This is the reason why in the literature, *e.g.* see [AME03], the mass is expressed in the atomic-mass unit and not in keV.

Another advantage of using Method (1) is that values in keV or in u give equivalent information since the application $\mathcal{C}$ is bijective. Therefore Method (1) should be preferred over Method (2) when calculating both mass and mass excess values, even if for mass calculations (in keV) it leads to a slight increase of the uncertainty compared to Method (2).

7.1.2 Cross-checks of the accuracy of ISOLTRAP

Magnetic field and frequency shifts

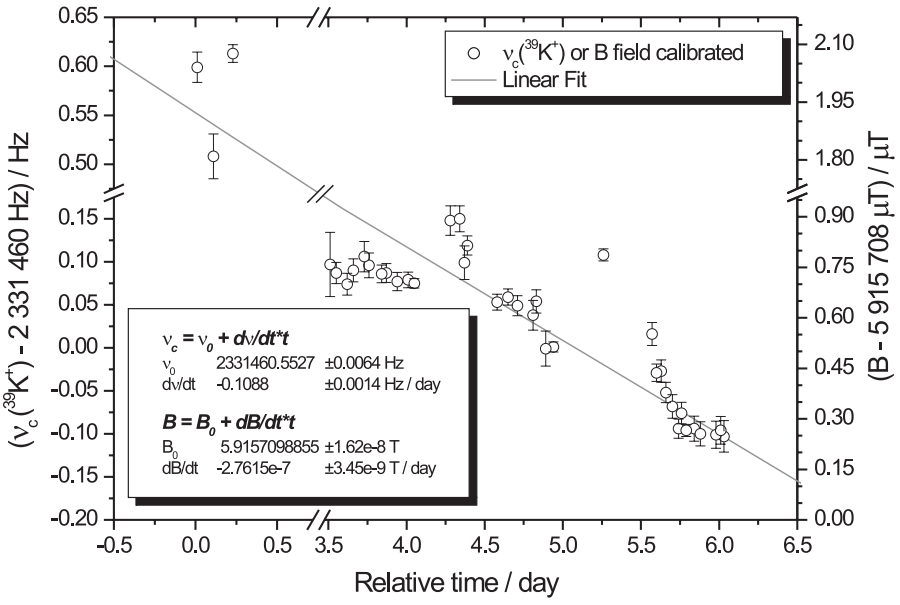

FIGURE 7.3: *Magnetic field or frequency fluctuations for ^{39}K.*

As previously explained in the analysis procedure, one of the most crucial points for the high-precision cyclotron frequency determination is the magnitude and the small variations of the magnetic field during the measurements. In order to validate the mass-determination procedure described in the former section, and especially to quantify the

magnetic drift, the cyclotron frequency of $^{39}K^{+}$ has been plotted as a function of time (see Fig. 7.3). In addition to a linear drift, small oscillations due to a temperature dependence can be observed. The corresponding magnetic field $B = m/q \cdot \omega_c$ has been derived taking the mass of ^{39}K as given in the literature [AME03].
From the linear fit of the data points the following relative drift of the frequency and thus of the magnetic field is calculated:

$$\frac{\delta\nu_c}{\delta t}\frac{1}{\nu_c} = \frac{\delta B}{\delta t}\frac{1}{B} = -1.95(3) \cdot 10^{-9}\ \mathrm{h}^{-1}, \tag{7.30}$$

which almost agrees with the corrected value deduced from systematic studies in [Kell02, Kell03a] (see footnote 2 p105). The difference might be explained by the flux creep $f(t) = 1 - D \ln \frac{t}{\tau}$ ([Kell03a] and references therein), which is not constant over time, and might have changed since the last systematic studies in 2001/2002. Moreover, the larger value might also be explained by the fact that for the study in [Kell03a] the magnetic field value was monitored by measuring a cyclotron resonance every quarter of an hour. In order to reach the same statistics in the reference files, the ion accumulation in the measurement trap has been increased. The careful analysis of the resulting data and frequency-shift correction, as described in the following paragraph, might have contributed to slightly overestimating the slope of the magnetic-field decay. In this work, the references are spread over a larger period, and were not initially meant for a calibration of the magnetic-field decay. Thus the fluctuation of the magnetic field over the few hour period might have led to an underestimation of the slope. Since the temperature stabilization for the magnet cryostat (see Chapter 5) was not implemented at the time when the measurements presented here were performed, the values of the relative decay of the magnetic field has to be investigated again, but remains in the order of 10^{-9} h^{-1} (see Section 5.3.1).

Space charge and ion contamination frequency dependence

In the present work, it has been assumed that the electric potential in the trap is ideal, *i.e.* purely quadrupolar. However, an ion cloud induces image currents in the trap electrodes and therefore perturbs the electric field [Beck01]. Even though the cyclotron frequency is independent of the electric field (under the condition that the field is homogenous), it is sensitive to the number of ions present in the trap and to their local space charge as mentioned in Section 4.3.3.

To investigate and eventually correct for a space charge effect, the data files were analyzed taking into account the number of ions detected in each cycle. For each set of data bins the resonance frequency was determined. From the plot $\nu_c = f(\mathrm{N_{Ions}})$, any ion-count dependence can be observed. The slope of a linear fit gives information on the space charge effect, and the so called Z-class frequency is extrapolated to one single ion in the trap after correction of the detector efficiency [Kell03a].

Not only space charge induces frequency shifts, but a different mass species ion contamination as well. As an example, excited isomeric states, either unknown at the time of the measurement or not possible to resolve with the spectrometer, can induce such an effect [Boll92].

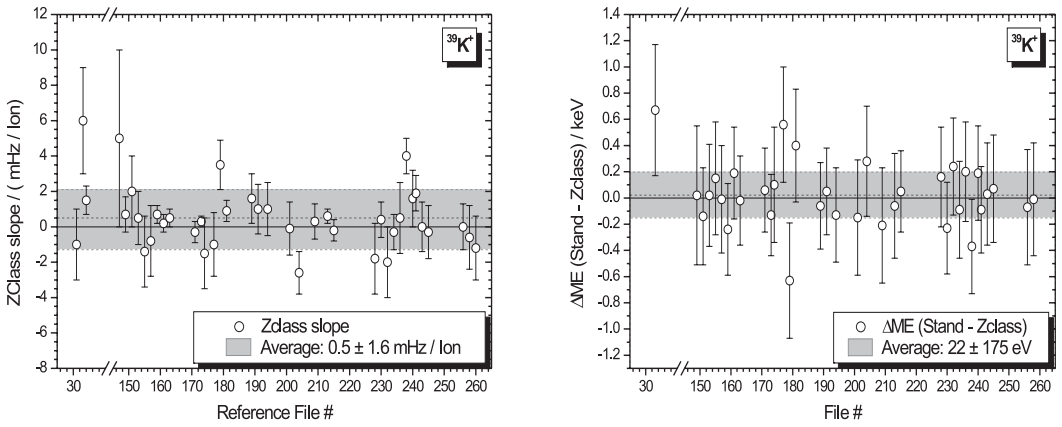

FIGURE 7.4: *Space charge dependance for ^{39}K.*
Left: the slope of the linear trend of the charge space dependency. Right: the frequency difference between standard and Z-class method. For more details see text.

As shown in Fig. 7.4, the Z-class slope for the $^{39}K^{+}$ delivered by the ISOLTRAP off-line ion source is equal to zero within the error bars. This means that not only the stable-isotope beam is not contaminated, but also that if bins with up to a few couple of ions per shot are taken, the frequency determination is not affected. As a comparison, the mass excess calculated with this method and the one which takes all ions into account are plotted. It turns out that the difference is negligible.

All the results presented in this work (Section 7.1.3) are given after such an ion-count-class analysis. As for stable $^{39}K^{+}$, the consequences on the cyclotron frequency, and thus on the mass, for the short-lived isotopes are negligible. Only the uncertainty is affected since the statistical uncertainty increases due to the binning of the data.

Measurements of well-known masses

To check the optimization procedure and the accuracy of the experiment, a mass determination of 'well-known' masses is performed. The aim of this is two-fold: first, as an off-line test, it confirms the accuracy of the spectrometer, and second, during an on-line run it allows to determine any systematic shift and trend of the isotopic chain [Mukh04a].

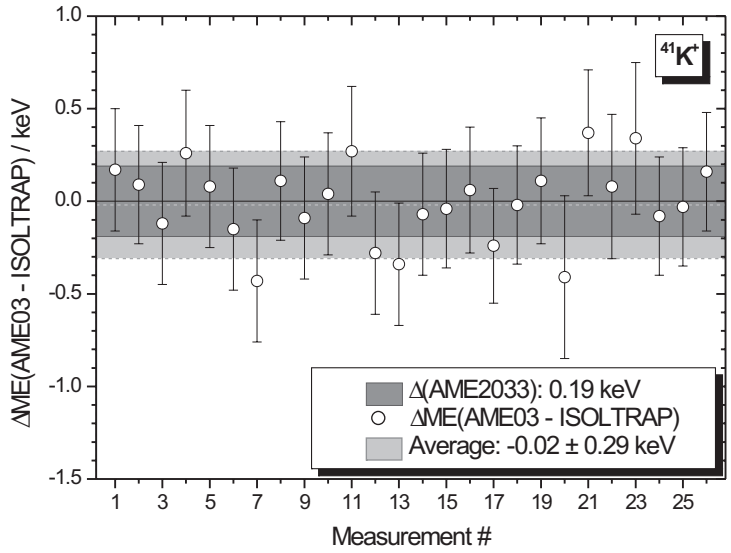

FIGURE 7.5: *Cross-check measurements for $^{41}K^{+}$, with $^{39}K^{+}$ as a reference. The dark gray area represents the uncertainty of the mass given in [AME03], whereas the light gray area gives the precision of the* ISOLTRAP *measurements at the $8 \cdot 10^{-9}$ level.*

As an example, Fig. 7.5 shows for each single file the mass excess for $^{41}K^{+}$ extracted from the data which is compared to the tabulated mass [AME03]. The light gray area gives the precision of the ISOLTRAP measurements at the $8 \cdot 10^{-9}$ level.

7.1.3 Masses of K isotopes

Mass excess values of the investigated potassium isotopes

The analysis procedure explained in the previous section has been used for all the different isotopes of the potassium run. Table 7.4 summarizes the results for the mass excess of the investigated isotopes. The mass determination of potassium isotopes from ^{35}K ($\tau_{1/2}$=178ms) up to ^{46}K ($\tau_{1/2}$=105s) have been performed with a precision of better than $1.6{\cdot}10^{-8}$, which reduces the mass uncertainty in the vicinity of ^{39}K by a factor of up to 40 for the neutron-deficient side (^{35}K) and close to 80 for the neutron-rich potassium isotopes (^{44}K).

The results of the ISOLTRAP measurements are presented in Fig. 7.6 and are compared with the literature values [AME03, NNDC*]. The results for the well-known isotopes ^{37,38,39}K are shown as a cross check for the measurement process and the reliability of ISOLTRAP.

TABLE 7.4: *Frequency ratios relative to $^{39}K^{+}$ and mass excess of potassium isotopes.*

Isotope	$\tau_{1/2}$	Frequency ratio [a] ν_c^{ref}/ν_c	ME_{exp} [b] in keV	ME_{lit} [c] in keV	ΔME lit-exp
^{35}K	178 ms	0.897 962 555 (14)	−11 172.73 (0.54)	−11 168.90 (20.00)	4.12
^{36}K	342 ms	0.923 455 783 (10)	−17 416.83 (0.39)	−17 426.17 (7.78)	−9.56
^{37}K	1.22 s	0.948 917 615 (8)	−24 800.45 (0.35)	−24 800.20 (0.09)	0.25
^{38}K	7.64 m	0.974 472 668 (11)	−28 800.69 (0.45)	−28 800.69 (0.45)	−0.01
^{43}K	22.3 h	1.102 584 812 (11)	−36 575.19 (0.46)	−36 593.24 (8.95)	−17.62
^{44}K	22.1 m	1.128 271 957 (12)	−35 781.29 (0.47)	−35 809.61 (35.78)	−28.71
^{45}K	17.3 m	1.153 914 244 (14)	−36 615.36 (0.56)	−36 608.19 (10.26)	7.36
^{46}K	105 s	1.179 612 626 (20)	−35 413.71 (0.76)	−35 418.32 (15.55)	−4.29

[a] Using $^{39}K^{+}$ as a reference.
[b] M(^{39}K) =38 963 706.68 (0.20) μu [NNDC*], and 1u=931494.009 (7) keV [AME03]
[c] Values from [AME03], http://www.nndc.bnl.gov/masses/mass.mas03.txt.

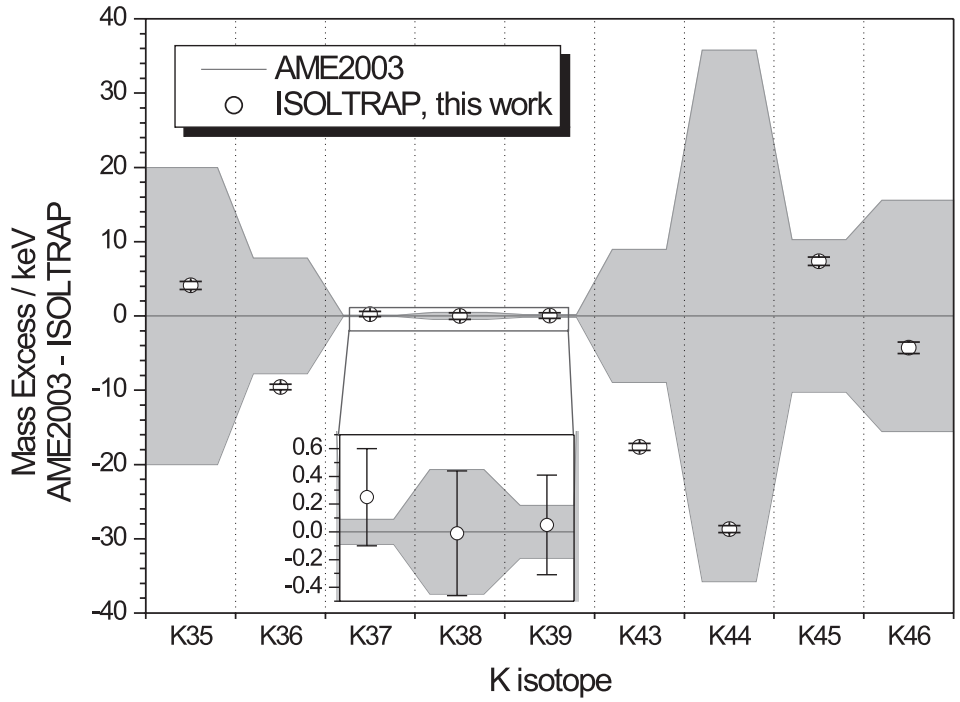

FIGURE 7.6: *Mass excess of the potassium isotopes from this work and literature [AME03]. The mass of ^{39}K is given as a cross-check.*

Application of the new mass values

The mass is one of the fundamental properties of the nucleus, therefore the consequences of mass measurements in physics are manyfold. A brief description of the results for each potassium isotope will be presented in the following paragraphs. The physics case concerning the IMME and the mass of ^{35}K will be further discussed in Section 7.2.

^{35}K: As demonstrated in Chapter 2, the currently adopted relation of the IMME is a quadratic form. However, the approximations and the assumptions for the perturbation by the Coulomb force have failed to describe a few particular cases where higher order terms are needed to fully understand the Coulomb displacement energies between members of a multiplet. At present the $A = 35$, $T = 3/2$ quartet shows a significant deviation from the quadratic form with a cubic term $d = -4.5\ (3.5)$ keV. Since the uncertainty of the quartet is mainly due to the lack of knowledge of the mass of ^{35}K, a high-precision mass measurement of ^{35}K (ME = -11 172.73 (54) keV) as well as a thorough study of all the members of the $A = 35$, $T = 3/2$ quartet have been performed, and the consequences with respect to the quadratic form of the IMME have been analyzed. The detailed discussion is presented in Section 7.2.

^{36,37}K: Accurate experimental mass values serve as a stringent test of nuclear models. As shown in Fig. 7.7, the respective masses of the neutron deficient ^{36,37}K isotopes are crucial for the astrophysical rp-process.

Short-lived radioactive isotopes are created by cataclysmic stellar processes, like an explosion of a star. During this explosive event, nucleosynthesis processes, such as rapid proton capture (rp)-process strongly compete with radioactive β^+ decay. For reliable calculations and understanding of the reactions involved, the masses of the involved exotic nuclides have to be known with high precision and accuracy. The ^{36,37}K isotopes are created during the so-called S-Cl-Ar rp-production cycle, their mass determination will improve the knowledge of the pathway for the low proton number elements [Scha01, Scha06].

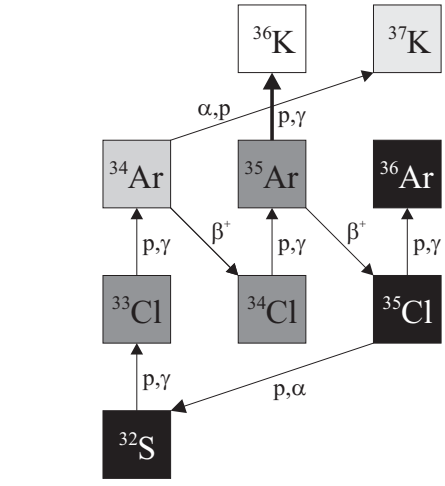

FIGURE 7.7: *The S-Cl-Ar cycle in the rp-process.*

In particular, the case of ^{36}K is important due to the fact that the nucleosynthesis pathway mainly depends on the ^{35}Ar(p,γ)^{36}K reaction [Wies94*]. The discussion is similar

to the one presented in [Mukh04a] for ^{22}Mg. Concerning the case of ^{36}K with a mass excess of ME_{exp} = -17 416.83 (39) keV, a slight discrepancy has been observed with the literature value (ME_{lit} = -17 426.17 (7.78) keV) [Goos71]. The deviation of the literature value is probably due to the fact that the mass of ^{36}K was indirectly measured via the ^{36}Ar(p,n)^{36}K reaction. In addition, the (p, n) calibration measurement have been recalibrated [Free76, Audi05*].
The mass of ^{36}K has also an impact on the IMME check for the $A = 36$, $T = 1$ triplet and $A = 36$, $T = 2$ quintet [Äyst81, Garc95]. As explained in Chapter 2, only n-plets with $n \geq 4$ can give information about higher orders of the IMME. Therefore, the result of the triplet will not be further discussed. The the consequences for the quadratic form of the IMME are presented in Section 7.2 together with the $A = 35$, $T = 3/2$ quartet.

It should be noted that the ISOLTRAP value did not contribute significantly to improve the mass uncertainty of ^{37}K (-24 800.45 (35) keV), since it was already known better than the precision of the experiment performed here: $\sigma(m)/m$ =8·10^{-9}. However, the value presented in this work shows a very good agreement with the adopted mass excess of ^{37}K: -24 800.20 (9) keV [AME03], which gives strong confidence in our data.

^{38}K and ^{38}K^m: The mass value of the $N = Z$-isotope ^{38}K contributes to superallowed β^+-decay studies and tests of the standard model for fundamental physics as *e.g.* the conserved vector current (CVC) hypothesis, and the unitarity of the Cabibbo-Kobayashi-Maskawa (CKM) quark-mixing matrix, as discussed in [Kell02, Kell04a, Mukh04a].

Concerning the superallowed β^+ decay, the excited isomeric state ^{38}K^m (and not the ground state isomer) is involved together with its daughter nuclide ^{38}Ca. The excitation energy between the two isomeric states is well determined – E^m = 130.50 (28) keV – by measuring the internal transition energy of ^{38}K^m(IT)^{38}K, where ^{38}K^m is produced with the ^{38}Ar(p,n)^{38}K^m reaction. The mass determination of either one of the two isomeric states is therefore enough to contribute to a CVC test. In specific radioactive beam preparation and together with resonant laser ionization using RILIS [Köst02], the ISOLTRAP experiment showed its ability to perform pure isomeric mass determination [Roos04]. With an excitation time of $T_{RF} = 900$ ms, the resolving power was about 2·10^6, *i.e.* one order of magnitude higher than needed to resolve the two isomers. Therefore a mixture of both states was not possible. However, in the present work only one of the isomeric states has been observed. For this reason, the resulting mass determination could not be clearly assigned directly to any of the two isomeric states. The excited state ^{38}K^m is shorter lived (924 ms) than the ground state ^{38}K (7.64 m). During the cyclotron frequency determination procedure, radioactive nuclides decay and produce characteristic peaks in the time of flight spectrum, when the total duration of the ISOLTRAP measurement cycle is longer than the half-life of the investigated nuclide. The careful analysis of the cyclotron resonance files performed with an excitation time of 1.2 s (see Appendix E) did not show any

decay peaks. Moreover, the obtained mass value agrees with the literature value of the ground state, therefore it can be concluded that the ground state ^{38}K and not the excited isomeric state was directly measured.

^{39}K: Even though ^{39}K was used as the reference for all potassium measurements, all the backward information flow from the investigated nuclides provided a slight contribution to the mass determination of ^{39}K [Audi05*]. Indeed in [AME03], the mass evaluation from all experimental data is done by solving a system of linear equations. Arising from this method, the so called information-flow matrix represents the contribution of every single mass to the others. In the present work, the mass 'determination' of well-known nuclides as ^{37}K and ^{38}K, for on-line cross references and data consistency, slightly contributes to the ^{39}K mass excess value (ME$_{\mathrm{exp+lit}}$=-33 806.95 (12) keV, instead of ME$_{\mathrm{lit}}$ = -33 807.01 (19) keV [Audi05*]), which is of interest for calibration purposes, since ^{39}K is used as an alkali reference mass in many experimental setups.

^{43,44,45,46}K: 'Magic' proton and neutron numbers are a simple approach to explain shell closure effects and predict local stability of 'magic' isotopes. During the last decades it has been observed that those 'magic' numbers show a strange behavior. They disappear and appear again depending on the proton or neutron number. Those 'wizard' effects have been for example studied in [Guén05a, Guén05b]. In the case of the neutron rich potassium isotopes, the study of a shell closure around $N = 20$, close to the proton $Z = 20$-closed shell, can be investigated by means of the two-neutron separation energy (S_{2n}) plots (see Fig. 7.8). In the neighborhood of the $Z = 20$ shell from ^{37}S to ^{45}Ca, the disintegration energies show a shell effect crossing the magic number [Lind54]. Moreover, with the new mass determination of ^{35}K, and $N = 16$, the possible shell reincarnation at $N = 16$ [Ozaw00, Stan04] can be investigated.

In this work, the mass determination of the neutron-rich side of the potassium isotopes contributes to the improvement of the knowledge close to the $Z = 20$ shell closure and to resolve as well some discrepancies. Previous work [Lind54, Benc59] led to two different mass values for ^{43}K. Thus, the adopted value in [AME03], which results from averaging of those input data, has a large uncertainty ME(^{43}K) = -36 593 (9) keV. The value presented in this work shows a relative discrepancy of a bit more than two standard deviation. However, the adopted values result from indirect mass determination, in this case the β^{-} decay from ^{43}K to ^{43}Ca, and therefore it can not be fully trusted even if well documented [Audi05*].

For the case of $^{44-46}$K, the former investigations on the decay implies large uncertainties, especially in the case of ^{44}K [Ajze70, Levk70]. Concerning the respective cases of ^{45}K and ^{46}K, the uncertainties arising from the reactions ^{46}Ca(t,α)^{45}K and ^{48}Ca(d,α)^{46}K, are in the order of ten keV, moreover they are quite outdated and not well documented (see

[Waps03] and references therein). Given the fact that the measurements presented in this work agree with the literature values and since the respective uncertainties are a factor 20 to 80 times smaller than the ones given in [AME03], discussion about any discrepancies of the data is irrelevant.

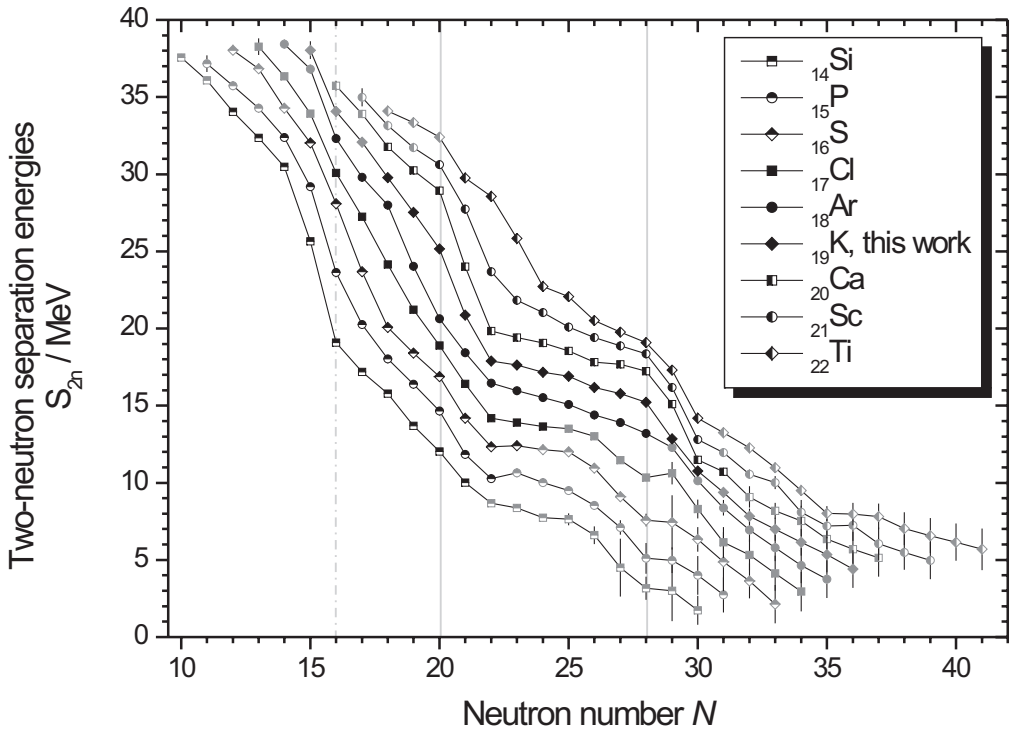

FIGURE 7.8: *Two-neutron separation energies in the neighborhood of K isotopes. The data represented with gray symbols are estimated values from systematic trends, and the uncertainty on the S_{2n} value is larger than 100 keV. The data in black results from experimental data including this work. In the figure the neutron closed shells $N = 20$ and $N = 28$ are shown. The dashed line at $N = 16$ indicates the possible neutron shell reincarnation for neutron-rich isotopes.*

7.2 Test of the IMME

It has been pointed out that the two potassium isotopes ^{35}K and ^{36}K are involved in the $A = 35$, $T = 3/2$ quartet and in the $A = 36$, $T = 1$ triplet, as well as in the $A = 36$, $T = 2$ quintet of IMME, respectively. Therefore, the high-precision mass determination on those two masses contributes to the test of the quadratic form of the IMME by investigating in more detail the quartet and the quintet. In Tab. 7.5 and 7.6, the updated masses

of the multiplets are summarized taking into account the values presented in this work. Unfortunately, to fully contribute to the $A = 36$ quintet, a precise and accurate mass determination of ^{36}Ca ($\tau_{1/2}$ = 102 (2) ms) is still missing. Since this nuclide is within reach of ISOLTRAP from the half-life point of view, further mass measurements for the test of the IMME with respect to the $A = 36$, $T = 2$ quintet are planned.

TABLE 7.5: *Mass Excess for the $A = 35$, $T = 3/2$ quartet.*

Nucleus	T_z	ME^{gs}_{exp} [a] / keV	E^{*}_{exp} [b] / keV	ME^{tot}_{exp} / keV
^{35}K	$-3/2$	$-11\,172.73\ (0.54)$ [c]	—	$-11\,172.73\ (0.54)$
^{35}Ar	$-1/2$	$-23\,047.41\ (0.75)$	$5\,572.71\ (0.17)$	$-17\,474.70\ (0.77)$
^{35}Cl	$1/2$	$-29\,013.54\ (0.04)$	$5\,654\ (2)$	$-23\,359.54\ (2.00)$
^{35}S	$3/2$	$-28\,846.36\ (0.10)$	—	$-28\,846.36\ (0.10)$

[a] Values from [AME03].
[b] Values from [Brit98].
[c] This work.

TABLE 7.6: *Mass Excess for the $A = 36$, $T = 2$ quintet.*

Nucleus	T_z	ME^{gs}_{exp} [a] / keV	E^{*}_{exp} [b] / keV	ME^{tot}_{exp} / keV
^{36}Ca	-2	$-6\,440.00\ (40.00)$	—	$-6\,440.00\ (40.00)$
^{36}K	-1	$-17\,416.83\ (0.39)$ [c]	$4\,282.2\ (2.50)$ [d]	$-13\,137.70\ (2.40)$ [e]
^{36}Ar	0	$-30\,231.54\ (0.03)$ [f]	$10\,851.6\ (1.50)$	$-19\,379.94\ (1.50)$
^{36}Cl	1	$-29\,521.86\ (0.07)$	$4\,299.70\ (0.08)$	$-25\,222.16\ (0.11)$
^{36}S	2	$-30\,664.07\ (0.19)$	—	$-30\,664.07\ (0.19)$

[a] Values from [AME03].
[b] Values from [Endt90, Brit98, Endt98].
[c] This work.
[d] Extracted from the ground state (this work) and the excited state values (see [e])
[e] Value from [Garc95] and corrected for relativistic effect and for the ^{35}Ar mass [AME03].
[f] See Section 7.4 in [Waps03].

From the mass excess values, the coefficients $a,\ b,\ c$ of the quadratic terms and the possible coefficient d of the cubic form of the IMME can be derived. Eq. (2.42) represents the quadratic form of the IMME, and links the mass of the nuclides to their isospin projection T_z. Since the mass excess is only an offset relative to the mass number of a given set of isobars, this equation is also valid for the mass excess. The coefficient a will take care of this difference. The same argument is also valid for higher order terms in the IMME. Therefore, in the following the different coefficients corresponding to the respective quadratic and cubic forms of the IMME are calculated using the mass excess and not the mass of the nuclei.

7.2.1 Fitting the coefficients of the IMME

Assuming a given n-plet of isospin T and its members with isospin projection on the z-axis $\mathbf{T}_\mathrm{z} = \left\{T_\mathrm{z}(k)\right\}_{[\![0;2T]\!]}$, where $n = 2T+1$ and $T_\mathrm{z}(k) = -T+k$, the n-dimensional vector representing the mass values of the n-plet can be written as $\mathbf{Y} = \left\{ME\big(T_\mathrm{z}\,(k)\,\big)\right\}_{[\![0;2T]\!]}$.

Assuming a given polynomial order m for the IMME and a given isospin projection T_z such as:

$$M(T_\mathrm{z}) = \sum_{i=0}^{m} x_i \cdot T_\mathrm{z}^i \,, \tag{7.31}$$

the IMME relation between the members of the n-plet can be written as a set of n linear equations, that can be summarized under the following matrix form:

$$\mathbf{Y} = \mathbf{AX}, \tag{7.32}$$

with a set of parameters $\mathbf{X} = \{x_k\}_{[\![0;m]\!]}$ which represent the $m+1$ coefficients of the m degree polynomial form of the IMME, and $\mathbf{A} = \{A_{ik}\}_{[\![0;2T]\!]\times[\![0;m]\!]}$ with $A_{ik} = T_\mathrm{z}(k)^i$ representing the matrix elements of the different powers of the isospin projection.

Since the matrix $\mathbf{A}$ is regular, Eq. (7.32) can be inverted. To derive the parameters for the quartets and the cubic form of the IMME ($m = 3$), in the literature [Bene79, Anto83, Guim03] the cubic $x_3 = d$ term is often taken to be[5]:

$$\begin{aligned} d &= \frac{ME\,(-3/2) - 3ME\,(-1/2) + 3ME\,(1/2) - ME\,(3/2)}{6} \\ \sigma(d) &= \frac{\sigma\big(ME(-3/2)\big) + 3\sigma\big(ME(-1/2)\big) + 3\sigma\big(ME(1/2)\big) + \sigma\big(ME(3/2)\big)}{6}\,, \end{aligned} \tag{7.33}$$

which basically corresponds to the inversion of Eq. (7.32). But it is implicitly assumed that there is no weighing of the input data for the fit. This assumption usually leads to a slight overestimation of the uncertainty of $\sigma(d)$.

Taking into account the symmetric uncertainties on the mass (respectively mass excess) of $\mathbf{Y}$, the linear equation (7.32) becomes ([Linn63] and Appendix 5 of [Audi81]):

$$\mathbf{A}^\top\,\mathbf{WY} = \mathbf{A}^\top\,\mathbf{WAX}, \tag{7.34}$$

where $\mathbf{W} = \{W_{ik}\}_{[\![0;m]\!]\times[\![0;m]\!]}$ with $W_{ik} = \delta_{ik}/\left(\sigma\big(ME(i)\big)\cdot\sigma\big(ME(k)\big)\right)$ and δ_{ik} being the Kronecker delta function.

Eq. (7.34) can be inverted as well since $\mathbf{E} = \mathbf{A}^\top\,\mathbf{WA}$ is a normal (symmetric and regular) matrix:

$$\mathbf{X} = \mathbf{E}^{-1}\,\mathbf{A}^\top\,\mathbf{WY} \tag{7.35}$$

[5]To simplify the notation $ME\big(T_\mathrm{z}\,(k=i)\,\big)$ will be written as $ME\,(i)$

The diagonal elements of $\mathbf{E}^{-1}$ are the squared uncertainties on the adjusted masses, and the non-diagonal terms are the coefficients for the correlations between the parameters.

The results for the $A = 35$, $T = 3/2$ quartet, and the $A = 36$, $T = 2$ quintet, under the assumption of quadratic and cubic form of the IMME, are given in the following Tables 7.7 and 7.8:

TABLE 7.7: *The $A = 35$, $T = 3/2$ quartet and the consequences for the IMME.*

ME(T_z)	a / keV	b / keV	c / keV	d / keV	χ^2_n
Quadratic	-20470.7 (0.8)	-5891.2 (0.2)	205.0 (0.4)	—	8.8
Cubic	-20468.1 (0.2)	-5884.0 (2.4)	203.8 (0.6)	-3.2 (1.1)	—

TABLE 7.8: *The $A = 36$, $T = 2$ quintet and the consequences for the IMME.*

ME(T_z)	a / keV	b / keV	c / keV	d / keV	χ^2_n
Quadratic	-19379.1 (0.7)	-6043.6 (0.8)	200.6 (0.3)	—	0.9
Cubic	-19380.3 (1.5)	-6043.3 (1.1)	202.1 (1.8)	-0.7 (0.8)	1.1

The consequences of the new potassium mass values concerning the IMME are the following: for the cubic term, the $A = 35$ quartet shows a deviation from the quadratic form of the IMME, whereas the $A = 36$ quintet agrees with the adopted form within one standard deviation. In the latest compilation [Brit98], the $A = 35$, $T = 3/2$ quartet was already reported to slightly deviate, and the $A = 36$, $T = 2$ quintet was following the adopted quadratic form with a cubic term equal to $d = -0.56\ (1.62)$ keV. In [Brit98] the reduced χ^2 for the quintet is close to 3, and therefore indicates a probable non-consistent set of data.

However, if the two cases presented in this work are compared, it can be observed that for the $A = 35$ quartet none of the coefficients of the quadratic form agrees within one standard deviation with the corresponding coefficient value for the cubic form. This clearly indicates a strong discrepancy and is an argument in favor of using higher terms to describe the IMME. In the case of the $A = 36$ quintet, which now shows no deviation within a standard deviation, the uncertainties on the coefficients are larger and almost all the coefficients agree with the corresponding one. The reason for the larger uncertainties and the data agreement is the lack of knowledge of the ground state of ^{36}Ca. Until a new high precision mass measurement is performed, no final conclusions about the validity of the quadratic form in case of the quintet can be drawn. However assuming the quadratic form of the IMME being valid for the $A = 36$, $T = 2$ quintet, the mass value of ^{36}Ca can

be extrapolated from the other members of the multiplet. In this case the estimate of the ^{36}Ca mass excess is ME_{IMME}=-6490.3 (6) keV. This value slightly deviates (1.25σ) from the previously adopted value [AME03] but has close to two orders of magnitude smaller uncertainty.

Thus, the following section is only focussed on the 3 standard uncertainty deviation from the quadratic form of the IMME for the $A = 35$, $T = 3/2$ quartet, investigating and discussing the different sources of the deviation. The updated plot for the cubic term of the IMME and their associated uncertainty is given in Fig. 7.9.

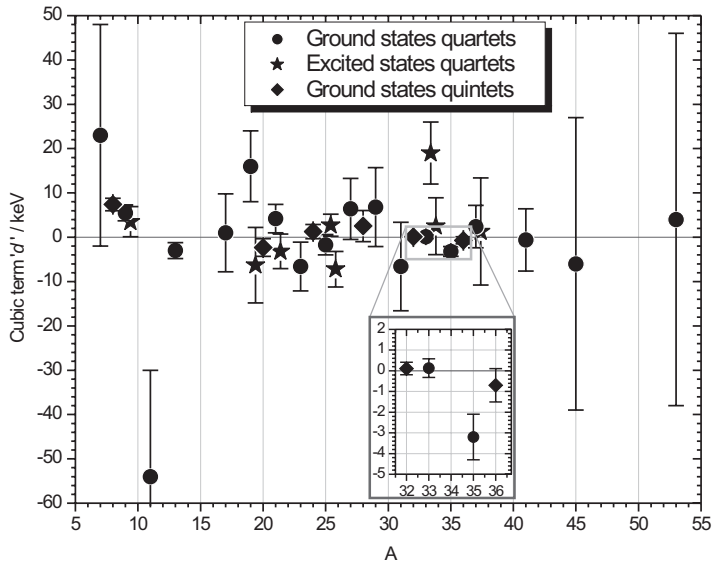

FIGURE 7.9: *Updated compilation of the deduced coefficient d of the cubic term for quartets, including this work.*
The four points shown in the inset correspond to the $A = 33$ and $A = 35$ quartets, and $A = 32$ and $A = 36$ quintets for which at least one member has been measured at ISOLTRAP *[Herf01a, Blau03a]. The two points on the right hand side of the inset, i.e. the $A = 35$ quartet and the $A = 36$ quintet, arise from the work presented here.*

7.2.2 Checking the data for the IMME

The results given in Tab. 7.7 show a discrepancy for the $A = 35$, $T = 3/2$ quartet from the quadratic form of the IMME. In order to better understand the reasons of the deviation and to find out the responsible causes of the higher order terms in the IMME (if any), it will be assumed in a first step that the quadratic form of the IMME is correct and one (or more) of the masses involved exhibit a systematic shift, or the excited states are wrongly assigned.

In the case of a quartet, six input values are taken into account for the IMME: four ground state masses and two excitation energies for the $T_z = \pm 1/2$-intermediate states. To look for evidence of any deviation for the adopted values, the IMME and other analytic procedures are applied.

Assuming a quadratic form of the IMME

As compared to usually diverging global mass prediction models, *e.g.* [Coma88, Jäne88, Mass88, Möll88, Tach88, Gori01], local theories such as IMME are known to provide much more accurate predictions with uncertainties as low as a few keV. In fact, one of the main interests of studying the IMME is the mass prediction of one unknown member of a given multiplet, which is especially of interest for reliable calculations in nuclear astrophysics. If the IMME is a m-degree polynomial form, then from the mass excess of $m+1$ members of a n-plet with $n > m+1$, the mass of the $n-m-1$ unknown masses can be deduced.

Direct mass determination: In the following paragraph it is assumed that only one of the four mass excess values (and excitation energies) is wrongly assigned or unknown. Respectively in Tab. 7.9 and Tab. 7.10 the different mass excess predictions of the supposedly 'unknown' nuclides are shown, respectively from direct mass calculation and from the fit parameters given in Tab. 7.7.

TABLE 7.9: *Mass prediction assuming a quadratic form of the IMME.*

Nucleus	ME^{tot}_{cal} in keV	$ME^{tot}_{cal} - ME^{tot}_{lit}$ in keV	E^{*}_{cal} in keV
^{35}K	$-11191.8\ (6.5)$	$-19.2\ (6.5)$	—
^{35}Ar	$-17468.3\ (2.8)$	$6.4\ (2.9)$	$5579.1\ (2.9)$
^{35}Cl	$-23365.9\ (0.8)$	$-6.4\ (2.2)$	$5647.6\ (0.8)$
^{35}S	$-28827.2\ (6.5)$	$19.2\ (6.5)$	—

The drawback of this method is that only the mass excess of the isobaric analog state (IAS) can be predicted, *i.e.* the mass excess of the ground states for the $T_z = \pm 3/2$ members and the sum of the ground state and excitation energy for the other members. The estimated excitation energy is given under the assumption that the mass of the ground state is equal to the value in [AME03], including the uncertainty.

The results in Tab. 7.9 show a deviation for all nuclides. This is explained, since it is assumed that one of the masses of the quartet is wrong. In the following $C_{k[\![1;4]\!]}$ are the correct values of the quartet and $W_{k[\![1;4]\!]}$ the wrong masses corresponding to C_k. It is assumed that the given quartet includes a set of masses as $\{C_i; C_j; C_k; W_l\}$ where

the (i, j, k, l) are all different and take their values in $[\![1; 4]\!]$. Three out of the four mass predictions $W_{k[\![1;3]\!]}$ corresponding to $C_{k[\![1;3]\!]}$ are inaccurate since they are deduced from a set of data including the wrong mass $\{C_i; C_j; W_l\}$. The last one will show a deviation too, but for the opposite reason: it is the 'correct' mass extrapolation of C_l corresponding to W_l (found in the literature) and calculated from $\{C_i; C_j; C_k\}$. Therefore no conclusion can be drawn concerning the wrong candidate. However, it can be observed that the 'deviation' between [Brit98, AME03] and the prediction increases proportionally to $|T_z|$, which indicates that the wrong mass could be one of the excited IAS (^{35}Ar or ^{35}Cl).

TABLE 7.10: *Mass prediction assuming a quadratic fit.*

$\mathrm{ME}(T_z) = a + bT_z + cT_z^2$			
Nucleus	$\mathrm{ME}^{\mathrm{tot}}_{\mathrm{cal}}$ in keV	$\mathrm{ME}^{\mathrm{tot}}_{\mathrm{cal}} - \mathrm{ME}^{\mathrm{tot}}_{\mathrm{lit}}$ in keV	$\mathrm{E}^{*}_{\mathrm{cal}}$ in keV
^{35}K	$-11172.9\ (1.2)$	$-0.2\ (1.3)$	—
^{35}Ar	$-17473.9\ (0.8)$	$0.8\ (1.1)$	$5573.5\ (1.1)$
^{35}Cl	$-23365.0\ (0.8)$	$-5.5\ (2.1)$	$5648.5\ (0.8)$
^{35}S	$-28846.4\ (1.2)$	$0.0\ (1.2)$	—

Complementary information is provided by Tab. 7.10. The values presented in the table are the mass excess extrapolations using the parameters arising from the quadratic fit. The uncertainty on the calculated values follow from the uncertainty of the parameters a, b, c (see Tab. 7.7). The error of prediction is smaller than the deviation to the literature values of the quartet members except for ^{35}Cl, which is the member with the largest error bars. From the discussion previously drawn, it could have been directly concluded that the wrong candidate is the $T_z = 1/2$ member. However, due to the 2 keV uncertainty on the IAS, it has at least close to seven times less influence than the other members, therefore the fit is biased due to the lack of knowledge on the excited state of ^{35}Cl. Indeed, in the $A = 33$, $T = 3/2$ quartet case and using the same arguments, the 'breakdown' of the IMME [Herf01a, Herf01c] could have been supposed to arise from the ^{33}Ar member, which has the largest uncertainty (4 keV). The 'revalidation' of the IMME [Pyle02] shows that the excited state of the ^{33}Cl was erroneous. Therefore even if those direct mass extrapolation methods seem to indicate a deviation of the excited $T_z = 1/2$ IAS for ^{35}Cl, caution is advised since this chlorine isotope is also the least significant member in the quartet.

Mirror nuclides properties: Among a given multiplet of the IMME, the $\pm T_z$ members are mirror nuclides, *i.e.* the proton number of one is equal to the neutron number of its mirror and vice versa. Assuming a pure quadratic form of the IMME, specific relations between the mirror nuclei-members of the IMME as mirror energy differences (MED) [Zuke02], and mirror energy sums (MES) can be calculated. For a quadratic form of the

IMME, the MED (respectively MES) for mirror nuclides (with isospin projection $\pm T_z$) is given by:

$$MED(T_z) = ME(-T_z) - ME(T_z) = -2bT_z, \quad (7.36)$$

$$\text{and} \quad MES(T_z) = ME(-T_z) + ME(T_z) = 2a + 2cT_z^2. \quad (7.37)$$

Another way to investigate and identify the wrong candidate is to use the Coulomb displacement energy (CDE) for a given mutliplet. It is defined as:

$$CDE(T_z) = ME(T_z + 1) - ME(T_z) \quad (7.38)$$

$$= b + (2T_z + 1)c. \quad (7.39)$$

For mirror nuclei with isospin projection $T_z = \pm 1/2$, a special relation between the two quantities CDE and MED is given by:

$$CDE(T_z) = -MED(T_z), \text{ with } T_z = -1/2. \quad (7.40)$$

Eqs. (7.36) and (7.37) imply a direct relation between the mirror members and the quadratic coefficients of the IMME as summarized in Fig. 7.10.

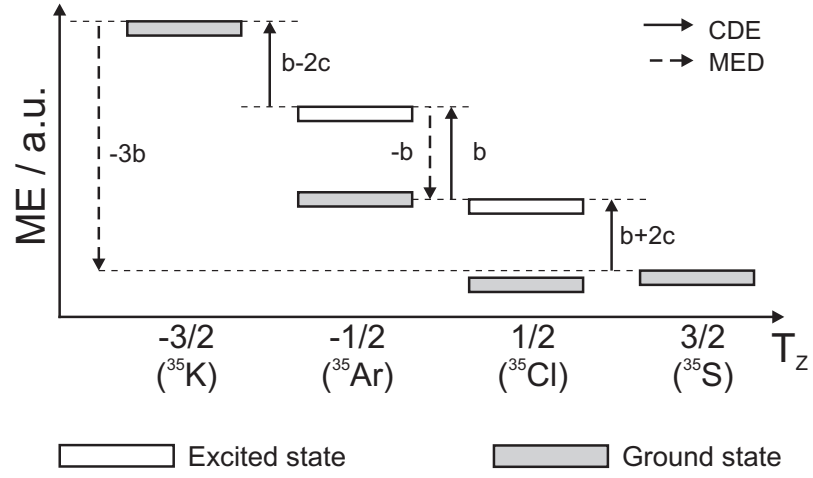

FIGURE 7.10: *Isospin mixing effect for quartets.*
MED and CDE energies are presented in this figure. The values for the MED and CDE are given under the assumption that the quadratic form of the IMME is valid, where b and c are the respective coefficient for the linear and quadratic term in T_z.

The same work and checks as previously studied can also be performed with those tools. Comparing the expected MED, MES, as well as the CDE with the values resulting from the quadratic fit of the $A = 35$, $T = 3/2$ members gives additional information to track the deviating mass or energy.

Tab. 7.11 presents the MED and MES values for the $A = 35$, $T = 3/2$ quartet. For this study, the mass difference and sum of mirror nuclides are compared to the values calculated using the a, b, c coefficients from the quadratic fit. Again the ground state members of the quartet do not show a deviation from the theoretically expected value assuming a quadratic form of the IMME. Concerning the $|T_z|$-members, the discrepancy with the commonly accepted quadratic form are shown.

TABLE 7.11: *Mirror energy difference and sum for the $A = 35$, $T = 3/2$ quartet of the IMME.*

$\mathrm{ME}(T_z) = a + bT_z + cT_z^2$ / in keV			
MED:	[AME03] and this work	From fit	
	ME($-T_z$) $-$ME(T_z)	$-2bT_z$	Δ
^{35}K $-^{35}$S	17673.7 (0.6)	17673.5 (0.6)	0.2
^{35}Ar $-^{35}$Cl	5884.8 (2.1)	5891.2 (2.4)	6.3
MES:	[AME03] and this work	From fit	
	ME($-T_z$) + ME(T_z)	$2a + 2cT_z^2$	Δ
^{35}K $+^{35}$S	$-$40019.0 (0.6)	$-$40019.2 (2.4)	0.2
^{35}Ar $+^{35}$Cl	$-$40834.2 (2.1)	$-$40838.9 (1.6)	4.7

At this point, taking into account the mass extrapolations and results from Tab. 7.9 to 7.11, it can be concluded that one of the two masses of the excited states of the $A = 35$, $T = 3/2$ quartet might be wrong, if the IMME has a pure quadratic form.

It is now possible with the CDE to target the candidate. Every member of the quartet is arbitrarily fixed to the mass value as found in [AME03] and to the value of ^{35}K deduced in the present work. From this starting point the mass of the other members of the quartet are extrapolated according to the CDE relations Eq. (7.38) and Fig. 7.10. The mass difference between experimental values and CDE estimates are given in Tab. 7.12.

TABLE 7.12: *Coulomb displacement energy for the $A = 35$, $T = 3/2$ quartet of the IMME.*

$\mathrm{ME}(T_z) = a + bT_z + cT_z^2$				
	$\mathrm{ME_{Exp}} - \mathrm{ME_{cal}}$ / keV			
Nucleus	$^{35}\mathrm{K_{fixed}}$	$^{35}\mathrm{Ar_{fixed}}$	$^{35}\mathrm{Cl_{fixed}}$	$^{35}\mathrm{S_{fixed}}$
^{35}K	—	0.9 [0.9]	$-$5.4 [2.1]	0.1 [0.5]
^{35}Ar	$-$0.9 [0.9]	—	$-$6.3 [2.1]	$-$0.8 [0.8]
^{35}Cl	5.4 [2.1]	6.3 [2.1]	—	5.5 [2.0]
^{35}S	$-$0.1 [0.5]	0.8 [0.8]	$-$5.5 [2.0]	—

The uncertainties on the mass excess differences between experimental data and theoretical extrapolations are not given since they are strongly correlated to the uncertainty arising from the fit of the quadratic IMME to the experimental data. The values given in brackets correspond to the uncertainty on the mass difference from the experimental data only. Without the ^{35}Cl member the experimental data agree with the extrapolation within one standard deviation. As far as ^{35}Cl is concerned, a mean deviation of about -5.7 (2.1) keV is observed. It can be due to the fact that ^{35}Cl is the member with the largest uncertainty but it is the only nuclide that shows discrepancies of 2.5–3 standard deviations. The IAS of ^{35}Cl used in the IMME is an excited state, therefore the deviation can arise from either the mass excess of the ground state or from the excitation energy.

Excitation energies: The measurements of excited states are given by the study of nuclear collisions and subsequent γ-emission corresponding to the de-excitation of the reaction products. Those collisions are relativistic, therefore a correction should be applied to the energy of the emitted γ. However, those corrections are not taken into account in the literature when giving the energies of the excited states. The aim of this paragraph is to quantify the relativistic correction.

The 4-momentum vector $\mathbf{p} = (E, \vec{p})$ of a particle of mass m is derived from its energy E and its momentum $\vec{p}$. It defines the conservation laws

$$\begin{aligned} \mathbf{p}^2 \equiv E^2 - \|\vec{p}\|^2 c^2 &= m^2 c^4 && (7.41)\\ E &= m_0 c^2 + K && (7.42)\\ &= \gamma m_0 c^2 = m c^2, && (7.43) \end{aligned}$$

where K is the kinetic energy of the particle, m_0 the mass of the particle at rest, and m the relativistic mass given by:

$$\begin{aligned} m &= \gamma m_0 && (7.44)\\ \gamma = \frac{1}{\sqrt{1-\beta^2}} \quad &\text{and} \quad \beta = \|\vec{v}\|/c. && (7.45) \end{aligned}$$

The velocity of the particle is given by $\vec{v} = \vec{p}/E$.

In a special momentum base, $\vec{p} = (p_\parallel,\ p_{\perp_1},\ p_{\perp_2})$, and viewed from a frame with a velocity $\vec{v}^*_{\mathrm{R/R'}} = \vec{v}^* = v^*\vec{e}_\parallel$ (thus $\beta^* = v^*/c$) moving along $\vec{e}_\parallel$ of the of the laboratory frame, the 4-momentum vector $\mathbf{p}^*$ can be described by:

$$\mathbf{p}^* = \begin{bmatrix} E^* \\ p^*_\parallel \\ p^*_{\perp_1} \\ p^*_{\perp_2} \end{bmatrix} = \begin{bmatrix} \gamma^* & -\gamma^* v^* & 0 & 0 \\ -\gamma^* v^* & \gamma^* & 0 & 0 \\ 0 & 0 & 1 & 0 \\ 0 & 0 & 0 & 1 \end{bmatrix} \cdot \begin{bmatrix} E \\ p_\parallel \\ p_{\perp_1} \\ p_{\perp_2} \end{bmatrix} \qquad (7.46)$$

where $\gamma^* = 1/\sqrt{1-\beta^{*2}}$.

For a particle p of rest mass $m_{\rm p}$ impinging on a target with an kinetic energy of $K_{\rm p}^{\rm Lab}$ in the laboratory, the Lorentz transform to the corresponding frame of center of mass [Herf01c] leads to:

$$\gamma = 1 + \frac{K_{\rm p}^{\rm Lab}}{m_{\rm p}c^2} \text{ and } \beta = \sqrt{1 - \frac{1}{\gamma^2}}. \tag{7.47}$$

With the relation $\beta^{\rm cm} = m_{\rm p}\gamma\beta/(\gamma m_{\rm p} + m_{\rm Target})$ and using Eqs. (7.41), (7.42) and (7.42), the kinetic energies of the proton, the target and thus the total kinetic energy available in the center-of-mass frame are:

$$\begin{aligned} K_{\rm p}^{\rm cm} &= (\gamma^{\rm cm}\gamma(1-\beta^{\rm cm}\beta) - 1)m_{\rm p}c^2 & (7.48)\\ K_{\rm Target}^{\rm cm} &= (\gamma^{\rm cm} - 1)m_{\rm Target}c^2 & (7.49)\\ K^{\rm cm} &= K_{\rm p}^{\rm cm} + K_{\rm Target}^{\rm cm}. & (7.50) \end{aligned}$$

As an example the reaction $^{34}S + p \rightarrow^{35} Cl^* \rightarrow^{35} Cl + \gamma$ can be decomposed into two parts. In the center-of-mass frame, where ^{35}Cl* is at rest, it follows that:

- The proton impact leads to an energy of the Cl* to be $Q + K^{\rm cm}$.
- During the γ-decay, the photon does not take all the energy available, some is used for the recoil of the Cl. To get access to the excited state from the energy of the emitted photon, a small correction has to be taken into account:

$$\begin{aligned} K(^{35}Cl) &= \frac{E_\gamma}{2M(^{35}Cl)c^2} & (7.51)\\ &\approx 80 \text{ eV, for a 5.6 MeV-}\gamma. & (7.52) \end{aligned}$$

With respect to the precision of the resonant states, this correction is negligible.

7.2.3 Discussion

In the previous Section it was assumed that the IMME follows a pure quadratic form. The study of the different members indicates that either the mass of the ground state of ^{35}Cl or its excited state member (or both) might be wrong. However, due to the relatively large uncertainty on this quartet member, further investigation is needed to draw a conclusion. For completeness, all the ground state mass values for members of the quartet with mass number $A = 35$ and isospin $T = 3/2$, as well as the excited energies for ^{35}Cl and ^{35}Ar will be investigated and indications for the deviation of the IMME will be discussed.

Checking the literature values

Ground states: The Atomic Mass Evaluation [AME03] is a compilation of all direct and indirect ground state mass measurements. In the $A = 35$, $T = 3/2$ quartet four ground state masses are involved:

- In this work the mass excess of ^{35}K has been for the first time directly determined by a Penning trap measurement technique. Only few cases showed a discrepancy to the literature that could not have been resolved, as *e.g.*, ^{36}Ar (see Section 7.4 of [Waps03] and references therein). Moreover, the precision of the mass excess given in this work is 40 times smaller than the adopted value and agrees with it. Therefore, it can be concluded that the mass excess of ^{35}K is accurate as well.

- The mass excess of ^{35}Ar results from an indirect mass measurement by means of the ^{35}Cl(p,n)^{35}Ar reaction. Three input data are taken. However, one of them [Azue78] deviates by 3.4 keV (close to two standard deviations) from the adopted value. Nevertheless, this deviation alone is not sufficient to explain the discrepancy of the quadratic form of the IMME.

- The mass of ^{35}Cl has been determined by direct rf-measurements [Smit71], which contribute about 79% to the mass determination. Since the value is coming from a direct measurement, it is quite reliable and can be assumed to be accurate.

- The mass excess of ^{35}S is mainly determined (95%) by a β-endpoint measurement of the ^{35}S(β^-)^{35}Cl reaction, which was thoroughly studied for the presumed existence of a 17 keV-neutrino, see [Waps03] (Section 7.3 and references therein). Even though the data reported in [Waps03] are labeled as 'well documented but not consistent with other well documented data', the discrepancies observed are in the order of less than 0.4 keV [Altz85, Ohi85, Simp89, Chen92, Berm93, Mort93]. While those relatively small uncertainties and deviations from the adopted value are not sufficient to draw conclusions on the existence or absence of the 17 keV-neutrino, they are precise enough to presume the mass value of ^{35}S is accurate, since no systematic trends were found in the literature.

The careful study of the ground states did not show any deviation from the adopted values [AME03], except maybe for ^{35}Ar. In [Waps03], this nuclide is labeled as 'secondary data', *i.e.*, where the mass is known from only one type of data, in the present case experimental input from the ^{35}Cl(p,n)^{35}Ar reaction, and is not cross-checked by a different connection, thus small deviations are possible.

Excited states: The values reported in this work for the excited states are taken from [Endt90, Brit98, Endt98, NNDC*] and references therein. The adopted value for the IAS excited state of ^{35}Ar does not show a strong deviation from the experimental data. In addition, the different estimates for the excited state in Tab. 7.9 and Tab. 7.10 do not deviate

by more than one standard deviation and are far off from any other known excited state of ^{35}Ar. This is a clear indication that the calculations are biased. Therefore, it can be concluded that the excited state is correctly assigned.
For the excited state of ^{35}Cl, as summarized in [Endt90], the many experimental data are not precise enough and show as well some discrepancies [Hube72a] (and references therein). The energy level scheme of ^{35}Cl exhibits a 'double' peak around 5.65 MeV, which has been thoroughly investigated [Wats67, Grau69, Hube72a, Fant73, Meye76]. Previous work on the IMME showed that the energy of the excited state for ^{33}Cl was wrongly calculated from the center-of-mass to the laboratory frame [Herf01a, Herf01c]. From the raw data of the proton energy in the laboratory frame [Meye76], the excitation energy has been calculated using the relativistic equations presented in Section 7.2.2 and compared to the values given in the above mentioned references. No major deviation was found. A detailed analysis of the resonant state of ^{35}Cl and a discussion of the separation and the spin assignment of the two 5.65-MeV states can be found in [Fant73]. The excitation energy resulting from the mean values of the data gives the respective energies of 5646 (2) keV and 5654 (2) keV. The second excited state at 5654 (2) keV is the commonly adopted value for the $T = 3/2$ IAS. However, the different mass and excitation energy calculations performed in the previous section (Tab. 7.9, 7.10 and Tab. 7.12) agree with each other within one sigma, and thus demonstrate the possibility of a 'wrong' excited state deviating by close to -6 keV. Unfortunately, the calculated excitation energy corresponds exactly to the second excited peak. When using this state rather than the adopted one, a cubic term $d = 0.8\ (1.0)$ is found. The possibility of a misassignment of the IAS excited state can therefore be concluded. Moreover the Q-value found in [Hube72a] shows a deviation of about 3 keV as compared to [AME03] for the ^{34}S(p,γ)^{35}Cl. In the case of the $A = 33$ quartet [Pyle02] an unexpected shift of a few keV was revealed for the excited states of ^{33}Cl. This shift was sufficient to explain the observed 'breakdown' of the IMME [Herf01a] and revalidated the quadratic form of the IMME [Pyle02]. Such a trend can also be the source of the deviation for the $A = 35$, $T = 3/2$ quartet.

Are higher order terms needed to describe the IMME?

In the above discussion it was assumed that the IMME has a pure quadratic form and an indication for a possible wrong mass and/or excitation energy was found. Even though the adopted quadratic form of the IMME is enough to describe the mass-surface for a given multiplet, recent experimental and theoretical studies pointed out the possibility of a deviation from the quadratic form and the need for higher order terms in the IMME.

The excited state assignment of ^{35}Cl can be validated with simulation based on a theoretical model without isospin mixing [Brow88]. The 3/2$^+$ excited state corresponding to the IAS in the $A = 35$, $T = 3/2$ quartet shows a preferential branching ratio towards the 5/2$^+$ state lying at 3 MeV [Brow05*]. Compared to the decay scheme of bound

states in ^{35}Cl, where the 5 651 (4) keV and 5 646 (4) keV states decay towards the 5/2$^+$ and the 7/2$^-$ state respectively, it can be concluded that there is no misassignment of the IAS in ^{35}Cl. Theoretical calculations based on sd-shell model calculations [Orma89] with isospin dependent interaction can also contribute to test the validity of the quadratic form of the IMME. Simulations show as well a deviation from the quadratic form of the IMME [Brow05*] of the same magnitude for the cubic term but with the opposite sign, *i.e.* $d = 3.1$. The reasons of the sign difference are not clear yet but the IMME quadratic form seems to be insufficient to describe the $A = 35$, $T = 3/2$ quartet from both experimental and theoretical side.

As mentioned in Chapter 2, the pure two-body Coulomb perturbation approximation to derive the IMME neglects the off-diagonal part of the iso-vector and iso-tensor components of the Coulomb force. However, the Coulomb force might introduce an isospin mixing which causes a shift in the levels of the different quartet members and leads to a higher order polynomial form in T_z.
It has been demonstrated in [Henl69] that corrections to the quadratic form of the IMME can be used. The correction cubic term d is expected to be proportional to $Z\alpha c$, where Z is the proton number, α the fine structure constant, and c the coefficient of the quadratic form of the IMME. However, the calculated d values are found to be smaller than $Z\alpha c$. This can be explained by the fact that the second order corrections are 'absorbed' in the a, b, c coefficients. Isospin violation of the nuclear interaction inducing a small isospin-breaking component can also lead to higher order terms in the IMME [VIsa05*]. If the bare nuclear interaction has a three-body component, and if it is isospin violating, it would automatically lead to a cubic T_z^3 coefficient. In the vicinity of the $A = 35$, $T = 3/2$ quartet members unexpected isospin-breaking and -mixing effects have been recently observed for the 7/2$^-$ and 13/2$^-$ states between the ^{35}Cl and ^{35}Ar mirror nuclides [Ekam04]. If the isospin T is a good quantum number, the $E1$ transitions are identical in mirror nuclei, which is not the case. The reason is an isospin mixing of the $|7/2^-\rangle$ and $|5/2^+\rangle$ levels.
From both theoretical calculations and experimental data a non-zero cubic d coefficient (or higher terms) is (are) possible.

Status on the IMME

The thorough study of the $A = 35$, $T = 3/2$ quartet of the IMME shows a discrepancy from the accepted quadratic form with a cubic term $d = -3.2\ (1.1)$. Even though conflicting experimental data have been found in the literature, theoretical predictions based on isospin-mixing dependent models indicate some possible deviation too. Moreover, recent experimental data identify isospin mixing effects in the vicinity of the $A = 35$, $T = 3/2$ quartet. Therefore, no definitive conclusion can be drawn at this point concerning a new 'breakdown' of the IMME. Further experimental investigations and data recheck are needed. For example a direct measurement of the ^{35}Ar ground state should

be performed with the Penning trap technique. Additional decay studies and spin assignment checks for the ^{35}Cl and ^{35}Ar mirror nuclides can be done in order to find new isospin-mixing effects for lower spin levels. Finally, new challenges are opened to theoretical simulation in order to reproduce with better precision and higher accuracy the experimental data.

Chapter 8

Outlook

With the installation of a Channeltron setup a gain of the detection efficiency by about a factor 3 was achieved which allowed to reach nuclides further away from stability. Without the new detector system, the recent mass determination of the neutron-rich isotopes of zinc up to ^{81}Zn ($\tau_{1/2}$=290ms) [Baru07*] would not have been possible.

In general, the statistical uncertainty of a frequency measurement is given by the empirical formula [Boll01]:

$$\Delta\nu_{\mathrm{FWHM}} = \frac{k}{\sqrt{N_{\mathrm{stat}}} \cdot T_{\mathrm{RF}}}, \tag{8.1}$$

where N_{stat} is the accumulated number of ions of interest, T_{RF} the duration of the quadrupolar excitation and k a constant, which is experimentally found to be equal to 0.8. A high resolution can be achieved under two main conditions: Firstly, the investigated nuclide is sufficiently long-lived in order to 'survive' the excitation cycle of a few hundred milliseconds, and secondly the production yield at ISOLDE has to be higher than a few hundred radioactive ions per proton pulse in order to collect enough statistics. This limitation is due to the overall beam transport efficiency of about 1% from the ISOLDE target area to the precision Penning trap. With the installation of the new detection system, the required statistics can be reached within a shorter period. However, for further tests of the IMME, *e.g.* for the $A = 17$, $T = 3/2$ quartet where the two ground states of ^{17}Ne and ^{17}N are not well known, the statistical gain is not sufficient to reach the appropriate precision on the mass measurement for ^{17}N.

In order to improve the precision in the frequency determination, a new excitation scheme based on the Ramsey method [Rams90], *i.e.* time separated oscillating fields, has been studied [Geor05] and is under commissioning. Experimental attempts to apply the time-separated oscillatory fields have been performed previously [Boll92, Klug93] but due to the lack of theoretical description of the shape of the resonance curve this technique was so far not used for high-precision mass measurements. Fig. 8.1 shows an experimental curve for a two-fringe excitation.

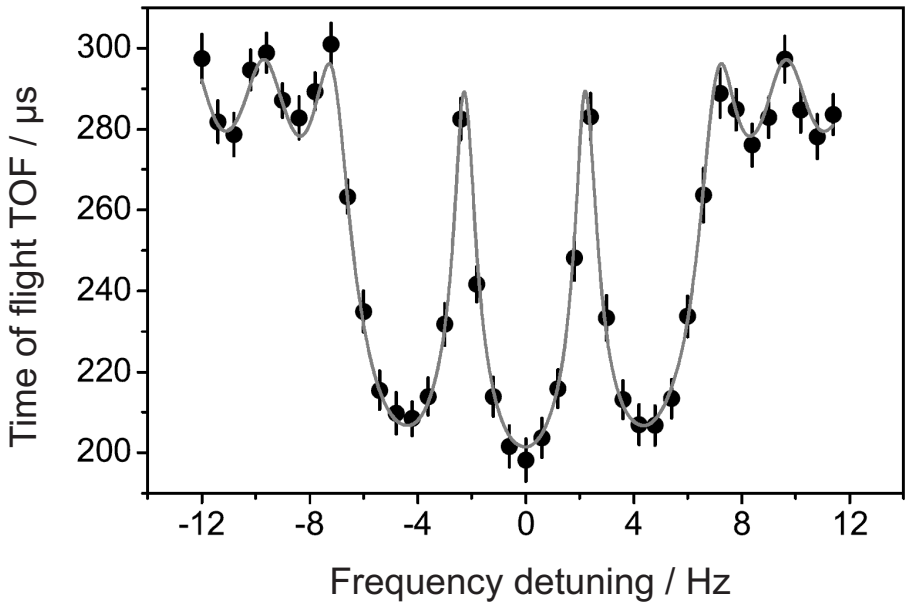

FIGURE 8.1: *Typical TOF resonance for Ramsey excitation scheme with a two-fringes ($T_{\mathrm{RF}} = 100$ ms per fringe) excitation and 100 ms waiting time [Geor05].*
The experimental data points are fitted with the theoretical expected line shape.

Together with the Ramsey technique, new higher-order standard excitations (*e.g.* octupolar rf-fields [Schw03]) are currently investigated . The first results have shown a much narrower resonance peak than for a standard quadrupolar excitation. For an octupolar excitation the resonance peak occurs at $2\nu_{\mathrm{c}}$, so that the relative frequency uncertainty $\sigma(\nu_{\mathrm{c}})/\nu_{\mathrm{c}}$ is decreased by a factor 2. In addition, the higher order harmonics involved in the octupolar excitation result in an even more narrow peak than the FWHM expected from a simple Fourier transform. Thus, a significant improvement on the cyclotron frequency determination can be achieved. Nevertheless, the theoretical description of the line shape in case of an octupolar excitation is not known yet, which is a disadvantage to the well-understood Ramsey excitation scheme.

In addition to the investigation of new excitation schemes, the use of highly-charged ions might give a better precision of the frequency measurements. In general, the measurements at ISOLTRAP are performed with singly charged ions, since the beam delivered by ISOLDE is almost always singly-positively-charged. The relative precision on the mass is inversely proportional to the excitation frequency for the applied quadrupolar excitation [Boll01, Kell03a]:

$$\frac{\sigma(m)}{m} \propto \frac{1}{\nu_{\mathrm{c}} \cdot \sqrt{N_{\mathrm{stat}}} \cdot T_{\mathrm{RF}}}. \tag{8.2}$$

The higher the charge state, the higher the cyclotron frequency since $\nu_c = qB/(2\pi m)$ and thus, a better precision can be achieved. New upcoming Penning trap experiments such as, *e.g.*, MATS [Blau05b*] or TITAN [Dill03], plan to handle highly charged ion beams using a charge breeder (EBIS – or EBIT – for electron beam ion source – or trap – [Elli95]) in order to reach the required charge-state. For stable masses this advantage is already exploited by SMILETRAP [Berg02]. Therefore with the application of highly-charged ions, either a better precisoin can be reached in shorter time, and/or in the case of very short-lived nuclides, the same precision can be achieved with collecting less statistics.

To summarize, the unique combination of the new detector setup, that improves the detection efficiency by a factor 3, and the new Ramsey or octupolar excitation schemes that improves the precision (for a given time) of the mass determination as well as using highly-charged ions, makes it possible to further investigate short-lived and rarely produced isotopes, as *e.g.* ^{17}N for IMME tests.

Chapter 9

Conclusion

The aim of the technical development in this thesis was the improvement of the ion detection efficiency to perform mass measurements on nuclides with either shorter half-lives or lower production yields than encountered before. The physics case addressed in the present work was high-precision mass measurements on potassium isotopes for the study and test of the Isobaric Multiplet Mass Equation, including ^{35}K for the $A = 35$, $T = 3/2$ quartet and ^{36}K for the $A = 36$, $T = 2$ quintet.

Concerning the new detection setup, a complete simulation of the last stage of the ISOLTRAP experiment from the precision trap to the ion detector including the excitation schemes has been performed. A detailed presentation of the Penning trap device has been given in order to describe the dipolar and quadrupolar excitations used for the manipulation of the ion cloud to perform the resonant cyclotron frequency determination [Gräf80]. The precision Penning trap, the drift tubes, and the ion detector have been implemented in a dedicated simulation software (SimIon) to compute the ion trajectories from the Penning trap to the detector. In order to reproduce the experimental resonance curves and to save computation time, the initial sets of ion distributions including the resonant cyclotron quadrupolar excitation have been simulated using the equation of motion given in Chapter 3. After testing and comparing the simulation results with the experimental data of the old MCP-detector system, the design of the new Channeltron detector-based setup has been implemented in the simulation in order to optimize the beam transfer to the ion-to-electron conversion dynode, which assures an increased detection efficiency. The simulations demonstrated a gain of a factor close to 3, and the feasibility study showed the possibility to use the Channeltron detector and to focus the ions into its aperture plate. Therefore the design of the new detector setup has taken into account the different constraints as space, vacuum, and high voltage insulation. The Channeltron detector has been put into operation at ISOLTRAP and the observed detection efficiency gain of about a factor 2.8 is in excellent agreement with the simulations performed.

For a test of the IMME and to understand the sources of a possible deviation from the commonly adopted quadratic form, the complete derivation of the isobaric multiplet mass equation has been presented. The mass determination of short-lived potassium radionuclides was discussed, where the obtained relative mass uncertainty is below $\sigma(m)/m$ =1.6·10^{-8}. The resulting high-precision mass values for the neutron deficient potassium isotopes (^{35}K and ^{36}K) were used as a stringent test of the IMME. The latest compilation by [Brit98] highlighted a possible deviation for the $A = 35$, $T = 3/2$ quartet, whereas the IMME was validated for the $A = 36$, $T = 2$ quintet within the error bars. In the literature [Jäne69, Herf01a, Pyle02] the 'breakdown' and the revalidation of the IMME have been already studied. The results from this work are the following:

- The deviation of the $A = 35$, $T = 3/2$ quartet has been confirmed experimentally with a cubic term $d = -3.2\ (1.1)$. The different sources of possible misassignment for excited states or wrong mass values have been investigated. Even though the deviation has been pointed out by experimental data, as presented in this work and in [Ekam04], as well as by isospin-mixing-based shell model calculation [Orma89], particular care should be taken before claiming a 'breakdown' of the IMME. In fact, from the theoretical predictions and the experimental data the same strength of the cubic term d is found, but with opposite sign. Moreover, as in [Pyle02], an unexpected shift of excited states could re-validate the IMME. Assuming the IMME being a purely quadratic form, two possible sources of deviation have been pointed out. Firstly, the ground state of ^{35}Ar that shows a small discrepancy in the Atomic Mass Evaluation [AME03], which can be easily solved by a direct Penning trap measurement. Secondly, the excited state of ^{35}Cl is a doublet decay-peak, therefore the energy level is not precise enough. However, simulations tend to validate the spin assignment on the IAS at 5.654 (2) keV-level for ^{35}Cl. Further experimental investigation on the possibly wrong mass(es) as well as more precise theoretical calculations are therefore required.

- The $A = 36$, $T = 2$ quintet does not show a deviation from the quadratic form of the IMME with a cubic term $d = -0.7\ (0.8)$. However, the mass uncertainty of the lowest isospin projection ^{36}Ca ($\sigma(m) = 40$ keV) is to large in order to draw conclusions about the quadratic form of the IMME for the $A = 36$ quintet.

Further tests on the quadratic form of the IMME are underway. In particular the $A = 17$, $T = 3/2$ quartet for which the mass of both ground state members ^{17}Ne and ^{17}N can be significantly improved. ^{17}Ne has been recently measured at ISOLTRAP and the data are under evaluation. However the chemical properties and the low production yield of ^{17}N constitute a challenge for high-precision mass measurement. The installation of the new Channeltron system with its improved detection efficiency of a factor of 2.8 and the use of the Ramsey excitation technique [Rams90, Geor05] will contribute to reaching the required uncertainty for this nuclide and thoroughly study the $A = 17$, $T = 3/2$ quartet.

Appendixes

Appendix A

Influence of the fit parameters

To analyze the experimentally obtained time-of-flight cyclotron resonance curves, a theoretical function has to be used in order to fit the data. The function is given by the following formula [Köni95a]:

$$TOF(\omega_{\mathrm{RF}}) = \int_0^{z_{\mathrm{detector}}} \sqrt{\frac{m}{2\big(E_0 - q \cdot V(z) - \mu(\omega_{\mathrm{RF}}) \cdot B(z)\big)}} dz \tag{A.1}$$

The initial energy E_0 depends on the ions radius after the excitation of the magnetron motion. By application of a quadrupolar excitation at ω_{RF} for the time T_{RF}, the magnetron motion will be converted into cyclotron motion. At $\omega_{\mathrm{RF}} = \omega_{\mathrm{c}} = \omega_+ + \omega_-$, the ion motion after the excitation is a pure cyclotron motion. This leads to a final motion radii that is given by [Köni95a]:

$$\begin{aligned}\rho_{\pm}(\omega_{\mathrm{RF}}, t) = \;& e^{-\frac{\delta}{2m}t} \cdot e^{\imath\frac{1}{2}(\omega_{\mathrm{RF}}-\omega_{\mathrm{c}})t} \cdot \\ & \left\{ \rho_{\pm}^0 \cosh(\omega_{\mathrm{B}} e^{\imath\theta t}) \mp \frac{1}{2} \frac{\rho_{\pm}^0[\gamma\omega_{\mathrm{c}} + \imath(\omega_{\mathrm{RF}} - \omega_{\mathrm{c}})] + \rho_{\mp}^0 k_{\mathrm{RF}}^{\pm}}{\omega_{\mathrm{B}} e^{\imath\theta}} \sinh(\omega_{\mathrm{B}} e^{\imath\theta t}) \right\}\end{aligned} \tag{A.2}$$

The motion can be separated into the magnetron and the cyclotron motion, where the energy of the ion before ejection is given by the superposition of the energy of these two motions:

$$\begin{aligned} E_{\mathrm{rad}}(\omega_{\mathrm{RF}}, t) = \;& E_{\mathrm{rad}}^{+} + E_{\mathrm{rad}}^{-} \\ = \;& \tfrac{1}{2} m \left(\rho_+(\omega_{\mathrm{RF}}, t) \cdot \omega_+\right)^2 + \tfrac{1}{2} m \left(\rho_-(\omega_{\mathrm{RF}}, t) \cdot \omega_-\right)^2 \end{aligned} \tag{A.3}$$

Since $\omega_+ \gg \omega_-$, in most of the cases the contribution of the magnetron motion can be neglected, except for off-resonance ions (base line) when $\rho_+(\omega_{\mathrm{RF}}, t)$ is close to zero.

From the fit of the TOF cyclotron curve, the initial values of the parameters are obtained as given in Tab. A.1. However, sometimes it is required to fix one or several of these parameters to allow the fit to converge. In the following, the influence of each parameter on the fit curve will be investigated.

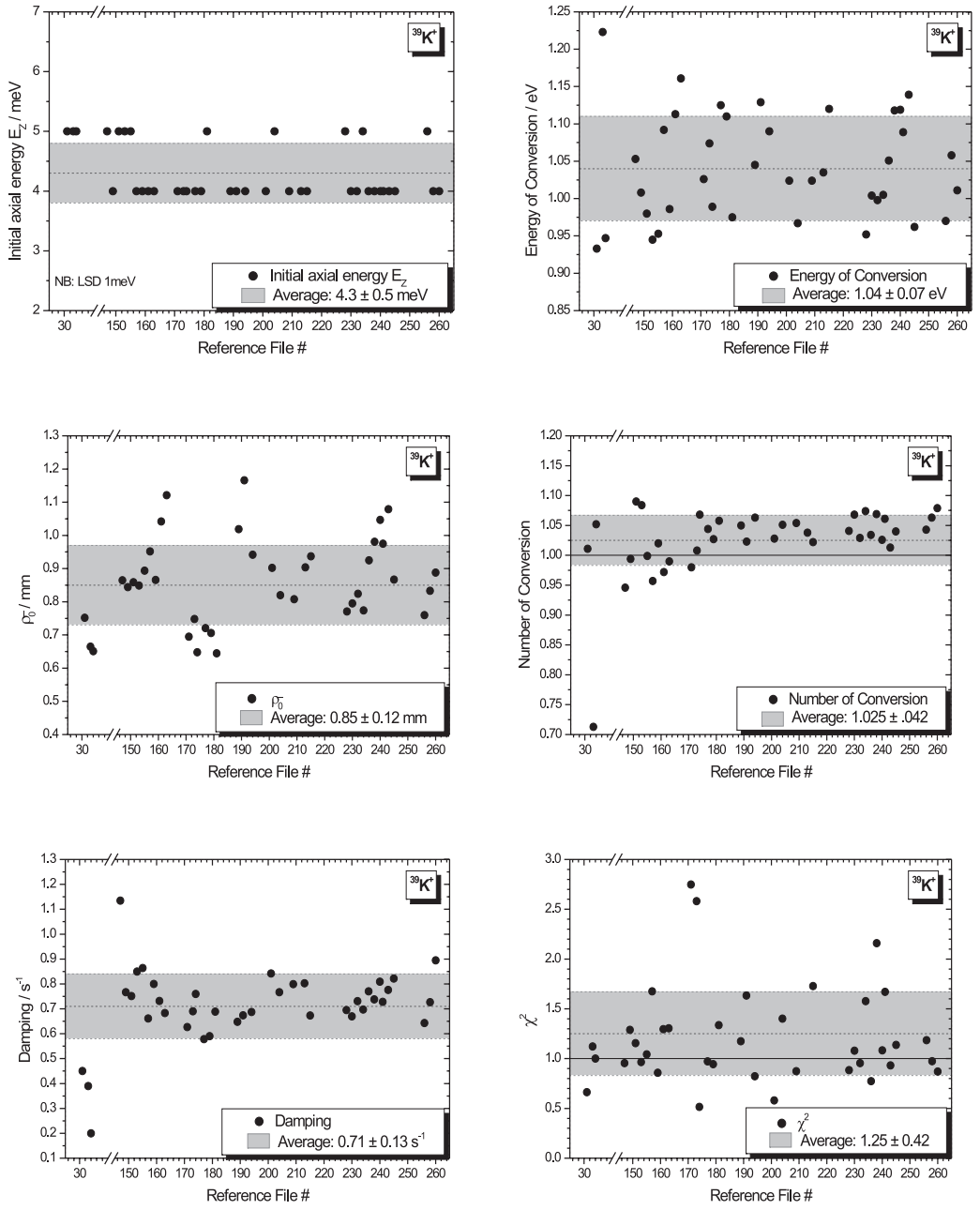

FIGURE A.1: *Mean average of the different fit parameters extracted from reference files for $^{39}K^{+}$ ions.*

Error bars are not shown in the figures since they are correlated to how well the other parameters are fitted, or far from the optimum value if fixed.

TABLE A.1: *Overview of the parameters used to fit the theoretical line shape to the experimental data points.*

Name	Typical value for $^{39}K^{+}$	Description
ν_c	2 331 460 Hz	Cyclotron resonance frequency, $\nu_c = qB/(2\pi m)$
E_z	4.3(5) meV	Initial axial energy of the ion at the upper correction tube
E_{conv}	1.04(7) eV	Axial energy of the ion at the entrance of the drift tube #2
ρ_-	0.8(1) mm	Magnetron radius before the quadrupolar excitation
ρ_+	0 mm	Cyclotron radius before the quadrupolar excitation
Conv	1.02(4)	Number of conversions of the two radial motions
A_{Damp}	0.7(1) s^{-1}	Damping due to collision with rest gas
T_{RF}	900 ms	Excitation time

To produce the figures presented in this appendix, all the parameters have been fixed to nominal values (see Fig. A.1 and Tab. A.1) except the one the section is about, in order to visualize the effect on the TOF curve.

The cyclotron frequency ν_c

See Fig. A.2.
Since ν_c represents the center frequency of the resonance curve, the fit curve shifts in the frequency dimension, in case ν_c is fixed to a wrong value.
If the given center frequency is too far away from the real value, the fit does not converge and the programm crashes.

The axial energy E_z

See Fig. A.3.
The parameter E_z is used to determine the initial energy of the ions at the upper correction tube, *i.e.* the ions are extracted from the precision Penning trap to the first drift tube with the axial energy E_z.

After the first drift tube (in drift tubes #2 and #3), the radial energy of the ions is converted into axial energy due to the coupling of the magnetic moment with the magnetic-field gradient. So only the TOF between the trap and the first drift tube is affected by the value of E_z. Thus for all the ions, the total TOF increase, if E_z decreases, or vice versa due to the change of the TOF from the ejection until the first drift tube.
Therefore a change of E_z leads to a shift of the TOF for all ions.

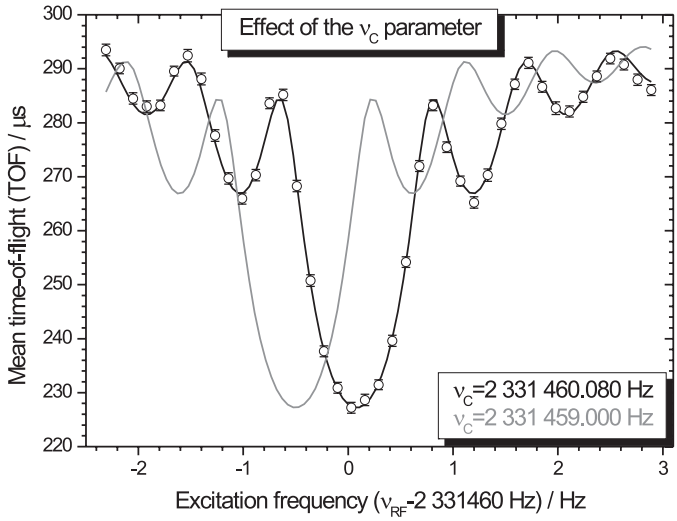

FIGURE A.2: *Effect of the ν_c parameter.*
The fit curve shifts in the frequency dimension, in case ν_c is fixed to a wrong value.

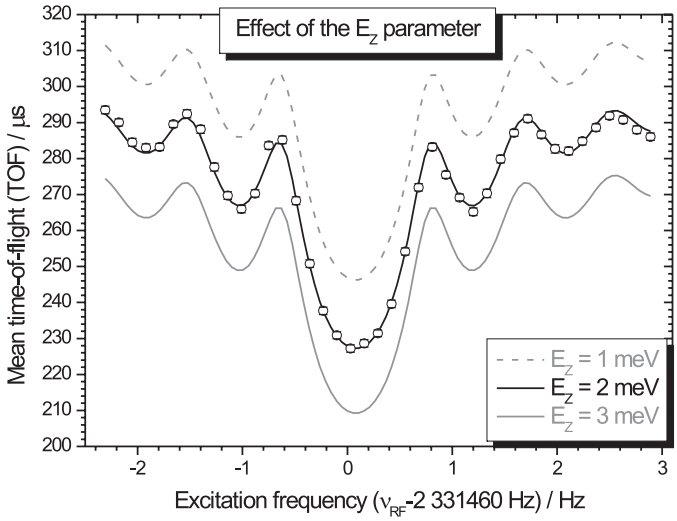

FIGURE A.3: *Effect of the E_z parameter.*
A change of E_z leads to a shift of the time of flight for all ions.

The conversion energy E_{conv}

E_{conv} is the axial energy of the ion at the entrance of the second drift tube. In the 2^{nd} and 3^{rd} drift tube, the radial energy is converted into axial energy. Thus E_{conv} represents the mean energy of the ion before the conversion.

Let us assume that there is no adiabatic conversion from radial to axial energy, *e.g.* by a very steep magnetic field gradient. The ions will not spend the same time in the tube section #2 and #3 due to their initial energy. With the conversion, it makes obvious that the slowest ions are the most influenced by the conversion of the energy whereas for excited ions it is just a secondary effect. Thus, the E_{conv} parameter mainly influences off-resonance ions (base line). Either the base line increases, if E_{conv} decreases, or vice versa, see Fig. A.4.

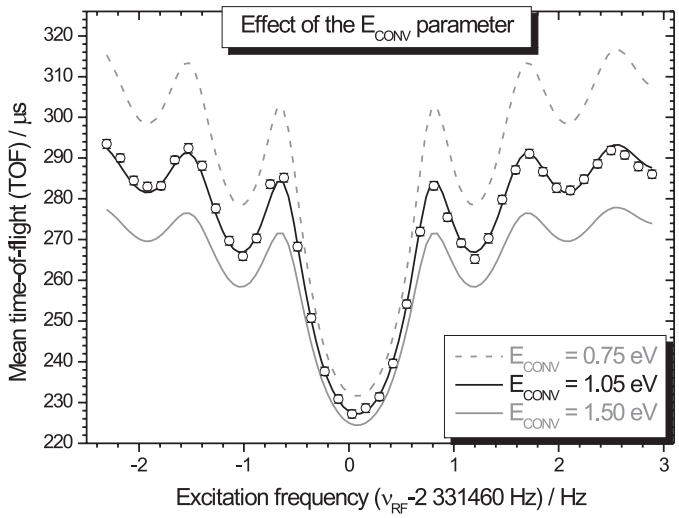

FIGURE A.4: *Effect of the E_{conv} parameter.*
The time of flight shifts mainly for off-resonance ions. The base line shifts in the same direction than E_{conv}.

The magnetron ρ_- and cyclotron ρ_+ radius

See Fig. A.5.
The parameters ρ_- and ρ_+ are used to determine the magnetron and cyclotron radius, respectively, after the magnetron dipolar excitation and before the cyclotron quadrupolar excitation. ρ_+ is expected to be zero at that time and therefore it is not used as a free parameter for the fit.

If ρ_- is set to a wrong value, the initial radial energy determined by this radius will change according to Eq. (A.1) and (A.2). For not excited ions (base line) the effect is negligible due to the low value of ω_-. But for excited ions, *i.e.* with a dominant contribution of the cyclotron motion, the effect is clearly visible. Increasing (decreasing) ρ_- leads to a shorter (longer) TOF of exited ions.

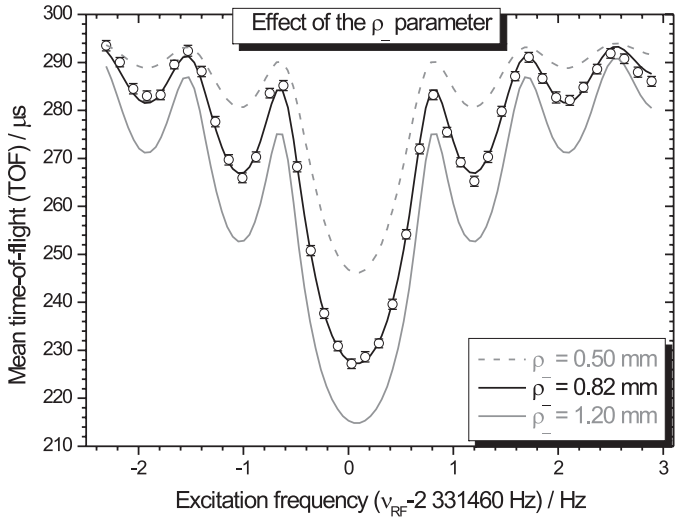

FIGURE A.5: *Effect of the ρ_- parameter.*
TOF shift for excited ions. Increasing (decreasing) ρ_- leads to a shorter (longer) TOF of exited ions.

The damping A_{Damp}

See Fig. A.6.
The parameter $A_{\mathrm{Damp}} = \delta/m$ describes the damping of the ion motion due to the collisions of the ions with the rest gas atoms and molecules. In fact, to be accurate, A_{Damp} should be called mobility of the ions, rather than real damping.
If the value is set, *e.g.*, too large, the base line will not be any longer a straight line. Especially the side bands are suppressed as shown in Fig. A.6. The damping parameter is a very weak parameter and needs often to be fixed in order to let the fit converge.

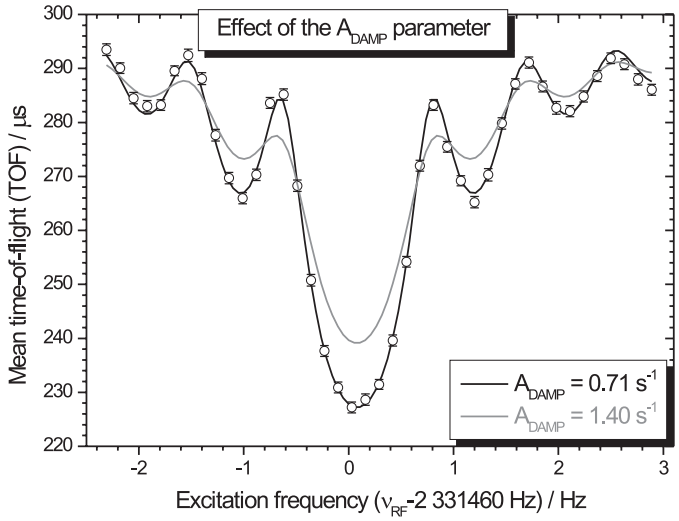

FIGURE A.6: *Effect of the A_{Damp} parameter.*
The shape of the curve changes due to the A_{Damp} parameter, especially the straight base line shows a slope and side bands are suppressed.

The conversion number $C\mathrm{onv}$

See Fig. A.7.
$Conv$ is used to determine the number of conversions between pure magnetron motion to pure cyclotron motion.

Because of the rectangular shaped excitation in time space, the Fourier Transformation into frequency space gives a "$\sin(\alpha x)/x$" modulation of the radii, *i.e.* a side band structure. Here the parameter α mainly depends on the product $T_{\mathrm{RF}} \cdot C\mathrm{onv}$. In addition, the coupling between the two eigenmotions (magnetron and cyclotron) changes the 'x' variable to $x = \sqrt{(\omega_{\mathrm{RF}} - \omega_{\mathrm{c}})^2 + k_0^2}$ where k_0 is a function of the conversion number.

By setting a wrong value to Conv, the general shape of the curve will change as described in [Köni95b] due to the variation of the α parameter and the role of the coupling k_0.

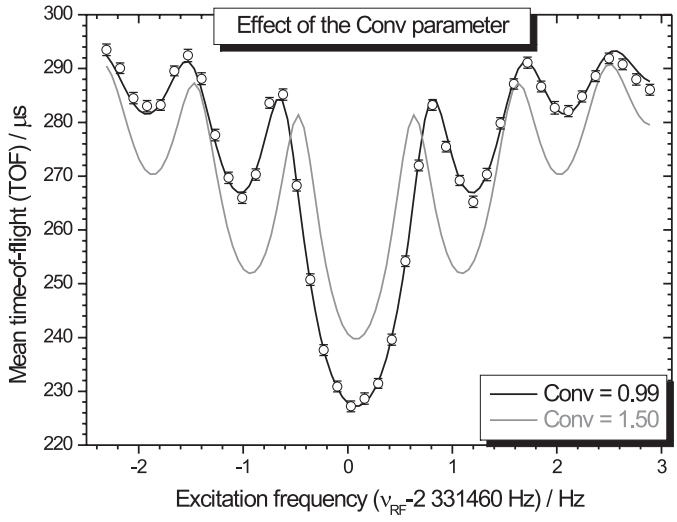

FIGURE A.7: *Effect of the $C\mathrm{onv}$ parameter.*
The shape of the curve changes because of the product: $T_{\mathrm{RF}} \cdot C\mathrm{onv}$.

The excitation time T_{RF}

See Fig. A.8.
T_{RF} is used to determine the excitation time. This is not really a parameter since the value is read directly in the raw experimental data file. For explanation purposes, it can be fitted to see the effect on the resonance curve.

Because of the rectangular shaped excitation in time space, the Fourier Transform into frequency space gives a "$\sin(x)/x$" modulation of the radii, if the coupling constant k_0 is neglected. This is not a fair approximation since without the coupling there is no resonant structure. However, for simple explanation purposes, it will be assumed to be so.

Furthermore the width of the resonance changes according to a change of T_{RF}. The width of the resonance $\Delta\nu_{\mathrm{FWHM}}$ is then given by $\Delta\nu_{\mathrm{FWHM}} = 1/T_{\mathrm{RF}}$ (in reality with the coupling term $\Delta\nu_{\mathrm{FWHM}} = k/T_{\mathrm{RF}}$, where $k \approx 0.8$). By setting a wrong value T_{RF}, the general shape of the curve simply scales. Moreover the A_{Damp} parameter is also affected since the whole shape is modulated by a exponential $e^{-A_{\mathrm{Damp}} \cdot T_{\mathrm{RF}}/2}$. In the example given here the slight damping parameter has not been corrected. Therefore a small difference in the TOF can be observed.

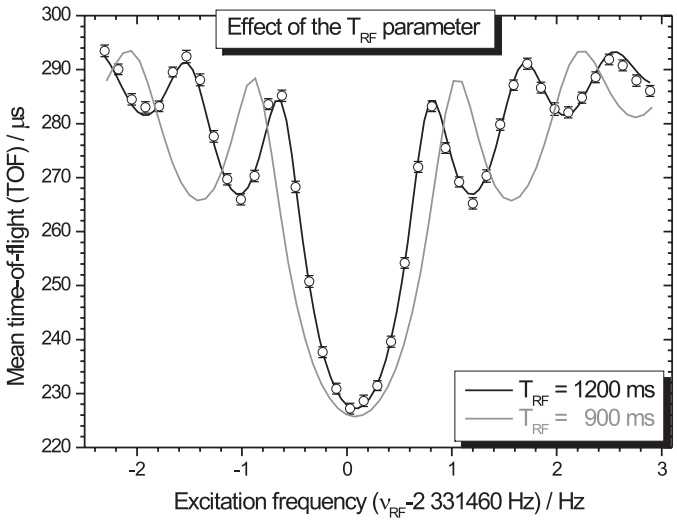

FIGURE A.8: *Effect of the T_{RF} parameter.*
The shape of the curve changes because of the product $\Delta\nu_{\mathrm{FWHM}} \propto 1/T_{\mathrm{RF}}$.

Appendix B

The optimization procedure of ISOLTRAP

B.1 How to optimize the ion transfer to the ISOLTRAP time-of-flight detector

In order to obtain a TOF resonance on the MCP5v/Channeltron detector, the ion transfer, *i.e.* the overall efficiency of the setup, has to be optimized step wise.

As the ISOLTRAP transfer beam line (shown in Fig. B.1[1]) contains about every meter a MCP detector, the transport efficiency after each trap or set of steerers, lenses, and deflectors can be checked. This appendix describes the 'standard' ISOLTRAP optimization procedure and explains how to tune at least the most important parameters out of more than 150 ISOLTRAP parameters needed to guide the ions to the final detector. To illustrate the different steps, some scans obtained during the optimization procedure for $^{39}K^{+}$ are given. The timing scheme of a frequency measurement procedure is shown in Fig. B.3

In this chapter, the optimal pathway will be the beam line of the apparatus. However to optimize the setup the beam line path is not always followed exactly. In the following the purpose of almost all devices will be described.

[1] All the devices (lenses, deflectors, steerers) mentioned in the report are given in Fig. B.1

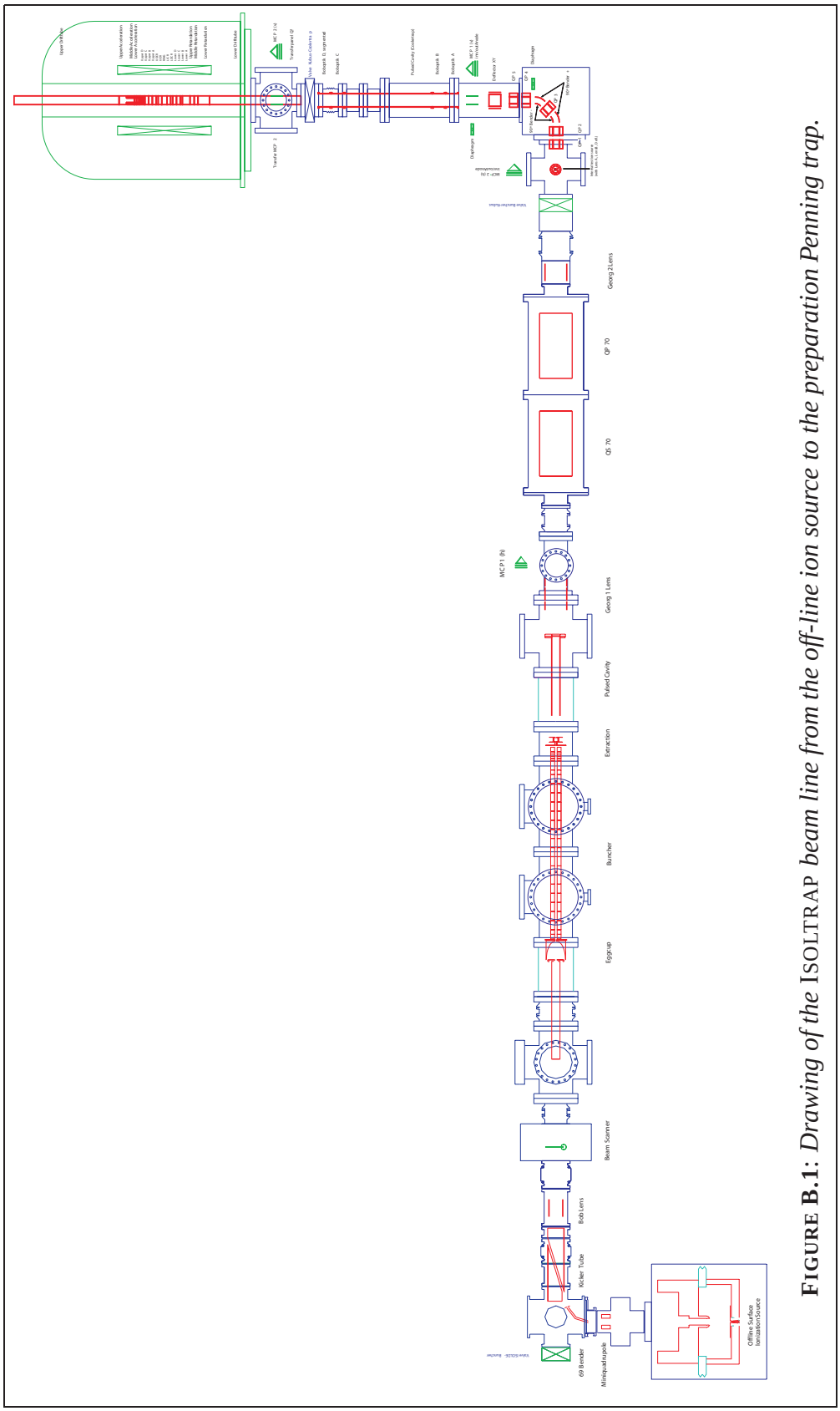

FIGURE B.1: *Drawing of the* ISOLTRAP *beam line from the off-line ion source to the preparation Penning trap.*

B.2 From the ion source to the RFQ-ion beam cooler and buncher

B.2.1 Transfer optimization between the off-line ion source and the RFQ

[buncher ejection-MCP1h][2]

For the mass measurement of radionuclides, the magnetic field needs to be calibrated. This is done both before and after the cyclotron frequency measurement of the investigated ion via the cyclotron frequency measurement of a stable ion, for which the mass is well known. These ions are provided by an off-line reference ion source.

For the optimization procedure described here, $^{39}K^{+}$ ions from the off-line ion source are used. As this ion source is off axis to the beam line (Fig. B.1), deflectors, lenses and quadrupoles have to be used to optimize the ion transfer towards the RFQ-buncher located in a 60-kV high-voltage cage. The mini-quadrupole, the 69° deflector, the kicker bender, and the Bob lens are used to optimize the injection into the buncher. While measuring the signal just after the buncher on MCP1h, the voltages applied to the quadrupoles and steerers can be scaned to optimize the injection into the buncher.

In case the ISOLDE beam is used, the high voltage which is put on the cage has also to be scanned. The ion beam of ISOLDE is defined at 60 keV $\pm$ a few eV. Thus, to get the maximum number of ions, the cage has to be put to the same potential (the ions produced by ISOLDE are singly charged so 1V on the cage corresponds to 1eV for the ions). For the test ion source it is not needed to do a HV scan because both, ion source and HV cage, are exactly at the same potential.

B.2.2 RFQ Settings

[buncher ejection-MCP1h]

A RFQ can be used to guide an ion beam along the experimental axis. Applying an rf-amplitude on four segmented rods in a buffer-gas filled cell and storing the ions, the motion of the ions can be damped in all directions. Furthermore, if a DC-voltage is applied to the rods, the RFQ can be used as a mass separator device. So the buncher parameters have to be set correctly corresponding to the ions of interest. Amplitude and frequency values of the DS345 for different ion species are listed in Table B.1. The He gas pressure is always $6{\cdot}10^{-6}$ mbar at the entrance of the RFQ.

[2] After each section the signal used as the process trigger as well as the detector used for the ion signal are given.

TABLE B.1: *Typical amplitude and frequency settings for different ions.*

Ion	Amplitude (V)	Frequency (MHz)
$^{23}Na^{+}$	0.25	1.09
$^{39}K^{+}$	0.35	1.04
$^{85}Rb^{+}$	0.75	0.99
$^{133}Cs^{+}$	0.85	0.99

B.3 From the RFQ-buncher to the preparation Penning trap

After cooling and bunching the initial continuous beam from the off-line ion source or the ISOLDE target, the ions are delivered in 1 μs bunches to the preparation trap. The number of ions in a bunch depends linearly on the accumulation time in the buncher. This accumulation time is set via a beam gate: **Delay#2** (see Fig. B.3, step 3).

B.3.1 From the buncher to the 90° bender

Extraction of the ions out of the buncher [buncher ejection-MCP1h/2h]

Although MCP1h can be used to see the extracted beam, MCP2h is used for horizontal beam-line tuning because it is further away from the buncher extraction region and thus stronger effects of the extraction settings can be observed while tuning the voltages.

As some electrode values depend on other electrode values, two-dimensional (2D) scans can be performed to get the best settings. This is also possible for X-Y-deflectors, as *e.g.*, for the extraction electrodes HV steerer X&Y.

First pulsed cavity: HVPulseDown [buncher ejection-MCP1h/2v]

Since the buncher is on 60 kV, the ion energy after extraction is still at 60 keV, and thus too high to pass the 90° bender. To slow down the ions, *i.e.* to lower their potential energy, a pulsed voltage (**HVPulseDown**) is applied to a drift tube in order to give the ions the correct energy that allows them to be bent towards the preparation Penning trap.

The **HVPulseDown** timing has also to be set correctly (see Fig. B.3, step 5a): Indeed all ions ejected from the buncher have the same energy (E = 60 keV), but it is of course not the case for their velocity $v = \sqrt{2E/m}$, which is mass dependent. In order to reduce the energy of the ions of interest, the pulsing has to be applied at a certain time (**Delay#4**[3]

[3] **Delay#4** is **Delay#2** in the Mass Measurement program.

Fig. B.3, step 5a), *i.e.* when the ions are in the middle of the pulsed drift tube. Therefore, a delay scan is performed to set the correct timing of this pulse.

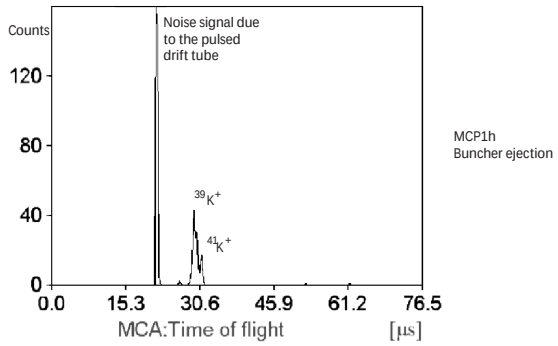

FIGURE B.2: *Timing on MCP1h for $^{39}K^+$ and $^{41}K^+$ provided by the ion source.*

Lenses and quadrupoles [buncher ejection-MCP2h]

After setting the values for the energy of the beam, the transfer line until the 90° bender has to be optimized. For that, different devices are used: Lenses *e.g.* Georg1&2, and quadrupoles, *e.g.* QS70 left/right for the steering only. The voltages applied to these devices have to be scanned in order to get the maximum count rate on MCP2h.

B.3.2 From the 90° bender to the preparation Penning trap

MCP1v is a MCP with a phosphor screen, which is used to visualize the ion beam shape after the 90° bender. This gives indications on the spatial resolution of the beam, so that further optimizations can be done at this stage to get a better beam profile, before going on with the next part of the optimization.

The 90° bender [buncher ejection-MCP1v/2v]

In this part, the ion beam is bent towards the preparation trap. To do that, two 45° benders are in use, in addition with five quadrupoles to steer and focuss/defocuss the beam (see Fig. B.1). The voltages of the inner(-) and outer(+) bender are kept constant. The values have been calculated using ion trajectory simulation studies. The ion energy is adjusted to bent the ions upwards. Therefore the first pulsed cavity voltage and **Delay#4** have to be tuned after that step. The voltages of the quadrupoles QP1/5 and QP2/4 can also be adjusted to optimize the signal on MCP2v.

Transfer from the 90° bender to the preparation trap [buncher ejection-MCP2v]

To tune the transfer line between the bender and the first Penning trap, the Bob optic lenses and the second pulsed cavity (**switch(-)**) have to be optimized. However, the MCP2v is quite large, and close to the devices, so their effect is barely visible on that MCP. It is only possible to roughly optimize the above mentioned ion optics while looking on MCP2v. The real fine tuning of the elements is performed while shooting through the preparation trap (MCP3v).

B.4 The preparation Penning trap

The lower trap of the ISOLTRAP setup is a 20 cm long cylindrical Penning trap with an entrance and exit bore of $\sim$2 mm diameter. Looking on the signal just after the trap (MCP3v) is more sensitive and gives more information on how close the ion beam is relative to the magnetic field and experimental axis.

B.4.1 Shooting through the preparation trap [buncher ejection-MCP3v]

Normally the preparation Penning trap is filled with helium buffer gas (P $\approx$ 1–3$\cdot 10^{-6}$ mbar) for the mass selective buffer-gas cooling [Sava91]. If that pressure would be applied during shooting through optimization, the ions could scatter in the trap, so any information about the injection would be lost. To avoid this, the He gas inlet is closed while shooting through.

After having decreased the pressure, a two-dimensional scan of the cube deflectors X&Y can be performed. This step is really critical for the injection in the first Penning trap. The voltages of the lenses Bob A, B, C, D can be checked and a two-dimensional scan of the Bob deflector X&Y be performed to optimize the ion signal on MCP3v while shooting through the lower trap. At that point the second pulsed cavity is in use but still not optimized because it is aimed to help the capture of the ions in the preparation Penning trap.

B.4.2 Trapping in the preparation Penning trap

While trapping the ions, the He pressure has to be increased again in the trap and the correct timing set (Fig. B.3, step 6) for applying the voltage to the lower endcap of the preparation Penning trap. As the time of flight is quite linear with the square root of the mass of the ions (not exactly true because of all the ion optics), the trigger timing can be set with the Quantum Composer for closing electrostatically the trap to realize a mass selective capture of the ions of interest.

Second pulsed cavity [LT[4] ejection-MCP3v]

The ions coming from the 90° bender have too much axial energy to be captured in the first Penning trap. Therefore the same principle as used before can be applied: the potential energy of the ions is lowered in a pulsed cavity, called **switch(-)**(see Fig. B.3 step 5b).
This switch plays exactly the same role as the first switch (**HVPulseDown**): It slows down the ions to allow them to be trapped. So both, voltage (equivalent to energy) and delay time (**Delay#3**) for this switch have to be scanned to optimize the capture and trapping of the ions of interest.

Excitation scheme [LT ejection-MCP3v]

While storing the ions in the preparation Penning trap, different excitation schemes can be applied to prepare a pure, isobaric free ion beam for the precision trap. Here, with the mass selective He buffer gas cooling technique [Sava91] a mass resolving power of up to $R = \frac{m}{\Delta m}(\text{FWHM}) = 10^5$ can be reached. As shown in the Fig. B.3, the scheme for the preparation trap is the following:

- Axial cooling time (step 7): during this time the axial motion of the ions is damped due to the He buffer gas.
- Magnetron excitation (step 8): the magnetron radius of all ions is increased via a dipolar excitation at the magnetron frequency ν_-.
- Cooling (step 10): applying a mass dependent quadrupolar excitation at $\nu_c = qB/(2\pi m)$ in the trap filled with He gas, only the ions whose own cyclotron frequency matches the applied frequency are centered. Finally, only the ions of interest are extracted while others hit the endcap.

In order to improve the resolving power and the transmission efficiency of the preparation Penning trap, the frequency and the amplitude of the magnetron as well as of the cyclotron excitation have to be scanned (see Tab. B.2). A cooling resonance with a resolving power of $6{\cdot}10^4$ is shown in Fig. B.4.

[4]LT: Lower Trap *i.e.* cylindrical preparation Penning trap.

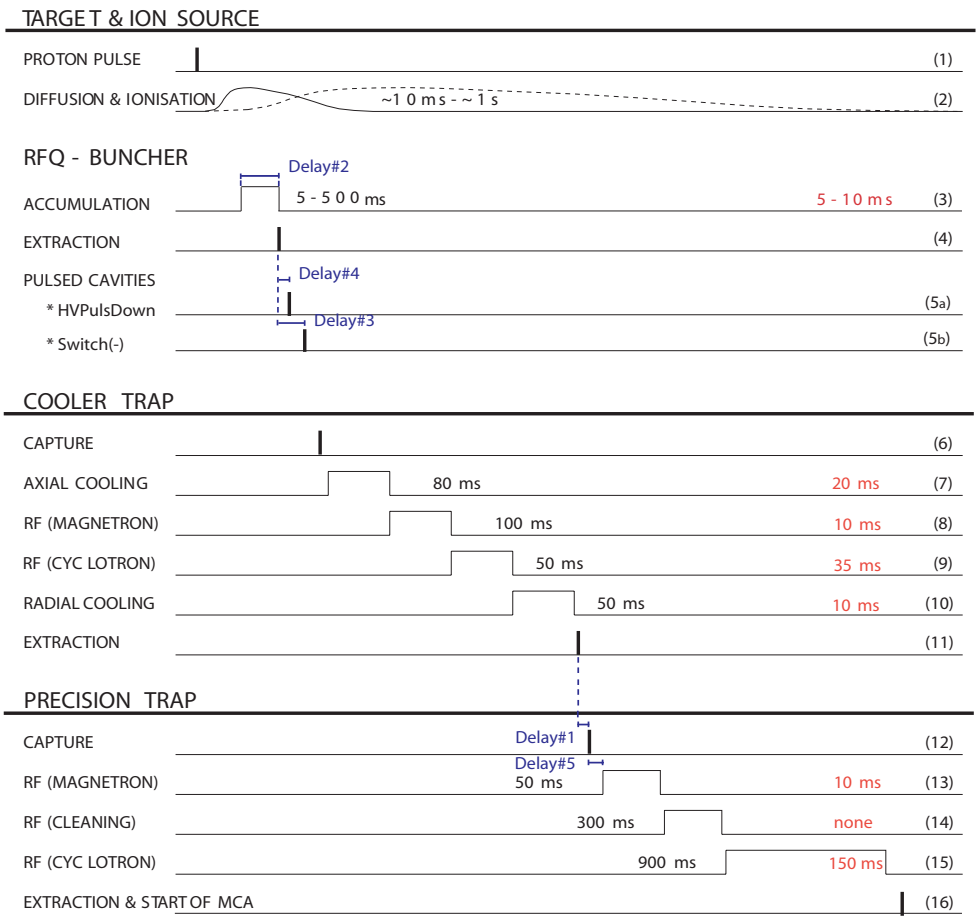

FIGURE B.3: *Excitation scheme.*
Numbers given are corresponding to the excitation time applied for long cycles (black), e.g. for $^{85}Rb^{+}$, and short cycles (red), e.g. for $^{74}Rb^{+}$ and very short lived nuclides.

B.5 From the lower trap to the precision trap

[LT ejection-MCP3v/4v]

The beam line optics between the two Penning traps is composed of deflectors and lenses to optimize the transfer from the lower trap to the upper one. Some of those devices can be scanned while looking on MCPs 3v or 4v in order to increase the signal, but for the same reasons as before for the transmission to the preparation Penning trap, the MCPs size does not allow a sufficiently sensitive optimization with respect to the magnetic field axis.

To process step wise, the different deflectors and lenses along the transfer line have to be optimized one after the other. As explained before, some devices are dependent

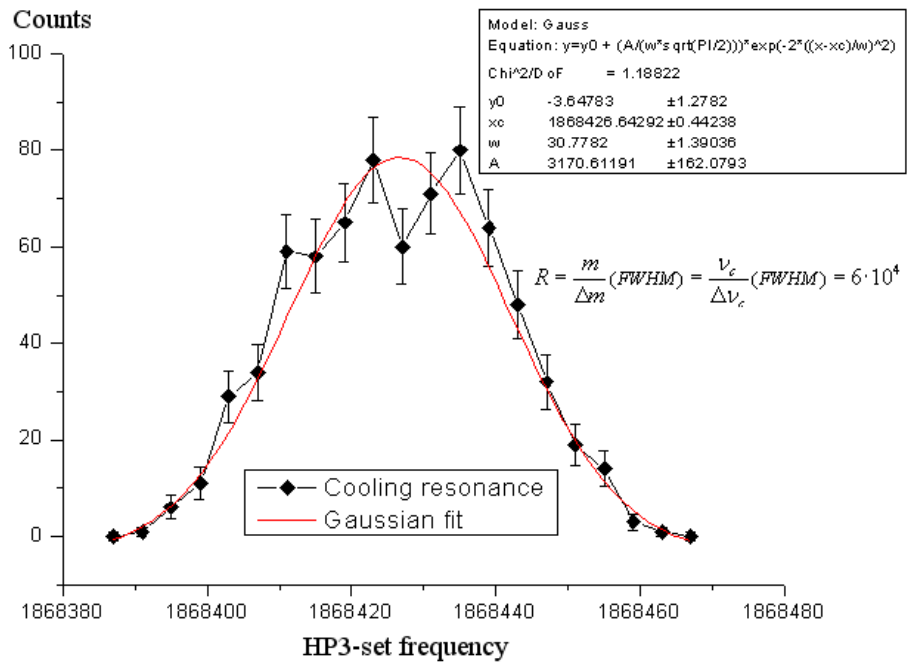

FIGURE B.4: *Cooling resonance in the preparation trap for $^{39}K^+$. A resolving power of close to 10^5 is reached.*

on each other so 2D scans for the deflectors have to be performed (*e.g.* Deflectors: LT1 X&Y, LT2 X&Y, UT1 X&Y, and UT2 X&Y) and one dimensional scans for the lenses.

So a first quick transfer optimization on MCP4v has to be performed and then continued on MCP5v while shooting through the upper trap.

B.6 From the precision trap to MCP5v/Channeltron

B.6.1 Shooting through the trap [LT ejection-MCP5v/Channeltron]

The precision trap is a hyperbolic Penning trap with two endcaps, each of them having a 5 mm diameter entrance and exit bore. The MCP5v and the Channeltron are placed in a distance of 1.2 m upstream from the center of the trap. Thus, if an ion beam reaches the detector while shooting through this trap, the ion beam is well centered along the vertical axis. While shooting through, all trap electrodes are set to about -10.6V to avoid that some of them play the role of an electrostatic lens and help the ions going through the trap.

B.6.2 UT[5] trapping and TOF resonance

Capture time [UT ejection-MCP5v/Channeltron]

After shooting through the upper trap the ions have to be captured. In opposite to the lower trap there is no pulsed cavity to give the ions the correct energy to reach the upper trap and be captured. Instead deceleration electrodes are used.

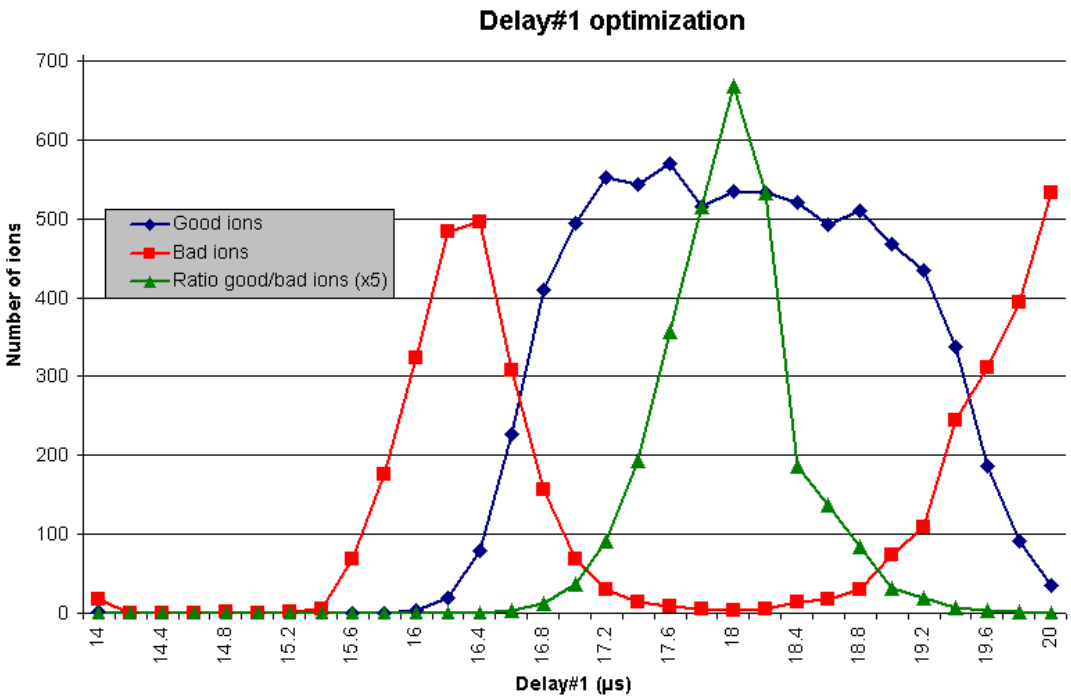

FIGURE B.5: *Optimization of the delay#1 timing (capture UT).*

The capturing time in the upper trap can be scanned (**Delay#1** Fig. B.3 step 12). The method consists in recording the ion number as a function of the capture time. Indeed the ejection condition from the preparation trap produces an ion bunch, which spacial resolution is a few times smaller compared to the size of the the trap . If the ion bunch is captured at the correct time, a maximal ion number will be trapped and then detected, whereas if the capture time is detuned, part of the ion bunch is lost. The ion count rate follows a Gaussian distribution. However, a better resolution can be reached using a special ejection scheme. Instead of switching the ring and endcaps electrodes at once, a ramping scheme is used. During the ramping (see Section 4.4.1) 'hotter' (or 'faster') ions are ejected, *i.e.* those with larger axial energy that encountered the field inhomogeneity, whereas only 'cool' (or 'slow') ions, *i.e.* with low axial energy, are kept in the trap until

[5]UT: Upper Trap *i.e.* hyperbolic precision Penning trap.

the ejection pulse is applied. The ions ejected before the ejection pulse, due to their axial energy, correspond to a wrong capture time. Taking the ratio of the 'cooled'/'hot' ions improves the signal-to-noise ratio, and narrows the full-width-at-half-maximum (FWHM) of the capture time curve as shown in Fig. B.5. With this method the correct capture timing is determined, which corresponds to the capture of the ion in the center of the trap.

After having a successful capture of the ions, a certain excitation scheme can be applied (see Fig. B.3, steps 13-15) to see a TOF resonance on the last MCP/Channeltron. Similar to the lower trap, frequency scans as well as amplitude scans have to be performed, for both magnetron and cyclotron excitation for the upper trap.

Frequency and amplitude scan [UT ejection-MCP5v/Channeltron]

To increase the magnetron radius of the ion motion, a dipolar magnetron excitation has to be applied (Fig. B.3, step 13). As the radius determines (without excitation scheme) the radial energy that is converted into axial energy in the drift tubes, a minimum in the TOF is expected at the magnetron resonance frequency (see Fig. B.6). After having set a correct value for the magnetron frequency, the excitation amplitude has to be tuned to avoid ion losses in the trap.

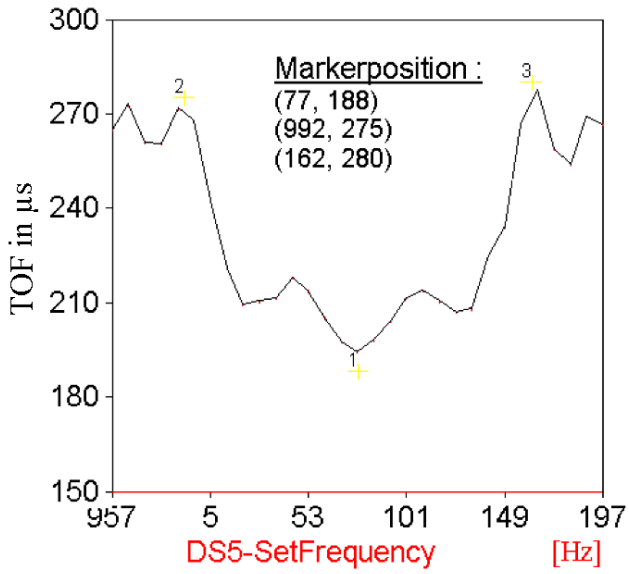

FIGURE B.6: *Magnetron frequency scan for $^{39}K^{+}$ in the precision trap. Time of flight of the ions to the detector as a function of the applied magnetron excitation frequency (**DS5 Frequency**).*

After increasing the ion motion radius, a quadrupolar excitation is applied to convert the magnetron motion into cyclotron motion and vice versa (Fig. B.3, step 15). That conversion is resonant for a frequency equal to the cyclotron frequency ν_c. So looking on the TOF curve the cyclotron frequency can be found corresponding to the minimum TOF in the resonance. The conversion depends on the product $T_{\mathrm{RF}} \cdot A_{RF}$ where T_{RF} is the excitation time and A_{RF} the amplitude of the quadrupolar RF excitation. Keeping the T_{RF} time constant the amplitude can be scanned to see one full conversion (Point#1 on the Fig. B.7. The other points #2 and #3 indicate respectively 2 and 4 full conversions. For more details see also Appendix A.

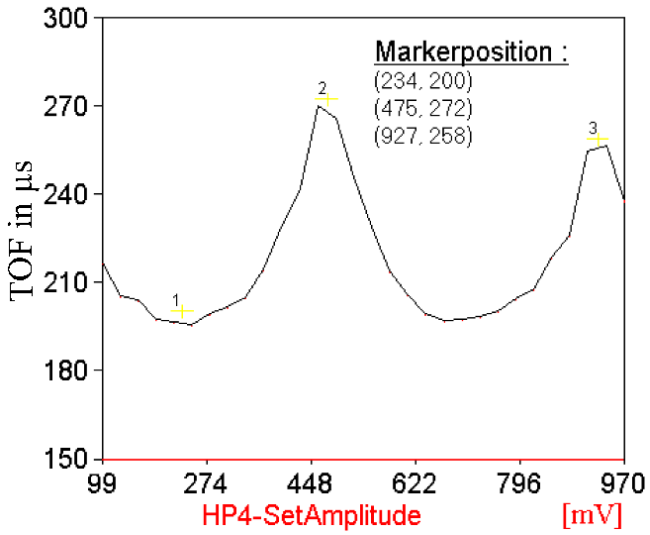

FIGURE B.7: *Cyclotron amplitude scan for $^{39}K^{+}$ in the precision trap.*
*TOF of the ions to the MCP5v/Channeltron as a function of the applied cyclotron amplitude (**HP4Amp**) for $^{39}K^{+}$. Position#1 marks one full conversion from pure magnetron to pure cyclotron motion.*

Phase scan [UT ejection-MCP5v/Channeltron]

The dipolar magnetron excitation is phase dependent. As the ion bunch from the lower trap is about 1 μs and the magnetron frequency in the order of 1 kHz, it can be considered that all ions have about the same phase. Doing a scan of **Delay#5** (Fig. B.3, step 13) the best phase can be chosen when to apply the dipolar excitation and get a deeper peak in the resonance, *i.e.* a shorter TOF in resonance, which decreases the statistical uncertainty on the determination of the cyclotron frequency (see Fig. B.8, for more explanation see [Blau03b]).

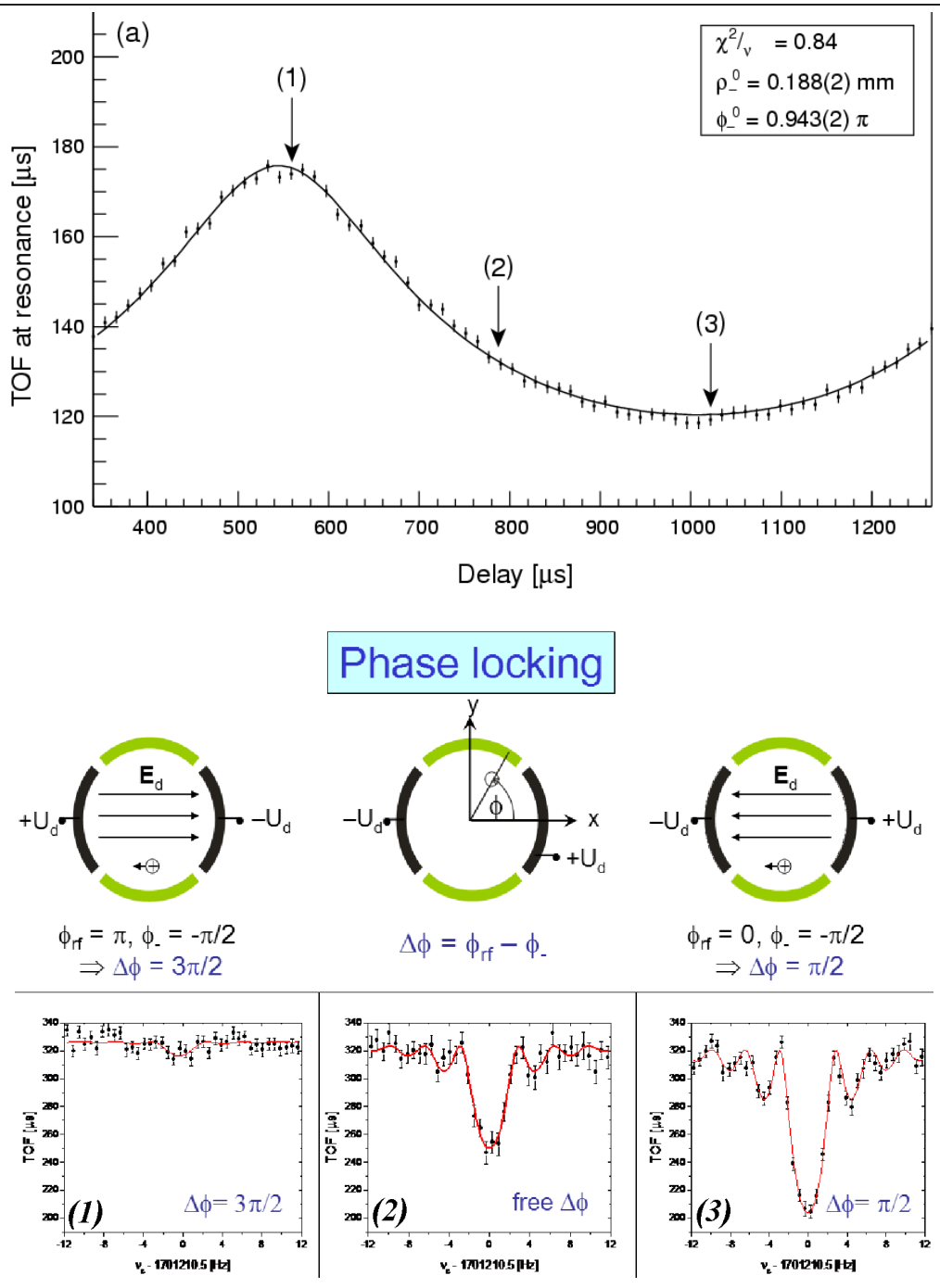

FIGURE B.8: *Influence of the magnetron phase on the TOF resonance curve. (top) Phase scan with the corresponding experimental points (see [Blau03b, Kell03b]). (bottom) Time-of-flight resonances for different phase differences between initial magnetron motion and applied magnetron excitation.*

Optimization of the drift tubes voltages [UT ejection-MCP5v/Channeltron]

The aim of the eight drift tubes (DT) after the upper trap is to extract the ions (DT#1) and to slow the ions in the DT#2 and DT#3 where the gradient of the magnetic field is maximal. The conservation of the magnetic moment of the ions leads to a conversion of the radial energy to axial energy, so ions in resonance reach the detector within a shorter time of flight whereas the ions off resonance with less energy gain need more time. DT#4 to DT#8 are finally used to transport and focus the ions to the final MCP5v/Channeltron detectors.

B.7 First mass measurement results after the optimization of ISOLTRAP

After a first round of this optimization procedure, a TOF resonance curve can be observed on either MCP5v or Channeltron detector, as illustrated in Fig. B.9.

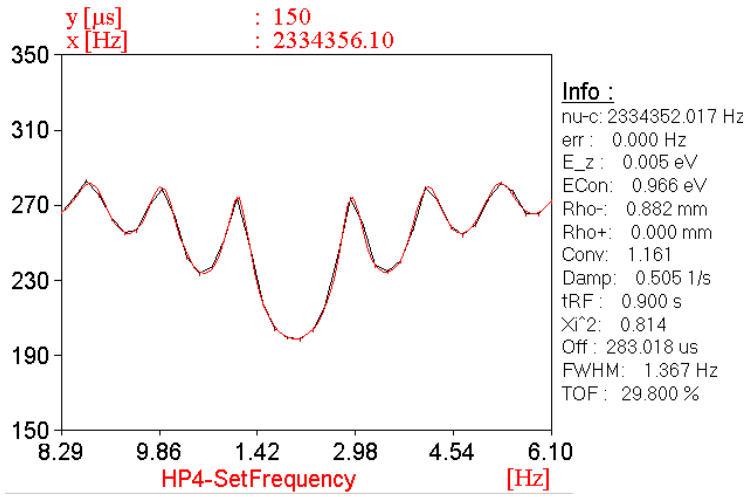

FIGURE B.9: *Optimized TOF resonance of $^{39}K^{+}$ with an excitation time of 900 ms.*

To check the ISOLTRAP accuracy, so called cross-reference measurements have to be performed. A reference mass, then an 'unknown' mass, and again a reference mass to correct for magnetic field fluctuations and drifts have to be measured. Results for $^{39}K^{+}$ as mass reference and $^{41}K^{+}$ as mass of interest are given in Fig. B.10.

In a few hours of measurements ISOLTRAP reached a precision of $1{\cdot}10^{-8}$ (about $\sigma(m) = 400$ eV) on the mass of ^{41}K, and in very good agreement with the literature value [AME03].

				Magnetic field disp:			Relative mass dependent error:	Syst err :	8.00E-09
				dB/dT (min^{-1})=	6.35E-11		1.6E-10		
	Data File		Time	Center	Err	ω_ref (interpolated		Ratio r	Err r	Err r corrected
MEAS	K41_011.dat	13	05/11/2003 11:27	2220480.122	0.0282	2334351.3647	0.0179	1.0512822617	1.6E-08	1.58E-08
REF	K39_012.dat	14	05/11/2003 11:46	2334351.375	0.0257					
MEAS	K41_013.dat	15	05/11/2003 12:39	2220480.128	0.018	2334351.4060	0.0164	1.0512822773	1.1E-08	1.28E-08
REF	K39_014.dat	16	05/11/2003 13:17	2334351.428	0.0212					
MEAS	K41_015.dat	17	05/11/2003 14:09	2220480.159	0.021	2334351.4525	0.0198	1.0512822838	1.3E-08	1.45E-08
REF	K39_016.dat	18	05/11/2003 14:40	2334351.467	0.0288					

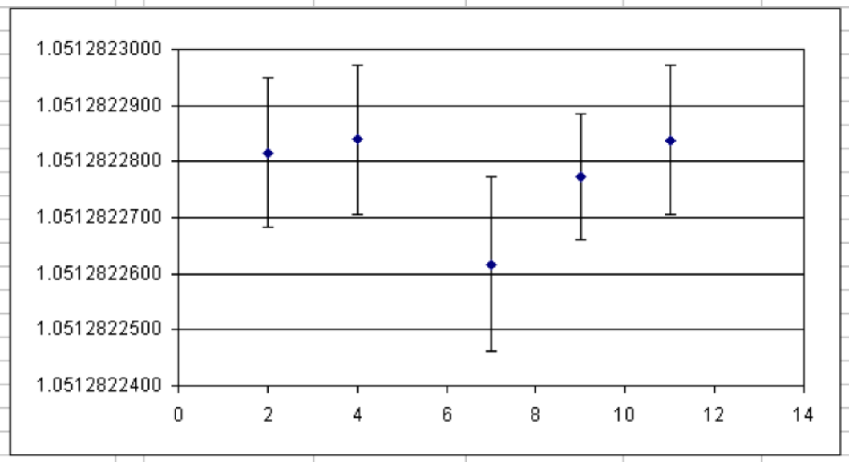

MEAN :				
1.0512822784	6.2E-09	inner		
	5.4E-09	outer		
Relative error	5.9E-09			
Abs. Final error	1.0E-08			
Rel Final error	1.0E-08			
Corrected ratio :				
1.0512822787	1.0E-08			

ISOLTRAP not corrected	40.9618262	3.2E-07	-35558.67	0.30
ISOLTRAP final	4.09618E+01	4.6E-07	-35558.65	0.43
			Diff :	-0.42
AME 2002			-35559.07	0.19

FIGURE B.10: *Precision of measurements: cross mass measurement $^{41}K^{+}$ vs. $^{39}K^{+}$. Accuracy check of* ISOLTRAP. *The mass of $^{41}K^{+}$ is measured while $^{39}K^{+}$ is used as a reference mass for the magnetic field calibration. The mass excess difference to the literature value is 420 eV with an uncertainty of 430 eV.*

List of devices and delays

In the following tables the most important parameters concerning delay/trigger times, frequencies and amplitudes are listed.

TABLE B.2: *Devices used for the magnetron and cyclotron excitation in the lower and upper Penning trap.*

	ω_c	ω_-
Lower Trap	Agilent3 Amplitude Agilent3 Frequency	DS6 Amplitude DS6 Frequency
Upper Trap	HP4 Amplitude HP4 Frequency	DS5 Amplitude DS5 Frequency

TABLE B.3: *Delays used for the process timings.*

Delay #1	Capture UT
Delay #2	Beam Gate
Delay #3	Second pulsed cavity: Switch(-)
Delay #4*	First pulsed cavity
Delay #5	Gate for phase locking
Delay #6	Magnetron phase locking

*In the Mass Measurement program, the so called **Delay #2** is **Delay #4** (**HVPulseDown** delay).

Appendix C

Advanced regulation systems

Because PID controllers are easy to program, industrial regulation systems mainly use controllers based on this technique. However, the PID monarchy suffers the revolution of the systems with a pure delay as *e.g.* chemical reactors [Mikl96] or thermal diffusion systems, or as the temperature stabilization presented in this work. Indeed, the derivative action is just a nice mathematical solution proposed to realize part of the feedback loop, but this is nothing less than a mathematical whim. Assuming $y(t)$ the signal to be regulated and $y^*(t)$ the value to be followed, the derivative action is only taking the left-side derivative of the curve, assuming it to be equal to the value of the derivative. Unfortunately, in the case of system with a delayed response, this does not work properly anymore.

The idea of advanced regulation and control is to exactly compensate for the delay, which correspond to a 'prediction' of the evolution of the system without external perturbations [MSaad00*]. This kind of delayed systems can be regulated under some particular conditions. The system has to be asymptotically stable, *i.e.* if no orders are send to the system, it should not diverge. In addition to the fact that the system has to be asymptotically stable, the roots for the system have to be stable as well.

Assuming those stability conditions being fulfilled, the last, but not least, master piece of the advanced regulation is to precisely determine the differential equation that characterizes the input/output behavior of the system [Land97].

The following sections will give an example for a more elaborate temperature regulation system than the one presented in Section 5.3.1.

C.1 Characterization of the system

C.1.1 From continuous to discrete system

It should be first of all emphasized that in most of the cases, the transfer functions are given as a Laplace transform of the differential equation of the system:

$$\mathcal{SYS}_{\text{cont}} : \frac{Y_{\text{cont}}(p)}{U_{\text{cont}}(p)} = \frac{B_{\text{cont}}(p)}{A_{\text{cont}}(p)} = G_{\text{cont}}(p), \tag{C.1}$$

where $Y_{\text{cont}}(p)$ and $U_{\text{cont}}(p)$ are the Laplace transform of the regulated signal $y_{\text{cont}}(t)$ and the order function sent to the system $u_{\text{cont}}(t)$, respectively.

The Laplace transform assumes a continuous system, and in many applications as the one studied here, all signals are sampled. Therefore the transfer function is changed because of the sampling time realized under the condition of the Shanon theorem, *i.e.* the sampling time is small compared to the variation time of the system.
In order to represent the sampled system $\mathcal{SYS}_{\text{samp}}$, the so-called $\mathcal{Z}$-transform is used. For $f_{\text{cont}}(t)$ a function and $f_{\text{samp}}(t)$ the corresponding T-sampled function, the relations between $F(z) = \mathcal{Z}\left[f_{\text{cont}}(t)\right](z)$ and Laplace $F_{\text{samp}}(p) = \mathcal{L}\left[f_{\text{samp}}(t)\right](p)$ transform are:

$$f_{\text{samp}}(t) = \sum_{k=-\infty}^{+\infty} f(kT)\delta(t-kT), \tag{C.2}$$

$$F_{\text{samp}}(p) = \sum_{k=-\infty}^{+\infty} f(kT)e^{kTp} = \big(F(z)\big)_{z=e^{Tp}}, \tag{C.3}$$

where T is the sampling time.

It has to be noted that sampling a function changes the the transfer function, and therefore the property of the system. To avoid any aliasing due to the sampling of the function, additional second order anti-aliasing filters (AAF) can be implemented between the signal and the Analog-to-Digital convertor (ADC):

$$\mathscr{F}(p) = \left(\frac{\omega_0}{p^2 + 1.4\omega_0 p + \omega_0^2}\right)^k, \text{ with } k\text{>2}. \tag{C.4}$$

C.1.2 Parametric identification of the system

In order to simplify the equations for the sampled system regulation the following notations are presented:

- Instead of indexing both continuous and discrete functions, only continuous functions and all related operators will be indexed as f_{c}. Discrete functions will be simply noted with f.

- As illustrated in Eq. (C.2) and (C.3) the $\mathcal{Z}$-transform is T-dependent. Therefore, for a given time t, $f_{\rm c}(t) = f(kT) = f(k'T')$ depending on the sampling time. The same is true for indexing a previous sample $f_{\rm c}(t - t_0) = f(kT - lT) = f(k'T' - l'T')$. For a better readability the sampled function will be noted as being T-independent: $f(kT) \stackrel{def}{=} f(t)$ and $f(t - lT) \stackrel{def}{=} f(t - l)$. If needed the notation $T_{\rm s}$ will be used for the sampling rate.
- To simplify the notation of a delayed signal the delay operator q^{-1} is introduced. Its fundamental property is $\forall d \in \mathbb{N},\ (q^{-1})^d f(t) = (q^{-d}) f(t) = f(t - d)$.

As for the continuous system defined in Eq. (C.1), the sampled system can be expressed as:

$$\mathcal{SYS}: \quad A(q^{-1})y(t) = B(q^{-1})u(t - d - 1), \tag{C.5}$$

$$A(q^{-1}) = 1 + a_1 q^{-1} + \cdots + a_{n_a} q^{-n_a}, \tag{C.6}$$

$$B(q^{-1}) = b_0 + b_1 q^{-1} + \cdots + b_{n_b} q^{-n_b}, \tag{C.7}$$

where d is the response delay of the system. Note that to this point, there is no direct relation between the coefficients of the polynomial form $A(q^{-1})$ (respectively for B) and $A_{\rm cont}(p)$.

The system as described in Eq. (C.5) can be written under the following parametric form [Land86, Larm86, Land97]:

$$\mathcal{SYS}: \quad y(t) = \varphi(t - 1)^\top \theta, \tag{C.8}$$

$$\text{with} \quad \varphi(t-1) = \begin{bmatrix} -y(t-1) \\ \vdots \\ -y(t-n_a) \\ u(t-d-1) \\ \vdots \\ u(t-d-1-n_b) \end{bmatrix} \text{ and } \theta = \begin{bmatrix} a_1 \\ \vdots \\ a_{n_a} \\ b_0 \\ \vdots \\ b_{n_b} \end{bmatrix}. \tag{C.9}$$

where '$^\top$' is the transposition operator.

Either on-line real time parametrization and identification of the system, or off-line can be performed. To do so, the following least mean square criteria has to be minimized:

$$\chi^2[\widehat{\theta}(t)] = \frac{1}{t} \sum_{k=1}^{t} \left(y(k) - \varphi(k-1)^\top \widehat{\theta}(t) \right)^2 \cdot \lambda^{t-k}, \tag{C.10}$$

where $\lambda \in [0; 1]$ represents the 'memory' of the system. The order $u(t - k - 1)$ that was applied in the past has a factor λ^{t-k} less effect than $u(t - 1)$.

Under the assumption $\lambda = 1$ and the condition that the following matrix $\Psi(t)$ defined as $\Psi(t) = \sum_{k=1}^{t} \varphi(k-1)\,\varphi(k-1)^{\top}$ is regular and invertible, the solution of the estimates for the parameter $\widehat{\theta}(t)$ is given by:

$$\widehat{\theta}(t) = [\Psi(t)]^{-1} \sum_{k=1}^{t} \varphi(k-1) y(k). \tag{C.11}$$

The values of the parameter θ and thus the coefficients of the polynomial forms $A(q^{-1})$ and $B(q^{-1})$ are given at the limit:

$$\lim_{t \to +\infty} \widehat{\theta}(t) = \theta(t). \tag{C.12}$$

To this point it should be reminded that this parametric representation does depend on the sampling time.

C.1.3 Matrix representation of the system

Up to here the transfer function, which represents the system, has been given as the output to input ratio (y/u). To easily handle the regulation problem, a more powerful but less intuitive matrix representation can be used as illustrated in Fig. C.1.

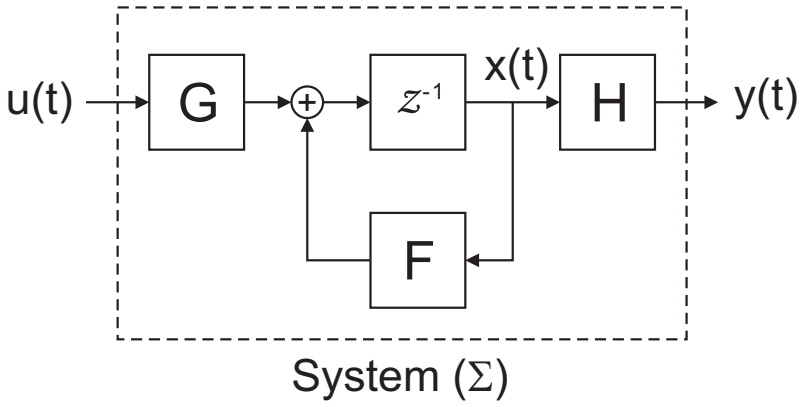

FIGURE C.1: *Standard matrix representation of a system.*

It can be demonstrated [MSaad00*] that the system $\mathcal{SYS}$ defined in Eq. (C.5) can be written with a slightly modified definition of $A(q^{-1})$, see Eq. (C.6), and $B(q^{-1})$, see Eq. (C.6), assuming the system to be physically realizable, the index $n = n_a$ and b_k is equal to zero if $k > n_b$:

$$\Sigma \left\{ \begin{array}{rcl} x(t+1) & = & Fx(t) + Gu(t-d) \\ y(t) & = & Hx(t) \end{array} \right. , \tag{C.13}$$

where $(F, G, H, E) \in \mathbb{R}^{n\times n} \times \mathbb{R}^{n\times 1} \times \mathbb{R}^{1\times n} \times \mathbb{R}^{1\times 1}$. $x(t)$ represents the internal status of the system and for most of the cases it is not possible to directly measure it, since the status vector members have no real physical interpretation.

One possible Matrix representation is given by:

$$\begin{aligned} F &= \begin{bmatrix} -a_1 & -a_2 & \cdots & -a_n \\ & & & 0 \\ & I_{n-1} & & \vdots \\ & & & 0 \end{bmatrix}, \; G = \begin{bmatrix} 1 \\ 0 \\ \vdots \\ 0 \end{bmatrix}. \\ H &= \begin{bmatrix} b_1 - b_0 a_1 & \cdots & b_n - b_0 a_n \end{bmatrix} \end{aligned} \tag{C.14}$$

Note that a system is asymptotically stable if and only if $\lim_{t\to+\infty} F^t = 0$.

It has to be emphasized here as well that this matrix representation depends on the sampling time T_s, too. Fortunately at this point, 'simple' relation links the matrix representation of a continuous and discrete system:

$$F = e^{F_\mathrm{c} T_\mathrm{s}}, \; G = \left(\int_0^{T_\mathrm{s}} e^{F_\mathrm{c}\tau} d\tau \right) G_\mathrm{c} \text{ and } H = H_\mathrm{c}. \tag{C.15}$$

Under the condition the matrixes can be inverted, the matrix representation can be derived from $(F_\mathrm{c}, G_\mathrm{c}, H_\mathrm{c})$ for any sampling time T_s.

Delayed systems

The problem of the delayed response is a bit more easy to handle with discrete function than for the continuous more, since the dimension of the matrixes are finite.

If the continuous system has a τ-delayed response time, the discrete system can be decomposed as follow: $\tau = (l-1)T_\mathrm{s} + \eta T_\mathrm{s}$, where $l \in \mathbb{N}^*$, $\eta \in [0; 1[$, and $(l-1)$ represent a full sample delay and η a fraction of the sample delay. The system Σ as described in Eq. (C.13) can be rewritten as:

$$\Sigma_\mathrm{delayed} \left\{ \begin{array}{rcl} x(t+1) & = & Fx(t) + G_0 u(t-l+1) + G_1 u(t-l) \\ y(t) & = & Hx(t) \end{array} \right. , \tag{C.16}$$

where $G_0 = \left(\int_0^{T_\mathrm{s}-\tau} e^{F_\mathrm{c}\eta} d\eta \right) G_\mathrm{c}$ and $G_1 = e^{F_\mathrm{c}(T_\mathrm{s}-\tau)} \left(\int_0^{\tau} e^{F_\mathrm{c}\eta} d\eta \right) G_\mathrm{c}$.

Finally the delayed system can be written as if there were no 'obvious' delay as:

$$\Sigma \left\{ \begin{array}{rcl} x_\mathrm{e}(t+1) & = & F_\mathrm{e} x_\mathrm{d}(t) + G_\mathrm{e} u(t) \\ y(t) & = & H_\mathrm{e} x_\mathrm{e}(t) \end{array} \right. , \tag{C.17}$$

with 'extended' system vector and matrixes:

$$x_{\mathrm{e}}(t+1) = [x(t)\, u(t_l) \cdots u(t-1)]^{\top}, \tag{C.18}$$

$$F_{\mathrm{e}} = \begin{bmatrix} e^{FcT_{\mathrm{s}}} & G_0 & G_1 & \cdots & 0 \\ 0 & 0 & I & \cdots & 0 \\ \vdots & \vdots & \vdots & \ddots & \vdots \\ 0 & 0 & 0 & \cdots & I \\ 0 & 0 & 0 & 0 & 0 \end{bmatrix}, \tag{C.19}$$

$$G_{\mathrm{e}} = \begin{bmatrix} 0 \\ \vdots \\ I \end{bmatrix}, \tag{C.20}$$

$$H_{\mathrm{e}} = [I\, 0 \cdots 0], \tag{C.21}$$

where the 0 and I are respectively 0-filled matrix and unitary matrix with appropriate dimensions.

In the following the index 'e' will be omitted. Indeed a system with a delay can be at some point 'extended' to a system without any delay, since Eq. (C.13) with $d = 0$ and Eq. (C.16) are alike.

C.2 Regulation of the sampled system

Let us now assume that the temperature regulation system has been thoroughly characterized, as explained in the previous section. Since the aim of the regulation is to follow a step-like function $y^*(t)$, *i.e.* a constant temperature of the magnet bore, the proposed solution for the regulation of the system will be based on additional integration module [MSaad00*], which will allow no statical error while following the desired set point, and a rejection of all step-like disturbance sources, like the room temperature.

As previously mentioned, the system can be described by the following matrix relation:

$$\Sigma \begin{cases} x(t+1) = Fx(t) + Gu(t) \\ y(t) = Hx(t) \end{cases}. \tag{C.22}$$

For the demonstration of this controller, the following hypotheses have to be true:

- Hypothesis 1: The matrix $\mathscr{C}(F,G)$ defined as bellow obey the Kalman criteria, *i.e.* $\mathrm{rk}\big(\mathscr{C}(F,G)\big) = n$, where n is the dimension of the system:

$$\mathscr{C}(F,G) = [G\ FG \cdots\ F^{n-1}G]. \tag{C.23}$$

- Hypothesis 2: The matrix $\mathscr{O}(H,F)$ defined as bellow obey the Kalman criteria, *i.e.* $\mathrm{rk}\big(\mathscr{O}(H,F)\big) = n$, where n is the dimension of the system:

$$\mathscr{O}(H,F) = \begin{bmatrix} H \\ HF \\ \vdots \\ HF^{n-1} \end{bmatrix}. \tag{C.24}$$

- Hypothesis 3: $\lim_{z\to 0} H(zI_n - F)^{-1}G \neq 0$.

Within those hypothesizes, an advanced regulation system for the temperature stabilization will be discussed. The particularity of the proposed regulation is that any step-function-like noise is rejected.

C.2.1 Simple feedback

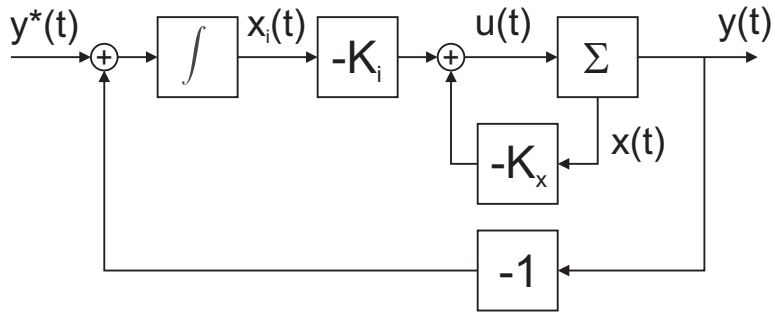

FIGURE C.2: *Regulation loop, assuming the status of the system being accessible.*

Fig. C.2 shows the scheme of the proposed regulation system. The integrated status $x_i(t)$ is defined as $x_i(t+1) = y^*(t) - Hx(t)$. Injecting this relation to the system Eq. (C.22), it can be extended to:

$$\Sigma_a \begin{cases} \begin{bmatrix} x(t+1) \\ x_i(t+1) \end{bmatrix} = \begin{bmatrix} F & 0 \\ -H & 0 \end{bmatrix} \begin{bmatrix} x(t) \\ x_i(t) \end{bmatrix} + \begin{bmatrix} G \\ 0 \end{bmatrix} u(t) + \begin{bmatrix} 0 \\ 1 \end{bmatrix} y^*(t) \\ y(t) = \begin{bmatrix} H & 0 \end{bmatrix} \begin{bmatrix} x(t) \\ x_i(t) \end{bmatrix} \end{cases} \tag{C.25}$$

or

$$\Sigma_a \begin{cases} x_a(t+1) = F_a x_a(t) + G_a u(t) + G_* y^*(t) \\ y(t) = H_a x_a(t) \end{cases} \tag{C.26}$$

where $x_a(t) = \begin{bmatrix} x(t) \\ x_i(t) \end{bmatrix}$, $F_a = \begin{bmatrix} F & 0 \\ -H & 0 \end{bmatrix}$, $G_a = \begin{bmatrix} G \\ 0 \end{bmatrix}$, $G_* = \begin{bmatrix} 0 \\ 1 \end{bmatrix}$, and finally $H_a = \begin{bmatrix} H & 0 \end{bmatrix}$.

From Fig. C.2 the feedback loop of the regulated system Σ_{reg_a} can be described by:

$$\Sigma_{\mathrm{reg}_a} \left\{ \begin{array}{rcl} x_a(t+1) & = & \left[\begin{array}{cc} F-GK_x & -GK_i \\ -H & 0 \end{array} \right] x_a(t) + \left[\begin{array}{c} G \\ 0 \end{array} \right] u(t) + \left[\begin{array}{c} 0 \\ 1 \end{array} \right] y^*(t) \\ y(t) & = & \left[\begin{array}{cc} H & 0 \end{array} \right] x_a(t) \end{array} \right. \tag{C.27}$$

with $K_a = [K_x \; K_i]$. Note that $F_a - G_a K_a = \left[\begin{array}{cc} F-GK_x & -GK_i \\ -H & 0 \end{array} \right]$.
The error on the static response of the regulated system is zero, if and only if the real part of all roots of the equation defined as $\det(zI_{n+1} - F_a + G_a K_a) = 0$ is negative.

It is possible to chose $n+1$ regulation stable and fast roots $\{z_{c,i}\}_{i\in[1;n+1]}$ [Land97] such as:

$$\prod_{i=1}^{n+1}(z - z_{c,i}) = z^{n+1} + \sum_{k=1}^{n+1} \alpha_k z^{n+1-k}. \tag{C.28}$$

The matrix K_a is completely determined by the relation:

$$K_a = (V_\alpha - V_{F_a})^\top \, [\mathfrak{T}(F_a)]^{-1} [\mathscr{C}(F_a, G_a)]^{-1} \tag{C.29}$$

where:

$V_\alpha = [\alpha_1 \cdots \alpha_{n+1}]^\top$,
$V_{F_a} = [a_1 \cdots a_{n+1}]^\top$,
the Kalman criteria is true for $\mathscr{C}(F_a, G_a)$ within the hypothesis 1 and 3,
and the regular Toeplitz matrix $\mathfrak{T}(F_a) = \left[\begin{array}{ccccc} 1 & a_0 & \cdots & \cdots & a_n \\ 0 & 1 & a_0 & \cdots & a_{n-1} \\ \vdots & \ddots & \ddots & \ddots & \vdots \\ 0 & \ddots & \ddots & \ddots & a_0 \\ 0 & 0 & \cdots & 0 & 1 \end{array} \right]$. (C.30)

C.2.2 Estimating the internal status of the system

Unfortunately the internal status of a system is not accessible in most of the cases, either because some/all of the components of $x(t)$ do not correspond to any physical parameter, or because there is no sensor to measure it. The hypothesis 2 allows to find a matrix M such as the estimated $\widehat{x}(t)$ can be written as:

$$\mathcal{O}\Sigma \left\{ \begin{array}{rcl} \widehat{x}(t+1) & = & F\widehat{x}(t) + Gu(t) + M\big(y(t) - \widehat{y}(t)\big) \\ \widehat{y}(t) & = & H\widehat{x}(t) \end{array} \right. . \tag{C.31}$$

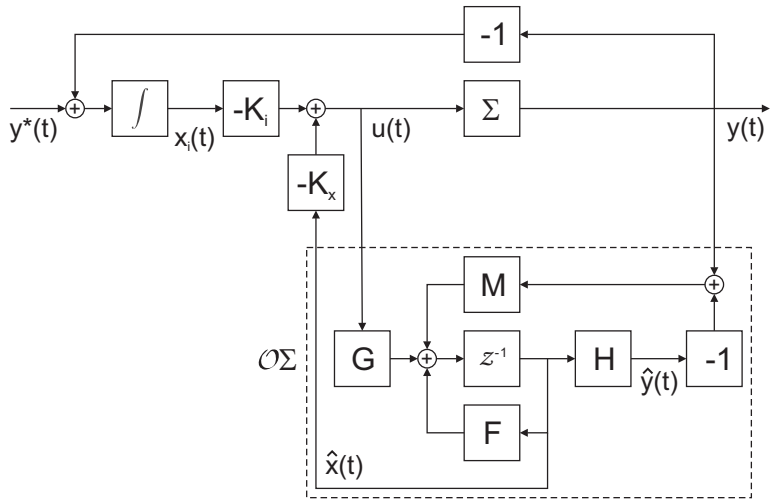

FIGURE C.3: *Regulation loop, estimating the status of the system.*

With the estimation error $\widetilde{x}(t) = x - \widehat{x}$, and $u(t) = -K_x\widehat{x}(t) - K_i x_i(t)$ the new regulated system (see Fig. C.3) can be written as:

$$\mathcal{O}\Sigma_{\mathrm{reg}_a} \begin{cases} \begin{bmatrix} x(t+1) \\ x_i(t+1) \\ \widetilde{x}(t+1) \end{bmatrix} = \begin{bmatrix} F - GK_x & -GK_i & GK_x \\ -H & 0 & 0 \\ 0 & 0 & F - MH \end{bmatrix} \begin{bmatrix} x(t) \\ x_i(t) \\ \widetilde{x}(t) \end{bmatrix} + \begin{bmatrix} 0 \\ 1 \\ 0 \end{bmatrix} y^*(t) \\ y(t) = \begin{bmatrix} H & 0 & 0 \end{bmatrix} \begin{bmatrix} x(t) \\ x_i(t) \\ \widetilde{x}(t) \end{bmatrix} \end{cases} . \tag{C.32}$$

The regulated system is asymptotically stable if, and only if, the real part of all roots z_r of the equation defined as $\det(zI_{n+1} - F_a + G_a K_a)\det(zI_n - F + MH) = 0$ is such as $\Re(z_r) < 0$ [Land97].

Applying the $\mathcal{Z}$-transform the regulated-augmented system can be described with the following set of equations:

$$\begin{aligned} U(z) &= -K_x\widehat{X}(z) - K_i X_i(z) \\ zX_i(z) - zX_{i,0} &= Y^*(z) - Y(z) \\ z\widehat{X}(z) - z\widehat{X}_0 &= (F - MH)\widehat{X}(z) + GU(z) + MY(z). \end{aligned} \tag{C.33}$$

To simplify the equation, it will be assumed that the initial conditions $X_{i,0}$ and $\widehat{X}_0$ are identically equal to 0.

The $X_i(z)$ and $\widehat{X}(z)$ can be eliminated and the set values send to the system can be described by the relation:

$$\begin{aligned} zU(z) &= -zK_x(zI_n - F + MH)^{-1}GU(z) \\ &\quad -zK_x(zI_n - F + MH)^{-1}MY(z) \\ &\quad -K_i[Y^*(z) - Y(z)]. \end{aligned} \tag{C.34}$$

The hypothesis 2 implies that $zI_n - F + MH$ is a regular matrix:

$$(zI_n - F + MH)^{-1} = \frac{\mathrm{Adj}(zI_n - F + MH)}{\det(zI_n - F + MH)} = \frac{\mathfrak{A}(z)}{P_o(z)}, \tag{C.35}$$

where $\mathfrak{A}(z) = \mathrm{Adj}(zI_n - F + MH)$ represents the co-factor matrix of $zI_n - F + MH$. Since $zI_n - F + MH$ is regular, the corresponding determinant $P_o(z)$ is a Hurwitz polynomial form so that Eq. (C.34) can be simplified by $P_o(z)$ without creating any instability in the system. It leads then to :

$$-K_iP_o(z)Y^*(z) = z[P_o(z) + K_x\mathfrak{A}(z)G]U(z) + [zK_x\mathfrak{A}(z)M - K_iP_o(z)]Y(z) \tag{C.36}$$

which is the standard RST form of a regulation system with:

$$\begin{aligned} T(z) &= -K_iP_o(z) \\ S(z) &= [P_o(z) + K_x\mathfrak{A}(z)G] \\ R(z) &= zK_x\mathfrak{A}(z)M - K_iP_o(z). \end{aligned} \tag{C.37}$$

Coming back to the sampled-time space, Eq. (C.37) can be written as:

$$\begin{aligned} T(q^{-1}) &= -q^{-n}K_iP_o(q) \\ S(q^{-1}) &= q^{-n}\left[P_o(q) + K_x\mathfrak{A}(q)G\right] \\ R(q^{-1}) &= q^{-n}\left[qK_x\mathfrak{A}(q)M - K_iP_o(q)\right]. \end{aligned} \tag{C.38}$$

C.2.3 Step-like-function noise rejection

The studied system was considered as being ideal in a sense that no perturbations or noise disturb neither the regulation nor the system itself. Here the demonstration of step-like-function noise rejection for both the regulation signal $u(t)$ and the regulated signal $y(t)$ is developed.

Assuming step-like-function noises $v_u(t)$ and $v_y(t)$, as shown in Fig. C.4, the error $\widetilde{X}(z) = X(z) - \widehat{X}(z)$ on the internal status of the system can be derived from Eq. (C.22) and (C.32) (in the $\mathcal{Z}$-transform space), using the corresponding perturbed signals $U_p(z) = U(z) + V_u(z)$, respectively $Y_p(z) = Y(z) + V_y(z)$. Note that $V_u(z) = V_y(z) = V(z)$,

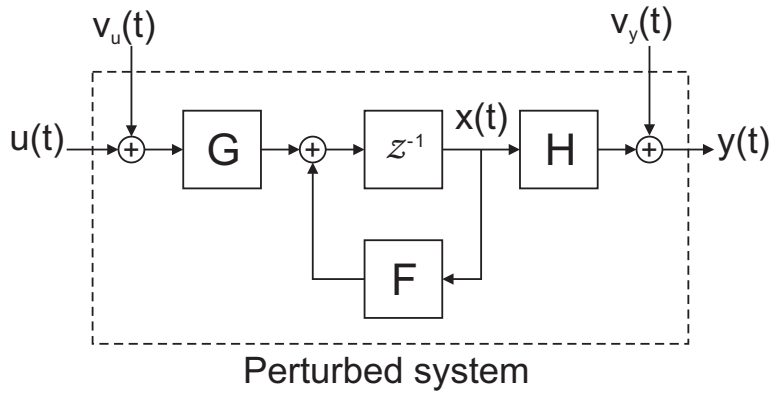

FIGURE C.4: *Matrix representation of an input- and output-noisy system.*

since both are supposed to be step-like, the index correspond to where they appear in the system. It follows:

$$\begin{aligned} z\widetilde{X}(z) &= F\widetilde{X}(z) - MH\widetilde{X}(z) + GV_u(z) - MV_y(z) \\ &= (F - MH)\widetilde{X}(z) + (G - M)V(z). \end{aligned} \tag{C.39}$$

The error on the internal status can be written as:

$$\widetilde{X}(z) = (zI_n - F + MH)^{-1}(G - M)V(z). \tag{C.40}$$

The noises are rejected if $\widetilde{x}(t)$ converges to zero. The Laplace-transform of the step function is $V(p) = 1/p$. Using the final value theorem, it writes:

$$\begin{aligned} \lim_{t\to\infty} \widetilde{x}(t) &= \lim_{p\to 0} p\widetilde{X}(p) \\ &= \lim_{p\to 0} p\frac{\mathfrak{A}(p)}{P_o(p)}\frac{1}{p} = 0. \end{aligned} \tag{C.41}$$

The result indicates that the step-like noises are rejected with the studied regulation.

If the studied system does not fulfill the hypothesis presented in Section C.2, the problem can be divided into subsystems, such as the hypothesis are verified. Thus the presented work can applied to the subsystem which fulfill the conditions.

C.3 Realization of the advanced regulation system

What has to be done first at ISOLTRAP is the identification and the characterization of the system to be regulated for the determination of the response-time delay. A detailed procedure is presented in Section C.1.2 and in [Zieg42]. If the delay is larger than a few

minutes then two possibilities are open to improve the temperature regulation of the system: either the delay time is reduced so that simple PID regulation loops can be applied, or the advanced regulation as presented in this Appendix has to be implemented.

First experimental results show a delay in the order of ten minutes. Due to the space constraints and the relatively old design of the magnet-dewar and trap system, the air flow, thus the heat conductance is not good enough to ensure a fast response of the system. The recent installation of additional heaters helped to reduce the delay, but it is still to large for a simple PID regulation. One possible technical development is to install a resistor chain between the bore of the vacuum tubes and the magnet dewar. This solution allows to have an almost homogeneous temperature in the trap region, however the space requirements for the implementation of the solution might not be fulfilled with the present design of the ISOLTRAP setup. Concerning the advanced regulation, it can be implemented following the steps presented in this work, first with a simple feedback loop, then with estimating the internal state of the system. The major task is to chose the correct values z_r such as [Land97]:

$$\det(zI_{n+1} - F_a + G_a K_a)\det(zI_n - F + MH) = 0 \Rightarrow \Re(z_r) < 0, \tag{C.42}$$

to ensure performance and stability of the regulated system.

Appendix D

Design of the new detector of ISOLTRAP

The existing sandwich MCP system was replaced by a Channeltron-MCP system, where the MCP detector is foreseen as a spare detector in case the Channeltron fails during an on-line experiment. The technical solution chosen is to use a linear feedthrough to switch between the MCP and the Channeltron detector. The MCP setup is almost the same as described in [Otto90*], except for the holder. Indeed, when moving away the MCP to enable the off-axis Channeltron detection a new drift tube segment has been implemented to transfer and focus the ion beam.

D.1 Technical drawings

D.1.1 ISOLTRAP setup

In the following the technical drawings from the different parts are given:

- Channeltron support
- CF-100 linear feedthrough side flange
- CF-100 Channeltron side flange
- Insulators
- MCP support
- MCP HV insulators
- MCP HV plates
- MCP holders
- Drift tube
- MCP-tube support

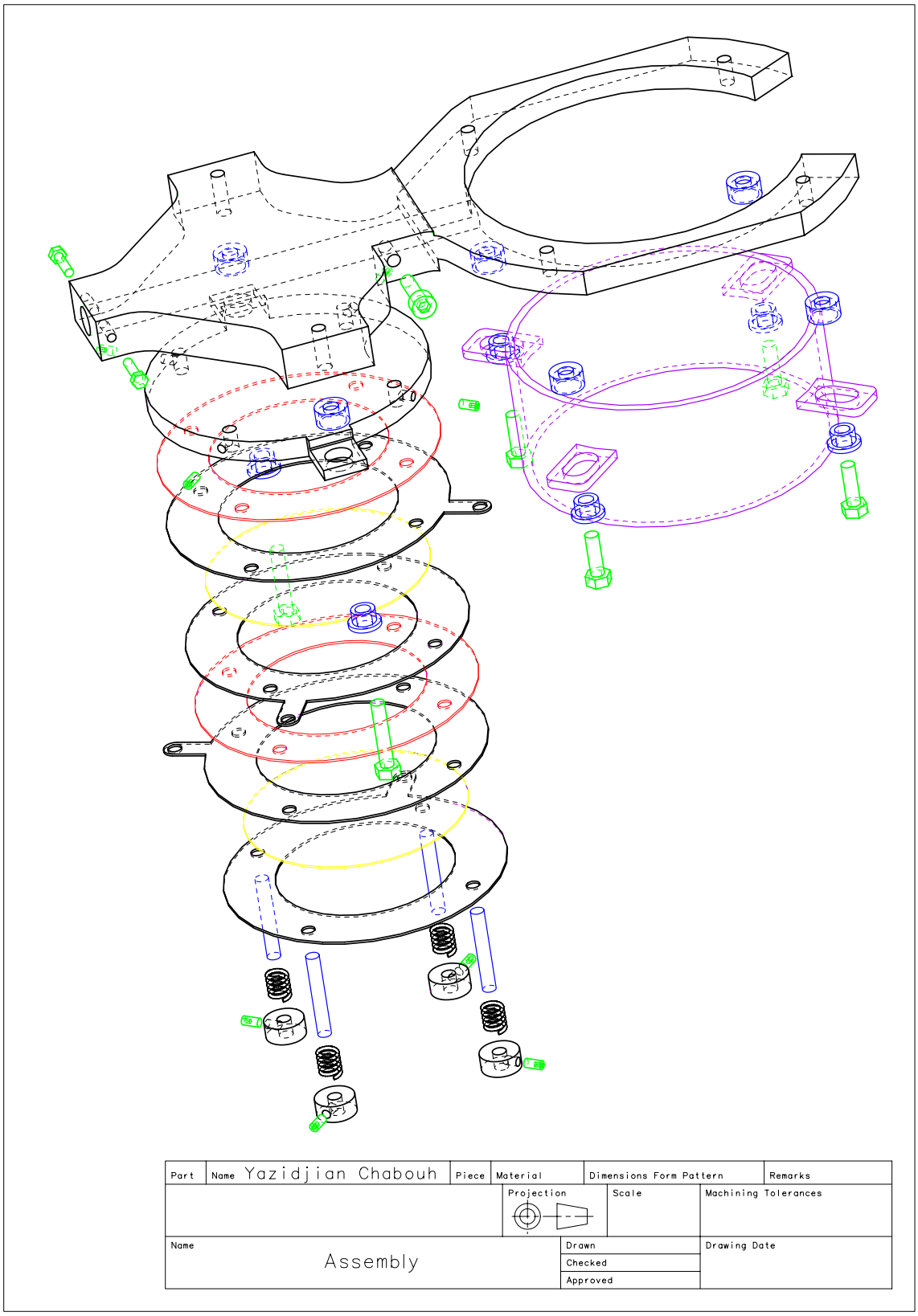

FIGURE D.1: *Setup assembly.*

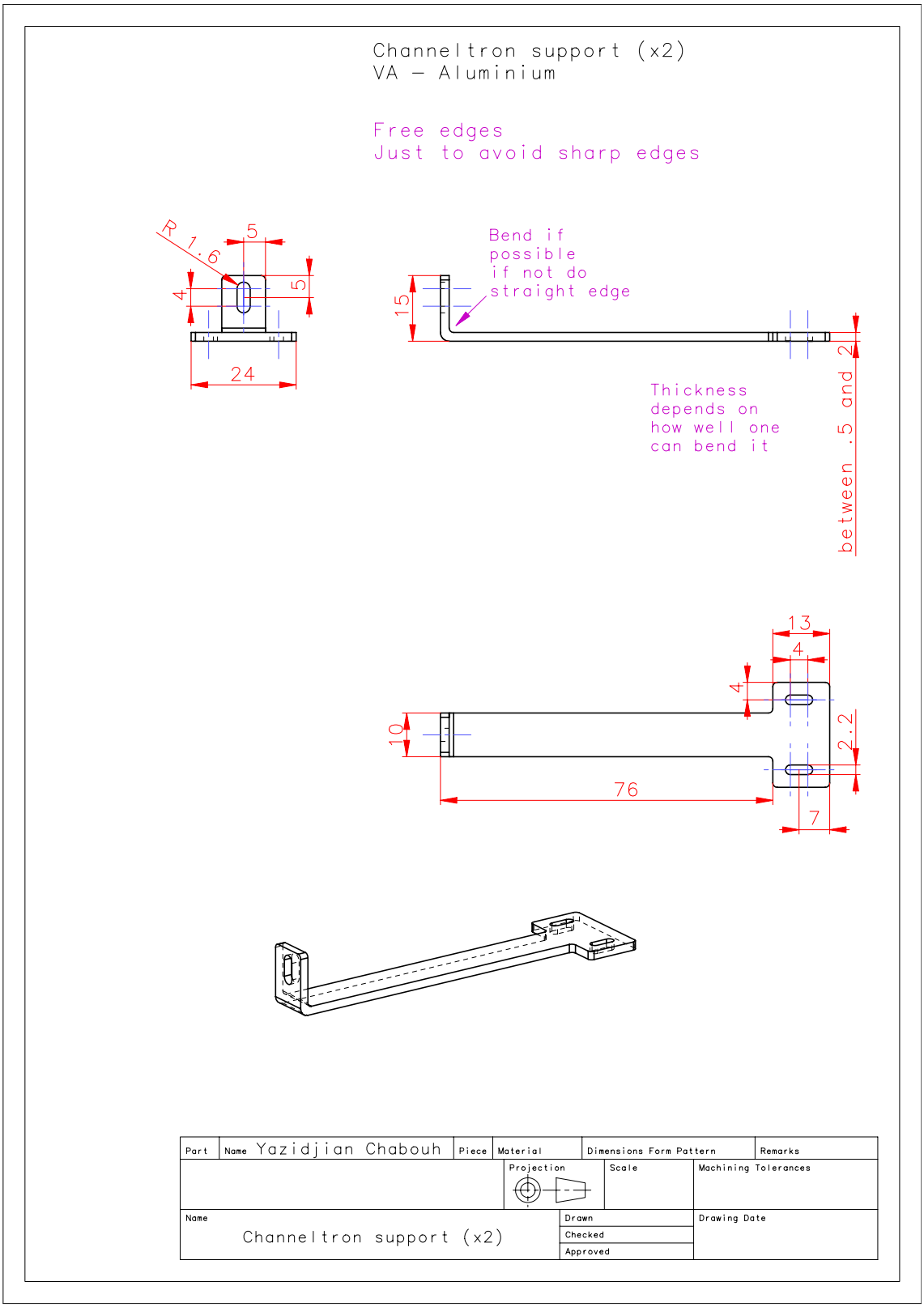

FIGURE D.2: ISOLTRAP *setup part 1: Channeltron support.*

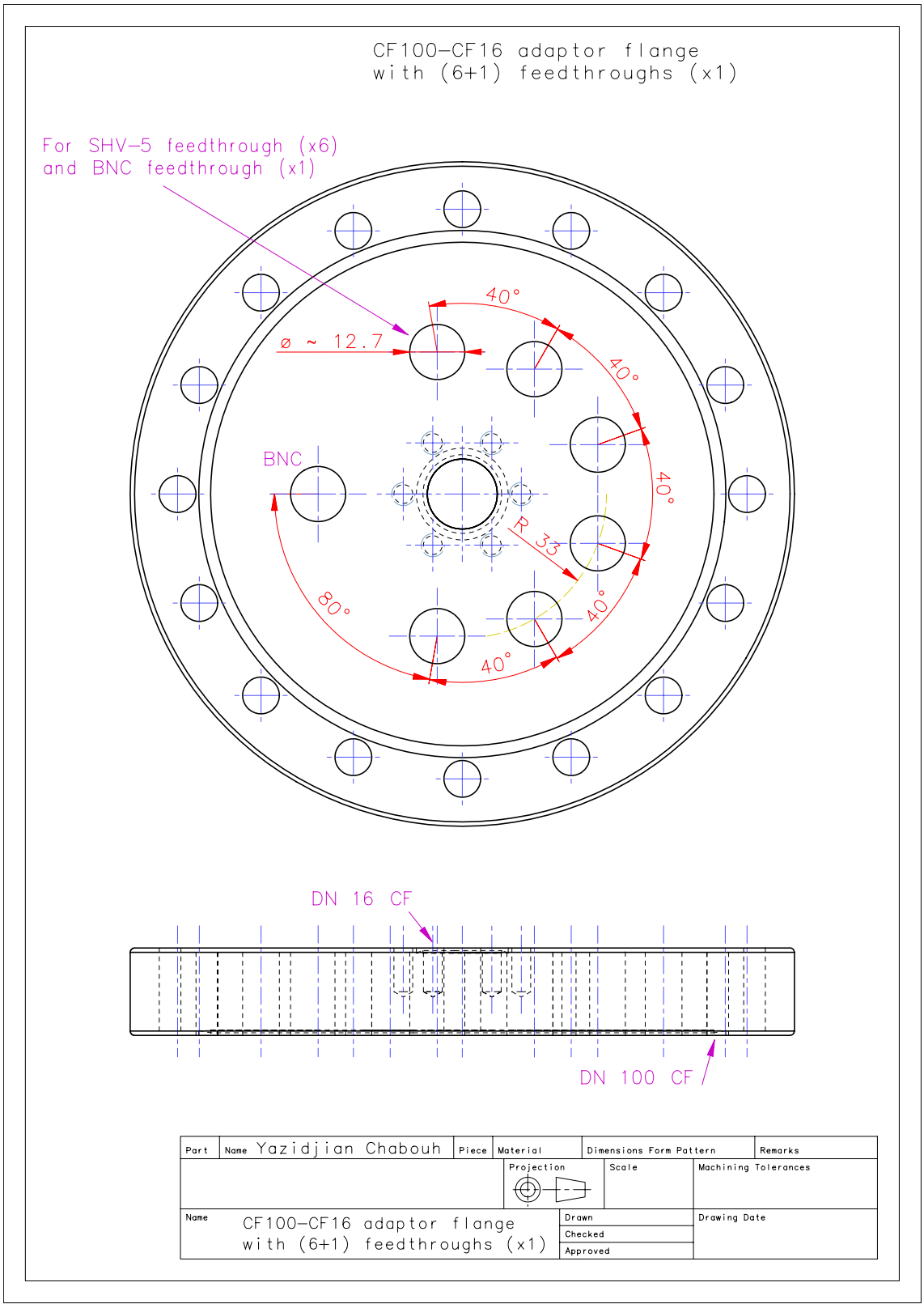

FIGURE D.3: ISOLTRAP *setup part 2: CF-100 to CF-16 adaptor flange (MCP).*

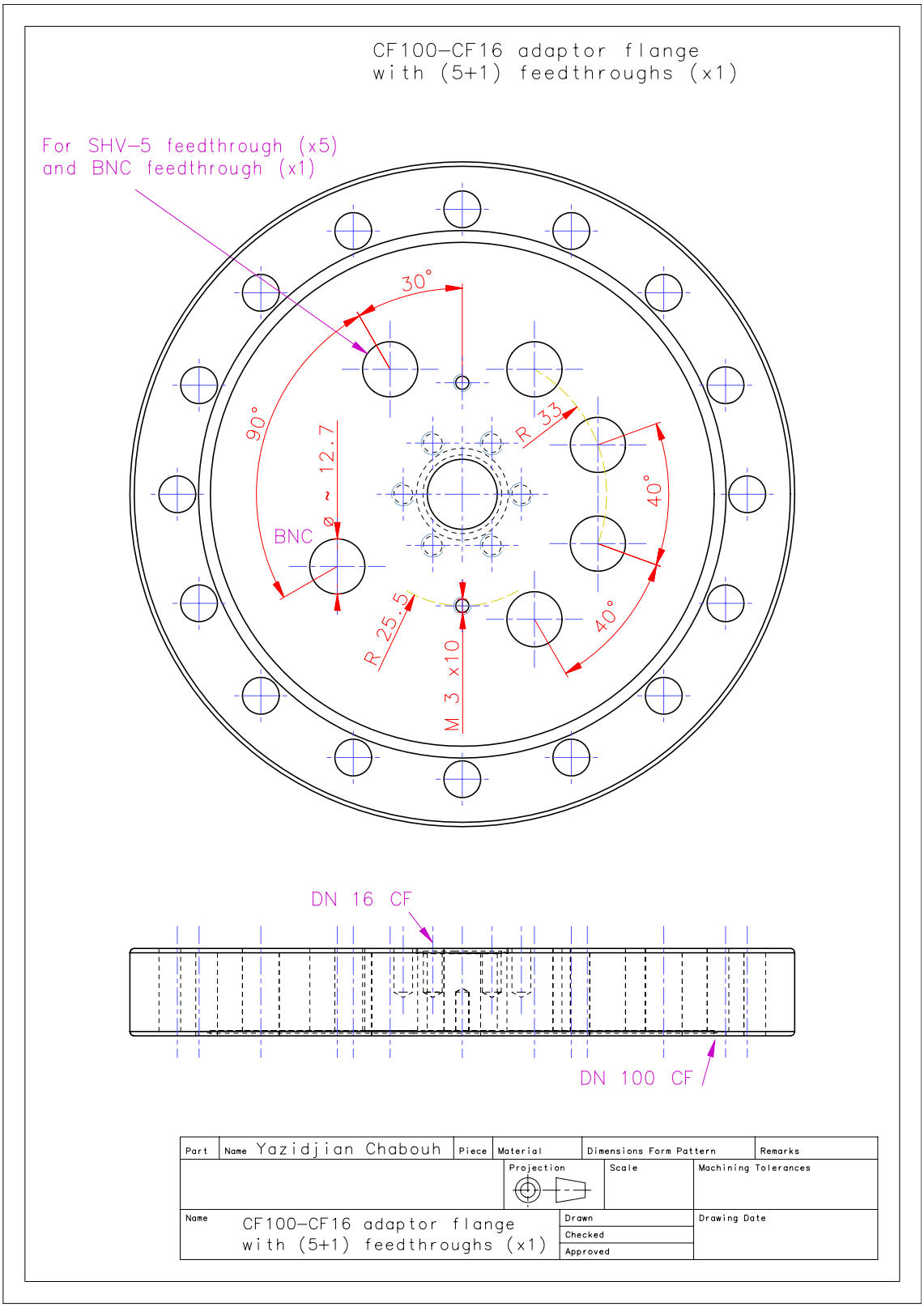

FIGURE D.4: ISOLTRAP *setup part 3: CF-100 to CF-16 adaptor flange (Channeltron).*

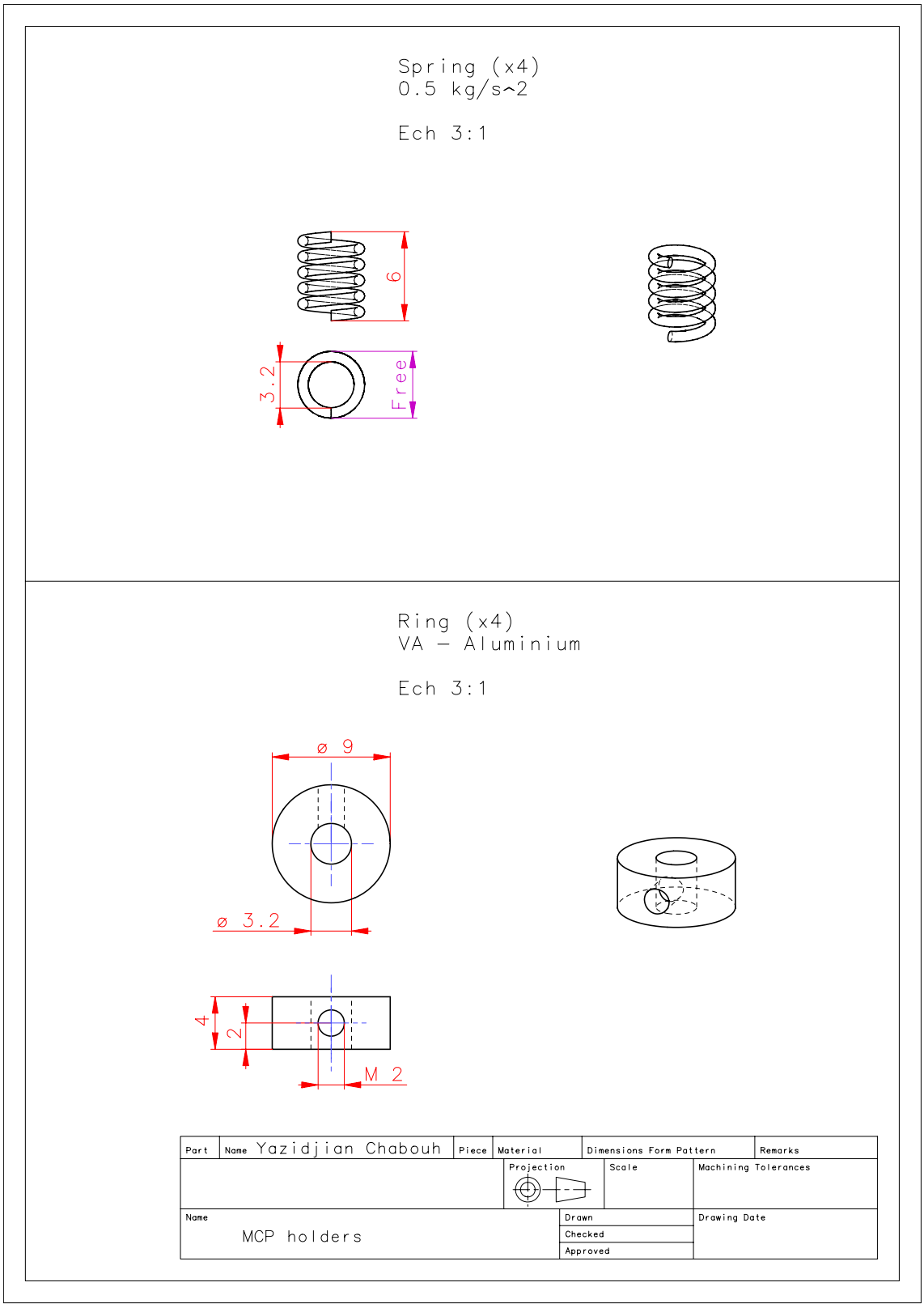

FIGURE D.5: ISOLTRAP *setup part 4: MCP holders.*

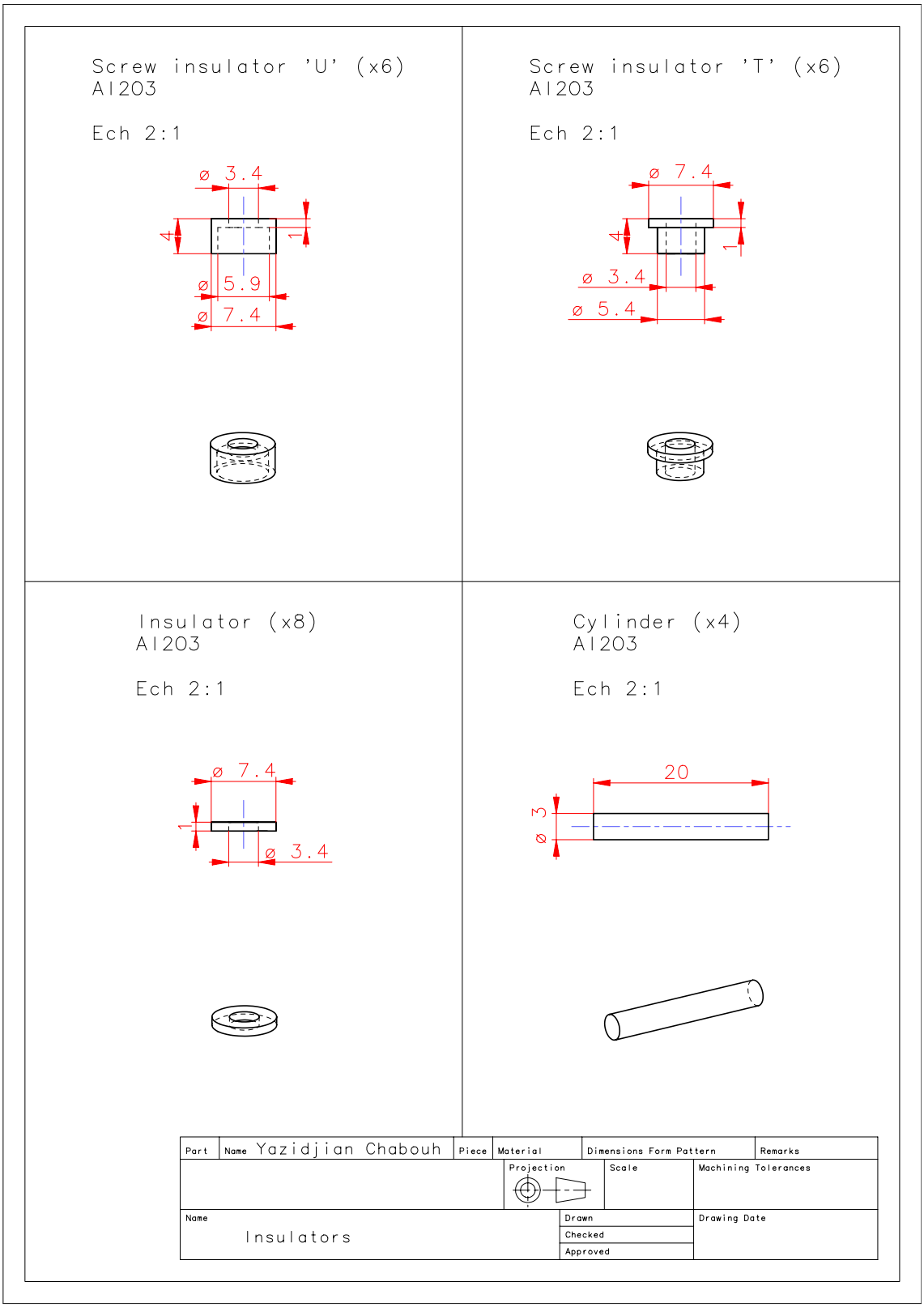

FIGURE D.6: ISOLTRAP *setup part 5: Insulators* Al_2O_3.

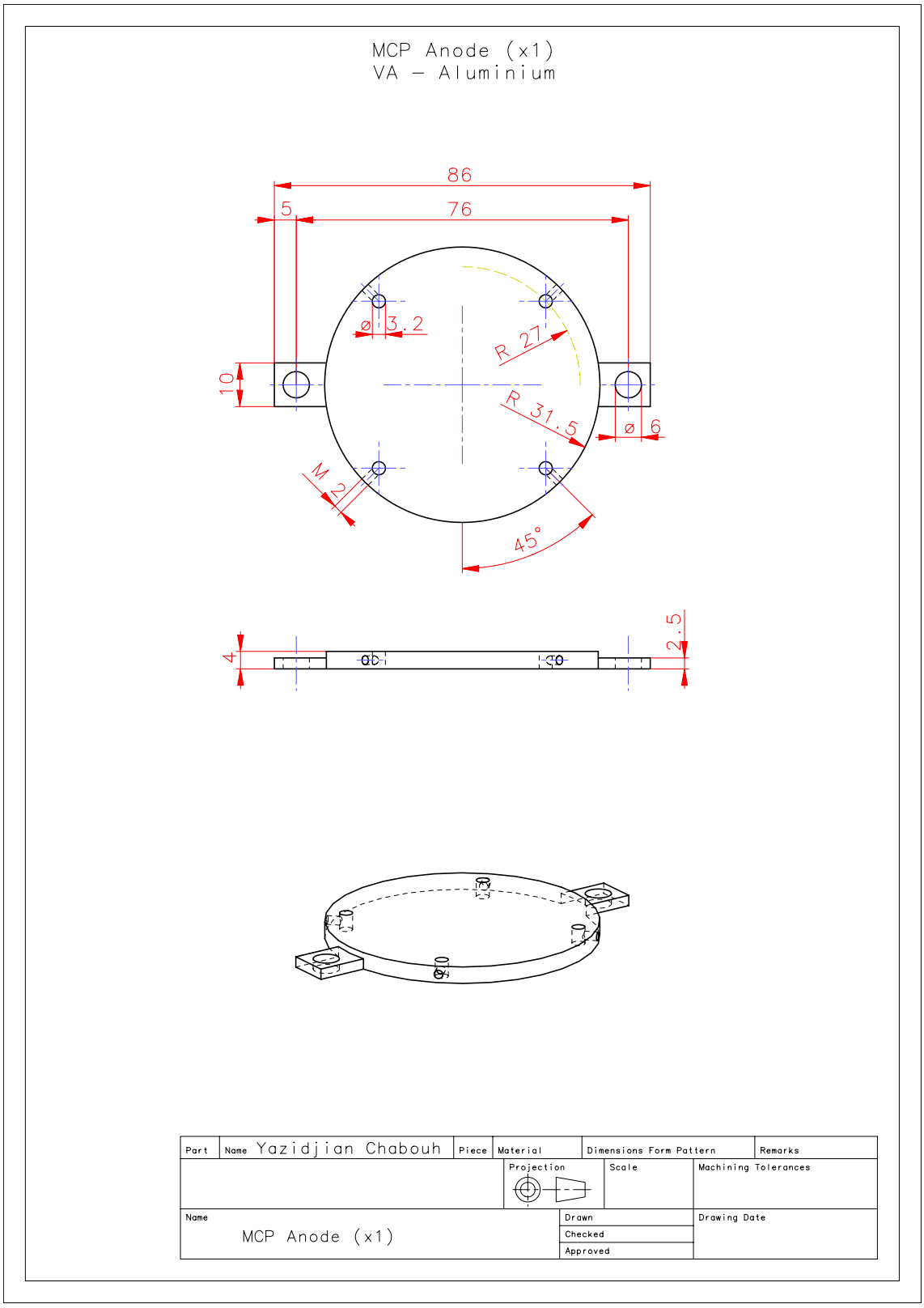

FIGURE D.7: ISOLTRAP *setup part 6: MCP anode.*

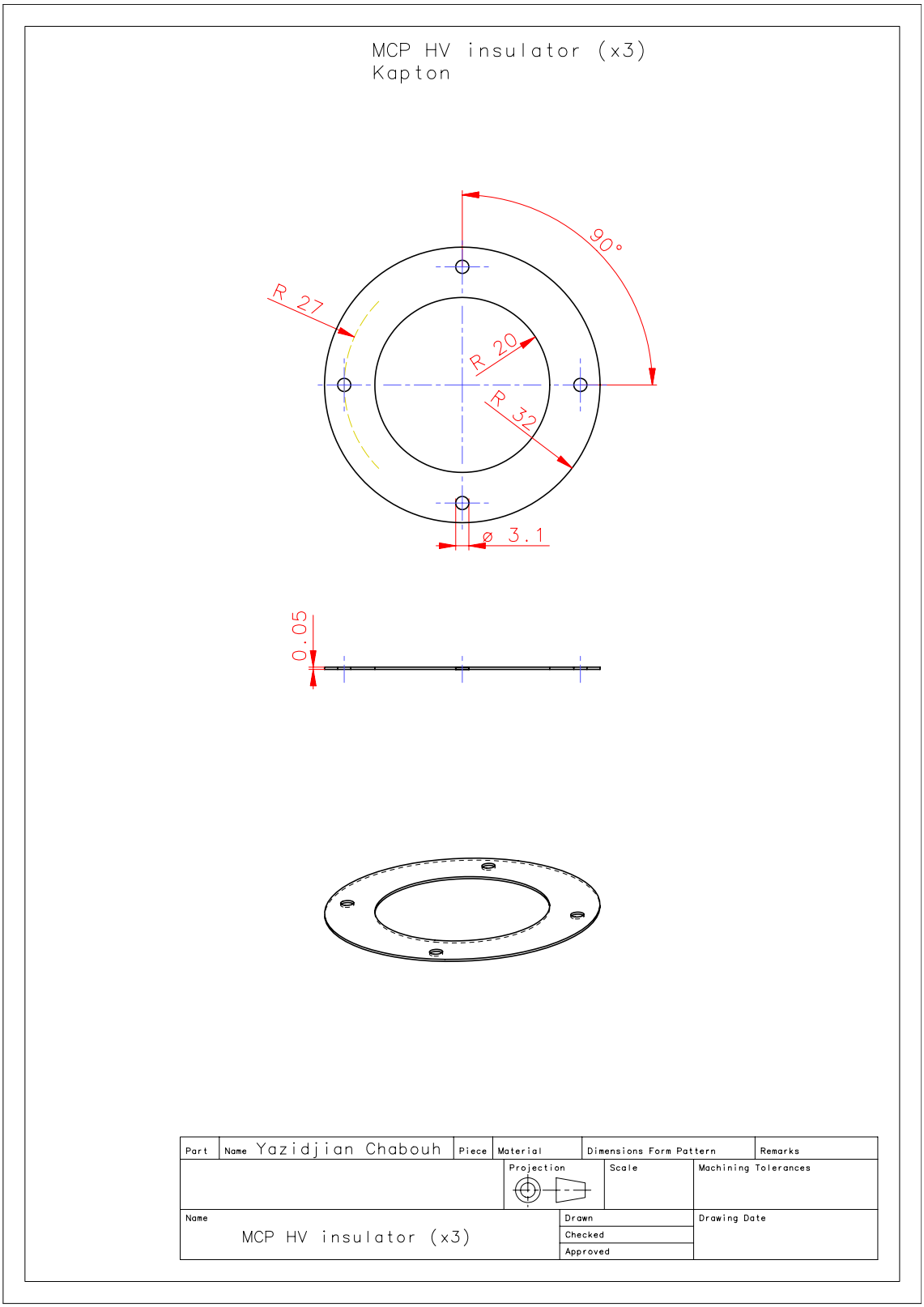

FIGURE D.8: ISOLTRAP *setup part 7: MCP HV insulators (Kapton).*

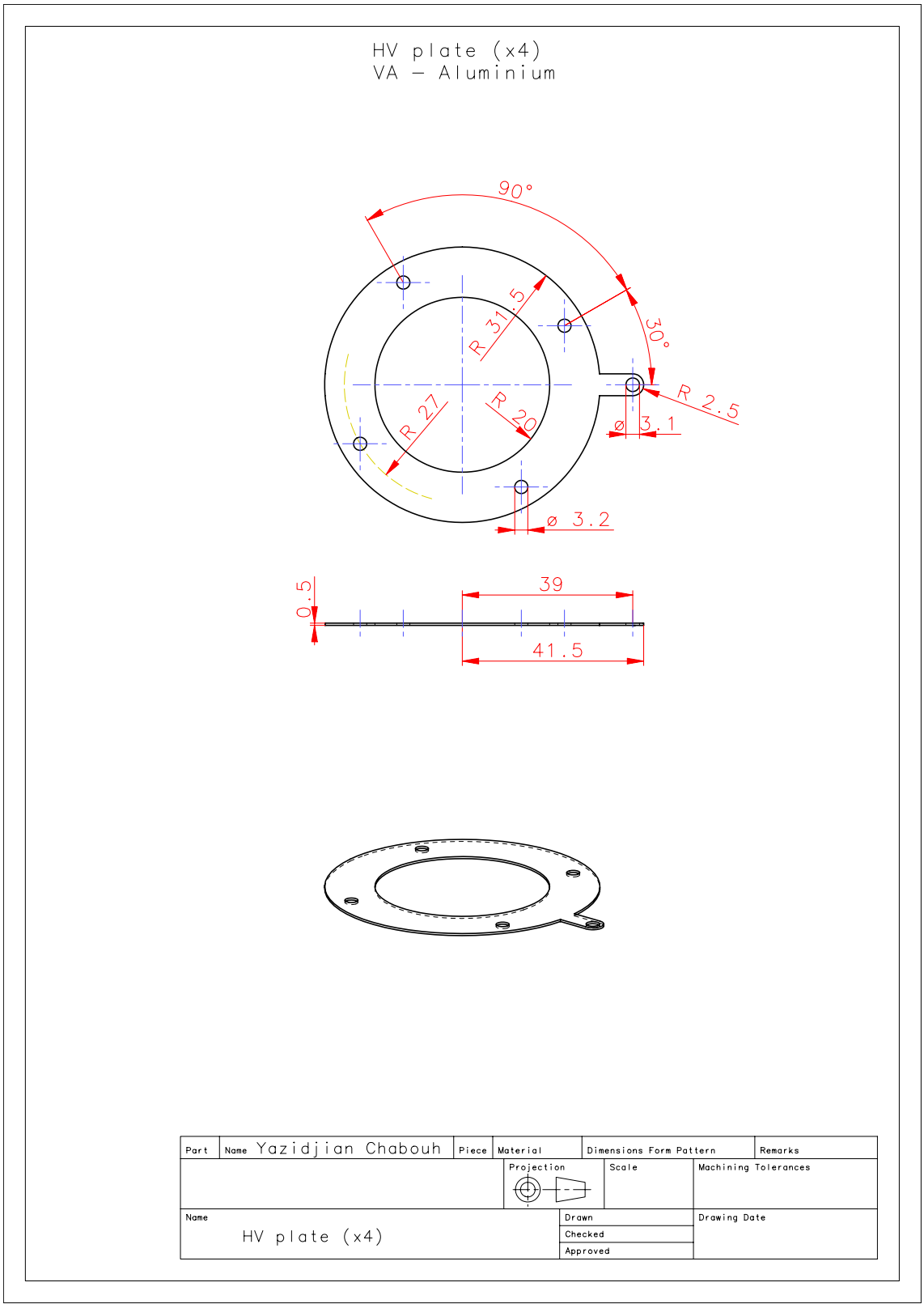

FIGURE D.9: ISOLTRAP *setup part 8: MCP HV plate.*

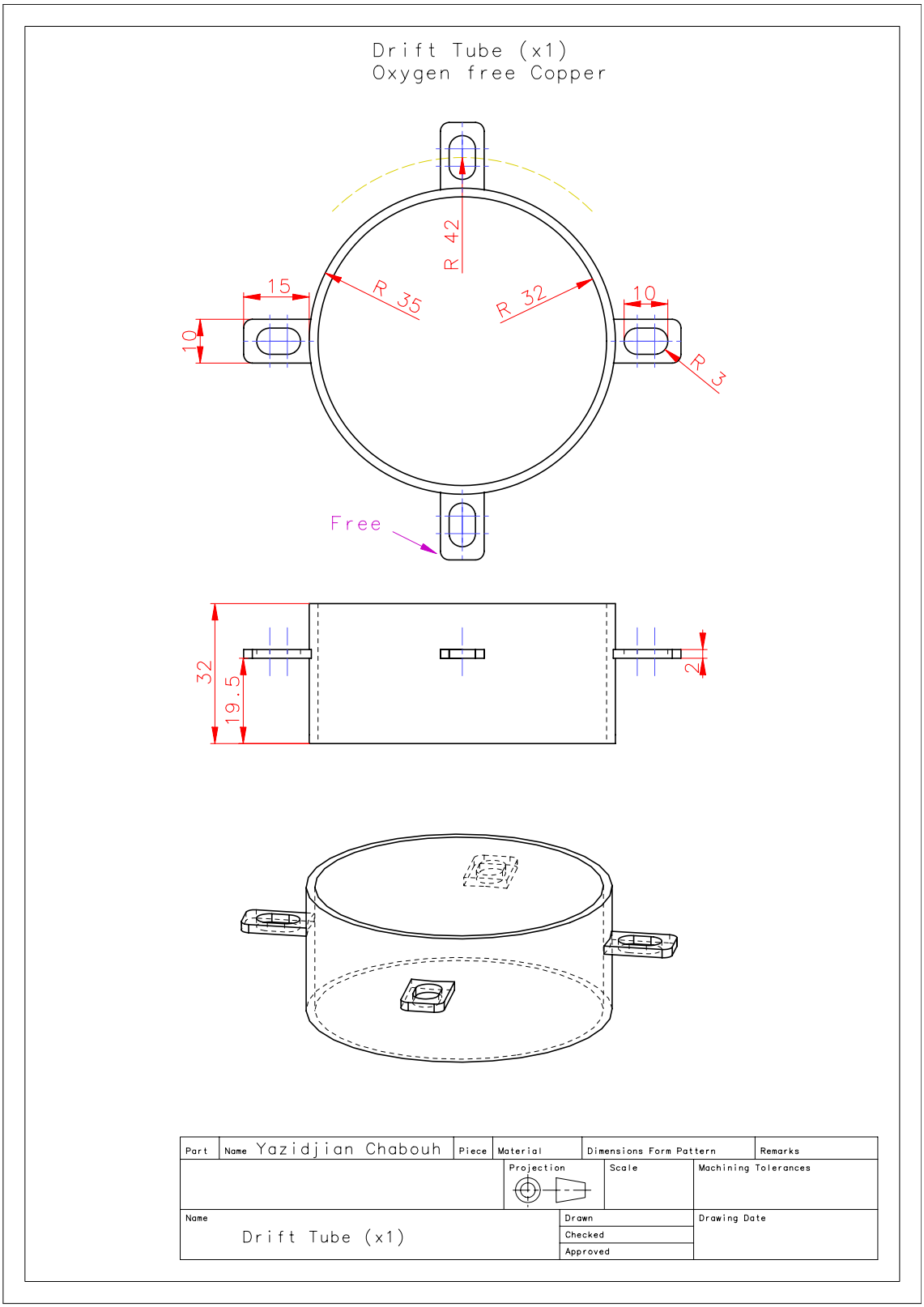

FIGURE D.10: ISOLTRAP *setup part 9: Drift tube.*

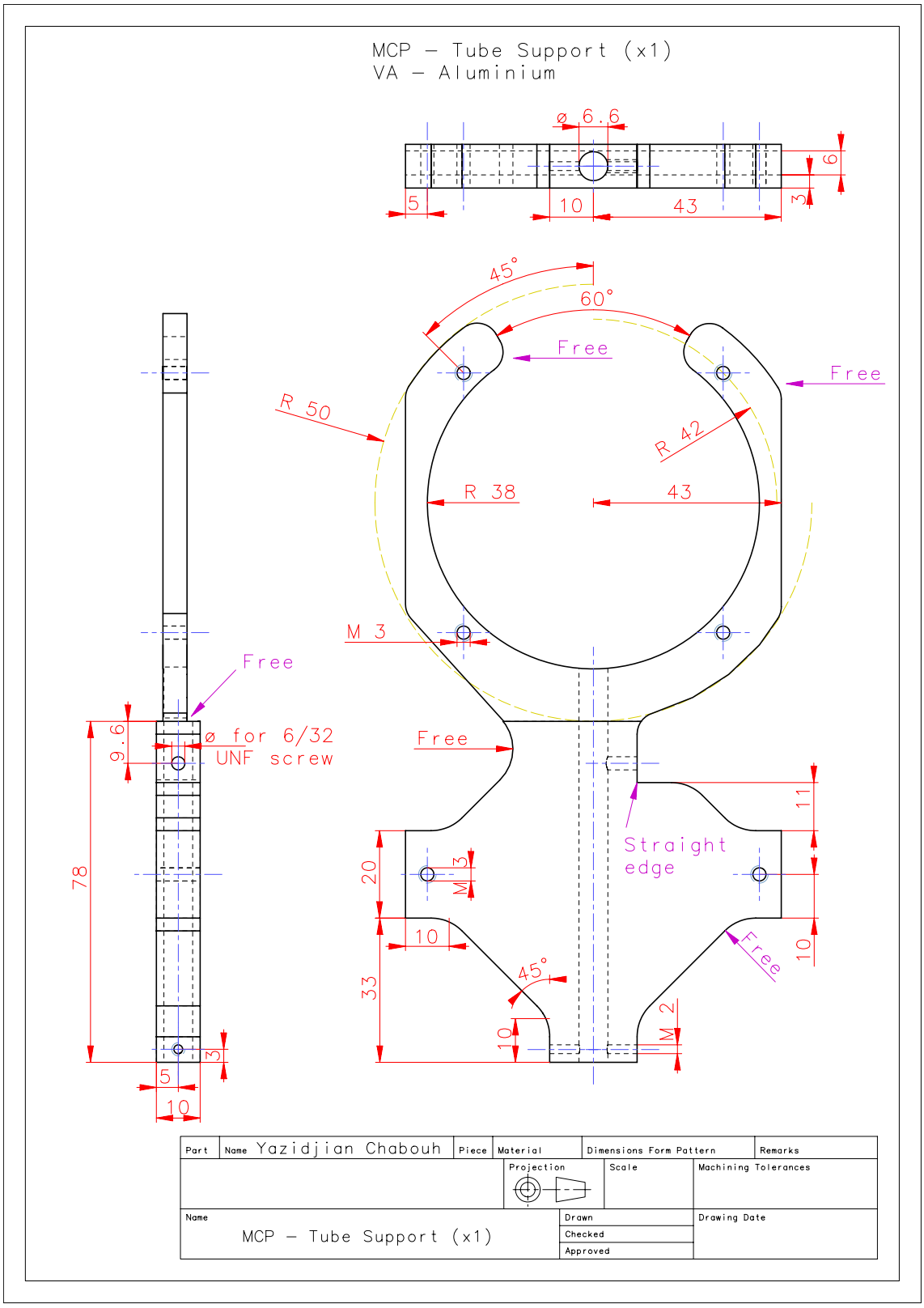

FIGURE D.11: ISOLTRAP *setup part 10: MCP – tube support.*

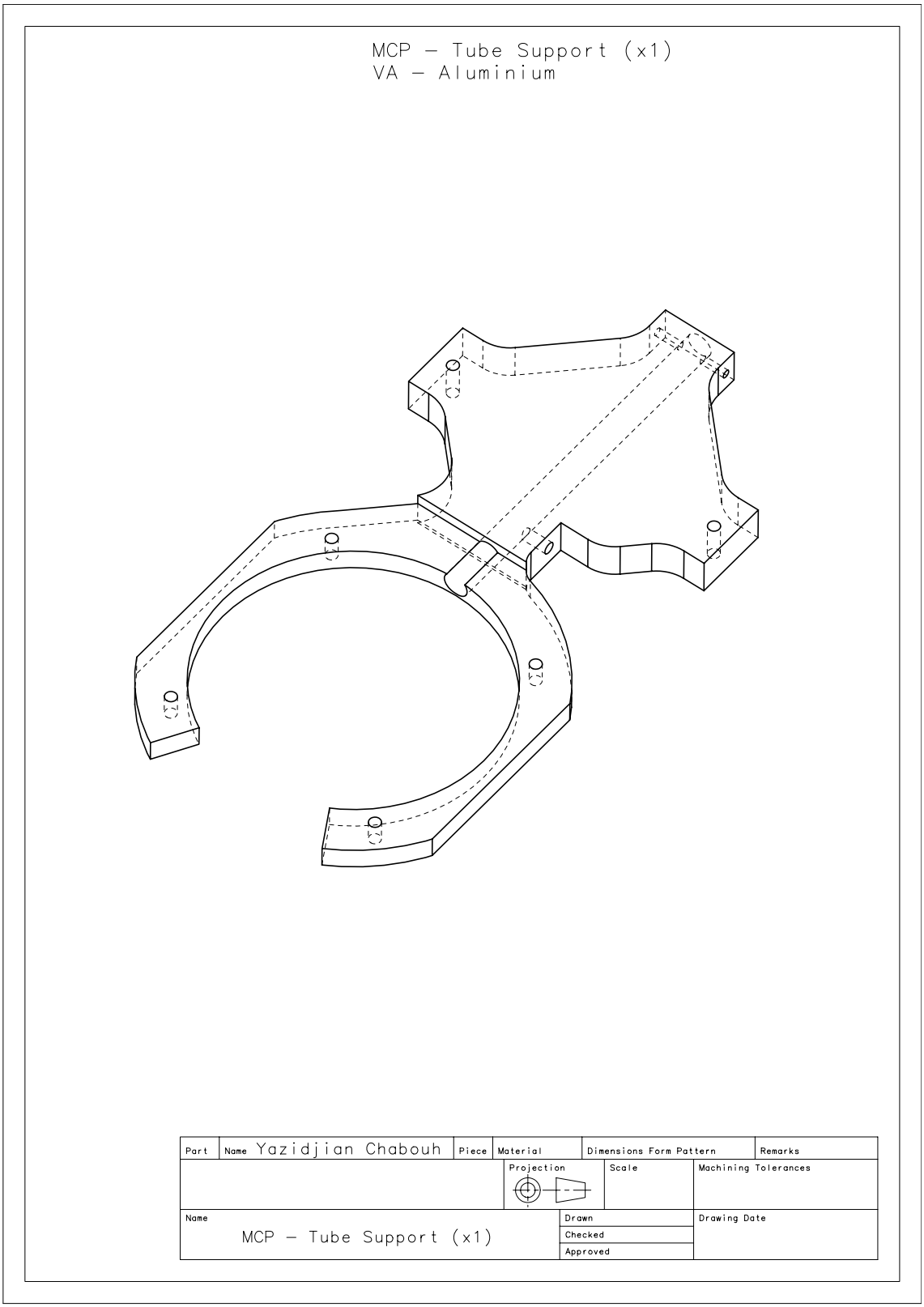

FIGURE D.12: ISOLTRAP *setup part 10: 3D-view, MCP – tube support.*

D.1.2 Mainz setup

A clone of this new detector setup has been also designed for Mainz. The main difference is that the cross where the setup has been mounted is a CF-150. Therefore, only the flanges, tube and Channeltron holders and the MCP-tube support have been scaled to fit. The insulators, MCP support, MCP HV insulators, MCP HV plates and MCP holders are the same.

- Channeltron support
- CF-150 linear feedthrough side flange
- CF-150 Channeltron side flange
- Drift tube
- MCP-tube support

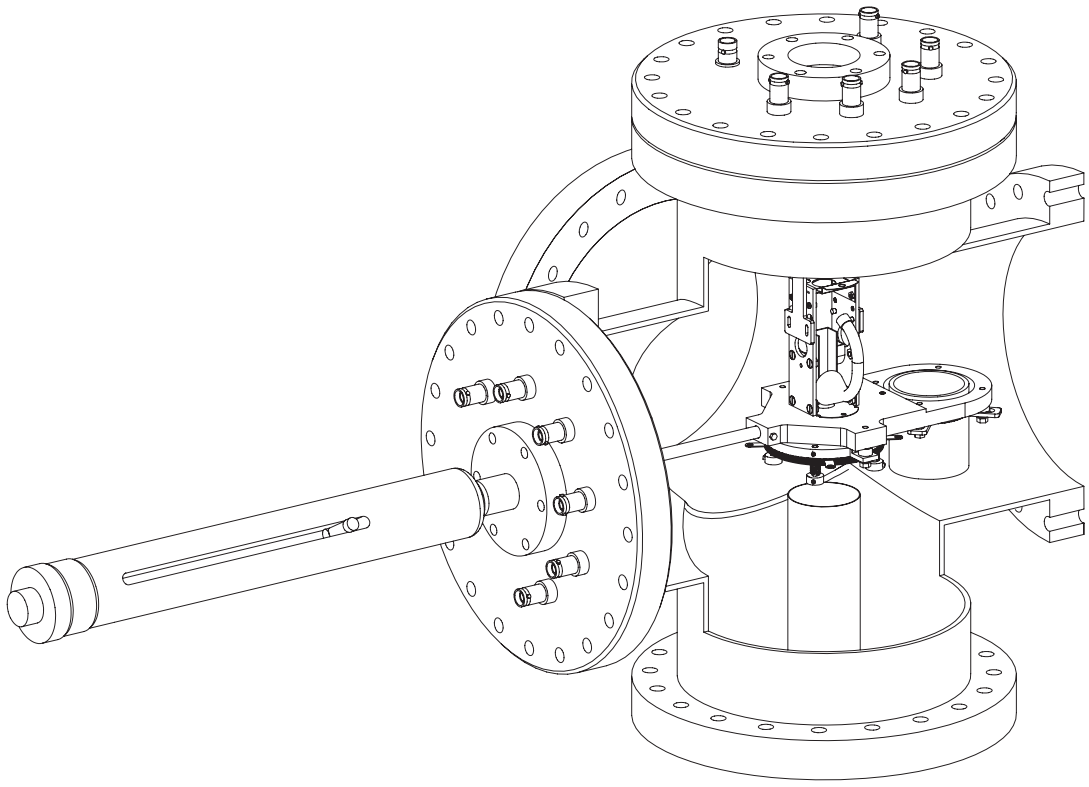

FIGURE D.13: *3D-view of the Mainz setup using the MCP detector.*

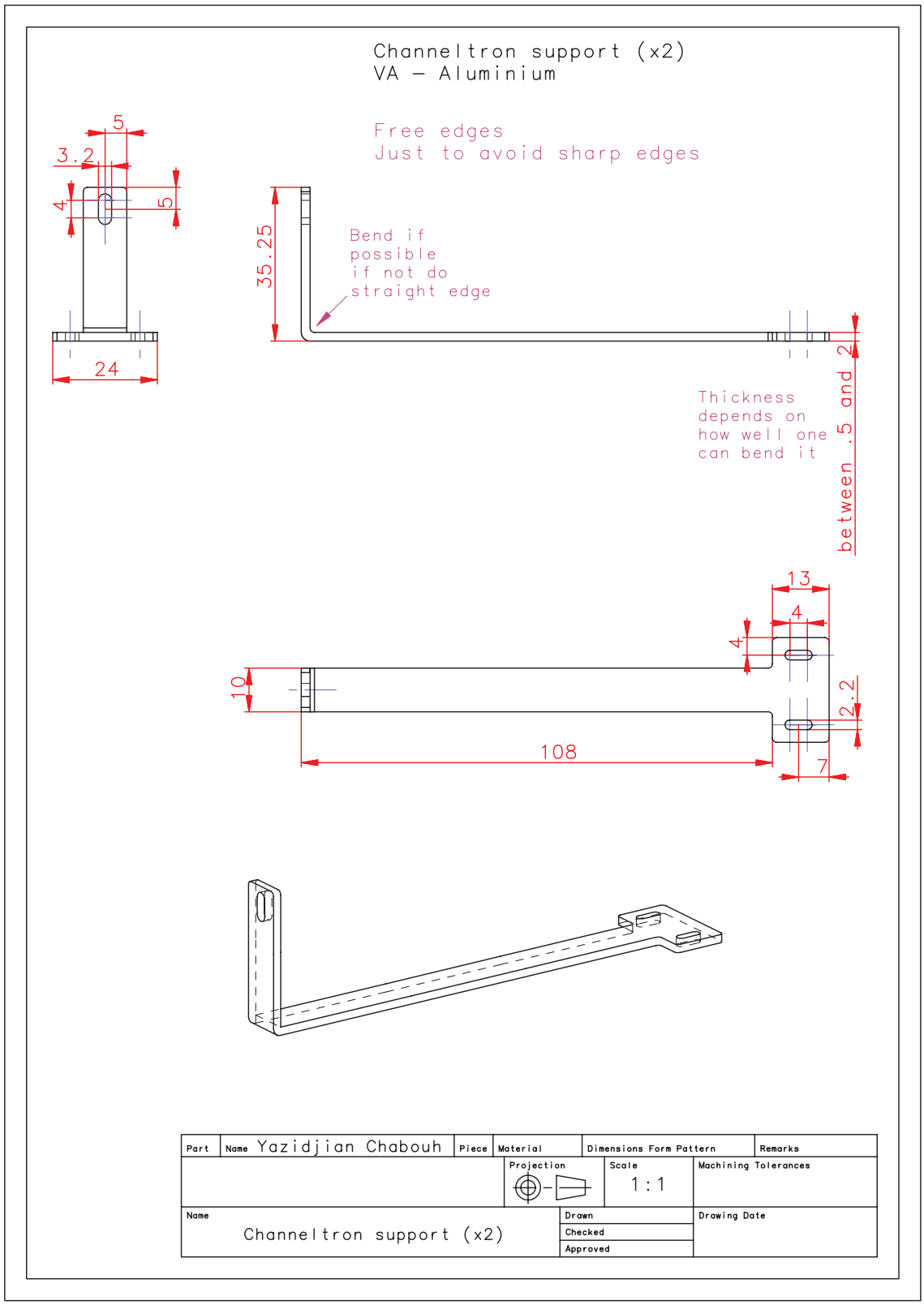

FIGURE D.14: *Mainz setup part 1: Channeltron support.*

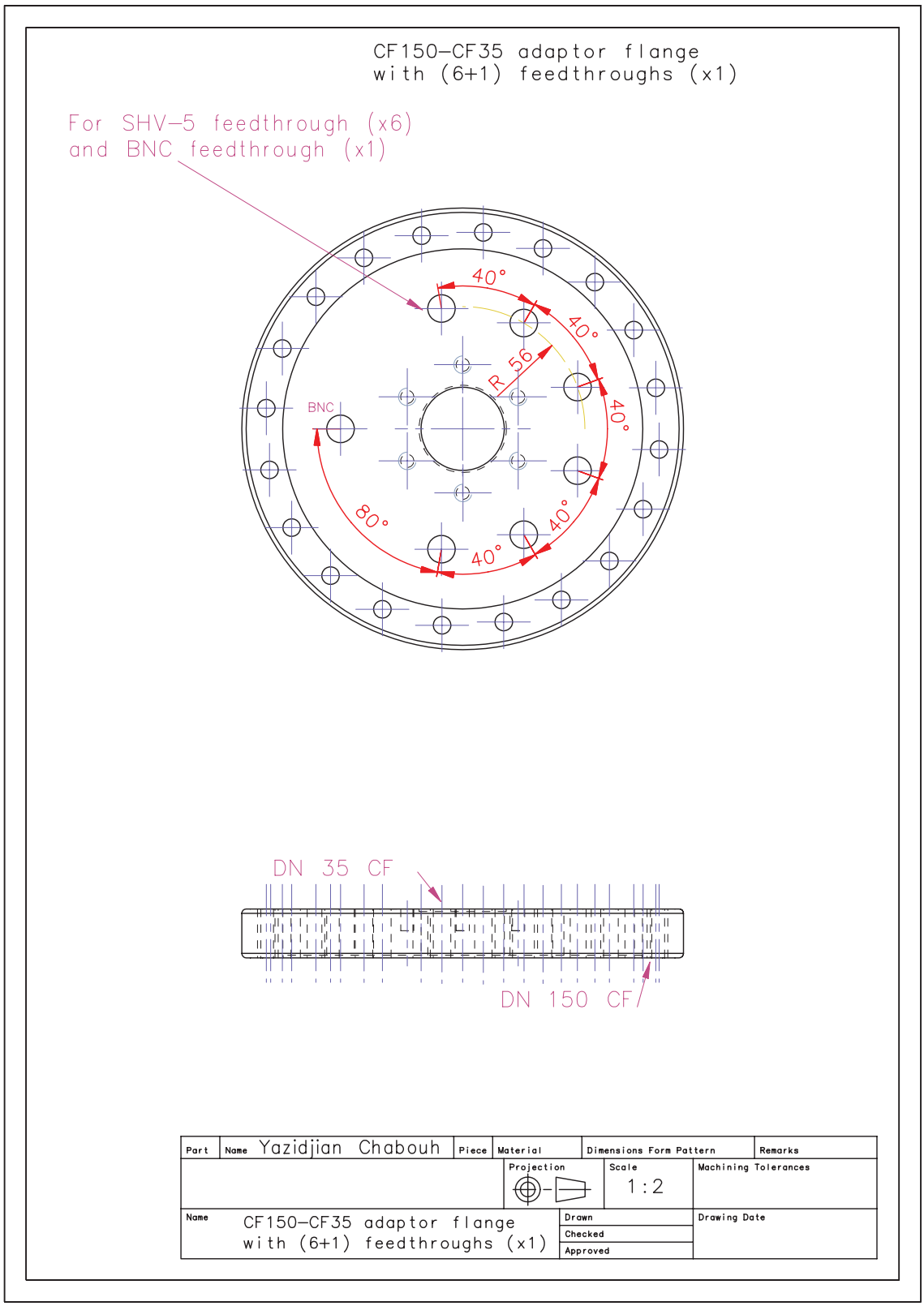

FIGURE D.15: *Mainz setup part 2: CF-150 to CF-35 adaptor flange (MCP).*

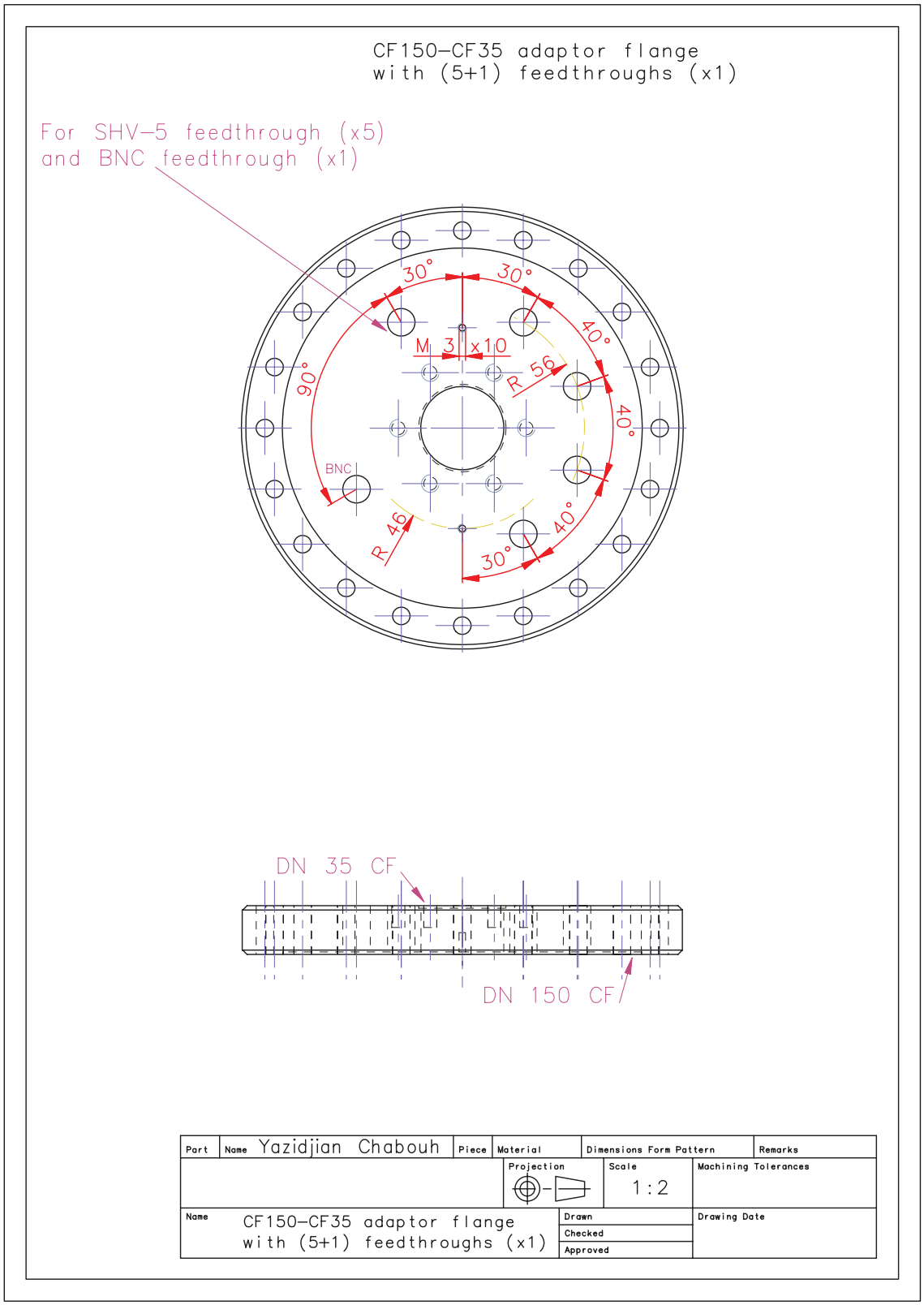

FIGURE D.16: *Mainz setup part 3: CF-150 to CF-35 adaptor flange (Channeltron).*

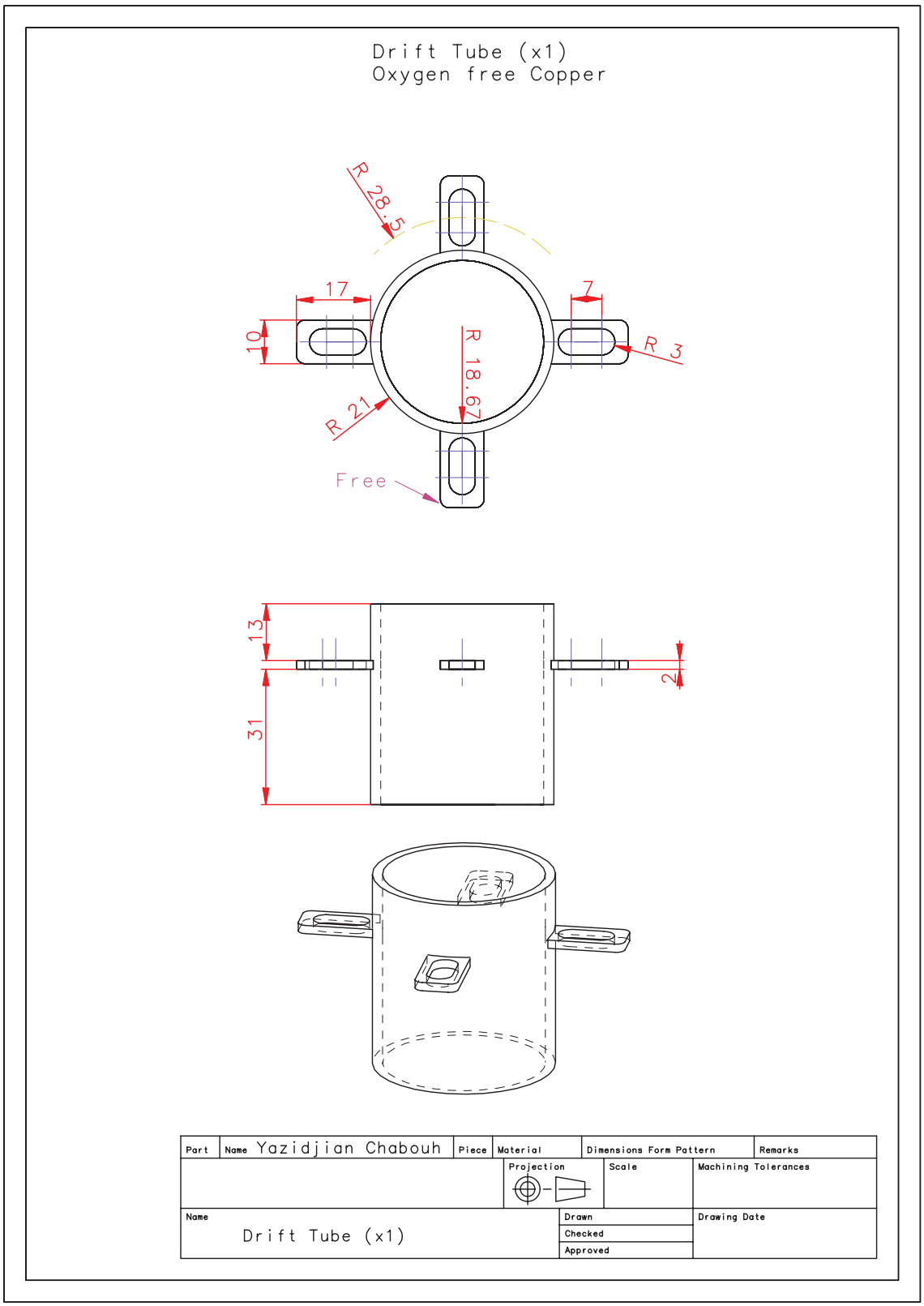

FIGURE D.17: *Mainz setup part 9: Drift tube.*

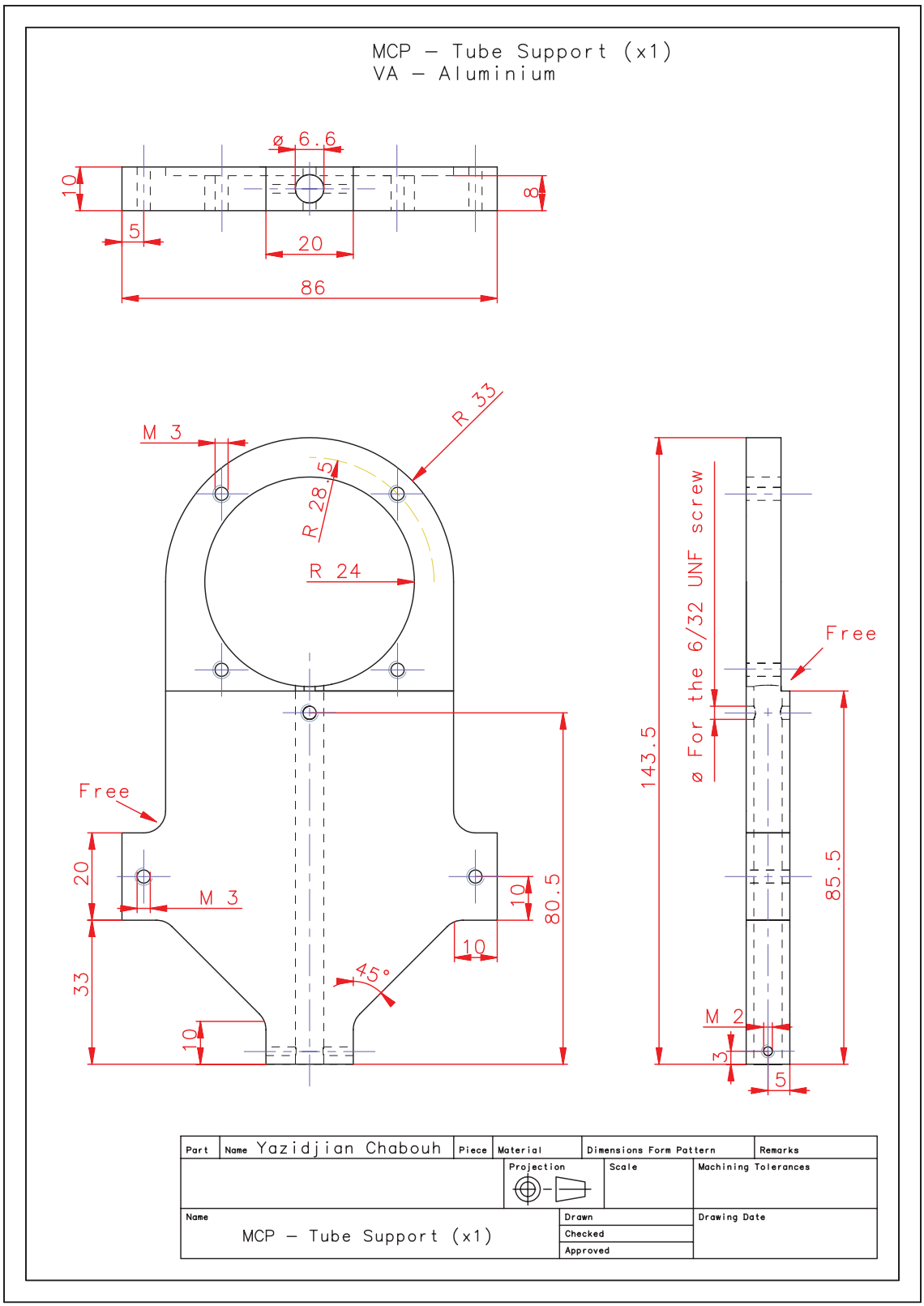

FIGURE D.18: *Mainz setup part 10: MCP – tube support.*

D.2 Pictures of the new setup at ISOLTRAP and Mainz

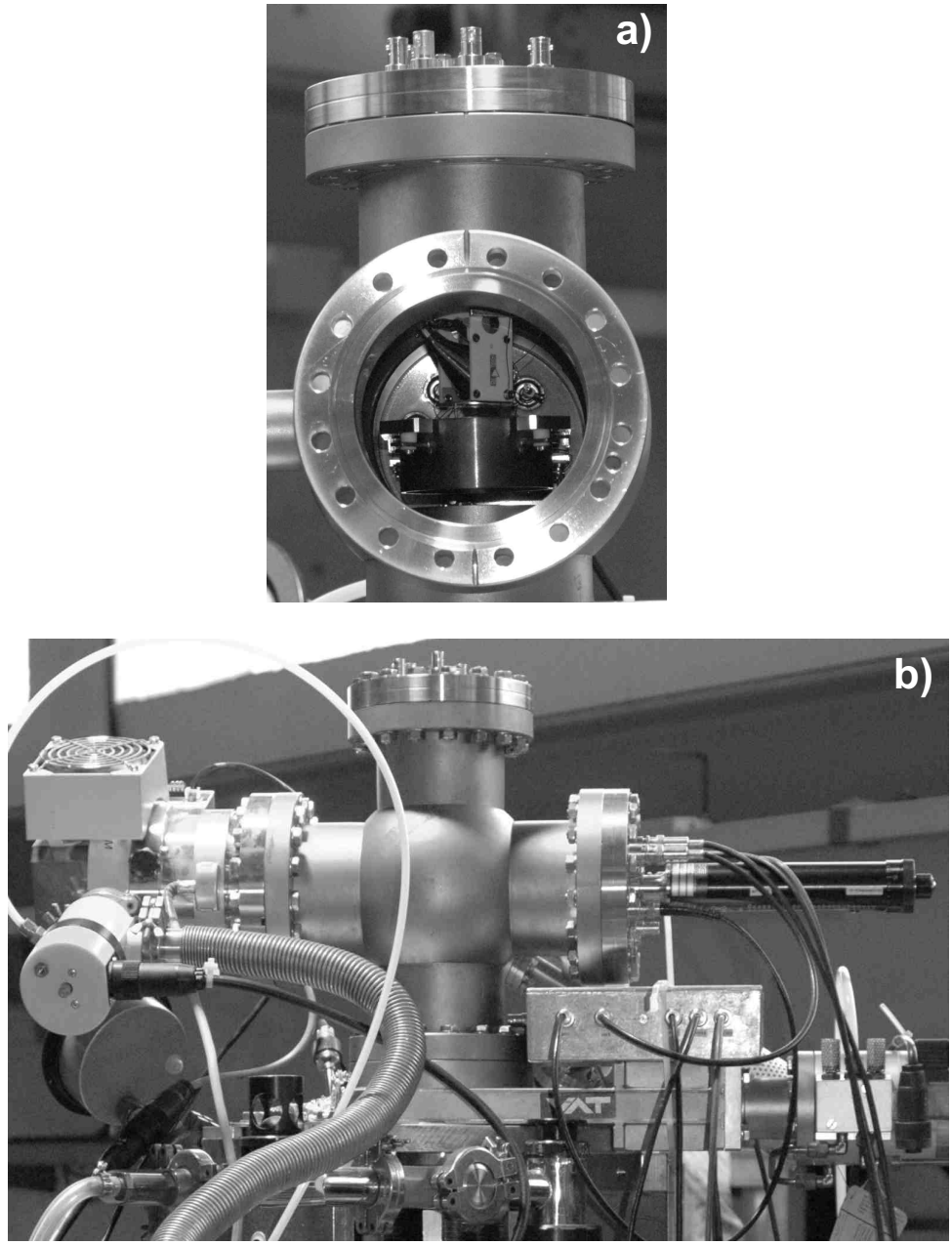

FIGURE D.19: *Pictures of the setup installed at* ISOLTRAP.
Photo a) shows the Channeltron detector together with the corresponding drift tube. The space constraint can be observed. b) represents the double cross where the new detection system is mounted.

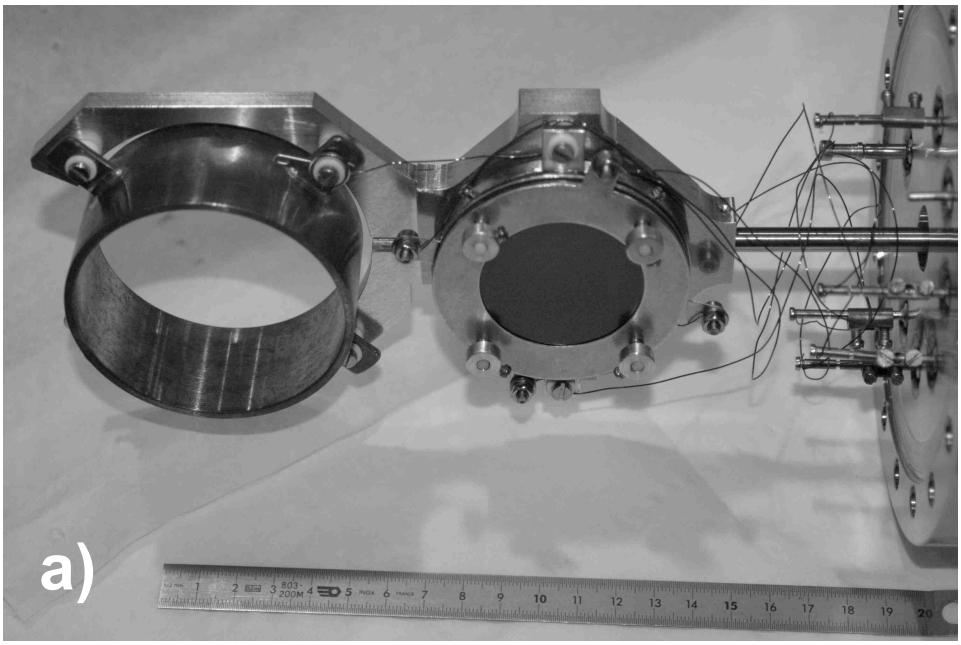

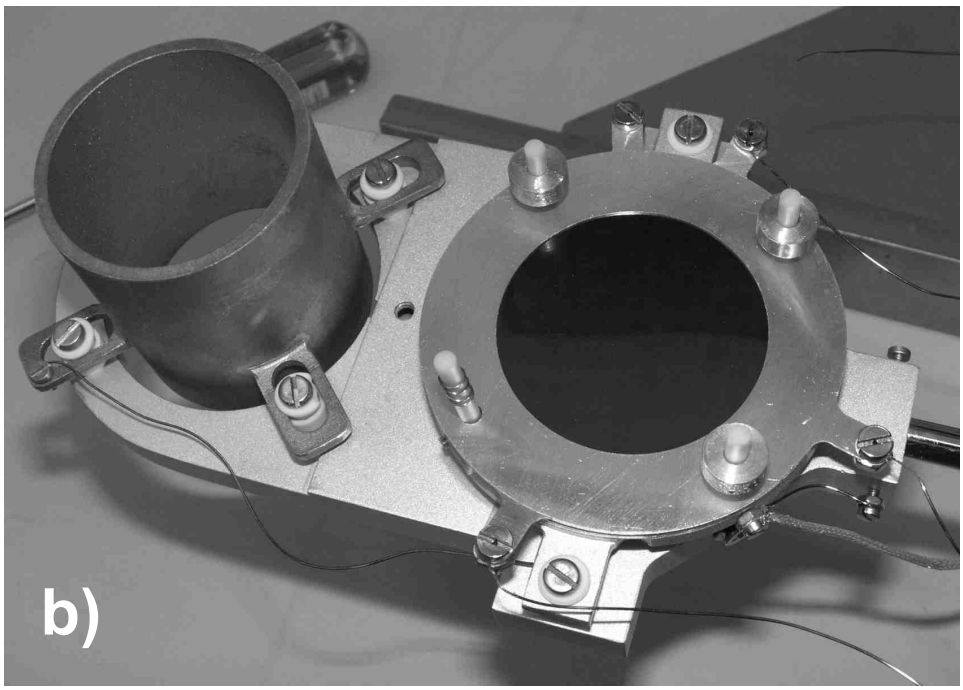

FIGURE D.20: *Pictures of the MCP – tube support.*
In a), the setup designed and machined for ISOLTRAP *is presented. In b), the corresponding setup for the Mainz experiment is shown.*

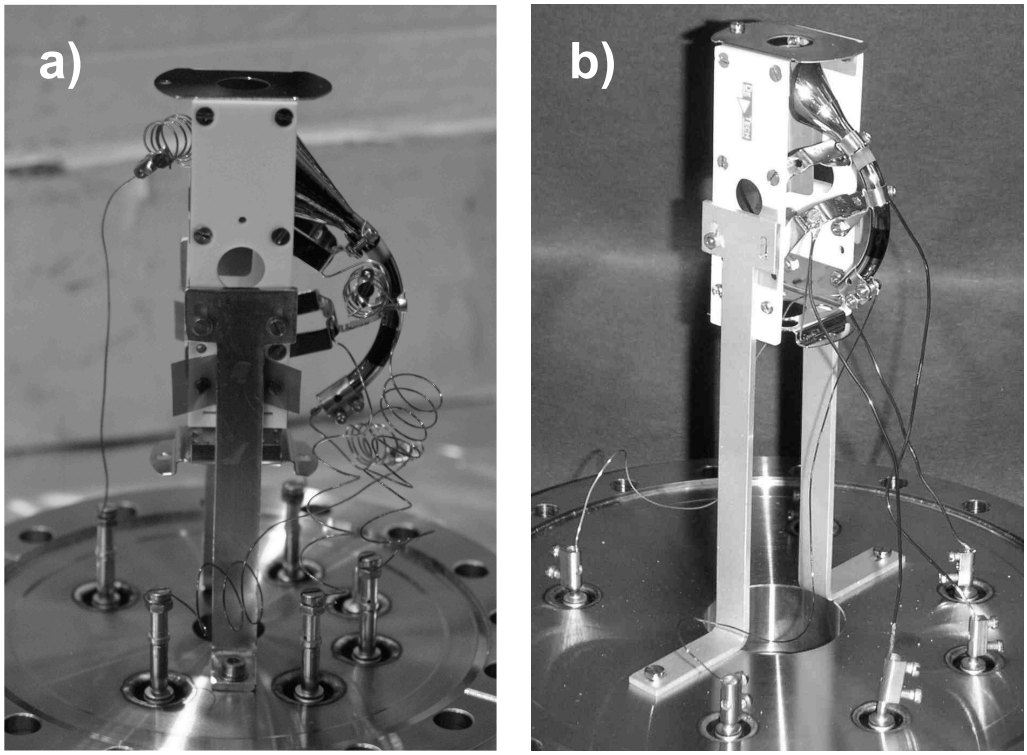

FIGURE D.21: *Pictures of the Channeltron.*
In a), the setup designed and machined for ISOLTRAP *is presented. In b), the corresponding setup for the Mainz experiment is shown.*

Appendix E

Cyclotron resonances of radioactive potassium isotopes

During the three-days-long run, the isotopic chain of potassium has been explored from ^{35}K for the neutron deficient side, up to ^{46}K for the neutron rich side. A total of 29 cyclotron resonances for radioactive potassium isotopes have been measured, together with 39 references of $^{39}K^{+}$. No ion contamination has been observed during the beam time.

TABLE E.1: *Frequency ratios relative to $^{39}K^{+}$ and mass excess of the potassium isotopes.*

Potassium isotope	$\tau_{1/2}$	Frequency ratio [a] ν_c^{ref}/ν_c	Number of resonances
^{35}K	178 ms	0.897 962 555 (14)	4
^{36}K	342 ms	0.923 455 783 (10)	3
^{37}K	1.22 s	0.948 917 615 (8)	7
^{38}K	7.64 m	0.974 472 668 (11)	3
^{43}K	22.3 h	1.102 584 812 (11)	3
^{44}K	22.1 m	1.128 271 957 (12)	4
^{45}K	17.3 m	1.153 914 244 (14)	3
^{46}K	105 s	1.179 612 626 (20)	2

[a] Using $^{39}K^{+}$ as a reference.

Figures E.1 to E.8 show a typical cyclotron resonance obtained for each radioactive potassium isotope. Fig. E.9 represents all reference masses recorded versus time. In the double scale y-axis the cyclotron frequency of $^{39}K^{+}$ and the magnetic field strength are plotted.

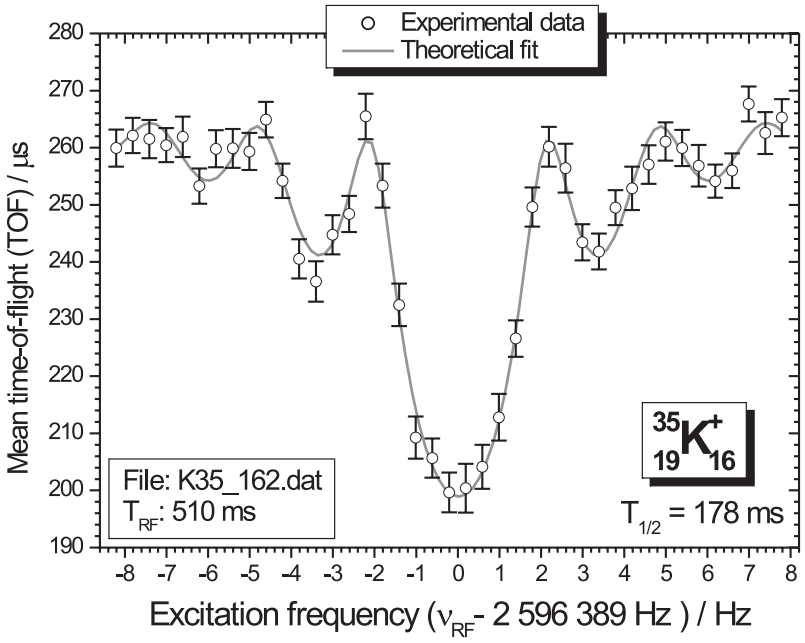

FIGURE E.1: *Cyclotron resonance for* $^{35}K^{+}$.

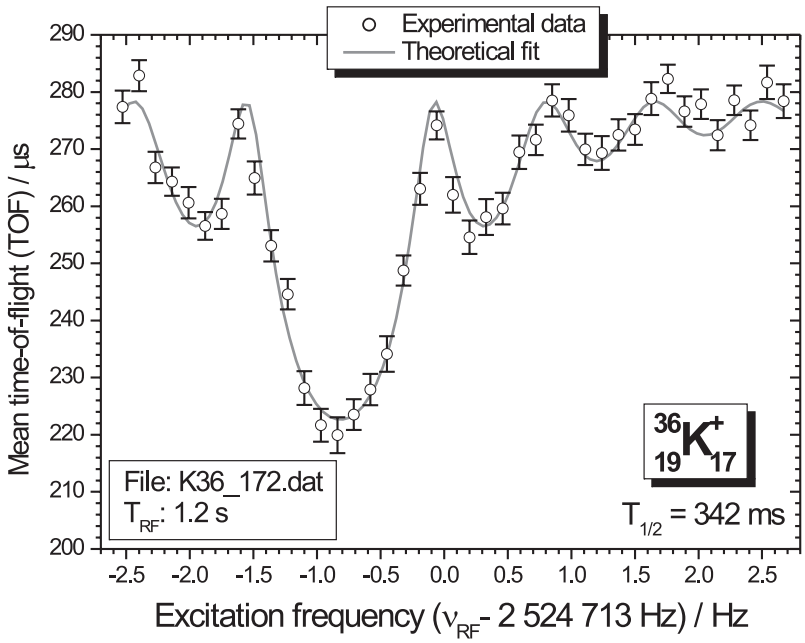

FIGURE E.2: *Cyclotron resonance for* $^{36}K^{+}$.

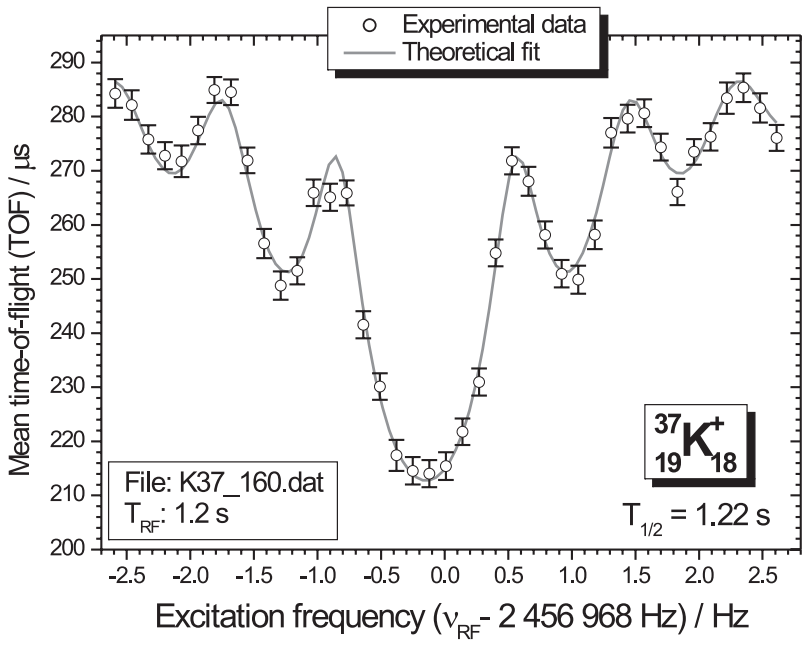

FIGURE E.3: *Cyclotron resonance for* $^{37}K^{+}$.

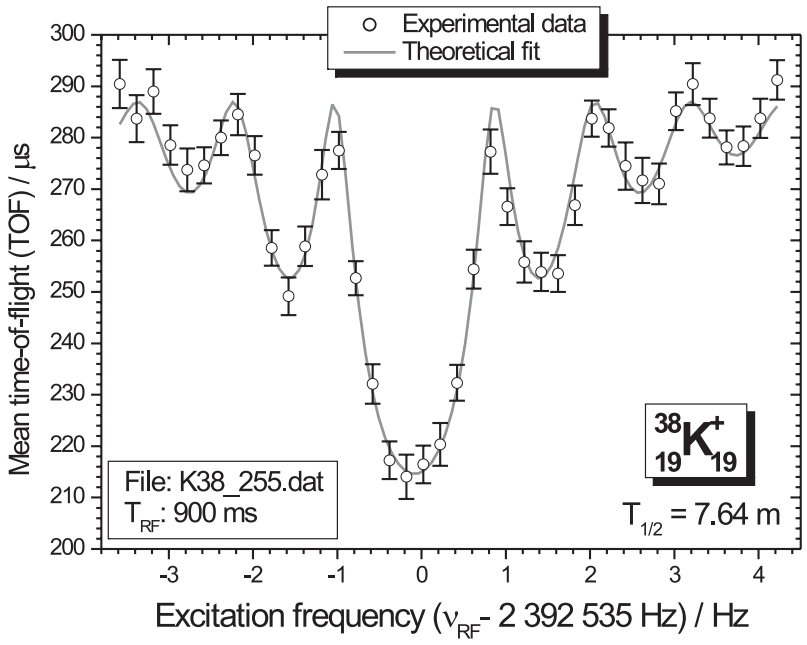

FIGURE E.4: *Cyclotron resonance for* $^{38}K^{+}$.

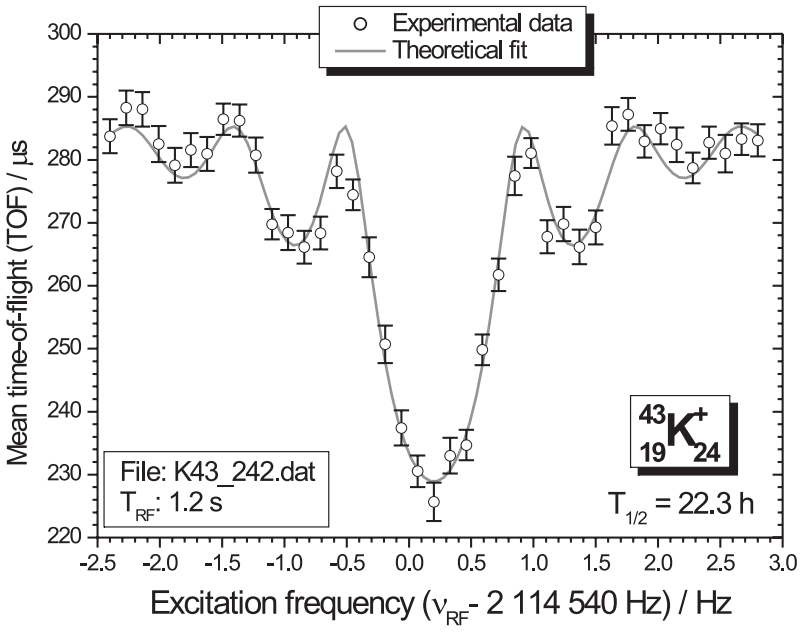

FIGURE E.5: *Cyclotron resonance for* $^{43}K^{+}$.

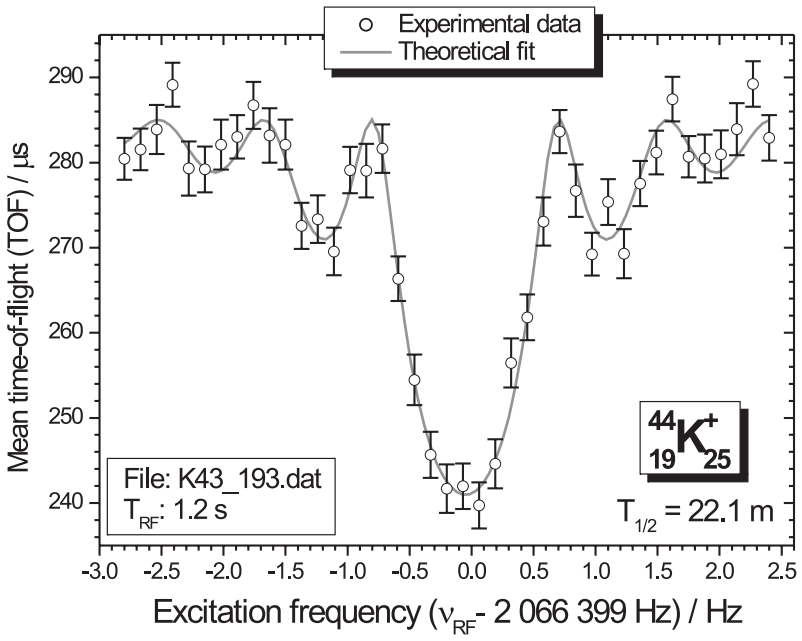

FIGURE E.6: *Cyclotron resonance for* $^{44}K^{+}$.

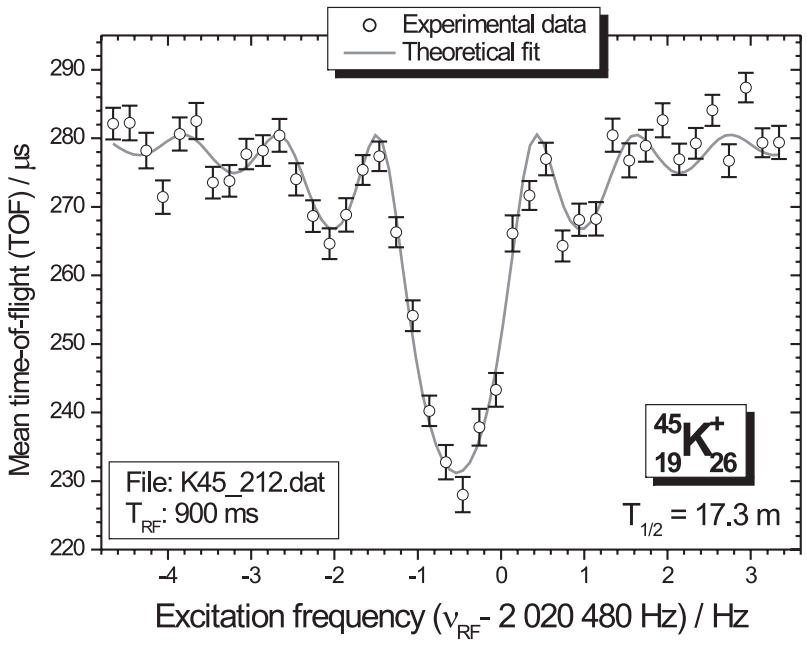

FIGURE E.7: *Cyclotron resonance for* $^{45}K^{+}$.

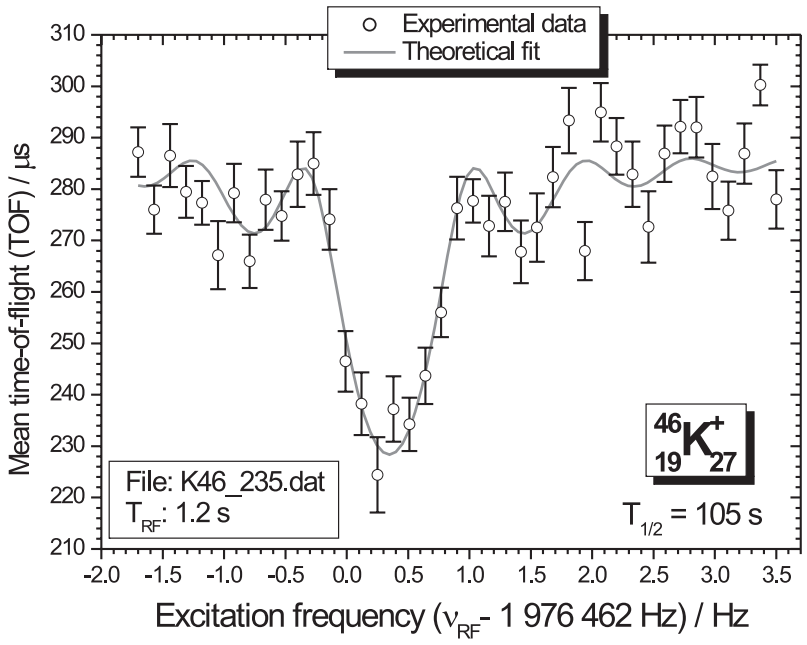

FIGURE E.8: *Cyclotron resonance for* $^{46}K^{+}$.

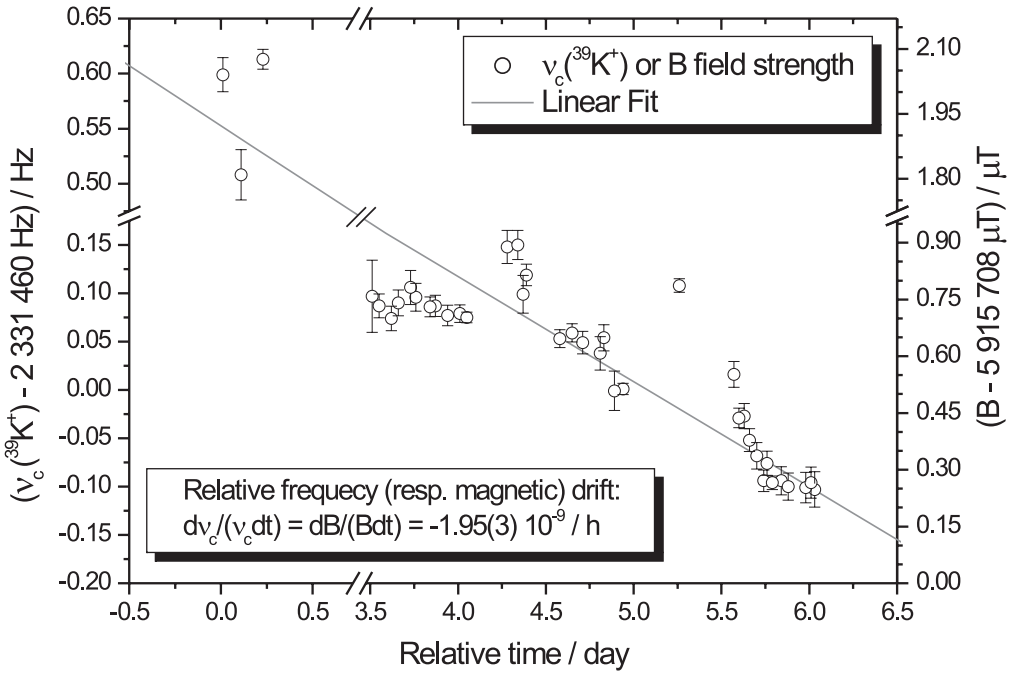

FIGURE E.9: *Magnetic field and/or frequency fluctuations for* ^{39}K.

Appendix F

List of publications

Articles

16 **High-accuracy mass measurements of neutron-rich Kr isotopes**
P. Delahaye, G. Audi, K. Blaum, F. Carrel, S. George, F. Herfurth, A. Herlert, A. Kellerbauer, H.-J. Kluge, D. Lunney, L. Schweikhard, and C. Yazidjian
Phys. Rev. C., submitted (2006).

15 **Towards high-accuracy mass spectrometry of highly charged short-lived ions at ISOLTRAP**
A. Herlert, S. Baruah, K. Blaum, M. Dworschak, S. George, C. Guénaut, U. Hager, F. Herfurth, A. Kellerbauer, S. Schwarz, L. Schweikhard, and C. Yazidjian
Int. J. Mass Spectrom. **251**, 131–137 (2006).

14 **Commissioning and first on-line test of the new ISOLTRAP control system**
C. Yazidjian, D. Beck, K. Blaum, H. Brand, F. Herfurth and S. Schwarz
Eur. Phys. J. A **25**, s01, 193–197 (2005).

13 **Extending the mass 'backbone' to short-lived nuclides with ISOLTRAP**
C. Guénaut, G. Audi, D. Beck, K. Blaum, G. Bollen, P. Delahaye, F. Herfurth, A. Kellerbauer, H.-J. Kluge, D. Lunney, S. Schwarz, L. Schweikhard, C. Weber, and C. Yazidjian
Eur. Phys. J. A **25**, s01, 35–36 (2005).

12 **Is $N = 40$ magic? The verdict from new, precision mass measurements**
C. Guénaut, G. Audi, D. Beck, K. Blaum, G. Bollen, P. Delahaye, F. Herfurth, A. Kellerbauer, H.-J. Kluge, D. Lunney, S. Schwarz, L. Schweikhard, C. Weber, and C. Yazidjian
Eur. Phys. J. A **25**, s01, 33–34 (2005).

11 Recent high-precision mass measurements with the Penning trap mass spectrometer ISOLTRAP
F. Herfurth, G. Audi, D. Beck, K. Blaum, G. Bollen, P. Delahaye, C. Guénaut, A. Kellerbauer, H.-J. Kluge, A. Herlert, D. Lunney, S. Schwarz, L. Schweikhard, and C. Yazidjian
Eur. Phys. J. A **25**, s01, 17–21 (2005).

10 ISOLTRAP pins down masses of exotic nuclides
K. Blaum, G. Audi, D. Beck, G. Bollen, M. Brodeur, P. Delahaye,S. George, C. Guénaut, F. Herfurth, A. Herlert, A. Kellerbauer, H-J. Kluge, D. Lunney, M. Mukherjee, D. Rodríguez, S. Schwarz, L. Schweikhard, and C. Yazidjian
J. Phys. G **31**, 1775–1778 (2005).

9 Mass measurements of $^{56-57}$Cr and the question of shell reincarnation at $N = 32$
C. Guénaut, G. Audi, D. Beck, K. Blaum, G. Bollen, P. Delahaye, F. Herfurth, A. Kellerbauer, H.-J. Kluge, D. Lunney, S. Schwarz, L. Schweikhard, and C. Yazidjian
J. Phys. G **31**, 1765–1770 (2005).

8 ISOLTRAP mass measurements of exotic nuclides at δm/m =10^{-8}
K. Blaum, G. Audi, D. Beck, G. Bollen, P. Delahaye, S. George, C. Guénaut, F. Herfurth, A. Herlert, A. Kellerbauer, H-J. Kluge, D. Lunney, M. Mukherjee, S. Schwarz, L. Schweikhard, and C. Yazidjian
Nucl. Phys. A **752**, 317c–320c (2005).

7 Mass spectrometry of atomic ions produced by in-trap decay of short-lived nuclides
A. Herlert, D. Beck, K. Blaum, F. Carrel, P. Delahaye, S. George, C. Guénaut, F. Herfurth, A. Kellerbauer, H.-J. Kluge, D. Lunney, M. Mukherjee, L. Schweikhard, and C. Yazidjian
New J. Phys. **7**, 44, 1–11 (2005).

6 Masses along the rp-process path and large scale surveys on Cu, Ni and Ga with ISOLTRAP
F. Herfurth, G. Audi, D. Beck, K. Blaum, G. Bollen, P. Delahaye, C. Guénaut, A. Kellerbauer, H.-J. Kluge, D. Lunney, D. Rodríguez, S. Schwarz, L. Schweikhard, G. Sikler, and C. Yazidjian
Nucl. Phys. A **746**, 487c–492c (2004).

5 Recent results from the Penning trap mass spectrometer ISOLTRAP
K. Blaum, G. Audi, D. Beck, G. Bollen, P. Delahaye, C. Guénaut, F. Herfurth, A. Kellerbauer, H.-J. Kluge, D. Lunney, D. Rodríguez, S. Schwarz, L. Schweikhard, C. Weber, and C. Yazidjian
Nucl. Phys. A **746**, 305c-310c (2004).

4 The mass of ^{22}Mg
M. Mukherjee, A. Kellerbauer, D. Beck, K. Blaum, G. Bollen, F. Carrel, P. Delahaye, J. Dilling, S. George, C. Guénaut, F. Herfurth, A. Herlert, H.-J. Kluge, U. Köster, D. Lunney, S. Schwarz, L. Schweikhard, and C. Yazidjian
Phys. Rev. Lett. **94**, 150801 1–4 (2004).

3 Population inversion of nuclear states by a Penning trap mass spectrometer
K. Blaum, D. Beck, G. Bollen, P. Delahaye, C. Guénaut, F. Herfurth, A. Kellerbauer, H.-J. Kluge, D. Lunney, S. Schwarz, L. Schweikhard, and C. Yazidjian
Europhys. Lett. **67**, 586–592 (2004).

2 Direct Mass Measurements on the Superallowed Emitter ^{74}Rb and Its Daughter ^{74}Kr: Isospin Symmetry-Breaking Correction for Standard-Model Tests
A. Kellerbauer, G. Audi, D. Beck, K. Blaum, G. Bollen, B.A. Brown, P. Delahaye, C. Guénaut, F. Herfurth, D. Lunney, H.-J. Kluge, S. Schwarz, L. Schweikhard, and C. Yazidjian
Phys. Rev. Lett. **93**, 072502 1-4 (2004).

1 Unambiguous identification of three β-decaying isomers in ^{70}Cu
J. Van Roosbroeck, C. Guénaut, G. Audi, D. Beck, K. Blaum, G. Bollen, J. Cederkall, P. Delahaye, H. De Witte, D. Fedorov, V.N. Fedoseyev, S. Franchoo, H. Fynbo, M. Gorska, F. Herfurth, K. Heyde, M. Huyse, A. Kellerbauer, H.-J. Kluge, U. Köster, K. Kruglov, D. Lunney, A. De Maesschalck, V.I. Mishin, W.F. Müller, S. Nagy, S. Schwarz, L. Schweikhard, N.A. Smirnova, K. Van de Vel, P. Van Duppen, A. Van Dyck, W.B. Walters, L. Weissmann, and C. Yazidjian
Phys. Rev. Lett. **92**, 112501 1-4 (2004).

Proceedings

7 High-precision mass measurements for reliable nuclear astrophysics calculations
A. Herlert, S. Baruah, K. Blaum, M. Breitenfeldt, P. Delahaye, M. Dworschak, S. George, C. Guénaut, U. Hager, F. Herfurth, A. Kellerbauer, H.-J. Kluge, D. Lunney, R. Savreux, S. Schwarz, L. Schweikhard, and C. Yazidjian
Proceedings of the International Symposium on Nuclear Astrophysics - Nuclei in the Cosmos - IX **NIC-IX**, 051 (2006).

6 High-precision mass measurements on neutron deficient neon isotopes
A. Herlert, S. Baruah, K. Blaum, P. Delahaye, S. George, C. Guénaut, F. Herfurth, H.-J. Kluge, D. Lunney, S. Schwarz, L. Schweikhard, C. Weber, and C. Yazidjian
FINUSTAR Conference, Kos, Greece 2005
AIP Conference Procedings **831**, 152–156 (2006).

5 ISOLTRAP Mass Measurements for Weak-Interaction Studies
A. Kellerbauer, G. Audi, D. Beck, K. Blaum, G. Bollen, P. Delahaye, S. George, C. Guénaut, F. Herfurth, A. Herlert, H.-J. Kluge, D. Lunney, M. Mukherjee, D. Rodríguez, S. Schwarz, L. Schweikhard, C. Weber, and C. Yazidjian
FINUSTAR Conference, Kos, Greece 2005
AIP Conference Procedings **831**, 49–54 (2006).

4 A Precision Mass Balance: The Penning Trap Mass Spectrometer ISOLTRAP
C. Yazidjian
Submitted to the Marie Curie Action Conference Proceedings (European Commission) (2005).

3 The CS framework – a LabVIEW based approach to SCADA systems
D. Beck, H. Brand, S. Götte, F. Herfurth, C. Rauth, R. Savreux, S. Schwarz, and C. Yazidjian
The 10th International Conference on Accelerator and Large Experimental Physics Control Systems

2 Laser ionization and Penning trap mass spectrometry – A fruitful combination for isomer separation and high-precision mass measurements
K. Blaum, D. Beck, G. Bollen, P. Delahaye, C. Guénaut, F. Herfurth, A. Kellerbauer, H.-J. Kluge, U. Köster, D. Lunney, S. Schwarz, L. Schweikhard, and C. Yazidjian
Proceedings of the V Int. Workshop on "Prospects for the development of laser methods in the study of nuclear matter", Poznan/Poland 2004
Hyp. Int. **162**, 173–179 (2005).

1 Study of ground- and low-lying nuclear states by combining laser ionization and Penning trap mass spectrometry
K. Blaum, D. Beck, G. Bollen, P. Delahaye, C. Guénaut, F. Herfurth, A. Kellerbauer, H.-J. Kluge, U. Köster, D. Lunney, S. Schwarz, L. Schweikhard, and C. Yazidjian
Proceedings of the XXXII Int. Workshop on 'Gross Properties of Nuclei and Nuclear Excitations' Hirschegg/Austria 2004, GSI Report, ISSN 0720-8715, 183-188 (2004).

Talks

23 August 2006
Invited seminar, Max Plank Institut für Kernphysik Heidelberg
• *"A new detector setup for* ISOLTRAP *and high-precision test of the IMME"*, Heidelberg, Germany

2-6 June 2004

3rd Joint Collaboration Meeting NIPNET, HITRAP, IONCATCHER RTDs

• *"A new LabVIEW based CS for* ISOLTRAP*"*, Krakow, Poland

18-20 April 2004

NIPNET Workshop on High-Precision Mass Measurements

• *"Technical improvements @* ISOLTRAP*: Towards mass measurements of very-short lived nuclides"*, Saariselkä, Finland

21-25 May 2003

2nd Joint Collaboration Meeting NIPNET, HITRAP, IONCATCHER RTDs

• "ISOLTRAP*: recent and future simulations"*,

• "REXTRAP *simulations: Charge exchange cross sections"*,

La Londe les Maures, France

Posters

3-8 September 2006

Trapped Charged Particles and Fundamental Physics Conference (TCP'06)

• *"Isospin symmetry in mirror nuclei: A study of the* $A = 35, T = 3/2$ *quartet with high precision mass measurement on* ^{35}*K at* ISOLTRAP*"*, Parksville, Vancouver Island, BC, Canada.

3-7 July 2006

Radioactive and Nuclear Beams Conference (RNB7)

• *"A test of the Isobaric Multiplet Mass Equation: High precision mass measurement on* ^{35}*K with the* ISOLTRAP *mass spectrometer"*, Cortina d'Ampezzo, Italy.

28-30 September 2005

Marie Curie Action: Making Europe more attractive for researchers

• *"A Precision Mass Balance: The Penning Trap Mass Spectrometer* ISOLTRAP*"*, Pisa/Livorno, Italy.

12-16 September 2004

Exotic Nuclei and Atomic Masses, ENAM 2004

• *"Commissioning and first on-line test of the new* ISOLTRAP *control system"*, Atlanta, USA.

19-27 August 2004

Euroschool on exotic beams 2004

• *"High precision mass measurements on* ^{35}*K for a test of the isobaric multiplet mass equation"*, University of Surrey GU2 7XH, United Kingdom.

Bibliography

[*] Notation: not quotable information, or references not available in journals are indexed with an asterisk.

[Ajze70] F. AJZENBERG-SELOVE AND G. IGO, *"A study of triton induced reactions in ^{37}Cl and ^{44}Ca"*, Nucl. Phys. A **142**, 641–648 (1970).

[Altz85] T. ALTZITZOGLOU *et al.*, *"Experimental Search for a Heavy Neutrino in the Beta Spectrum of ^{35}S"*, Phys. Rev. Lett. **55**, 8 799–802 (1985).

[AME03] *"The AME2003 atomic mass evaluation. (I) and (II)"*, See [Waps03] and [Audi03b] Nucl. Phys. A **729**, 129–676 (2003).

[Ande95] M. H. ANDERSON *et al.*, *"Observation of Bose-Einstein Condensation in a Dilute Atomic Vapor"*, Science, New Series **269**, 5221 198–201 (1995).

[Anto83] M.S. ANTONY, J. BRITZ, J.B. BUEB, AND A. PAPE, *"Mass defect of ^{13}B and the isobaric mass equation for the $A = 13$ quartet"*, Nucl. Instrum. Meth. A **527**, 567–579 (1983).

[Åström95] K.J. ÅSTRÖM AND T. HAGGLUND, *"PID controllers: Theory, Design and Tuning"*, Inst. Soc. of America (1995).

[Audi81] G. AUDI, *"Mesures de masses atomiques de noyaux exotiques"*, Ph.D Thesis, University of Orsay (1981).

[Audi03a] G. AUDI, O. BERSILLON, J. BLACHOT, AND A.H. WAPSTRA, *"The NUBASE evaluation of nuclear and decay properties"*, Nucl. Phys. A **729**, 3–128 (2003).

[Audi03b] G. AUDI, A.H. WAPSTRA, AND C. THIBAULT, *"The AME2003 atomic mass evaluation. (II). Tables, graphs and references"*, Nucl. Phys. A **729**, 337–676 (2003).

[Audi04*] G. AUDI, *"NUCLEUS-Win 2.1"*, http://amdc.in2p3.fr/web/nubdisp_en.html Download available at http://csnwww.in2p3.fr/AMDC/nucleus/nucWxp2.exe (2004).

[Audi05*] G. AUDI, *private communication* (2005).

[Audi06] G. AUDI, *"The history of nuclidic masses and of their evaluation"*, Int. J. Mass Spectrom. **251**, 85–94 (2006).

[Äyst81] ÄYSTO *et al.*, *"Decays of the $T_z = -2$ nuclei ^{20}Mg, ^{24}Si, and ^{36}Ca"*, Phys. Rev. C **23**, 2 879–887 (1981).

[Azue78] G. AZUELOS, G.R. RAO, AND P. TARAS, *"^{35}Cl$(p,n)^{35}$Ar threshold energy and its relation to the vanishing Cabibbo angle"*, Phys. Rev. C **17**, 443–446 (1978).

[Ban04] G. BAN *et al.*, *"Transport and cooling of singly charged noble gas ion beams"*, Nucl. Instrum. Meth. A **518**, 712 (2004).

[Ban05] G. BAN *et al.*, *"Measurements of the $\beta\nu$ angular correlation in nuclear β-decay"*, Nucl. Phys. A **752**, 67c–76c (2005).

[Baru07*] S. BARUAH, Ph.D Thesis, University of Greifswald, *in preparation.*

[Beck97] D. BECK, *"Massenbestimmung instabiler Isotope der Seltenen Erden um ^{146}Gd mit dem* ISOLTRAP*-Spektrometer"*, Ph.D Thesis, University of Mainz (1997).

[Beck01] M. BECK *et al.*, *"Space Charge Effects in a Gas Filled Penning Trap"*, Hyp. Int. **132**, 473–478 (2001).

[Beck03] M. BECK *et al.*, *"WITCH: a recoil spectrometer for weak interaction and nuclear physics studies"*, Nucl. Instrum. Meth. A **503**, 567–579 (2003).

[Beck04] D. BECK *et al.*, *"A new control system for* ISOLTRAP*"*, Nucl. Instrum. Meth. A **527**, 567–579 (2004).

[Benc59] N. BENCZER-KOLLER, A. SCHWARZSCHILD, AND C.S. WU, *"Decay of K^{43}"*, Phys. Rev. **115**, 108–114 (1959).

[Bene74] W. BENESON AND E. KASHY, *"First excited $A = 9$ isospin quartet"*, Phys. Rev. C **10**, 2633–2635 (1974).

[Berm93] G.E. BERMAN, M.L. PITT, F.P. CALAPRICE, AND M.M. LOWRY, *"New evidence against 17-keV neutrino emission in the β decay spectrum of ^{35}S"*, Phys. Rev. C **48**, rapid comm. R1–R4 (1993).

[Bene79] W. BENESON AND E. KASHY, *"Isobaric quartets in nuclei"*, Rev. Mod. Phys. **51**, 3 527–540 (1979).

[Berg02] I. BERGSTRÖM *et al.*, *"SMILETRAP – A Penning trap facility for precision mass measurements using highly charged ions"*, Nucl. Instrum. Meth. A **487**, 618–651 (2002).

[Bert70] G. BERTSCH AND K. KAHANA, *"T_z^3 term in the isobaric multiplet equation"*, Phys. Lett. B **33**, 3 193–194 (1970).

[Birg32] R.T. BIRGE, *"The calculation of errors by the method of least squares"*, Phys. Rev. **40**, 208–227 (1932).

[Blau02] K. BLAUM *et al.*, *"Carbon clusters for absolute mass measurements at* ISOLTRAP*"*, Eur. Phys. J. A **15**, 245–248 (2002).

[Blau03a] K. BLAUM *et al.*, *"The masses of ^{32}Ar and ^{33}Ar for fundamental tests"*, Phys. Rev. Lett. **91**, 260801 1–4 (2003).

[Blau03b] K. BLAUM *et al.*, *"Recent developments at* ISOLTRAP*: towards a relative mass accuracy of exotic nuclei below 10^{-8}"*, J. Phys. B **36**, 921–930 (2003).

[Blau04] K. BLAUM *et al.*, *"Population inversion of nuclear states by a Penning trap mass spectrometer"*, Europhys. Lett. **67**, 586–592 (2004).

[Blau05a] K. BLAUM *et al.*, *"*ISOLTRAP *mass measurements of exotic nuclides at $\delta m/m = 10^{-8}$"*, Nucl. Phys. A **752**, 317c–320c (2005).

[Blau05b*] K. BLAUM *et al.*, *"Design, Construction, Commissioning and Operation of* MATS*"*, Technical Design Report, submitted to GSI/FAIR Darmstadt (2005).

[Blau06] K. BLAUM, *"High-accuracy mass spectrometry with stored ions"*, Phys. Rep. **425**, 1–78 (2006).

[Bloc05] M. BLOCK *et al.*, *"The ion-trap facility* SHIPTRAP*. Status and perspectives"*, Eur. Phys. J. A **25**, s01, 49–50 (2005).

[Boll89] G. BOLLEN, *"Erste Massenmessungen an instabilen Isotopen mit Hilfe einer Penningfalle"*, Ph.D Thesis, University of Mainz (1989).

[Boll90] G. BOLLEN, B. MOORE, G. SAVARD, AND H. STOLZENBERG, *"The accuracy of heavy-ion mass measurements using the flight-ion cyclotron resonance in a Penning trap"*, J. Appl. Phys. **68**, 4355–4374 (1990).

[Boll92] G. BOLLEN *et al.*, *"Resolution of nuclear ground and isomeric states by a Penning trap mass spectrometer"*, Phys. Rev. C **46**, Rapid communication R2140–R2143 (1992).

[Boll96] G. BOLLEN *et al.*, "ISOLTRAP*: a tandem Penning trap system for accurate on-line mass determination of short-lived isotopes"*, Nucl. Instrum. Meth. A **368**, 675–697 (1996).

[Boll01] G. BOLLEN, *"Mass measurements of short-lived nuclides with ion traps"*, Nucl. Phys. A **693**, 3–18 (2001).

[Boll03] G. BOLLEN AND S. SCHWARZ, *"Ion traps for radioactive beam manipulation and precision experiments"*, Nucl. Instrum. Meth. B **204**, 466–473 (2003).

[Brad95] C. C. BRADLEY, C. A. SACKETT, J. J. TOLLETT, AND R. G. HULET, *"Evidence of Bose-Einstein Condensation in an Atomic Gas with Attractive Interactions"*, Phys. Rev. Lett. **75**, 1687–1690 (1995).

[Breh95] B. BREHM, J. GROSSER, T RUSCHEINSKI, AND M. ZIMMER, *"Absolute detection efficiencies of a microchannel plate detector for ions"*, Meas. Sci. Technol. **6**, 953–958 (1995).

[Brit98] J. BRITZ, A. PAPE, AND M. S. ANTONY, *"Coefficients of the isobaric mass equation and their correlations with various nuclear parameters"*, Atomic Data and Nuclear Data Tables **69**, 125–159 (1998).

[Brow86] L.S. BROWN AND G. GABRIELSE, *"Geonium theory: Physics of a single electron or ion in a Penning trap"*, Rev. Mod. Phys. **58**, 233 (1986).

[Brow88] B.A. BROWN AND B.H. WILDENTHAL, *"Status of the Nuclear Shell Model"*, Annu. Rev. Nucl. Part. Sci. **38**, 29–66 (1988).

[Brow05*] A. BROWN, *private communication* (2005).

[Burl01*] BURLE, *"Channeltron™ Electron Multiplier Handbook for mass Spectrometry"*, http://www.burle.com/cgi-bin/byteserver.pl/pdf/ChannelBook.pdf (2001).

[Caburn*] CABURN, http://www.caburn.co.uk

[Chen92] M. CHEN *et al.*, *"New Limits on the 17 keV Neutrino"*, Phys. Rev. Lett. **69**, 22 3151–3154 (1992).

[Coma88] E. COMAY, I. KELSON, AND A. ZIDON, *"Mass predictions by modified ensemble averaging"*, Atomic Data and Nuclear Data Tables **39**, 235–240 (1988).

[Cord82] R. CORDIA TAYLOR, M.C. HETTRICK, AND R.F. MALINA, *"Maximizing the quantum efficiency of microchannel plate detectors: The collection of photoelectrons from the interchannel web using an electric field"*, Rev. Sci. Instrum. **54**, 171–176 (1982).

[Cosy8.1*] *"COSY infinity 8.1"*, Michigan State University, http://bt.pa.msu.edu/index_files/cosy.htm

[Daly60] N.R. DALY, *"Scintillation Type Mass spectrometer Ion Detector"*, Rev. Sci. Instrum. **31**, 264–267 (1960).

[Davi95] K.B. DAVIS *et al.*, *"Bose-Einstein Condensation in a Gas of Sodium Atoms"*, Phys. Rev. Lett. **75**, 3969–3973 (1995).

[Deco02] B. DECONIHOUT, F. VURPILLOT, M. BOUET, AND L. RENAUD, *"Improved ion detection efficiency of microchannel plate detectors"*, Rev. Sci. Instrum. **73**, 1734–1740 (2002).

[Dill01a] J. DILLING, *"Direct mass measurements on exotic nuclei with* SHIPTRAP *and* ISOLTRAP*"*, Ph.D Thesis, University of Heildelberg (2001).

[Dill01b] J. DILLING *et al., "A physics case for* SHIPTRAP*: measuring the masses of transuranium elements"*, Hyp. Int. **132**, 491–495 (2001).

[Dill03] J. DILLING *et al., "The proposed* TITAN *facility at* ISAC *for very precise mass measurements on highly charged short-lived isotopes"*, Nucl. Instrum. Meth. B **204**, 492–496 (2003).

[Eide04] S. EIDELMAN *et al., "Particle physics booklet"*, Phys. Lett. **B592**, 1, Chapter 28: Particle detecors (2004).available on the PDG WWW pages (URL: http://pdg.lbl.gov/).

[Ekam04] J. EKAMAN *et al., "Unusual Isospin-Breaking and Isospin-Mixing Effects in the* $A = 35$ *Mirror Nuclei"*, Phys. Rev. Lett. **92**, 132502 1–4 (2004).

[Elli95] STEVEN R. ELLIOTT, *"Studies of highly charged ions with EBIT and super–EBIT"*, Nucl. Instrum. Meth. B **998**, 114–121 (1995).

[Endt90] P.M. ENDT, *"Energy levels of* $A = 21 - 44$ *nuclei (VII)"*, Nucl. Phys. A **251**, 1–803 (1990).

[Endt98] P.M. ENDT, *"Supplement to energy levels of* $A = 21$–44 *nuclei (VII)"*, Nucl. Phys. A **633**, 1–220 (1998).

[Fant73] B. FANT, J. KEINONEN, A. ANTTILA, AND M. BISTER, *"Investigation of Gamma Ray Transitions and Lifetimes in* ^{35}*Cl"*, Z. Physik **260**, 185–196 (1987).

[Ferr07*] R. FERRER, Ph.D Thesis, University of Mainz, *in preparation.*

[Fors01] O. FORSTNER, *"Beam-Preparation with* REXTRAP *for the* REX-ISOLDE *Experiment"*, Ph.D Thesis, University of TU Wien / CERN (2001).

[Frai06*] L.M. FRAILE, *private communication* (2006).

[Fras02] G.W. FRASER, *"The ion detection efficiency of microchannel plates (MCPs)"*, Int. J. Mass Spectrom. **215**, 13–30 (2002).

[Free69] J.M. FREEMAN, D.C. ROBINSON, AND G.L. WICK, *"The $^{35}Cl(p,n)^{35}Ar$ threshold and the vector interaction in the decay $^{35}Ar(\beta^+)^{35}Cl$"*, Phys. Lett. B **29**, 5 296–498 (1969).

[Free76] J.M. FREEMAN, *"(p,n) treshold measurements for accelerator calibration and the problem of Q-values reactions"*, Nucl. Instrum. Meth. **134**, 153–156 (1976).

[Frit01] T. FRITIOFF *et al., "Recent Progress with the* SMILETRAP *Penning Mass Spectrometer"*, Hyp. Int. **132**, 231–244 (2001).

[Frit02] T. FRITIOFF, *"Precision Improvements of Penning Trap Mass Measurements Using highly Charged Particles"*, Ph.D Thesis, University of Stockholm (2002).

[Garc95] A. GARCÍA *et al., "^{36}Ca β decay and the isobaric multiplet mass equation"*, Phys. Rev. C **51**, 6 3487–3488 (1995).

[Geor05] S. GEORGE, *"Application of the Ramsey method in high-precision Penning trap mass spectrometry"*, Master Thesis, University of Münster (2005).

[Gori01] S. GORIELY, F. TONDEUR, AND J.M. PEARSON, *"A Hartree-Fock nuclear mass table"*, Atomic Data and Nuclear Data Tables **77**, 311–381 (2001).

[Goos71] D.R. GOOSMAN, K.W. JONES, E.K. WARBURTON, AND D.E. ALBURGER, *"Masses and Half-Lives of ^{20}Na, ^{24}Al, ^{28}P, ^{32}Cl, and ^{36}K from the (p,n) Reaction"*, Phys. Rev. C **4**, 1800–1804 (1971).

[Guén05a] C. GUÉNAUT *et al., "Is $N = 40$ magic? The verdict from new, precision mass measurements"*, Eur. Phys. J. A **25**, s01, 33–34 (2005).

[Guén05b] C. GUÉNAUT *et al., "Mass measurements of $^{56-57}Cr$ and the question of shell reincarnation at $N = 32$"*, J. Phys. G **31**, 1765–1770 (2005).

[Guim03] V. GUIMARÃES *et al., "Structure of the unbound ^{11}N nucleus by the (^3He,^6He) reaction"*, Phys. Rev. C **67**, 064601 1–8 (2003).

[Gräf80] G. GRÄFF, H. KALINOWSKY, AND J. TRAUT, *"A direct determination of the proton electron mass ratio"*, Z. Phys. A **297**, 35–39 (1980).

[Grau69] A. GRAUE *et al., "A study of the ^{35}Cl levels by means of the ^{34}S(^{3}He,d)^{35}Cl reaction"*, Nucl. Phys. A **136**, 577–591 (1969).

[Hage04] U. HAGER, *"Precision measurement of atomic masses of radioactive nuclei employing Penning trap technique"*, Master Thesis, University of Hamburg (2004).

[Hage07*] U. HAGER, Ph.D Thesis, University of Jyväskylä, *in preparation.*

[Hard05] J. C. HARDY AND I. S. TOWNER, *"Superallowed $0^+ \rightarrow 0^+$ nuclear β decays: A critical survey with tests of the conserved vector current hypothesis and the standard model"*, Phys. Rev. C **71**, 055501 1–29 (2005).

[Heis32] W. HEISENBERG, *"Über den Bau der Atomkerne. I "*, Z. Physik **77**, 1 (1932).

[Henl69] E.M. HENLEY, AND C.E. LACY, *"Simple model for corrections to the Isobaric Multiplet Mass Equation"*, Phys. Rev. **184**, 1228–1229 (1969).

[Herf01a] F. HERFURTH *et al., "Breakdown of the Isobaric Multiplet Mass Equation at $A = 33, T = 3/2$"*, Phys. Rev. Lett. **87**, 142501 1–4 (2001).

[Herf01b] F. HERFURTH *et al., "A linear radiofrequency ion trap for accumulation, bunching, and emittance improvement of radioactive ion beams"*, Nucl. Instrum. Meth. A **469**, 254 (2001).

[Herf01c] F. HERFURTH, *"Ein neuer Ionstrahlkühler und -pulser für* ISOLTRAP *und Massenmessungen an radioaktiven Argonisotopen"*, Ph.D Thesis, University of Heidelberg (2001).

[Herf03] F. HERFURTH *et al., "Mass measurements and nuclear physics – recent results from* ISOLTRAP*"*, J. Phys. B **36**, 931–939 (2003).

[Herf05] F. HERFURTH *et al., "Recent high-precision mass measurements with the Penning trap mass spectrometer* ISOLTRAP*"*, Eur. Phys. J. A **25**, s01, 17–21 (2005).

[Herl06] A. HERLERT *et al., "Towards high-accuracy mass spectrometry of highly charged short-lived ions at* ISOLTRAP*"*, Int. J. Mass Spectrom. **251**, 131–137 (2006).

[Hoff99] E. DE HOFFMANN, J. CHARETTE AND V. SROOBANT, *"Spectrométrie de masse. Cours et exercices corrigés"*, **Dunond** 2^{e} édition. (1999).

[Hube72a] P. HUBERT *et al.*, *"Étude des états excités du noyau ^{35}Cl. (I) Courbe d'excitation de la réaction ^{34}S(p,γ)^{35}Cl, énergie et rapports d'embranchement des niveaux du ^{35}Cl"*, Nucl. Phys. A **195**, 485–501 (1972).

[Hube72b] P. HUBERT *et al.*, *"Étude des états excités du ^{35}Cl. (II) Vies moyennes"*, Nucl. Phys. A **195**, 502–512 (1972).

[Jäne69] J. JÄNECKE, *"The quartic isobaric multiplet mass equation"*, Nucl. Phys. A **128**, 632 (1969).

[Jäne88] J. JÄNECKE AND P.J. MASSON, *"Mass predictions from the Garvey-Kelson mass relations"*, Atomic Data and Nuclear Data Tables **39**, No. 2, 265–271 (1988).

[John83] I.P. JOHNSTONE, N. KUMAR, AND B. CASTEL, *"Isospin mixing in the lowest $T = 2$ state of ^{8}Be"*, Phys. Rev. C **27**, 846–851 (1983).

[Jone90] H.F. JONES, *"Groups, representations and physics"*, **IOP Publishing** Bristol (1990).

[Kell01] A. KELLERBAUER, T. KIM, R.B. MOORE, P. VARFALVY, *"Buffer gas cooling of ion beams"*, Nucl. Instrum. Meth. A **469**, 276–285 (2001).

[Kell02] A. KELLERBAUER, *"A study of the accuracy of the Penning Trap mass spectrometer* ISOLTRAP *and Standard-Model tests with superallowed beta decays"*, Ph.D Thesis, University of Heidelberg (2002).

[Kell03a] A. KELLERBAUER *et al.*, *"From direct to absolute mass measurements: A study of the accuracy of* ISOLTRAP*"*, Eur. Phys. J. D **22**, 53-64 (2003).

[Kell03b] A. KELLERBAUER, *"Recent improvements of ISOLTRAP: absolute mass measurements of exotic nuclides at 10^{-8} precision"*, Int. J. Mass Spectrom. **229**, 107–115 (2003).

[Kell03c] A. KELLERBAUER *et al.*, *"Carbon Cluster Ions For a Study of the Accuracy of* ISOLTRAP*"*, Hyp. Int. **146/147**, 307–312 (2003).

[Kell04a] A. KELLERBAUER *et al.*, *"Direct mass measurements on the superallowed emitter ^{74}Rb and its daughter ^{74}Kr: Isospin-symmetry-breaking correction for Standard-Model tests"*, Phys. Rev. Lett. **93**, 072502 1–4 (2004).

[Kell04b] A. KELLERBAUER *et al.*, *"Towards high-precision mass measurements on ^{74}Rb for a test of the CVC hypothesis and the unitarity of the CKM matrix"*, Nucl. Phys. A **746**, 635c–638c (2004).

[Klug93] H.-J. KLUGE AND G. BOLLEN, "ISOLTRAP*: A tandem Penning trap mass spectrometer for radioactive isotopes"*, Hyp. Int. **81**, 5–26 (1993).

[Kolh03] V. KOLHINEN, *"Penning trap for isobaric purification of radioactive beams at IGISOL"*, Ph.D Thesis, University of Jyväskylä (2003).

[Köni95a] M. KÖNIG *et al.*, *"Quadrupole excitation of stored ion motion at the true cyclotron frequency"*, Int. J. Mass Spectrom. **142**, 95–116 (1995).

[Köni95b] M. KÖNIG, *"Präzisionsmassenbestimmung instabiler Cäsium- und Bariumisotope in einer Penningfalle und Untersuchung der Ionenbewegung bei azimuthaler Quadrupolanregung"*, Ph.D Thesis, University of Mainz (1995).

[Köst02] U. KÖSTER, *"Resonance ionization laser ion sources"*, Nucl. Phys. A **701**, 441 (2002).

[Kozl05] V. YU. KOZLOV, *"WITCH, a Penning trap for weak interaction studies"*, Ph.D Thesis, University of Leuven (2005).

[Kret92a] M. KRETZSCHMAR, *"Single Particle Motion in a Penning Trap"*, Phys. Scripta **46**, 544 (1992).

[Kret92b] M. KRETZSCHMAR, *"Excitation of Particle Motions in a Penning Trap"*, Phys. Scripta **46**, 555 (1992).

[Krot85] H.W. KROTO *et al.*, *"C_{60}: Buckminsterfullerene"*, Nature **318**, No 6042, 162–163 (1985).

[Kugl92] E. KUGLER *et al.*, *"The new* CERN-ISOLDE *on-line mass-separator facility at the PS-Booster"*, Nucl. Instrum. Meth. B **70**, 41 (1992).

[Kugl00] E. KUGLER, *"The* ISOLDE *facility"*, Hyp. Int. **129**, 23–42 (2000).

[Land86] I.D. LANDAU, K.M. M'SIRDI, AND M. M'SAAD, *"Techniques de modélisation récursives pour l'analyse spectrale paramétrique adaptative; Recursive modelling techniques for adaptive parametric spectral analysis"*, Traitement du Signal **vol 3**, n° 4-5, 183–204 (1986).

[Land97] I.D. LANDAU, R. LORANO, AND M. M'SAAD, *"Adaptive control"*, **Springer** Communication and Control engineering Series (1997).

[Larm86] P. DE LARMINAT, *"Stabilité robuste dans la commande adaptative indirecte passive"*, **INRIA** Rapport de recherche, n° 509, publication interne n° 282 (1986).

[Larm00] P. DE LARMINAT, *"Control d'état standard"*, **Hermès** Paris, France (2000).

[Levk70] V.N. LEVKOVSKIĬ, AND I.V. KAZACHEVSKIĬ, *"Decay of K^{44} and Sc^{44}"*, Soviet Journal of Nuclear Physics **11**, 271Yadernaya Fizika **11**, 483–484 (1970).

[Lind54] TORSTEN LINDQVIST AND ALLAN C. G. MITCHELL, *"Disintegration of ^{43}K"*, Phys. Rev. **95**, 444–446 (1954).

[Linn63] Y.V. LINNIK, *"Méthode de moindres carrés"*, **Dunond** (1963).

[Lunn99] D. LUNNEY, *"Mesures des propriétés statiques des noyaux: utilisation des pièges ioniques"*, École Juliot-Curie (1999).

[Lunn03] D. LUNNEY, J.M. PEARSON, AND C. THIBAULT, *"Recent trends in the determination of nuclear masses"*, Rev. Mod. Phys. **75**, 1021–1082 (2003).

[Majo05] F.G. MAJOR, V.N. GHEORGHE, AND G. WERTH, *"Charged Particle Traps : Physics and Techniques of Charged Particle Field Confinement"*, **Springer** Series on Atomic, Optical, and Plasma Physics (2005).

[Maki99] KYOKO MAKINO, MARTIN BERZ, *"COSY INFINITY version 8"*, Nucl. Instrum. Meth. A **427**, 338–343 (1999).

[Mass88] P.J. MASSON AND J. JÄNECKE, *"Masses from an inhomogeneous partial difference equation with higher-order isospin contributions"*, Atomic Data and Nuclear Data Tables **39**, No. 2, 273–280 (1988).

[Mess62] A. MESSIAH, *"Quantum Mechanics, Vol 2 (Amsterdam: North-Holland)"*, (1962).

[Meun87] J-L. MEUNIER, *"A simple demonstration of the Wigner–Eckart theorem"*, Eur. J. Phys. **8**, 114–116 (1987).

[Meye76] M.A. MEYER, I. VENTER, W.F COETZEE, AND D. REITMANN, *"Energy levels of ^{35}Cl"*, Nucl. Phys. A **264**, 13–29 (1976).

[Mikl96] E. MIKLOVICOVA, M.A. LATIFI, M. M'SAAD AND I. HEJDA, *"PID adaptive control of the temperature in batch and semi-batch chemical reactors"*, Chemical Eng. Sci. **51**, 11 1339–1344 (1996).

[MKS*] MKS, http://www.mksinst.com

[Möll88] P. MÖLLER AND J.R. NIX, *"Nuclear masses from a unified macroscopic-microscopic model"*, Atomic Data and Nuclear Data Tables **39**, No. 2, 213–223 (1988).

[Mort93] J.L. MORTARA *et al.*, *"Evidence against a 17 keV Neurtino from ^{35}S Beta Decay"*, Phys. Rev. Lett. **70**, 4 394–397 (1993).

[MSaad00*] M. M'SAAD, *"Lectures notes"*, Ecole Nationale Superieure d'Ingénieurs de Caen (2000–2003).

[Mukh04a] M. MUKHERJEE *et al.*, *"The mass of ^{22}Mg"*, Phys. Rev. Lett. **94**, 150801 1–4 (2004).

[Mukh04b] M. MUKHERJEE, *"The mass of ^{22}Mg and a concept for a novel laser ion source trap"*, Ph.D Thesis, University of Heidelberg (2004).

[Murt69] M. MURTHY, *"Isobaric analogue states in nuclei"*, J. Phys. A **2**, 672–676 (1969).

[NNDC*] *"NNDC"*, http://www.nndc.bnl.gov/masses/, especially "mass.mas03.txt".

[NumRec*] *"Numerical recipes in C: the art of scientific computing"*, (ISBN 0-521-43108-5) Cambridge University Press, http://www.nr.com (1988-1992).

[Ober97] J. OBERHEIDE, P. WILHELMS, AND M. ZIMMER, *"New results on the absolute ion detection efficiencies of a micro channel plate"*, Meas. Sci. Technol. **8**, 351–354 (1997).

[Ohi85] T. OHI *et al.*, *"Search for heavy neutrinos in the beta decay of ^{35}S. Evidence against the 17 keV heavy neutrino"*, Phys. Lett. **160B**, 322–324 (1985).

[Orma89] W. E. ORMAND AND B. A. BROWN, *"Empirical isospin-nonconserving Hamiltonians for shell-model calculations"*, Nucl. Phys. A **491**, 1 (1989).

[Otto90*] TH. OTTO, *"Technical drawings for the* ISOLTRAP *setup"*, (1990).

[Ozaw00] A. OZAWA *et al.*, *"New Magic Number, $N = 16$, near the Neutron Drip Line"*, Phys. Rev. Lett. **84**, 24 5493–5495 (2000).

[Pani76] J.A. PANITZ AND J.A. FOSESCH, *"Areal detection efficiency of channel electron multiplier arrays"*, Rev. Sci. Instrum. **47**, 44–49 (1976).

[Phill99*] PHILIPS SEMICONDUCTORS, *"Data sheet: 1N4150-1N4151; High-speed diodes"*, (1999).

[PSF7.16*] *"Poisson super fish 7.16"*, Los alamos, http://laacg1.lanl.gov/laacg/services/download_sf.phtml

[Pyle02] M.C. PYLE *et al.*, *"Revalidation of the Isobaric Multiplet Mass Equation"*, Phys. Rev. Lett. **88**, 122501 1–4 (2002).

[Raha06] S. RAHAMAN *et al.*, *"On-line commissioning of* SHIPTRAP*"*, Int. J. Mass Spectrom. **251**, 146–151 (2006).

[Raim97] H. RAIMBAULT-HARTMANN *et al.*, *"A cylindrical Penning trap for capture, mass selective cooling and bunching of radioactive ion beams"*, Nucl. Instrum. Meth. B **126**, 378–382 (1997).

[Rain04] S. RAINVILLE, J.K. THOMPSON, AND D.E. PRITCHARD, *"An Ion Balance for Ultra-High-Precision Atomic Mass Measurements"*, Science **303**, 334–338 (2004).

[Rama83] S. RAMAN, A.T. JURNEY, D.A. OUTLAW, AND I.S. TOWER, *"^{34}Cl supperallowed β decay"*, Phys. Rev. C **27**, 3 1188–1198 (1983).

[Rams90] NORMAN F. RAMSEY, *"Experiments with separated oscillatory fields and hydrogen masers"*, Rev. Mod. Phys. **62**, 541–553 (1990).

[Ravn92] H.L. RAVN, *"Status and future developments of ion sources for on-line mass separators"*, Nucl. Instrum. Meth. B **70**, 107 (1992).

[Rodr02] D. RODRÍGEZ RUBIALES, *"A radiofrequency quadrupole buncher for accumulation and cooling of heavy radionuclides at* SHIPTRAP *and high precision mass measurements on unstable krypton isotopes at* ISOLTRAP*"*, Ph.D Thesis, University of Valencia (2002).

[Roos04] J. VAN ROOSBROECK *et al.*, *"Unambiguous identification of three β-decaying isomers in ^{70}Cu"*, Phys. Rev. Lett. **92**, 112501 1–4 (2004).

[Rusi95] S. M. RUSINKIEWICZ, *"Simultaneous Two-Ion Mass Spectroscopy"*, Bachelor of Science, University of Massachusetts Institute of Technology (1995).

[Sava91] G. SAVARD *et al.*, *"A new cooling technique for heavy ions in a Penning trap"*, Phys. Lett. A **158**, 247–252 (1991).

[Scha01] H. SCHATZ *et al.*, *"End Point of the rp Process on Accreting Neutron Stars"*, Phys. Rev. Lett. **86**, 3471 (2001).

[Scha06] H. SCHATZ, *"The importance of nuclear masses in the astrophysical rp-process"*, Int. J. Mass Spectrom. **251**, 293–299 (2006).

[Schm01] P. SCHMIT, "REXTRAP– *Ion accumulation , cooling and bunching for* REX-ISOLDE*"*, Ph.D Thesis, University of Mainz (2001).

[Schw98] S. SCHWARZ, *"Manipulation radioaktiver Ionenstrahlen mit Hilfe einer Paulfalle und direkte Massenmessungen an neutronenarmen Quecksilberisotopen mit dem* ISOLTRAP*-Experiment"*, Ph.D Thesis, University of Mainz (1998).

[Schw03] S. SCHWARZ *et al.*, *"The low-energy-beam and ion-trap facility at NSCL/MSU"*, Nucl. Instrum. Meth. B **204**, 507 (2003).

[Schw89] L. SCHWEIKHARD, *"Entwicklung neuer Methoden der Fouriertransformation-Ionenzyklotronresonanz-Massenspektrometrie"*, Ph.D Thesis, University of Mainz (1989).

[Schw90] L. SCHWEIKHARD, M. LINDINGER, AND H.-J. KLUGE, *"Parametric-mode-excitation/dipole-mode-detection Fourier-transform-ion-cyclotron-resonance spectrometry"*, Rev. Sci. Instrum. **61**, 3 1055–1058 (1990).

[Schw93] LUTZ SCHWEIKHARD AND ALAN G. MARSHALL, *"Excitation Modes for Fourier Tranform-Ion Cyclotron Resonance Mass spectrometry"*, J. Am. Soc. Mass Spectrom. **4**, 433–452 (1993).

[Schw05] L. SCHWEIKHARD, K. BLAUM, A. HERLERT, AND G. MARX, *"Atomic clusters and ion cyclotron resonance mass spectrometry: a fruitful combination"*, Eur. J. Mass Spectrom. **11**, 457–468 (2005).

[Seng60] S. SENGUPTA, *"Coulomb energies of Mirror nuclei"*, Nucl. Phys. **21**, 542–554 (1960).

[Seve06] N. SEVERIJNS, M. BECK AND O. NAVILIAT-CUNCIC, *"Tests of the standard electroweak model in beta decay"*, Rev. Mod. Phys., in print. (2006).

[Sim7.0] LLC IDAHO NATIONAL ENGINEERING & ENVIRONNEMENTAL LABORATORY, *"SimIon 7.0w-Win NT 05/09/2000"*, Copyright Bechtel BWXT Idaho, (1999).

[Simp89] J.J. SIMPSON AND A. HIME, *"Evidence of the 17-keV neutrino in the β spectrum of ^{35}S"*, Phys. Rev. D **39**, 7 1825–1836 (1978).

[Smit71] LINCOLN G. SMITH, *"Measurement of Six Light Masses"*, Phys. Rev. C **4**, 22–31 (1971).

[Stan04] M. STANIOU *et al.*, *"N=14 and 16 shell gaps in neutron-rich oxygen isotopes"*, Phys. Rev. C **69**, 034312 1–10 (2004).

[Tach88] TAKAHIRO TACHIBANA, MASAHIRO UNO, MASAMI YAMADA, AND SO YAMADA, *"Empirical mass formula with proton-neutron interaction"*, Atomic Data and Nuclear Data Tables **39**, No. 2, 251–258 (1988).

[VIsa05*] P. VAN ISACKER, *private communication* (2005).

[Waps03] A.H. WAPSTRA, G. AUDI, AND C. THIBAULT, *"The AME2003 atomic mass evaluation. (I) Evaluation of input data, adjustment procedures"*, Nucl. Phys. A **729**, 129–336 (2003).

[Wats67] D.D. WATSON, J.C. MANTHURUTHILL, AND F.D. LEE, *"Isobaric Analog States in ^{35}Cl"*, Phys. Rev. **164**, 1399–1407 (1972).

[Wies94*] M. WIESCHER, F.-K. THIELEMANN, K.-L. KRATZ, AND THE ISOLDE-REX COLLABORATION, *"A radioactive-ion beam experiment for the study of the astrophysical rp-process at* CERN-ISOLDE*"*, Letter of Intention, SCP CERN/ISC 94-21 ISC I 11, 1–6 (1994).

[Wign37] E. WIGNER, *"On the consequences of the symetry of the nuclear Hamiltonian on the spectroscopy of nuclei"*, Phys. Rev. **51**, 106–119 (1937).

[Wign58] E. WIGNER, *"Isotopic spin – A quantum number for nuclei"*, Proc. of the Robert A. Welch foundation conferences on chemical research, IV, 67–91 (1958).

[Wilk66] D.H. WILKINSON, *"The isobaric mass formula and coulomb energies in the 1p-shell"*, Proc. of the conference on isobaric spin in Nuclear Physics, A2, 30–59 (1966).

[Yazi05] C. YAZIDJIAN *et al.*, *"Commissioning and first on-line test of the new* ISOLTRAP *control system"*, Eur. Phys. J. A **25**, s01, 193–197 (2005).

[Yazi06] C. YAZIDJIAN *et al.*, accepted in Hyp. Int., (2006).

[Yazi07] C. YAZIDJIAN *et al.*, submitted to Phys. Rev. C, (2007).

[Zhao96] W.Z. ZHAO *et al.*, *"Ion storage and laser-induced fluorescence measurements in an RFQ trap"*, Nucl. Instrum. Meth. B **108**, 354–358 (1996).

[Zieg42] J.G ZIEGLER AND N.B. NICHOLS, *"Optimum Settings For Automatic Controllers"*, American Society of Mechanical Engineers (1942).

[Zuke02] A.P. ZUKER, S.M LENZI, G. MARTÍNEZ-PINEDO, AND A. POVES, *"Isobaric Multiplet Yrast Energies and Isospin Nonconserving Forces"*, Phys. Rev. Lett. **89**, 142502 1–4 (2002).

Acknowledgements, Danksagung, Remerciements

Mes pensées émues vont à mes différents directeurs de thèse (officiels, officieux ou ‘de complaisance’) Prof. Oscar Naviliat-Cuncic et Prof. Gilles Ban pour la partie française ainsi qu’au Prof. Klaus Blaum et au Prof. H-Jürgen Kluge pour la partie allemande, sans oublier mes encadrants locaux au CERN, que tous, j’ai usé jusqu’à la mœlle et qui doivent maudire du plus profond de leur être ce sombre jour, où ils ont accepté de m’exploiter comme esclave dans la galère expérimentale d’ISOLTRAP, ancrée depuis près d’un quart de siècle au port du CERN, quai ISOLDE, au bord du lac de Genève.

Hier mochte ich auch den deutsche ISOLTRAP-Teams von 2003 bis 2006 danken. Hierzu gehören Prof. Dr. Klaus Blaum, Dr. Dietrich Beck, Dr. Frank Herfurth, Prof. Dr. Alban Kellerbauer, Prof. Dr. Lutz Schweikhard, und der Vater das ISOLTRAP Experiment Prof. Dr. H.-Jürgen Kluge.

Here I would particularly acknowledge the almost over night support (24 hours per day, and the night if needed...) offered by Prof. Dr. Klaus Blaum during those 3 years spent at CERN. I also would like to thank the patience and the teaching skills of Dr. Dietrich Beck and Dr. Frank Herfurth for the steady explanation of the ‘How-To’ of the control system. Before meeting Prof. Dr. Alban Kellerbauer, erroneous and/or misleading terms were used, therefore I am very thankful for the nice precise and accurate discussions we had about uncertainties, standard deviations and errors bars. Je souhaiterais remercier de même Dr. Dave Lunney pour ces nombreuses idées, ainsi que le gardien de la table des masses atomiques Dr. Georges Audi pour sa contribution à la compilation des données du potassium. Au prof. M. M’Saad de l’ENSI–Caen, dont les cours n’ont pas toujours été considérés à leur juste valeur, je tiens à exprimer ma profonde gratitude pour son enseignement des notions ‘élémentaires’ de régulation, à mon sens indispansables à la culture de l’ingénieur moderne.

Merci a tous ceux qui m’ont aidé à supporter ces trois longues années d’emprisonnement au CERN. A mes compagnons d’infortune et mes voisins de cellule, Ulrike, Romain, Pierre, Martin et Sebastian sans oublier les differents clans d’ISOLDE (français, anglais, allemand, autrichien, italien, polonais, russe et même inuit) s’adresse ma sincère

reconnaissance. Une pensée amicale, aux personnes que j'ai eu l'occasion d'encadrer et qui ont dû me supporter (la réciproque étant vraie aussi d'ailleurs...), et en particulier à Nicolas Poilvert, qui superviser fût un réel plaisir.
Un grand merci au Club R.G. de l'ENSI Caen pour les fameuses 'vacances'. The Marie-Curie Fellowship' contract does not state about 'holidays', but 'thinking periods'... In fact they used to be drinking periods instead... Toujours avec modération bien sûr.
Je tiens aussi à remercier tout particulièrement 'Sensei MJ' pour son soutien constant, sa bonne humeur et ses leçons de Kendo façon 7 samouraïs, sans oublier les 'chtits 'Chtimis de Grenoble ainsi que leurs soirées spécial fondue(s) et rock (une seconde de silence pour les pauvres petons de Cat' et JF qui ont désespérément tenté de m'inculquer les mouvents de base). Et sans oublier Luke, qui a été attiré par le côté obscur des étoiles noires et qui a basculé vers le camp des sombres forces intergalactiques.
Un grand merci à 'K'arine pour ses coups de sang, ainsi que Nounours et Céline pour leurs concentrés de fichiers et d'idioties qui font toujours plaisir, tout spécialement vers 3h du matin en pleine période de faisceau et après 35h de veille.

Pour tout ceux qui n'ont pas été cités précédemment, je m'en excuse en prétextant que la place réservée dans ce mémoire ne serait pas suffisante pour tous vous remercier comme vous le méritez.

Quant aux autres, les oubliés volontaires et ceux qui ne se reconnaîtraient pas dans les précédentes catégories, c'est-à-dire les personnes qui ne m'ont pas aidé ou mis des bâtons dans les roues, que ces individus se rassurent. Je garderai gravé en mémoire leurs 'services précieux', et oublierai encore moins les sommets alpins de leurs désagréments administratifs, dont la cime n'a d'égal que la profondeur abyssale de leur incompétence.
A tous ces antipathiques oligarques bornés et apathiques technocrates népotiques de quatrième sous-sol, accidentellement réveillés durant leur repos diurne, s'adressent ma sincère inimitié et mon profond mécontentement. Confortant l'obscurantin univers vogonien, cette pseudo-élite malfaisante se complait avec délectation à appliquer aveuglément des règles surannées dans le seul but, non avouable, d'assurer la pérennité de leurs poussiéreux dossiers ordinaires et de faire perdurer leur sieste conventionnée. Toute proposition innovante sera accueillie par ces augustes personnes avec une moue dubitative, puis instantanément contestée et immanquablement rejetée par l'invocation mystique et souveraine d'un "Nous sommes débordés de travail à cause d'un problème informatique". Pour plus de clareté, traduisons en termes abscons : "Entre la pause café du matin, la cigarette et la collation de 10h, le déjeuner de midi et son pousse-café, le goûter de 16h, et les insuffisantes pauses syndicales qui nous ont été péniblement octroyées, nous trouvons à peine le temps de ranger nos affaires pour rentrer chez nous. Ainsi vous êtes bien candides si vous croyez que nous puissions nous permettre le luxe de bien vouloir condescendre à votre requête sibylline". Ces neurasténiques nombrilistes nous tracassent pour nous prouver qu'ils ne dorment pas. C'est magnifique, le fonctionnariat administratif, c'est comme ça.

En pénultième position, avant de finir ces remerciements sardonico-dithyrambiques, mes pensées se tournent vers mes parents, qui m'ont toujours encouragé et apporté leur soutien pour chaque décision que j'ai dû prendre, même si souvent, et à regrets, ces choix allaient à l'encontre des leurs sentiments personnels, en m'éloignant géographiquement chaque fois d'avantage du doux foyer familial.

Last but, not least I want here to thank the one without whom nothing would have been possible, in other words I acknowledge here the great work and help of . . . . myself.

A TOUS UN GRAND MERCI

Why waste time learning, when ignorance is instantaneous?

Calvin and Hobbes by Bill Watterson

Summary

Installed at the on-line isotope separator ISOLDE at CERN, the tandem Penning-trap spectrometer ISOLTRAP is designed to perform high-accuracy mass measurements on short-lived radionuclides. Based on the determination of the ion cyclotron frequency $\nu_c = qB/(2\pi m)$ in a strong magnetic field, the typical relative mass uncertainty is $\sigma(m)/m = 10^{-8}$ with a resolving power of up to $R = 10^7$. Accurate and precise mass values for specific unstable nuclides are important since they serve *e.g.* as a stringent test of nuclear models. The main part of this work is the design, installation and characterization of a new Channeltron-detector setup in order to increase the detection efficiency of ISOLTRAP by about a factor of 3. Since a detection efficiency close to 100% is reached, true single-ion experiments can be performed for the first time and exotic nuclides further away from the valley of stability and with very short half-lives are now accessible. Concerning mass measurements on short-lived nuclides, the masses of potassium isotopes from ^{35}K ($\tau_{1/2}$=178ms) up to ^{46}K ($\tau_{1/2}$=105s) have been measured with a relative precision of better than $1.6{\cdot}10^{-8}$. The accurate value of the ^{35}K mass contributes to a stringent test of the isobaric multiplet mass equation for the $A = 35$, $T = 3/2$ isospin quartet.

Keywords: Trapped ions — High resolution spectroscopy — Ion cyclotron resonance spectrometry — Nuclear counters — Nuclear models — Binding energy

Résumé

Situé auprès du séparateur isotopique en ligne ISOLDE du CERN, le spectromètre de masse ISOLTRAP, composé de pièges de Penning, est spécialement conçu pour une spectrométrie de masse de haute précision tout particulièrement pour les isotopes radioactifs de courte durée de vie. Reposant sur la mesure de la fréquence cyclotron $\nu_c = qB/(2\pi m)$ d'un ion piégé dans une cavité supraconductrice où règne un fort champ magnétique, la précision relative sur la masse atteinte par cette installation est de $\sigma(m)/m = 10^{-8}$ avec un pouvoir de résolution pour les ions contaminants de $R = 10^7$. Ces mesures réalisées pour des noyaux instables particuliers sont primordiales puisqu'elles servent de test draconien des modèles nucléaires. Le point principal de ce mémoire est la conception, l'installation et la caractérisation d'un nouveau détecteur Channeltron afin d'augmenter l'efficacité de détection d'ISOLTRAP d'un facteur proche de 3. Une efficacité de détection proche de 100% étant atteinte, il est désormais possible de manipuler un seul et unique ion mais aussi d'atteindre des noyaux exotiques encore plus éloignés de la vallée de stabilité et qui ont une durée de vie d'autant plus brève. Concernant la spectrométrie de noyaux à courte durée de vie, la masse des isotopes du potassium ^{35}K ($\tau_{1/2}$=178ms) au ^{46}K ($\tau_{1/2}$=105s) a été déterminée avec une incertitude relative inférieure à $1.6{\cdot}10^{-8}$. Cette justesse sur la masse du ^{35}K a contribué au test de l'équation de masse du multiplet isobarique pour le quartet de masse $A = 35$ et d'isospin $T = 3/2$.

Mots-clefs: Ions piégés — Spectroscopie à haute résolution — Spectrométrie de résonance cyclotronique ionique — Détecteurs de rayonnement — Modèles nucleaires — Energie de liaison